J. Hydrol. Hydromech., 67, 2019, 2, 113–120
DOI: 10.2478/johh-2018-0039

Experimental investigation of fine-grained settling slurry flow behaviour in inclined pipe sections

Pavel Vlasák*, Zdeněk Chára, Václav Matoušek, Jiří Konfršt, Mikoláš Kesely

Institute of Hydrodynamics of Czech Academy of Sciences, v. v. i., Pod Patankou 30/5, 160 00, Prague 6, Czech Republic.
E-mails: vlasak@ih.cas.cz; chara@ih.cas.cz; konfrst@ih.cas.cz
* Corresponding author. Tel.: +420 233109019. Fax: +420 233324861. E-mail: vlasak@ih.cas.cz

Abstract: For the safe and economical design and operation of freight pipelines it is necessary to know slurry flow behaviour in inclined pipe sections, which often form significant part of pipelines transporting solids. Fine-grained settling slurry was investigated on an experimental pipe loop of inner diameter D = 100 mm with the horizontal and inclined pipe sections for pipe slopes ranging from –45° to +45°. The slurry consisted of water and glass beads with a narrow particle size distribution and mean diameter d_{50} = 180 μm. The effect of pipe inclination, mean transport volumetric concentration, and slurry velocity on flow behaviour, pressure drops, deposition limit velocity, and concentration distribution was studied. The study revealed a stratified flow pattern of the studied slurry in inclined pipe sections. Frictional pressure drops in the ascending pipe were higher than that in the descending pipe, the difference decreased with increasing velocity and inclination. For inclination less than about 25° the effect of pipe inclinations on deposition limit velocity and local concentration distribution was not significant. For descending pipe section with inclinations over –25° no bed deposit was observed.

Keywords: Settling slurry; Effect of pipe inclination; Concentration distribution; Pressure drops; Deposition limit; Gamma-ray radiometry.

INTRODUCTION

Hydraulic pipeline transport is commonly used for transport of different bulk materials. Pipeline systems used in industrial applications, e.g. in mining, dredging, land reclamation, building, technological production lines and systems, long-distance product pipelines, or deep-ocean mining systems often contain inclined pipe sections (Thomas and Cowper, 2017; Van Wijket et al., 2016; Vlasak et al., 2012). From an operational point of view transport concentration, operational velocity and pressure drops are the most important parameters for transport pipelines design and operation. Very important - and one of the most difficult parameters to determine of a pipeline system transporting settling slurries - is the deposition limit velocity, V_{dl}, which is defined as the slurry velocity at which conveyed particles stop moving and start to form a deposit at the bottom of a pipe.

Settling slurries tend to stratify in horizontal and inclined parts of the pipeline system. The degree of stratification is sensitive to the flow velocity, slurry concentration, and affects both the pressure drops and the operational velocity at which the system should operate safe and without a danger of pipe blockage. The flow of settling slurry in a pipe may be defined as the flow with an asymmetrical concentration and velocity distribution. The slurry stratification, which affects the pressure drops and deposition limit velocity, depends on the angle of pipe inclination. Unfortunately, the effect of pipe inclination on flow conditions of settling slurries has not received an adequate attention up to now (Matousek et al., 2018).

Many theoretical and experimental studies have been carried out on transport of sand or fine particles in horizontal pipes (Gopaliya and Kaushal, 2016; Shook and Roco, 1991; Vlasak and Chara, 1999, 2009; Wilson et al., 2006). Wilson proposed a two-layer model for settling slurries with a fully stratified flow pattern (Wilson, 1976; Wilson et al., 2006). The layers differ in the local solids concentration and velocity. In each layer there is a difference in the velocities of the particles and the carrier liquid, which results in a transfer of energy from the fluid to the particles and from the particles to the pipe wall (Vlasak et al., 2017). The velocity difference between the solid and liquid phase, called slip velocity, is one of the mechanisms of particle transport in two-phase flow. Due to the slip velocity, there is difference between transport (C_d) and in situ (c_v) concentrations. Friction losses of heterogeneous slurries flow in a pipeline are strongly dependent on the concentration distribution (Matousek, 2002). A granular contact bed forms at the pipe invert, if the slurry velocity is slightly below the deposition limit. The bed slides along the pipe wall at velocities above the deposition limit and forms a stationary deposit below the deposition limit velocity. The contact bed is important contributor to the frictional pressure drops in settling slurry flow. The experimental data containing measured solids distributions are extremely scarce in the literature (Matousek et al., 2018).

EXPERIMENTAL EQUIPMENT AND MATERIAL

The experimental investigation was carried out in a pipe loop of inner diameter D = 100 mm made from smooth stainless steel pipes. The total length of the loop was 93 m, see Fig. 1. The horizontal (A) and inclinable (B) pipe sections are connected by abrasion resistant flexible hoses (12). Slurry flow was measured simultaneously in the ascending and the descending legs of the inclinable U-tube at slopes α varying from –45° to 45°. Slurry was prepared in a mixing tank (1) and pumped by a centrifugal slurry pump (GIW LCC-M 80-300) (2) with variable speed drive (Siemens 1LG4283-2AB60-Z A11) (3) to a measurement section of the loop.

The inclinable U-tube was used to determine the volumetric transport concentration C_d of the slurry using a method proposed by Clift and Clift (1981). Transparent viewing pipe sections (7) for visual observation of the slurry flow behaviour and deposition limit velocity V_{dl} were situated at the ends of the

horizontal pipe section (A) and ascending and descending inclinable section (B).

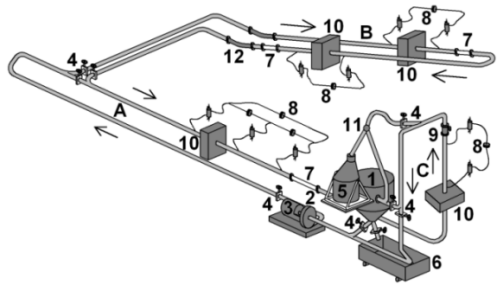

Fig. 1. Experimental test loop D = 100 mm (IH CAS, v. v. i., Prague).

A – horizontal section, B – inclinable section, C – short vertical section; 1 – mixing tank, 2 – centrifugal dredge pump, 3 – electric motor, 4 – slide valves, 5 – pycnometer, 6 – slurry output tank, 7 – transparent viewing pipe section , 8 – differential pressure transducer, 9 – electromagnetic flow meter, 10 – radiometric devices, 11 – flow divider, 12 – flexible hose.

The pressure drops were measured by Rosemount 1151DP differential pressure transducers (8) over 2-meter long measuring sections located in the horizontal and the inclined measuring sections. Slurry velocities were measured by a Krohne OPTIFLUX 5000 magnetic flow meter (9), mounted in the short vertical section (C) at the end of the circuit. The flow divider (11) and the sampling tank (5) allow for measuring of the flow rate and delivered concentration. For easier operation the loop is also equipped by slide valves (4) and a slurry output tank (6). Measurements were taken simultaneously in the ascending and descending sections of the loop from maximum values $V_{max} \approx 3.0$ m/s to values $V_{min} \approx 1$ m/s below the deposition limit velocity V_{dl}.

The loop was equipped with two gamma-ray density meters (10) placed on a special support and controlled by a computer. The support serves for vertical linear positioning of both the source and the detector to measure chord averaged vertical concentration profiles. The radiometric density meters consist of a γ-ray source (Caesium^{137}Cs, activity 740 MBq) and of a detector (a scintillating crystal of NaI(Tl)). A multi-channel digital analyser enables an evaluation of the energy spectrum of the detected signal. The measuring time period of 16 seconds was used to sense the local concentration at each position (Krupička and Matoušek, 2014; Vlasak et al., 2014).

The studied slurry consisted of rather fine glass beads B134 with narrow particle size distribution. Particle mean diameter d_{50} = 0.18 mm, d_{18} = 0.16 mm, d_{84} = 0.24 mm, particle density ρ_p = 2460 kg m^{-3}, Ar_{50} = 62.6) and water, the transport volumetric concentration C_d ranged from 12 to 34%. The slurry can be classified as partially stratified.

PRESSURE DROPS

The pressure drops, which depend on slurry concentration, C, and flow velocity, V, on physical properties of carrier liquid and conveyed particles, pipeline physical parameters, and of course on angle of the pipe inclination, α, that seems to be one of the most important flow parameter for transport pipeline design. The effect of pipe inclination on the pressure drops can be determined by using some semi-empirical correlations adapted to inclined pipes (Doron et al., 1997; Shook and Roco, 1991). The well-known Worster and Denny (1955) equation quantifies the effect of pipe inclination, α, on the total pressure drop, dp, over the pipe section, dL, or on hydraulic pressure gradient i = dp/dL, based on so called "the solids effect". The solids effect can be defined as the difference in pressure gradients between slurry and carrier liquid, $\Delta I = i_S - i_L$. For inclination α it is given as

$$-\Delta I\alpha = -(i_{S,\alpha} - i_L) = -\Delta i_0 \cos\alpha + (\rho_S - \rho_L)\, g \sin\alpha, \qquad (1)$$

where subscript S and L means slurry and liquid respectively, subscript α means flow in inclined pipe section and subscript 0 means flow in horizontal pipe section, ρ is the density, and g is the gravitational acceleration. The pipe inclination α has positive values in the ascending pipe ($\alpha = 0 \div +45°$) and negative values ($\alpha = 0 \div -45°$) in the descending pipe. The solids effect on the pressure drops in inclined flow consists of two parts – the frictional pressure drop (the first term on right-hand part of Eq. (1)) and the hydrostatic pressure (the second term on right-hand part of Eq. (1)).

Because the pressure gradient due to liquid flow friction i_L is independent of the pipe inclination, and the directly measured manometric pressure gradient $I_{S,\alpha}$ of slurry flow in the inclined pipe section is

$$I_{S,\alpha} = -i_L - (\, i_{S,0} - i_L\,) \cos\alpha + (\rho_S - \rho_L)\, g \sin\alpha, \qquad (2)$$

the slurry frictional pressure drop $i_{f,S,\alpha}$ in the inclined pipe is

$$i_{f,S,\alpha} = \; i_{L,0} + (i_{S,0} - i_L) \cos\alpha. \qquad (3)$$

Because the solid particles contribute to the frictional pressure drops through the solids effect according to Eq. (3), the frictional pressure drops should be the same at the same inclination angle for a positive or a negative slope. Thus, the slurry flow behaviour in ascending and descending inclined pipe sections should be also the same, including the distribution of solids in a pipe cross section. The Worster and Denny model neglects slip velocity V_{slip}, however, the slip velocity is not negligible in stratified and partially-stratified slurry flows in inclined pipe sections. The slip velocity depends on the difference between the mean in situ concentration, C_v, and the mean transport concentration, C_d. The difference becomes very important especially with increasing diameter of conveyed particles.

This is in contradiction with experimental results, which show that concentration distribution in ascending and descending pipes are different, and concentration profiles are sensitive to the angle of pipe inclination (Matoušek, 1996, 1997). The slurry was less stratified for ascending flow then for descending flow, and the difference increased with increasing size of conveyed particles. It is typical especially for partially-stratified inclined flow and is associated with the difference in velocity of a sliding bed in the ascending flow (slow sliding) and in the descending flow (fast sliding) (Matousek et al., 2018). Wilson and Byberg (1987) argued that Eq. (3) is theoretically valid for flow with a sliding bed, while for partially stratified flow the term cos α should be powered by a factor larger than unity. Gibert (1960) modified the Durand correlation for horizontal heterogeneous slurry flow to inclined flows with the power factor of cos α equal to 1.5 instead of 1.0.

Shook and Roco (1991) adapted the force balance equations of a two-layer model for inclined flow of partially stratified slurry. Doron et al. (1997) introduced a three layers model (a stationary bed, a moving bed, and suspended slurry flow). They assumed the uniform particle distribution in the bed layers and the distribution given by the turbulent diffusion equation in the suspended slurry layer. The model was verified by their own

experiments conducted in a pipe of D = 50 mm for pipe inclinations from –7° to +7°.

Layered models distinguish between transport and in situ concentrations and use for the hydrostatic pressure drops calculation the appropriate slurry density, based on the in situ concentration. Thus, the mean in situ concentration C_v should be used to calculate the static pressure drops in inclined pipe sections.

The results of directly measured pressure drops are manometric pressure drops, which for the glass beads slurry are illustrated in Fig. 2 for horizontal ($\alpha = 0$) and positive and negative slopes of the pipe sections (inclination angle α ranging from ±5° to ±45°). Fig. 2 shows the relationships $I_m(V)$, where a manometric pressure drop is expressed as the hydraulic gradient $I_m = -(\mathrm{d}p/\mathrm{d}L) / g\,\rho_w$, where ρ_w is the density of water.

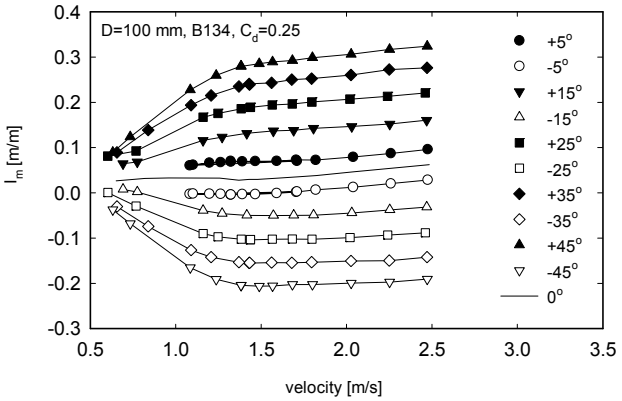

Fig. 2. Effect of the inclination angle α and flow velocity V on manometric pressure drops $I_{m,\alpha}$ (C_d = 0.25).

To recalculate the frictional pressure drops i from the measured manometric pressure drops I_m it is necessary to use the values of in situ concentration C_v , i.e. the values of C_v obtained by integrating concentration profiles over a cross section of the pipe. Because the measured values of C_v are available only at velocities where concentration profiles were measured, we used a linear interpolation of C_v values calculated for each measured velocity. The measured B 134 slurry can be classified as partially stratified; its mean in situ concentration C_v is dependent on flow velocity, especially for velocity close to and below deposition limit, as is illustrated in Fig. 3.

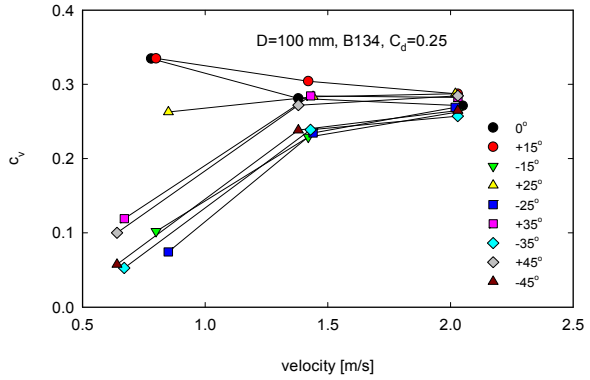

Fig. 3. Effect of the flow velocity V and inclination angle α on the slurry in situ volumetric concentration C_v (C_d = 0.25)

At velocities above deposition limit slurry concentration C_v remains approximately constant, only slightly higher than the transport concentration C_d. At velocities lower than V_{dl}, in situ concentration C_v decreased due to a stronger stratification of the flow throughout the loop, and forming of a sliding or stationary bed, where conveyed particles moved considerable slower than suspended particles and carrier liquid. The value of C_v decreased markedly for slurry velocity lower than the deposition limit.

The effect of pipe inclination α on frictional pressure drops i is illustrated in Fig. 4 for glass beads slurry of transport concentration C_d = 0.25 and pipe inclination from ± 5° to ± 45°. From pressure drops–velocity relationships it follows that frictional pressure drops for ascending and descending flow are not the same and hence do not agree with the assumption by the Worster-Denny formula (Eq. (3)). The data in Fig. 4 illustrates that Eq. (3) overestimates the frictional gradient in the ascending pipe section and vice versa for the descending section. The different effect of positive and negative inclination on frictional pressure drops can be accounted for using the layered models (Shook and Roco, 1991; Spelay et al., 2016; Wilson, 1976; Wilson et al., 2006).

The difference between ascending and descending flow and between horizontal and inclined flow increases from horizontal flow up to about inclination angle α = 25°, then slowly decreases. The difference decreases also with increasing flow velocity V. Maximum difference between horizontal and inclined flow are reached for slurry velocity close to the deposition limit V_{dl}. Frictional pressure drops in the ascending pipe are higher than that in the descending pipe, the difference decreases with increasing velocity and pipe inclination angle.

DEPOSITION LIMIT VELOCITY

The deposition limit velocity V_{dl} can be determined by a semi-empirical correlation or by applying principles of a mechanistic layered model. Durand and Condolios (1952) introduced the dimensionless deposition velocity for horizontal flow, the so called the Durand parameter

$$F_L = V_{dl} / (2g\,D\,(\rho_S/\rho_L - 1))^{1/2}. \quad (4)$$

The parameter F_L can be determined from an empirical nomogram as function of particle mean diameter and slurry concentration.

Since 1960, numerous correlations for deposition limit velocity have been developed, mostly based on dimensional analysis. Wilson (1976) determined for fully stratified slurry flow the deposition limit velocity from the force balance at slip point (i.e. the moment when the granular bed starts to slide) and introduced the well-known demi-McDonald nomogram (Wilson, 1979). To express the effect of pipe inclination α on deposition limit velocity V_{dl}, Wilson and Tse (1984) employed the difference between the Durand parameter F_L in an inclined and a horizontal pipe and introduced the change of Durand parameter

$$\Delta F_L = F_{L,\alpha} - F_{L,0}, \quad (5)$$

where $F_{L,\alpha}$ and $F_{L,0}$ is value valid for the inclined and horizontal pipe section, respectively. Wilson and Tse developed a computer program and after evaluation of their own experiments with narrow size distribution sand and gravel (from 1 to 6 mm in diameter) in a pipe of D = 76 mm they provided a nomogram relating ΔF_L with α. Their results were in agreement with measurements conducted by Hasimoto et al. (1980). De Hoog et al. (2017) also verified the Wilson-Tse nomogram for coarse material (gravel of d_{50} = 4.6, 6.3 and 12 mm) in a 100-mm pipe, and they found the maximum V_{dl} at the pipe inclination of about α = 30°.

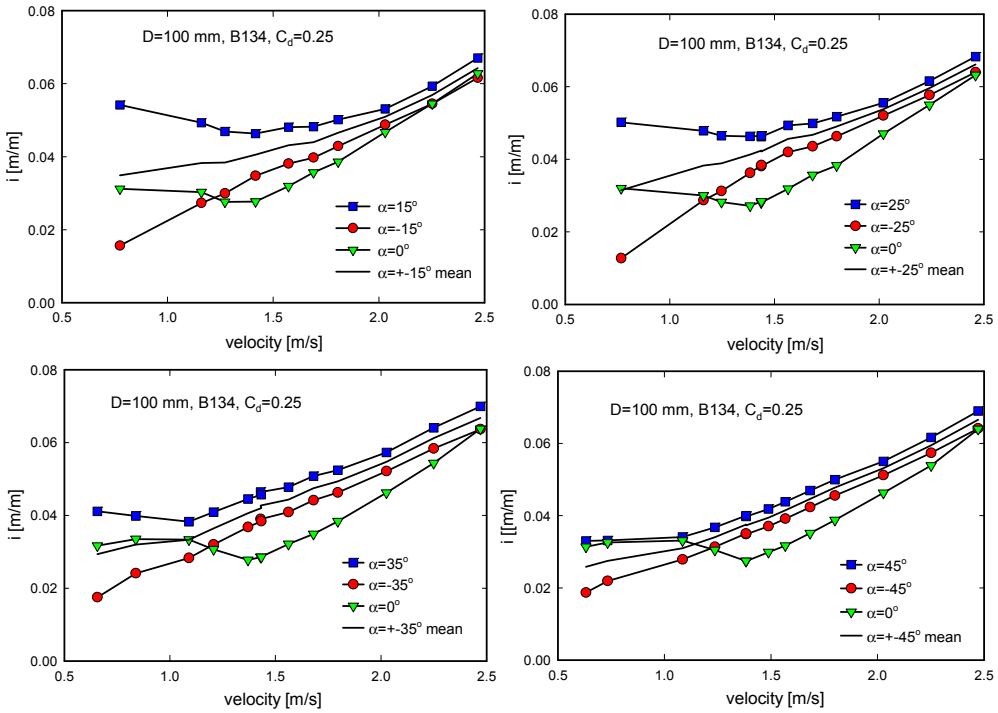

Fig. 4. Effect of the inclination angle α and flow velocity V on frictional pressure drops i.

Spelay et al. (2016) proposed two criteria for the effect of pipe inclination on the deposition limit velocity. The first is the Archimedes number

$$Ar = 4\, g\, \rho_L\, (\rho_p - \rho_L)\, d^3 /(3\mu_L^2), \tag{6}$$

where μ_L is the dynamic viscosity of the carrier liquid. The second is the turbulent suspension efficiency parameter

$$\mathrm{TSP} = (w / u_{*L,\,dl})\, \exp\,(d/D), \tag{7}$$

where w is particle terminal settling velocity, $u_{*L,\,dl}$ is the friction velocity of the carrier liquid at the deposition velocity. They suggested that the effect of inclination is negligible for $Ar < 500$ and TSP < 0.5, and recognized a trivial effect of the pipe inclination on deposition limit velocity for fine to medium sand and a significant effect for coarse sand and gravel.

The most often used method of an experimental determination of V_{dl} is a visual observation of a deposit formation in a transparent pipe section. In order to increase the accuracy of V_{dl} and reduce uncertainty, we combine visual observation and changes of the $i(V)$ diagram with application of radiometric measurement, i.e. to trace the velocity value at which a stationary bed first forms at the bottom of the pipe by measurement of local concentration in a layer close to the pipe invert. The deviation in determined values of V_{dl} may be considered satisfactory if it does not exceed say 20%.

In addition to chord-averaged concentration profiles, measured at three slurry velocities (i.e. above, below, and roughly at deposition limit V_{dl}), for each measured velocity V, a value of concentration, $c_{v,10}$, in the layer at a height of 10 mm above the pipe invert was measured to identify the origin of deposit at the bottom of the pipe.

From Fig. 5 it is obvious, that when the flow velocity V gradually decreased, $c_{v,10}$ remained nearly constant until the deposition limit is approached. For the flow velocity V close to the deposition limit, the local concentration $c_{v,10}$ gradually increased and relatively quickly reached a value typical for the

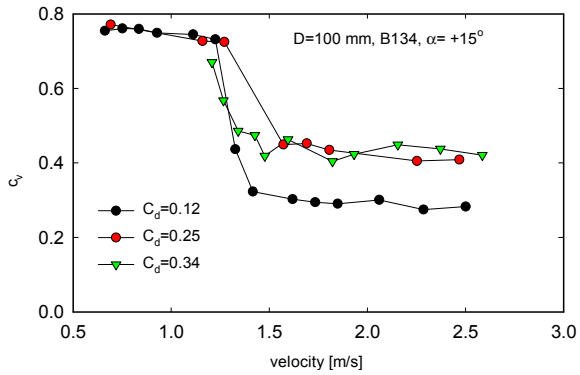

Fig. 5. Effect of the flow velocity V and slurry transport volumetric concentration C_d on chord averaged local concentration c_v in height y = 10 mm above pipe bottom.

stationary bed, since a bed layer is formed at a velocity lower than V_{dl}. Increasing of $c_{v,10}$ starts at V between 1.50 and 1.60 m/s and the stationary bed is formed at a slurry velocity below 1.25 m/s. The deposition limit should be between these two velocity values. By comparing the measured concentration profiles and the local concentration $c_{v,10}$, we estimated that the deposition on the pipe bed occurred at a local concentration value of $c_{v,10} \approx 0.50$. Thus the deposition velocity V_{dl} is reached, depending on the mean concentration, at about 1.40 m/s for a mean transport concentration C_d = 0.12 and 0.34 and pipe inclination of $\alpha = 15°$.

Table 1 shows the deposition limits obtained both by visualization method and by determining from the I/V diagrams. Obviously, the values are not very different from each other. The difference between values ranges from 5% to 15% for ascending flow. Significant differences are for descending flow, where, for so fine material as B134, it had often been difficult to identify the bed layer visually. From the experimental data we can see that the V_{dl} in the inclined pipes is slightly lower than in the horizontal pipe. Deposition limit V_{dl} in the ascend-

ing pipe section (determined by visual observation) reaches minimum values for an inclination angle α between 15° and 25°, then for higher pipe inclination it again slightly increased. On the contrary, in the descending pipe, the deposition limit values from the visual observation decreased significantly.

Table 1. Deposition limit, B134, $C_d = 0.25$.

α [°]	0	± 5	± 15	± 25	± 35	± 45
from I / V diagram						
V_{dl} [m/s]; $\alpha > 0$	1.50	1.35	1.38	1.43	1.43	1.50
V_{dl} [m/s]; $\alpha < 0$	1.50	1.34	1.38	1.43	1.43	1.50
from visualisation						
V_{dl} [m/s]; $\alpha > 0$	1.45	1.47	1.25	1.25	1.43	1.50
V_{dl} [m/s]; $\alpha < 0$	1.45		1.25	0.95	0.80	0.65

LOCAL CONCENTRATION DISTRIBUTION

Effect of pipe inclination on concentration distribution of partially stratified settling slurry flow behaviour was confirmed by measurement of chord-averaged local concentration profiles, $c_v(y)$.

Both the slurry flow behaviour in the pipe, and, in particular, the concentration distribution which significantly influences the degree of stratification and sliding bed friction, are important for the determination of the pressure losses and the deposition limit velocity. From the mutual comparison of the concentration distribution in ascending and descending pipe sections, the different structure of the flow and the influence of the slope of the pipe on the balance between the resisting of conveyed particles and stress produced by the flow of carrier liquid are obvious (Wilson, 1976, Wilson et al., 2006).

In Fig. 6 the effect of the angle of inclination on the shape of experimental chord-averaged concentration profiles, $c_v(y)$, is illustrated for three different slurry velocities V and pipe inclination from horizontal to +45° or –45° at constant transport concentration $C_d = 0.25$. The concentration profiles confirmed the stratified flow pattern in inclined pipe sections (Krupicka and Matousek, 2014; Vlasak et al., 2016, 2017). The concentration profiles showed different degrees of stratification for the positive and negative slope of the flow. For slurry velocity near and above the deposition limit the ascending flow was less stratified than the corresponding descending flow, the degree of stratification decreased with increasing angle of inclination.

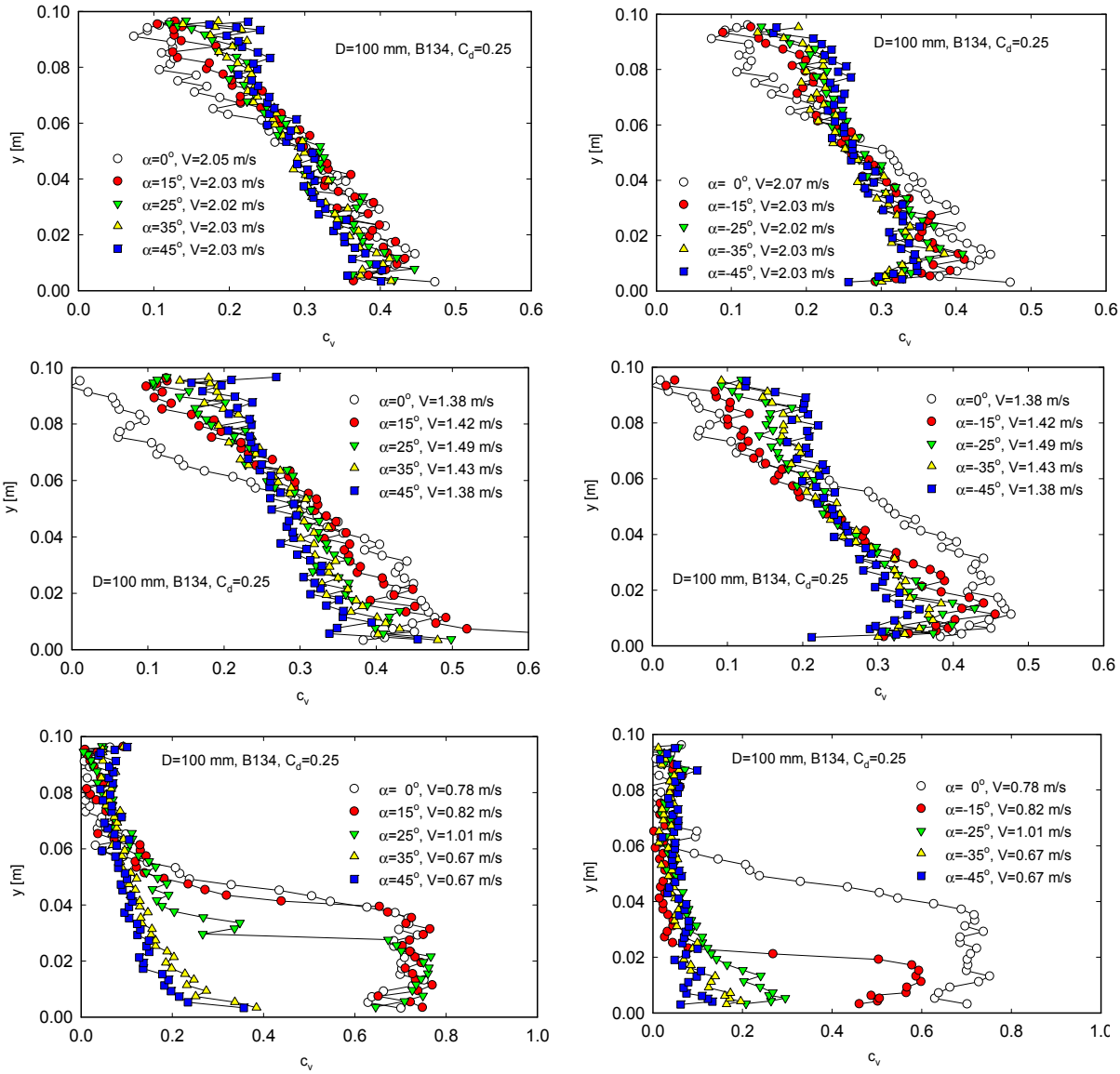

Fig. 6. Effect of the pipe inclination α on chord-averaged local concentration profiles ($C_d = 0.25$).

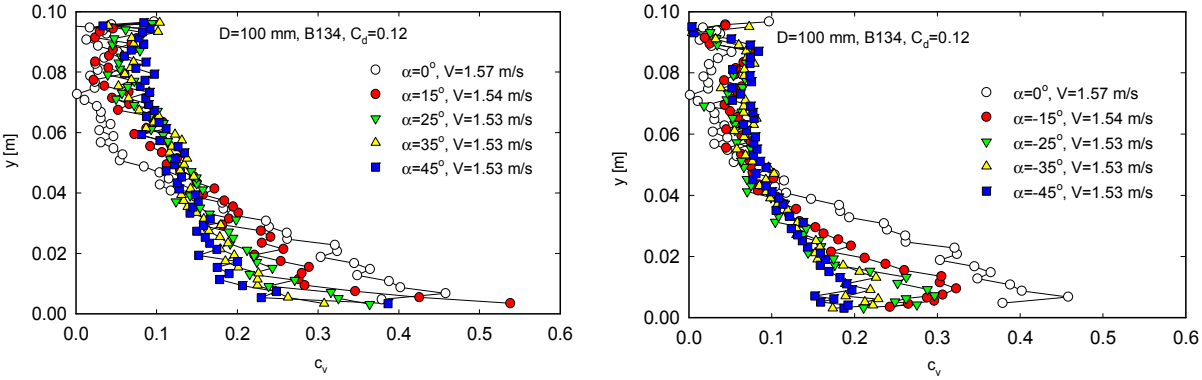

Fig. 7. Effect of the pipe inclination α on chord-averaged local concentration profiles ($C_d = 0.12$).

The thickness of the sliding bed tended to decrease with the increasing inclination angle, for slurry velocity $V \approx 2$ m/s no sliding bed was observed in ascending flows.

Local concentration reached a maximum near the pipe invert, however, for flow velocities above the deposition limit, i.e. $V \approx 2.0$ m/s, the slope of the concentration profile increased with increasing inclination angle α, see Fig. 6 (upper panels). Similar flow pattern was observed for velocities $V \approx 1.45$ m/s, i.e. close to the deposition limit (middle panels). For $V < V_{dl}$ sliding or stationary beds were observed in ascending pipe for inclination angle $\alpha < 30°$, for higher inclination angles ($\alpha > 30°$) the sliding bed disappeared (lower panel left). For descending flow the thickness of sliding bed was significantly less and the bed disappeared for pipe slope $\alpha > 15°$.

The slope effect on the concentration profiles was significant for low pipe inclination angles (i.e. for $\alpha < 25°$), however, the flow remained almost fully stratified. For the steeper slopes the degree of stratification was strongly affected (decreased) by the axial component of the gravity force the flow pattern did not exhibit any bed at inclination angle $\alpha > 30°$.

Similar behaviour was observed for lower transport concentration $C_d = 0.12$ (see Fig. 7). Slurry concentration in the bed layer significantly decreased with increasing inclination angle α, both for ascending and descending pipe sections. Local in situ concentration at the top of the pipe was higher in the ascending pipe section than that in the descending section. With increasing inclination angle the solid particles, due to the increasing effect of the axial component of the gravitational force, reached probably higher velocities and thus lower values of local in situ concentration.

The same flow behavior of the slurry was also observed for the highest measured transport concentration $C_d = 0.34$, see Fig. 8. Stratification of the slurry decreases with the increasing angle of inclination, the local concentration c_v in the upper part of the pipe increases, more pronounced in the ascending pipe section.

Difference between ascending and descending flows is illustrated in Fig. 9 for constant positive and negative couple of inclination angle α and different flow velocities V. For low inclination angle $\alpha = \pm 15°$ and velocity $V < V_{dl}$ a bed deposit was observed in both ascending and descending pipe legs. Bed layer in the descending pipe reached substantially lower values of local concentration c_v and deposit height y than that in the ascending pipe ($c_v \approx 0.60$ instead 0.75, and $y/D \approx 0.2$ instead 0.4). For velocity $V \approx V_{dl}$ a very thin deposit was observed in the ascending pipe only. For inclination angles $\alpha > \pm 35°$ no deposit was observed. It was confirmed that the effect of pipe inclination on concentration distribution for low values of inclination angle α was not significant, similarly as for pressure drops (Spelay et al., 2016; Vlasak et al., 2014, 2016, 2017). The local concentration in the ascending pipe section was always higher than that in the descending pipe section.

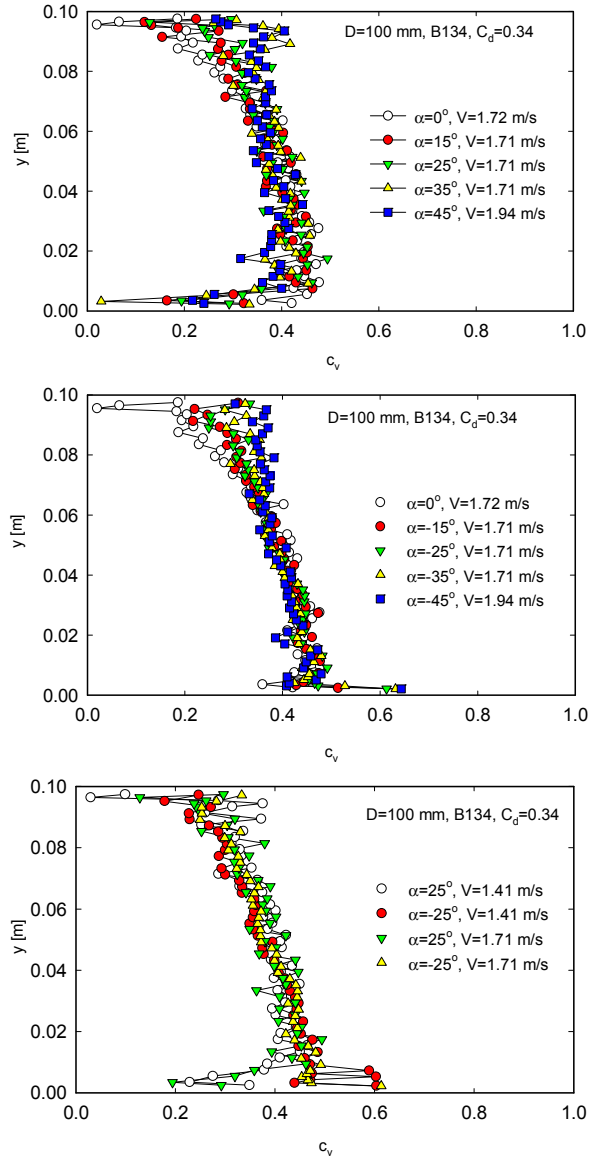

Fig. 8. Effect of the pipe inclination α on chord-averaged local concentration profiles ($C_d = 0.34$).

Deposition limit V_{dl} in the ascending pipe was slightly lower than that in the horizontal pipe ($V_{dl} \approx 1.5$ m/s); it decreased with increasing pipe inclination and slurry velocity. In the descending pipe no deposition limit was observed for angles $\alpha < -25°$.

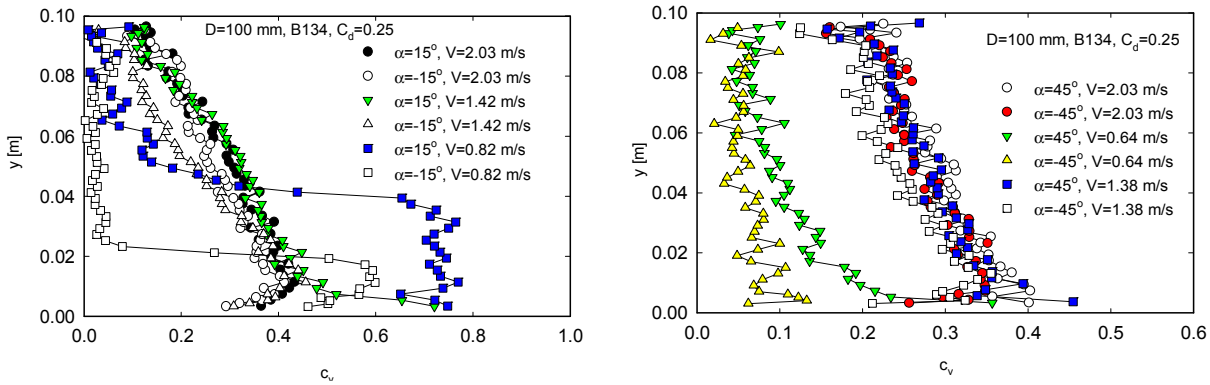

Fig. 9. Effect of mean slurry velocity V on chord-averaged local concentration profiles (C_d = 0.25).

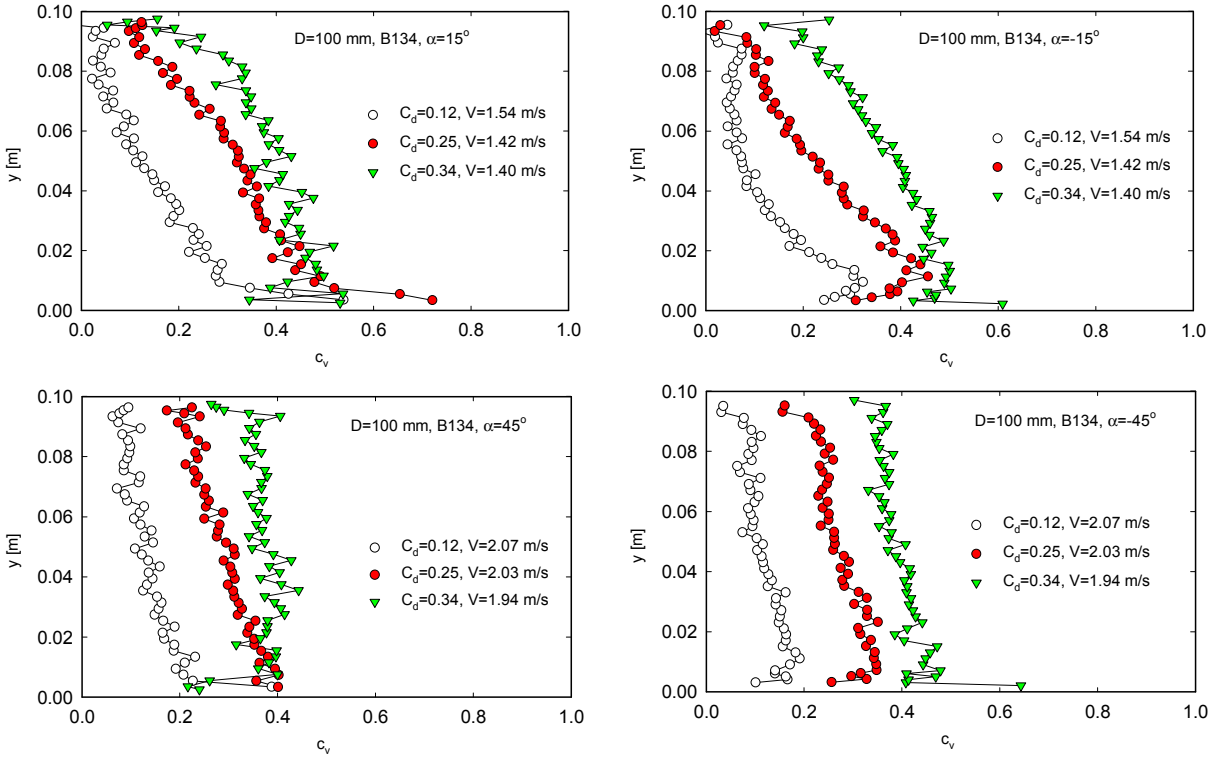

Fig. 10. Effect of transport concentration C_d on chord-averaged local concentration profiles for constant slurry velocity V and pipe inclination α.

The influence of the mean transport concentration C_d on the chord-averaged concentration profiles is illustrated in Fig. 10 for two values of the slurry flow velocity ($V \approx 1.5$ and 2.0 m/s). The graphs document decrease of the degree of stratification with increasing pipe slope and increasing transport concentration C_d. Whereas, for the angle of inclination $\alpha = \pm 15°$, the stratification is visible even for higher slurry velocities (see upper panels), for the angle of inclination $\alpha = \pm 45°$, the stratification was considerably smaller, and for V = 1.94 m/s and C_d = 0.34 it practically disappeared in the ascending pipe (see lower panel left).

CONCLUSIONS

The effect of pipe inclination, transport concentration, and mean velocity on flow behaviour of fine-grained settling slurry was studied in an experimental pipe loop of inner diameter D = 100 mm with inclinable pipe sections. The pressure drops, deposition limit velocity, and concentration distribution were studied for slurry of narrow particle size distribution glass beads (B134, mean diameter d_{50} = 180 μm) and water.

The visualization and local concentration measurements revealed the stratified flow pattern of the settling slurry in inclined pipe sections.

Frictional pressure drops in the ascending pipe were higher than that in the descending pipe; this fact is in contradiction with the assumption of the Worster-Denny formula. The difference decreased with increasing velocity and pipe inclination. Based on the conducted experiments it has been found that for fine-grained settling slurry the effect of the hydrostatic component of the pressure drops becomes more significant than the effect of the frictional pressure drops with increasing pipe inclinations.

Difference between ascending and descending flow and between horizontal and inclined flow increased from horizontal flow up to about inclination angle α = 25°, then slowly decreased.

The mean in situ concentration for descending flow was always lower than that for the ascending flow. For low inclination angle α lower than about ±25° the effect of pipe inclination on local concentration distribution was not significant.

The concentration profiles showed different degrees of stratification for the positive and negative slope of the pipe. For slurry velocity near and above the deposition limit the ascending flow was less stratified than the corresponding descending flow, the degree of stratification decreased with increasing angle of inclination. The slope effect on the concentration profiles was significant for low pipe inclination angle (i.e. for $\alpha < 25°$).

With increasing mean slurry velocity the local concentration in the bed layer decreased; this effect increased with increasing inclination angle.

Deposition limit in the inclined pipes was slightly lower than in the horizontal pipe, the minima reached the values of V_{dl} for an inclination angle α about 25°, then in the ascending pipe the deposition limit again slightly increased. For negative pipe inclination ($\alpha < -15°$) no bed deposit was observed.

Acknowledgement. Supports under the project 17-14271S of the Grant Agency of the Czech Republic, and RVO: 67985874 of the Czech Academy of Sciences are gratefully acknowledged.

REFERENCES

Clift, R., Clift, D.H.M., 1981. Continuous measurement of the density of flowing slurries. International Journal of Multiphase Flow, 7, 5, 555–561.

Doron, M., Simkhis, M., Barnea, D., 1997. Flow of solid-liquid mixtures in inclined pipes. International Journal of Multiphase Flow, 23, 313–323.

Durand, R., Condolios, E., 1952. Étude expérimentale du refoulement des matériaux en conduite. 2émes Journées de l´Hydralique, SHF, Grenoble.

Gibert, R., 1960. Transport hydraulique et refoulement des mixtures en conduites. Annales Des Ponts et Chaussees, 12, 307–374.

Gopaliya, M.K., Kaushal, D.R., 2016. Modeling of sand-water slurry flow through horizontal pipe using CFD. Journal of Hydrology and Hydromechanics, 64, 3, 261–272.

Hashimoto, H., Noda, L., Masuyama, T., Kawashima, T., 1980. Influence of Pipe Inclination on Deposit Velocity, Proc. HYDROTRANSPORT 7, BHR Group, Sendai, Japan, 4–6 November 1980, 231–244.

De Hoog, E., in't Veld, M., Van Wijk, J., Talmon, A., 2017. An experimental study into flow assurance of coarse inclined slurries. In: Proceedings of Transport and Sedimentation of Solids Particles, Prague, Czech Republic.

Krupicka, J., Matousek, V., 2014. Gamma-ray-based measurement of concentration distribution in pipe flow of settling slurry: vertical profiles and tomographic maps. J. Hydrology and Hydromechanics, 62, 2,126–132.

Matousek, V., 1996. Internal structure of slurry flow in inclined pipe. Experiments and mechanistic modelling, Proc. HYDROTRANSPORT 13, BHRG, Cranfield, UK, 1996, 187–210.

Matousek, V., 1997. Flow Mechanism of Sand-Water Mixtures in Pipelines. PhD Thesis. Delft University Press, Delft.

Matousek, V., 2002. Pressure drops and flow patterns in sand–mixture pipes. Experimental Thermal and Fluid Science, 26, 693–702.

Matousek, V., Krupicka, J., Kesely, M., 2018. A layered model for inclined pipe flow of settling slurry. Powder Technology, 333, 317–326.

Spelay, R.B., Gillies, R.G., Hashemi, S.A., Sanders, R.S., 2016. Effect of pipe inclination onthe deposition velocity of settling slurries. The Canadian Journal of Chemical Engineering, 94, 1032–1039.

Shook, C.A., Roco, M.C., 1991. Slurry Flow. Principles and Practice. Butterworth-Heinemann, Stoneham, USA.

Thomas, A.D., Cowper, N.T., 2017. The design of slurry pipelines – historical aspects. In: Proc. HYDROTRANSPORT 20, Melbourne, Australia, pp. 7–22.

Vlasak, P., Chara, Z., 1999. Laminar and turbulent flow experiments with yield-power law slurries. Powder Technology, 104, 200–206.

Vlasak, P., Chara, Z., 2009. Conveying of solid particles in Newtonian and non-Newtonian carriers. Part. Sci. Technol., 27, 5, 428–443.

Vlasak, P., Kysela, B., Chara, Z., 2012. Flow structure of coarse-grained slurry in horizontal pipe. Journal of Hydrology and Hydromechanics, 60, 2, 115–124.

Vlasak, P., Chara, Z., Krupicka, J., Konfrst, J., 2014. Experimental investigation of coarse particles-water mixture flow in horizontal and inclined pipes. Journal of Hydrology and Hydromechanics, 62, 3, 241–247.

Vlasak, P., Chara, Z., Konfrst, J., Krupicka, J., 2016. Distribution of concentration of coarse particle-water mixture in horizontal smooth pipe. Canadian Journal of Chemical Engineering, 94, 1040–1047.

Vlasak, P., Chara, Z., Konfrst, J., 2017. Flow behaviour and local concentration of course particles-water mixture in inclined pipes. Journal of Hydrology and Hydromechanics, 65, 2, 183–191.

VanWijk, J.M., Talmon, A.M., Van Rhee, C., 2016. Stability of vertical hydraulic transport processes for deep ocean mining: an experimental study, Ocean Eng., 125, 203–213.

Wilson, K.C., 1976. A unified physically based analysis of solid-liquid pipeline flow. In: Stephens, H.S., Streat, M., Clark, J., Coles, N.G. (Eds.): Proc. HYDROTRANSPORT 4. B.H.R.A., Cranfield, UK, Pap. A1.

Wilson, K.C., 1979. Deposition-limit nomograms for particles of various densities in pipeline flow. In: Proc. HYDROTRANSPORT 6, BHRA, Cranfield, UK, pp. 1–12.

Wilson, K.C., Byberg, S.P., 1987. Stratification-ratio scaling technique for inclined slurry pipelines. In: Proc. 12th International Conference on Slurry Technology, STA, Washington, USA, pp. 59–64.

Wilson, K.C., Tse, J.K.P., 1984. Deposition limit for coarse-particle transport in inclined pipes. In: Proc. HYDROTRANSPORT 9, BHRA Fluid Engineering, Cranfield, UK, pp. 149–169.

Wilson, K.C., Addie, G.R., Sellgren, A., Clift, R., 2006. Slurry Transport Using Centrifugal Pumps. Springer, US.

Worster, R.C., Denny, D.F., 1955. Hydraulic transport of solid materials in pipelines. P. I. Mech. Eng., 169, 563–586.

Received 15 August 2018.
Accepted 25 September 2018

J. Hydrol. Hydromech., 67, 2019, 2, 121–128
DOI: 10.2478/johh-2018-0040

Bank erosion of the Tŕstie stream: BANCS model predictions vs. real bank erosion

Zuzana Allmanová[1], Mária Vlčková[1], Martin Jankovský[2*], Matúš Jakubis[1], Michal Allman[1]

[1] Department of Forest Harvesting, Logistics and Ameliorations, Faculty of Forestry, Technical University in Zvolen, T.G. Masaryka 24, 960 53 Zvolen, Slovakia.
[2] Department of Forestry Technology and Constructions, Faculty of Forestry and Wood Sciences, Czech University of Life Sciences Prague, Kamýcká 129, 165 00 Prague 6 – Suchdol, Czechia.
[*] Corresponding author. Tel.: +420 22438 3729. E-mail: jankovskym@fld.czu.cz

Abstract: This paper focused on predicting the bank erosion through the Bank Assessment for Non-point source Consequences of Sediment (BANCS) model on the Tŕstie water stream, located in the western Slovakia. In 2014, 18 experimental sections were established on the stream. These were assessed through the Bank Erosion Hazard Index (BEHI) and the Near Bank Stress (NBS) index. Based on the data we gathered, we constructed two erosion prediction curves. One was for BEHI categories low and moderate, and one for high, very high, and extreme BEHI. Erosion predicted through the model correlated strongly with the real annual bank erosion – for low and moderate BEHI, the R^2 was 0.51, and for high, very high and extreme BEHI, the R^2 was 0.66. Our results confirmed that the bank erosion can be predicted with sufficient precision on said stream through the BANCS model.

Keywords: BANCS model; Bank erosion; Prediction curves.

INTRODUCTION

Bed-forming discharges, caused by heavy rainfall, extreme precipitation, and rapid snow melt in spring, occur in water courses more frequently, due to, among other things, the climate change. Extremely high discharges often lead to extreme catchment erosion rates. Problems caused by siltation of the drinking water reservoirs and erosion of fertile land into seas and oceans are becoming serious. Therefore, scientists and practitioners devote their attention to catchment erosion.

Bull (1997) conducted research of bank erosion in the upper part of the River Severn, UK, which has the total catchment area of 380 km^2. She used manual and photo-electronic erosion pins to estimate the bank erosion and observed annual erosion rates between 12.9 mm year^{-1} and 460.6 mm year^{-1}. Similarly, Foucher et al. (2017) studied bank erosion on a small agricultural lowland watershed in France that was strongly affected by anthropogenic pressure. They measured short term bank erosion through a network of erosion pins along the 1400 m long stream. As a result, they quantified the material transported from the stream during one single winter (2012–2013) and reported the mean erosion rate of 17.7 mm year^{-1} and a mean volume of transported material of 75 t km^{-1}. Veihe et al. (2011) carried out their study on the Harrested stream in Denmark. They conducted the research on a cohesive streambank that is centrally located within the tile-drained catchment of the stream. Bank erosion rates ranged from 17.6 to 30.1 mm year^{-1}.

On the other hand, Lawler et al. (1999) reported the results of an intensive direct field monitoring of bank erosion rate on 11 sites on 130 km of the Swale-Ouse catchment, located in northern England and spanning over 3 315 km^2. They reported that the mean bank erosion ranged from 82.7 mm to 440.1 mm over the period of 14.5 months. Laubel et al. (2003) conducted similarly substantial research on 91 banks of 15 Danish streams. They reported mean bank erosion rate 11 mm year^{-1} and found several site-specific factors that affect bank erosion rate, such as bank angle, bank vegetation cover, overhang, and estimated stream power.

In Central European conditions, among other authors, Jakubis (2014) studied the erosion rates on the Železnobreznický creek. He used manual erosion pins and estimated that the mean bank erosion was 112 mm year^{-1}. Jakubisová (2014) modelled the effects of extreme discharges on the bank stability and erosion rates of Železnobreznický creek. Through the Bank Stability and Toe Erosion Model she quantified the stability factor and the risk of bank erosion. Rusnák and Lehotský (2014) studied the long term (1987 to 2009) bank erosion of catchments in the north-eastern part of Slovakia through remote sensing. They studied Ondava (13.2 km long section) and Topľa (39.8 km long section) and found great lateral dynamics and substantial bank erosion on both streams. During the 1987–2009 period, about 120 ha of banks were eroded and about 92 ha were accumulated from both streams.

The research mentioned is a small subset of all research that quantifies and predicts bank erosion. The authors constructed their own models, which can, with greater or smaller precision, explain or predict erosion. Most of these models are, however, region specific and have little success in predicting bank erosion outside the region they were constructed. On the other hand, there are models such as the Bank Assessment for Non-point source Consequences of Sediment (BANCS) model, described in detail by Rosgen (1996, 1998, 2001a, 2001b, 2006). The BANCS model was tested globally, though most research focuses on the USA (Coryat, 2014; Jennings and Harman, 2001; Sass and Keane, 2012; Van Eps et al., 2004) or India (Bandyopadhyay et al., 2013; Ghosh et al., 2016). Thorough verification of this model in other regions, such as Europe (or more specifically Central Europe and Slovakia) is yet to be done.

The BANCS model consists of two indexes – the Bank Erosion Hazard Index (BEHI), and the Near Bank Stress Index (NBS) (Rosgen, 1996, 2001a, 2006, 2008). The BEHI serves to estimate the susceptibility of a bank to erosion. It is based on variables that influence the erosion intensity. The NBS index is a practical method to evaluate shear stress which acts upon a studied bank. The NBS approximates the erosional force of the outer one third of the water column acting on the eroded

bank (cutbank) at the bank-full stage flow. The direct erosion measurements and the subsequent BEHI and NBS index determination enable the construction of the erosion prediction curves for particular streams. Based on the predictions made through the BANCS model, we can localize stream sections that most need the stabilization measures.

This paper focuses on assessing, whether it is suitable to use the BANCS model and its prediction curves on a water stream in Slovakia. Other authors, who supported the use of the BANCS model for bank erosion predictions, focused on larger streams, whereas we focused on the model's suitability for small watersheds. This could aid caretaking of small watersheds, which are commonly the source of flash floods. We also determined whether higher BEHI and NBS indexes truly represent greater annual bank erosion.

MATERIALS AND METHODS

In May 2014, we established 18 experimental sections (ES) on the Tŕstie stream (Fig. 1). We established the ES between 13.70 and 16.53 km of the stream (14.65% of the stream length). The total length of the ES was 307 m (1.6% of the total main channel length). Detailed information about the established ES can be seen in Table 1. On each ES, we chosen one cross section (Table 2) where we inserted a toe pin into the toe of the bank to determine the real annual erosion according to Sass (2011), and measured input data for the BEHI and the NBS index. We also took soil samples from the banks for laboratory analyses of the granularity of the bank material, and evaluated the stratification of the banks.

Study area

The Tŕstie stream and its watershed (hydrological number 4-21-09-065) lays in the Biele Karpaty and Myjavská pahorkatina mesoregions. The Tŕstie stream stems on the eastern part of Čupec hill in Javorinská heights, elevated 212 m above sea level (GPS coordinates: 48°48'52.28"N, 17°38'55.38"E). In the village Hrachovište, Tŕstie flows into Jablonka stream, elevated 212 m above sea level. The characteristics of Tŕstie

Fig. 1. Localization of the experimental sections on Tŕstie creek.

Table 1. Information about the experimental sections established on Tŕstie creek.

	Distance from the mouth of the watershed (km)	Altitude (m above the sea level)	GPS coordinates	Length of ES (m)
ES1	13.70	396	48°49'20.4"N, 17°38'78.4"E	15
ES2	13.80	396	48°49'19.7"N, 17°38'78.1"E	15
ES3	13.90	397	48°49'23.9"N, 17°38'75.4"E	15
ES4	13.95	401	48°49'28.5"N, 17°38'75.7"E	15
ES5	14.01	409	48°49'33.6"N, 17°38'71.9"E	20
ES6	14.20	410	48°49'39.4"N, 17°38'72.5"E	20
ES7	14.30	414	48°49'43.1"N, 17°38'68.8"E	15
ES8	14.36	415	48°49'47.6"N, 17°38'68.2"E	20
ES9	14.41	419	48°49'53.1"N, 17°38'65.1"E	15
ES10	14.50	419	48°49'63.0"N, 17°38'60.7"E	20
ES11	14.75	442	48°49'76.3"N, 17°38'65.3"E	15
ES12	14.98	453	48°49'88.0"N, 17°38'59.6"E	20
ES13	15.11	468	48°49'92.2"N, 17°38'51.0"E	20
ES14	15.34	478	48°50'02.2"N, 17°38'39.3"E	15
ES15	15.67	500	48°50'17.9"N, 17°38'27.5"E	16
ES16	16.12	519	48°50'42.3"N, 17°38'30.3"E	20
ES17	16.23	535	48°50'47.0"N, 17°38'26.1"E	16
ES18	16.53	561	48°50'63.0"N, 17°38'20.4"E	15

Table 2. Information about dimensions of experimental cross sections.

	Mean depth of channel (m)	Maximum depth of channel (m)	Area of channel (m^2)	B (m)[a]	b (m)[b]
ES1	0.292	0.40	1.286	5.05	2.35
ES2	0.298	0.55	0.993	3.8	2.4
ES3	0.318	0.42	1.006	3.4	2.35
ES4	0.845	1.03	3.304	3.8	2.95
ES5	0.595	0.77	1.828	3.3	2.45
ES6	0.692	0.95	2.224	3.3	1.9
ES7	0.855	1.15	3.095	4.1	2.5
ES8	0.609	0.73	2.34	3.75	2.9
ES9	0.454	0.72	1.387	3.15	1.6
ES10	0.796	1.05	3.273	4.2	2
ES11	0.333	0.48	0.916	2.85	1.8
ES12	0.501	0.62	1.841	4.4	2.75
ES13	0.781	1.17	2.984	3.8	2
ES14	0.564	0.72	1.428	3.05	1.6
ES15	0.441	0.61	1.02	2.45	1.3
ES16	0.408	0.51	0.878	2.95	1
ES17	0.402	0.58	1.002	2.75	0.9
ES18	0.324	0.47	0.829	2.55	1.2

The dimensions were determined for the bankfull conditions of the channel. B (m)[a] = the width of the channel in the banks, b (m)[b] = the width of the channel in the bed

watershed are as follows: watershed area $S_p = 41.55$ km^2; length of main channel $L = 19.31$ km; length of tributaries $L_{tr} = 16.32$ km; stream network density $r = 0.85$ km km^{-2}; length of the watershed divide $O = 38.65$ km; length of thalweg $L_{tg} = 19.90$ km; mean width of the watershed $B_w = 2.08$ km; absolute gradient of stream $\Delta H_s = 440.48$ m; absolute gradient of watershed $\Delta H_w = 630.01$ m; slope of the thalweg $I_{tg} = 3.14\%$; average slope of watershed $I_w = 9.77\%$; average slope of the main channel $I_s = 2.28\%$; average altitude of watershed $\varnothing H_w = 525.99$ m above the sea level. Estimated T-year discharges according to OTN ŽP 3112-1:03 are as follows: $Q_{100} = 31.05$ m^3 s^{-1}, $Q_{50} = 26.23$ m^3 s^{-1} a $Q_1 = 4.65$ m^3 s^{-1}.

Furthermore, we estimated the mean annual discharge $Q_a = 0.37$ m^3 s^{-1} according to Szolgay et al. (1997). Szolgay et al. (1997) based their estimation on formula (Eq. 1) and data from 54 meteorological stations in Slovakia. They derived the empirical relationships (Eq. 2) for the Slovak conditions. These were subsequently used in equation (Eq. 3) to estimate Q_a.

$$\overline{Z} = \overline{O} + \overline{E} \quad \text{(mm)} \tag{1}$$

$$\overline{O} = \overline{Z} \cdot \left(1 - \frac{EP_{iSR}}{\sqrt{0.809 \cdot EP_{iSR}^{\ 2} + \overline{Z}^2}} \right) \quad \text{(mm)} \tag{2}$$

$$Qa = \frac{\overline{O} \cdot Sp \cdot 10^3}{t} \quad (\text{m}^3\ \text{s}^{-1}) \tag{3}$$

where: $\overline{Z}$ is the mean long term annual precipitation in the watershed (mm); $\overline{O}$ is the mean long term annual runoff in the watershed (mm); $\overline{E}$ is the mean long term annual climatic evaporation in the watershed (mm); EP_{iSR} is the potential evaporation index SR = $260.822 + 37.920\overline{T} + 0.077\overline{T}^3$ (mm); $\overline{T}$ is the mean long term annual temperature in the watershed (°C); and t is the constant of 31 557 600 seconds (one year expressed in seconds).

Geologically the watershed is situated in the flysch strata. The most frequent soil types are Cambisols (50% of the watershed area, mostly in the northern part of the watershed), luvisols cover about 20% of the watershed, rendzic and calcaric soils cover about 15% of the watershed, and planosols formed on about 5% of the watershed area. The average annual precipitation in the watershed is between 650 mm in the lower part of watershed, to 900 mm in the upper part of watershed (Stankoviansky and Frandofer, 2012).

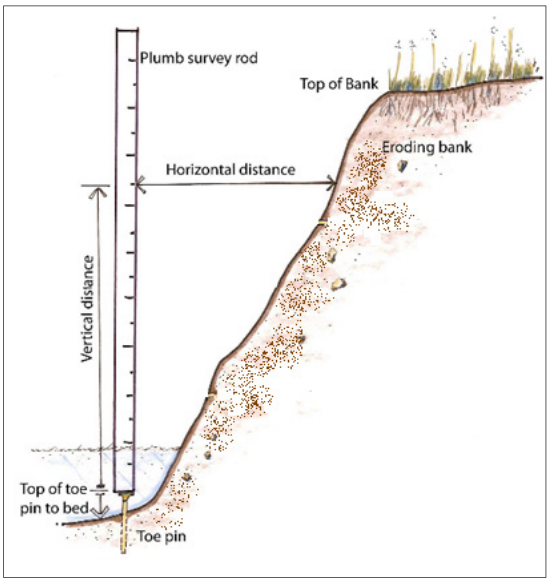

Fig. 2. Measurement of annual stream bank erosion. The toe pin is used as a control point at the toe of bank (edited Sass, 2011).

Forests cover almost half of the watershed (47%). Arable land covers another 27%, pastures cover 14%, and gardens and developed land cover about 12% of the watershed area. The stream section where we conducted our research is located springwards of Topolecká village. The section is almost fully covered by forest (98%) and the remaining 2% of the area are covered by pasture. We set-up no ES within the developed area.

According to Stankoviansky and Frandofer (2012), the landscape of the watershed was originally fully forested. However, it was deforested during the 14th century, when a nearby town of Stará Turá was developed. Subsequently, land use shifted to pasture and remained in this mode of use until the collectivization of agriculture, which took place during the second half of the 20th century. Collectivization, and the change of land structure it brought, increased the intensity of rainfall and snowmelt processes, frequency and intensity of mud floods, and the intensity of tillage erosion. Stankoviansky and Fandofer (2012) also mention forest disturbances as important events, that affect bank erosion. In the recorded history, windthrows that occurred in June 1999 and May 2010 caused the most severe damage within the watershed.

Measurements of real bank erosion

We started measuring the real annual erosion rates (EB) on May 2014 using erosion toe pins, according to Sass (2011). The 50 cm long, steel toe pins were installed perpendicularly into the toe of the banks (Fig. 2). We recorded the location of the toe pins using a GARMIN Colorado300 GPS device, placed a plumb survey rod perpendicularly to the toe pins, and measured the horizontal distances from the rod to the bank. After one year (on May 2015), we re-measured the horizontal distances at the same height levels. We then plotted the initial and re-measured shape of the bank, calculated the EB in m^2, and converted the EB outcome to m^3 m^{-1} (the volume of eroded material per one meter of the ES length).

The BEHI

We determined the BEHI score according to Rosgen (2006). We evaluated seven parameters on each ES (Table 3): (a) the ratio of the height of the studied bank (*BH*; see Fig. 3) to bankfull height (*BFH*; see Fig. 3); (b) the ratio of root depth (*RD*) to *BH*; (c) weighed root density (*WR*); (d) bank angle (*BA*); (e) surface protection (*SP*); (f) bank material (BM); and (g) stratification of the bank material (SBM).

We measured the *BH*, *BFH*, *RD*, and *BA*, and evaluated the BM through the sieve and densimetric tests of soil samples we took from each ES's bank. The assessments of the *WR* and *SP* were visual as well as the assessment of the SBM. To stratify the bank material, we assessed the bank layers.

To determine the total BEHI score, we first input the data into the BEHI worksheet (Rosgen, 2008) and converted them through the corresponding nomograms (Rosgen, 2006). Parameters (a) to (e) reached one of six states: very low (0–2 points), low (2–4 points), moderate (4–6 points), high (6–8 points), very high (8–9 points), and extreme (9–10 points). For parameter (f), we either added or subtracted 5–10 points to the total BEHI score, depending on the bank material (Rosgen, 2008).

Table 3. Assessment of individual experimental sections through the BEHI index.

ES		*BH* (m)	*BFH* (m)	*BH*/*BFH* (m)	*RD* (m)	*RD*/*BH* (m)	*R* (%)	*WR* (%)	*SP* (%)	*BA* (°)	BEHI	BEHI total
1	Value	1.15	0.34	3.38	0.84 H^a,G^b, S^d	0.73	49	35.7	50	63		
	Index			10		2.8		5.4	4.3	4.2	26.7	31.7 H
2	Value	2.32	0.23	10.08	0.39 H^a, F^c	0.16	40	6.72	5	61		
	Index			10		7.9		8.8	10	4.0	40.7	45.7 VH
3	Value	0.58	0.32	1.81	0.19 H^a, G^b	0.32	54	17.3	10	74		
	Index			7.2		5.6		7.7	10	5.3	35.8	35.8 H
4	Value	1.11	0.94	1.38	0.72 H^a,T^e	0.64	41	26.2	10	52		
	Index			4.5		3.2		6.2	10	3.5	27.4	27.4 M
5	Value	1.03	0.57	1.80	0.18 H^a	0.78	51	39.9	0	60		
	Index			7.2		2.7		5.0	10	3.9	28.8	28.8 M
6	Value	1.56	0.91	1.71	0.58 H^a, T^e	0.37	41	15.2	10	71		
	Index			6.8		5.2		8.0	10	5.0	35	35 H
7	Value	1.09	0.65	1.67	0.49 H^a, S^d	0.44	56	24.6	10	76		
	Index			6.7		4.1		6.3	10	5.4	32.5	47.5 VH
8	Value	0.87	0.72	1.2	0.73 H^a, T^e, S^d	0.83	57	47.3	45	87		
	Index			3.9		2.2		4.3	4.6	7.7	22.7	30.2 H
9	Value	0.76	0.58	1.31	0.62 H^a, S^d	0.81	62	50.2	10	90		
	Index			4.4		2.3		4.1	10	8.0	28.8	33.8 H
10	Value	0.82	0.48	1.70	0.37 S^d	0.45	35	15.7	10	37		
	Index			6.8		4.1		8.0	10	2.8	31.7	31.7 H
11	Value	0.57	0.45	1.26	0.46 H^a, S^d	0.80	30	24.6	35	56		
	Index			3.9		2.4		6.3	5.5	3.7	21.8	21.8 M
12	Value	1.06	0.51	2.07	0.78 H^a, S^d	0.73	59	43.1	75	45		
	Index			8.1		2.6		4.8	2.2	3.1	20.8	25.8 M
13	Value	1.07	0.82	1.30	0.76 H^a, T^e, S^d	0.71	56	39.7	40	46		
	Index			4.4		2.7		5.0	5.0	3.2	20.3	25.3 M
14	Value	0.78	0.78	1.0	0.46 H^a,G^b	0.59	64	37.7	70	53		
	Index			0		3.3		5.3	2.7	3.5	14.8	19.8 L
15	Value	1.03	0.62	1.66	0.43 H^a	0.41	35	14.3	55	69		
	Index			6.6		4.5		8.1	4.0	4.7	27.9	32.9 H
16	Value	0.58	0.58	1.0	0.49 H^a, S^d	0.84	42	35.2	95	46		
	Index			0		2.1		5.4	0.5	3.1	11.1	16.1 L
17	Value	0.68	0.68	1.0	0.48 H^a, F^c G^b	0.70	45	31.5	85	44		
	Index			0		2.7		5.7	1.5	3.0	12.9	17.9 L
18	Value	0.64	0.28	2.28	0.37 H^a	0.57	33	18.8	70	40		
	Index			8.2		3.5		7.8	2.7	2.9	25.1	25.1 M

H^a = Herbs: *Impatiens noli-tagere*, *Petasites hybridus*, *Geranium robertianum*, *Veronica montana*; G^b = Grass: *Carex* sp.; F^c =Ferns: *Athyrium filix – femina*; S^d = Shrubs: *Sambucus nigra*, *Padus racemossa*, T^e=Trees: *Corrylus avellana*, *Fagus sylvatica*, *Fraxinus excelsior*

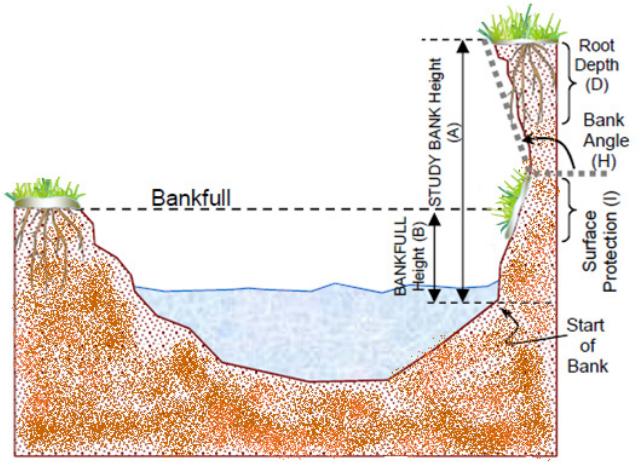

Fig. 3. BEHI characteristics (Rosgen, 2006).
Legend: Bank height (BH): is a height from start of a bank (point where is set into the bed steel pin) to the top of a bank; Bankfull height (BFH): is height from start of a bank (point where is set into the bed steel pin) to bankfull position; Surface protection (SP): is visually estimated as a percentage of bank covered by plants, trees, shrubs, or woody debris, boulders or other objects which can help prevent bank against erosion; Root density (RD): Is visual assessment of density of vegetation roots growing on a banks.

As for parameter (g), we added five points to the BEHI score if: (i) two separate layers were present; (ii) the layers spanned from the bank toe to the bankfull height; (iii) at least one of the layers consisted of an erosion prone material (such as sand, gravel or their combination). We added ten points to the BEHI score if more than two layers were present and conditions (ii) and (iii) were valid (Rosgen, 2008). Finally, we summed the points obtained for each parameter to determine the BEHI for the studied bank. The banks of each ES were then put into one of six categories of total BEHI index, thus estimating their erodibility potential – very low (< 9.9 points), low (10–19.9), moderate (20–29.9), high (30–39.9), very high (40–45), and extreme (45.1–50 points).

The NBS index

Rosgen (1996, 2001b) presents seven methods to determine the NBS index. In our research, we used method no. five, which uses the share of near bank maximum depth (H_{max}) and mean depth of channel ($H_{ø}$) at bankfull stage flow (Table 4). We measured the depth of the channel for bankfull stage each 0.5 m of the channel's width to establish the H_{max} and $H_{ø}$ at the bankfull stage. NBS index can reach six levels (Table 5): very low (VL), low (L), moderate (M), high (H), very high (VH), extreme (E) (Rosgen, 1996, 2001b, 2006, 2008). Higher NBS index values indicate larger bank erosion.

Table 4. Assessment of individual experimental sections by the NBS index.

ES	H_{max}	$H_{ø}$	H_{max} / $H_{ø}$	NBS index
1	0.41	0.33	1.24	L
2	0.55	0.29	1.89	H
3	0.42	0.31	1.32	L
4	1.03	0.67	1.53	M
5	0.77	0.59	1.30	L
6	0.95	0.69	1.37	L
7	1.15	0.69	1.66	M
8	0.73	0.48	1.52	M
9	0.27	0.45	1.57	M
10	1.05	0.79	1.32	L
11	0.50	0.33	1.51	M
12	0.62	0.48	1.29	L
13	1.17	0.89	1.31	L
14	0.72	0.56	1.28	L
15	0.61	0.44	1.38	L
16	0.51	0.46	1.10	L
17	0.58	0.49	1.18	L
18	0.47	0.32	1.46	L

Statistical analyses

After gathering the input data and determining the BEHI and NBS index, we assessed the relationships between the aforementioned characteristics through the regression and correlation analyses.

We first verified the hypothesis that higher BEHI values indicated higher EB through a regression and correlation analysis of the relationship between the BEHI and the EB. Similarly, we assessed the relationship between the NBS index and the EB. After verifying whether or not the relationships were statistically significant, we constructed the erosion prediction curves as a graphical representation of the relationship between the NBS index and the EB. All statistical analyses as well as the construction of the erosion prediction curves were conducted in the STATISTICA 10.0 program.

Construction of the prediction curves for the stream

We constructed the prediction curves by plotting the NBS values on the X axis, and the corresponding EB on the Y axis. The resulting linear regression lines represented individual categories of the BEHI. These trend lines were then used to predict the bank erosion. When constructing the prediction curves, we classified individual ES according to their BEHI category. Due to insufficient data in some categories, we merged the neighbouring BEHI categories as seen in studies by other authors (Coryat, 2014; Harmel et al., 1999; Kwan and Swanson, 2014; Sass, 2011).

Table 5. The evaluation of NBS index according to used method (Rosgen, 2001a, 2008).

Index NBS	Methods						
	(1)	(2)	(3)	(4)	(5)	(6)	(7)
Very low	Rosgen (1996)	> 3.0	< 0.20	< 0.4	<1.0	<0.8	<1.0
Low		2.21–3.0	0.20–0.40	0.41–0.60	1.0–1.5	0.8–1.05	1.0–1.2
Moderate		2.01–2.2	0.41–0.60	0.61–0.80	1.51–1.8	1.06–1.14	1.21–1.6
High		1.81–2.0	0.61–0.80	0.81–1.0	1.81–2.5	1.15–1.19	1.61–2.0
Very high		1.5–1.8	0.81–1.0	1.01–1.2	2.51–3.0	1.20–1.60	2.01–2.3
Extreme		< 1.5	>1.0	> 1.2	>3.0	> 1.6	>2.3

RESULTS AND DISCUSSION

The relationship between the EB and BEHI on particular ES is depicted in Fig. 4. The results of the regression and correlation analysis showed a strong relationship existed (R^2 = 0.73). The strength of the relationship indicates that we were able to determine the most endangered sections, as the sections with the most severe bank erosion reached the highest BEHI value. Strong correlations between the BEHI and the EB were also reported by Rosgen (1996, 2001b, 2008) in Colorado and Wyoming, Markowitz and Newton (2011) at the Birch Creek (New York state) or Dick et al. (2014) in Michigan.

On the other hand, there is also research available, where the relationship between the BEHI and the EB was weak or where there was no significant relationship whatsoever. These include studies by Coryat (2014), who found only a moderately strong relationship between the EB and the BEHI on the banks of the Stony Clove Creek (R^2 = 0.23), Macfall et al. (2014), who studied the Haw River in North Carolina or Saha and Mukhopadhyay (2014) on the Kunur River showed a weak relationship (R^2 = 0.14) between the EB and the BEHI.

Rosgen (1996) experienced discharges that were at most 60–70% of the bankfull stage. Researchers who experienced similar discharge stages, such as Markowitz and Newton (2011) or Dick et al. (2014), reported stronger relationships than authors who reported discharges greater than the bankfull stage. The authors who experienced greater than bankfull stage discharges include Coryat (2014), who reported high flood discharges that occurred during the hurricane Irene. He attributed the relatively weak relationship between the BEHI and the EB in his case to these extreme discharges. Macfall et al. (2014) too explain the weak relationship by the fact that the Haw River discharges frequently change from extremely low to extremely high. In our case, no extreme discharges occurred that would exceed the bankfull stage.

The relationship between the BEHI and the EB can be also affected by the precision with which the bank parameters are determined (e.g. the bank material, its stratification or the bank angles). In studies, where there was a weak relationship reported (Ghosh et al., 2016; Harmel et al., 1999; Kwan and Swanson, 2014), the authors used only visual assessments for bank parameters, whereas we used the sieve and densimetric tests to determine the bank material, and a laser clinometer to determine the bank angle. As Bigham et al. (2018) state, inaccurate determination of these parameters (especially study bank height, root depth, bank angle, and bank material) affects the estimation of the erodibility potential, thus affecting the relationship between the potential and the real erosion.

Of course, bank erosion depends on many other interconnected factors, be it climate, geology, vegetation, soil types and soil properties, human interaction with the channels, etc. (Sass, 2011). Besides the similar discharge stages and the fact that we measured the bank material and bank angles, the good fit of the BEHI and the EB could be caused by the relatively similar climatic conditions in our and Rosgen's research. Both Rosgen and we conducted the research in the humid continental climate zone. Geology of the studied areas was also similar – both our and Rosgen's study areas were located on sedimentary floors. Moreover, the studied streams had similar discharge behaviour throughout the year. Rosgen (1996) states that the discharges in the streams he observed culminate in spring and early summer due to snowmelt from the Rocky Mountains, with another culmination during summer due to extreme precipitation. We observed similar behaviour on the Tŕstie stream, which is located in the Biele Karpaty Mountains (a part of the Western Carpathians). These similarities contributed to the applicability of the BANCS model on the Tŕstie stream.

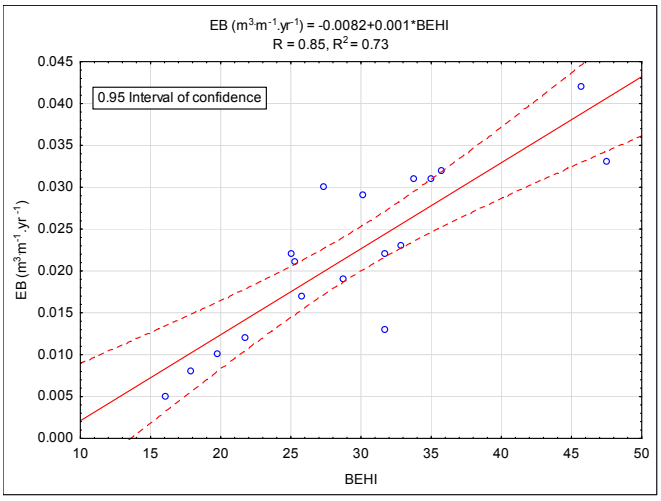

Fig. 4. Relationship between the BEHI and the observed annual stream bank erosion (EB) (m^3 m^{-1} yr^{-1}).

Conversely, there are environmental factors that could have prevented a better fit between the modelled and real bank erosion. Perhaps the most important is the fact, that Rosgen (1996) studied a large area with 49 streams, whereas we only applied his model to one low order stream with a small watershed. A larger area means a greater variability of vegetation, climate, and geology that translate to a more varied bank material composition, bank vegetation, channel characteristics, etc. The relationship between the BEHI and the EB could also be affected by the fact that Rosgen's study area experienced lower mean annual precipitation. The mean annual precipitation in Colorado is between 200 and 810 mm (Scott et al., 2003), whereas in the area where the Tŕstie watershed is located, Stankoviansky et al. (2012) report precipitation of 650 to 900 mm. Furthermore, the Rocky Mountains are a larger mountain ridge, with higher peaks that contain vegetation and climate zones not found within the Biele Karpaty Mountains. Even so, these differences did not outweigh the similarities of our and Rosgen's study areas.

The relationship between the EB and the NBS index had similar properties (Fig. 5). A coefficient R^2 = 0.63 showed there was a strong relationship between the EB and the NBS index. Harmel et al. (1999) studied the watershed of the Illinois River, and reached a substantially lower value of R^2 = 0.17. They identified the cause of such weak correlation was the method they used to determine the NBS index, which was, according to the authors, relatively easy to carry out, but less precise. They advise to employ the method of velocity gradients.

We were able to create two erosion prediction curves (Fig. 6) – one for the L and M BEHI categories (Eq. 4), and one for the H, VH, and E BEHI categories (Eq. 5).

$$EB\ (m^3\ m^{-1}\ yr^{-1}) = -0.036 + 0.0392\ NBS \quad (4)$$

$$EB\ (m^3\ m^{-1}\ yr^{-1}) = -0.0194 + 0.0325\ NBS \quad (5)$$

The constructed equations were used to estimate the erosion in particular ES, and the outcomes were subsequently compared to real EB (Table 6). The relationship between the predicted and real EB for L and M BEHI was moderately strong, with R^2 = 0.51. The relationship between the predicted and real erosion for H, VH, and E BEHI was stronger, with R^2 = 0.66. Many authors dealt with the problem of prediction curves.

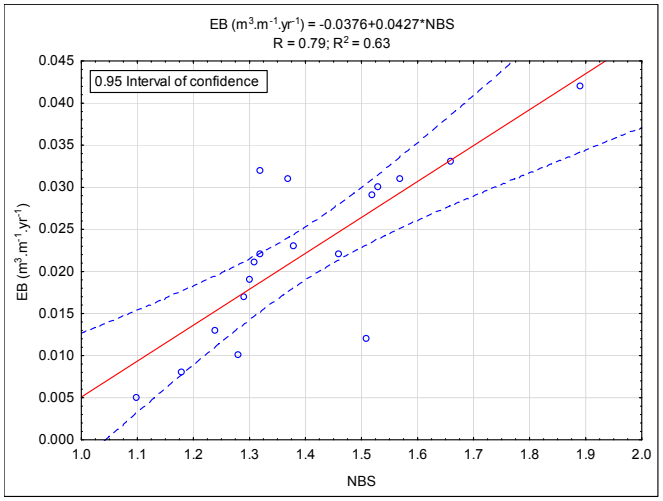

Fig. 5. Relationship between the NBS index and the observed annual streambank erosion.

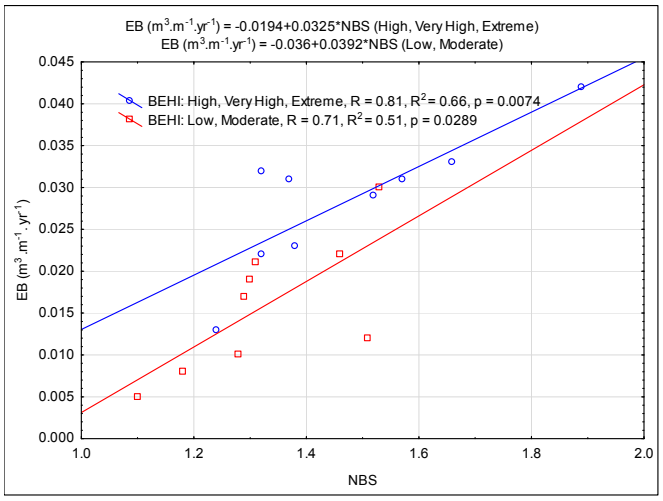

Fig. 6. Erosion prediction curves for Tŕstie creek.

Table 6. Comparison of real measured annual erosion rates (EB) (m^3 m^{-1} yr^{-1}) and predicted annual erosion (EBP) (m^3 m^{-1} yr^{-1}) by prediction curves.

	EB (m^3 m^{-1} yr^{-1})	EBP (m^3 m^{-1} yr^{-1})	Difference
ES1	0.013	0.021	–0.008
ES2	0.042	0.042	0
ES3	0.032	0.024	0.008
ES4	0.03	0.024	0.006
ES5	0.023	0.015	0.008
ES6	0.031	0.025	0.006
ES7	0.033	0.035	–0.002
ES8	0.029	0.030	–0.001
ES9	0.031	0.032	–0.001
ES10	0.022	0.024	–0.002
ES11	0.012	0.023	–0.011
ES12	0.017	0.015	0.002
ES13	0.021	0.015	0.006
ES14	0.01	0.014	–0.004
ES15	0.023	0.025	–0.002
ES16	0.005	0.007	–0.002
ES17	0.008	0.010	–0.002
ES18	0.022	0.021	0.001

Coryat (2014) constructed the prediction curve on the Stony Clove Creek for an H and VH BEHI. He reported a weak relationship (R^2 = 0.35). Similarly, low determination was also reported by Harmel et al. (1999). For E BEHI, they reported R^2 = 0.15, for H and VH BEHI categories, R^2 was 0.09, and for the M BEHI category, the R^2 was 0.32. They explain the weak relationships between the predicted erosion and the EB by the weak correlation of the NBS index with the EB.

Kwan and Swanson (2014) constructed the prediction curves for the Sequoia National Forest California catchment area based on data from multiple streams. They achieved better results, and some of their prediction curves can be used to predict EB in the catchment area. The coefficient of determination for the E BEHI category reached 0.76, for the H and VH categories it reached 0.37, for the M BEHI category is was 0.49, and for the L category is was 0.70. Sass (2011) reported that for the Black Vermillion watershed (north east Kansas), the coefficient of determination for the M BEHI category was 0.80, and for the H and VH categories it was 0.42. For the Piedmont region of North Carolina, the North Carolina State University constructed four prediction curves for the E BEHI category (R^2 = 0.91), the VH BEHI category (R^2 = 0.66), the H BEHI category (R^2 = 0.53), and for the M BEHI category, R^2 was 0.92 (North Carolina State University (NCSU) Stream Restoration Program, 1989). Perhaps the most important study, in which the prediction curves were constructed, is from Rosgen (1996). It shows the prediction curves for the Colorado region. The author reports a strong relationship, with an R^2 of 0.92, and for the Yellowstone region, where he reported an R^2 of 0.84.

CONCLUSION

We found that the BANCS model is a viable tool for predicting bank erosion on the Tŕstie stream. The BEHI proved to be an adequate predictor of bank erosion in this stream. However, the NBS index showed a greater variability, which lead to weaker relationships between the predicted and real erosion. This could be due to the method we used to determine the NBS index, as other methods could provide more precise results. A more precise determination of the NBS index could enable even better fitting curves for predicting erosion. The constructed erosion prediction curves can be used for the studied stream in years when the discharge reaches bankfull stage flow at Q_{50}. The prediction curves are not suitable for use when the flow is higher than bankfull stage flow or extremely low, because they would significantly overestimate or underestimate erosion from the banks.

We used an erosion prediction method that was never before used in Central Europe. The model bases the predictions on relatively easy to measure parameters and can predict bank erosion relatively precisely. In our next research, we plan to integrate the monitoring of high flow in channel and precipitation in the watershed into the BANCS model, as the current model does not take these characteristics into account, despite the fact that the amount of water in the stream channel is the most important factor influencing bank erosion rate.

Acknowledgements. This article was financed by project APVV-15-0714: Mitigation of climate change risk by optimization of forest harvesting scheduling.

REFERENCES

Bandyopadhyay, S., Saha, S., Ghosh, K., De, S.K., 2013. Validation of BEHI model through field generated data for as-

sessing bank erosion along the river Haora, West Tripura, India. Earth Sci. India, 6, 126–135.

Bigham, K.A., Moore, T.L., Vogel, J.R., Keane, T.D., 2018. Repeatability, Sensitivity, and Uncertainty Analyses of the BANCS Model Developed to Predict Annual Streambank Erosion Rates. JAWRA J. Am. Water Resour. Assoc., 1–17.

Bull, L.J., 1997. Magnitude and variation in the contribution of bank erosion to the suspended sediment load of the River Severn, UK. Earth Surface Processes and Landforms, 22, 12, 1109–1123.

Coryat, M., 2014. Analysis of the Bank assessment for non-point source consequences of sediment (BANCS) Approach for the prediction of streambank stability and erosion along Stony Clove Creek in the Catskills. Syracuse University, 78 p.

Dick, B.M., Hey, R., Peralta, P., Jewell, I., Simon, P., Peszlen, I., 2014. Estimating annual riverbank erosion rates – a dendrogeomorphic method. River Res. Appl., 30, 845–856.

Foucher, A., Salvador-Blanes, S., Vandromme, R., Cerdan, O., Desmet, M., 2017. Quantification of bank erosion in a drained agricultural lowland catchment. Hydrological Processes, 31, 6, 1424–1437.

Ghosh, K.G., Pal, S., Mukhopadhyay, S., 2016. Validation of bancs model for assessing stream bank erosion hazard potential (SBEHP) in Bakreshwar river of Rarh Region, Eastern India. Model. Earth Syst. Environ., 2, 1–15.

Harmel, R.D., Haan, C.T., Dutnell, R.C., 1999. Evaluation of Rosgen´s streambank erosion potential assessment in Northeast Oklahoma. JAWRA J. Am. Water Resour. Assoc., 35, 113–121.

Jakubis, M., 2014. Predikcia erózie brehu vodného toku metódou BANCS (BEHI–NBS). In: Rožňovský, J., Litschmann, T., Středa, T., Středová, H. (Eds): Extrémy oběhu vody v krajině. Mikulov, Czech Republic, 2014, 12 p. ISBN 978-80-87577-30-1.

Jakubisová, M., 2014. Modelovanie brehov erózie metódou BSTEM v súvislosti s extrémnymi prietokmi. In: Rožňovský, J., Litschmann, T., Středa, T., Středová, H. (Eds): Extrémy oběhu vody v krajině. Mikulov, Czech Republic, 2014, 17 p. ISBN 978-80-87577-30-1.

Jennings, G.D., Harman, W.A., 2001. Measurement and stabilization of streambank erosion in North Carolina. In: Proc. Int. Symp. Soil Erosion Research for the 21st Century. ASAE, Honolulu, HI, pp. 537–540.

Kwan, H., Swanson, S., 2014. Prediction of annual streambank erosion for Sequoia National Forest, California. JAWRA J. Am. Water Resour. Assoc., 50, 1439–1447.

Laubel, A., Kronvang, B., Hald, A.B., Jensen, C., 2003. Hydromorphological and biological factors influencing sediment and phosphorus loss via bank erosion in small lowland rural streams in Denmark. Hydrological Processes, 17, 17, 3443–3463.

Lawler, D.M., Grove, J.R., Couperthwaite, J.S., Leeks, G.J.L., 1999. Downstream change in river bank erosion rates in the Swale-Ouse system, northern England. Hydrological Processes, 13, 7, 977–992.

Macfall, J., Robinette, P., Welch, D., 2014. Factors influencing bank geomorphology and erosion of the Haw River, a high order river in North Carolina, Since European Settlement. PLoS One, 9, 12 p.

Markowitz, G., Newton, S., 2011. Using Bank Assessment for Non-Point Source Consequences of Sediment (BANCS) Model to Prioritize Potential Stream Bank Erosion on Birch Creek, Shandaken, Ashokan Watershed Stream Management Program (AWSMP). New York, 57 p.

North Carolina State University (NCSU) Stream Restoration Program, 1989. North Carolina Piedmont Region Bank Erosion Prediction Curve. Available at: http://www.bae.ncsu.edu/programs/ extension/wqg/srp/. Accessed 2 January 2014.

Rosgen, D.L., 1996. Applied River Morphology. Wildland Hydrology, Pagosa Springs, CO, 380 p.

Rosgen, D.L., 1998. Field Guide for Stream Classification. Wildland Hydrology, Pagosa Springs, CO, 193 p.

Rosgen, D.L., 2001a. A hierarchical river stability/Watershed-based sediment assessment methodology. In: Proc. 7th Federal Interagency Sedimentation Conference. Reno, NV, p. 13.

Rosgen, D.L., 2001b. A practical method of computing streambank erosion rate. In: Proc. 7th Federal Interagency Sedimentation Conference. Reno, NV, pp. 9–15.

Rosgen, D.L., 2006. Watershed assessment of river stability and sediment supply (WARSSS). Wildland Hydrology, Fort Collins, CO, 648 p.

Rosgen, D.L., 2008. River Stability: Field Guide. Wildland Hydrology, Fort Collins, CO, 214 p.

Rusnák, M., Lehotský, M., 2014. Povodne, brehová erózia a laterálne presúvanie koryta štrkonosných kľukatiacich vodných tokov (prípadová štúdia tokov Topľa a Ondava). Acta Hydrologica Slovaca, 15, 424–433.

Saha, S., Mukhopadhyay, S., 2014. A study on Kunur River, Eastern India. Int. J. Geol. Earth Environ. Sci., 4, 216–223.

Sass, C.K., 2011. Evaluation and development of predictive streambank erosion curves for Northeast Kansas using Rosgen's "BANCS" Methodology. Kansas State University, 141 p.

Sass, C.K., Keane, T.D., 2012. Application of Rosgen's BANCS model for NE Kansas and the development of predictive streambank erosion curves. J. Am. Water Resour. Assoc., 48, 774–787.

Scott, L.S., Collins, O.C., Diggs, M.D., 2003. Atlas of Colorado. A Teaching Resource. Downloaded 26. 02. 2018. Avaliable on http://www.unco.edu/hss/geography-gis/pdf/atlas/atlas-full-reduced.pdf, 194 p.

Stankoviansky, M., Frandofer, M., 2012. Reliéf katastrálneho územia Starej Turej a jeho recentný vývoj. Geogr. Cassoviensis, 6, 59–73.

Stankoviansky, M., Barka, I., Bella, P., Boltižiar, M., Grešková, A., Hók, J., Ištok, P., Lehotský, M., Michalková, M., Minár, J., Ondrášik, M., Ondrášik, R., Pecho, J., Pišút, P., Trizna, M., Urbánek, J., 2012. Recent landform evolution in Slovakia. In: Recent Landform Evolution: The Carpatho-Balkan-Dinaric Region. Springer, Dordrecht, Heidelberg, London, New York, pp. 141–175.

Szolgay, J., Hlavčová, K., Parajka, J., Čunderlík, J., 1997. Vplyv klimatickej zmeny na odtokový režim na Slovensku [The effect of climate change on the run-off regime in Slovakia]. Zborník NKP SR 6, 110 p.

Van Eps, M.A., Formica, S.J., Morris, T.L., Beck, J.M., Cotter, A.S., 2004. Using a Bank erosion hazard index (BEHI) to estimate annual sediment loads from streambank erosion in the West Fork White River watershed. In: Arkansas watershed advisory group conference proceedings: Self-sustaining solutions for streams, wetlands, and watersheds. pp. 125–132.

Veihe, A., Jensen, N.H., Schiøtz, I.G., Nielsen, S.L., 2011. Magnitude and processes of bank erosion at a small stream in Denmark. Hydrological Processes, 25, 10, 1597–1613.

Received 29 May 2017
Accepted 28 February 2018

J. Hydrol. Hydromech., 67, 2019, 2, 129–134
DOI: 10.2478/johh-2018-0038

Persistence of water repellency in coarse-textured soils under various types of forests in NW Spain

Elena Benito*, Eufemia Varela, María Rodríguez-Alleres

Departamento de Biología Vegetal y Ciencia del Suelo, Universidad de Vigo, 36310 Vigo, Spain.
* Corresponding author. Tel.: +34986812396. E-mail: rueda@uvigo.es

Abstract: The primary purpose of this work was to assess the persistence of water repellency in the surface horizon of coarse-textured soils under natural *Quercus robur* ecosystems, and *Pinus pinaster* and *Eucalyptus globulus* plantations, in the northwest of the Iberian Peninsula. Water repellency was determined by applying the water drop penetration test (WDPT) to soil samples collected from variable depths (0–40 cm). Measurements were made on field-moist samples obtained at the end of the dry period and on samples dried at 25ºC in the air. All soils exhibited very high (severe to extreme) water repellency in the topmost soil layer (0–5 cm) but no significant differences among the three plant species studied. Extreme persistence was observed down to 20 cm in the soils under eucalyptus and down to 10 cm in those under pine. The soils under oak were those exhibiting the highest variability in water repellency and the greatest decrease in it with increasing depth (especially in relation to soils under eucalyptus).

Water repellency exhibited significant positive correlation with the C content and C/N ratio of the soils. Soil water repellency was similar in the air-dried samples and field-moist samples.

Keywords: Soil water repellency; Forest soils; Soil organic carbon; Soil moisture; NW Spain.

INTRODUCTION

Water repellency is a natural property of soils which has been identified under a wide range of climatic conditions in many geographic areas (Dekker et al., 2005; Doerr et al., 2000). Soil water repellency (SWR) has traditionally been associated to semi-arid regions; in the last two decades, however, it has also been encountered in wet regions (e.g., Benito et al., 2016; Doerr et al., 2006; Jaramillo et al., 2000; Johnson et al., 2005; Rodríguez-Alleres et al., 2007). Repellency is largely found in sandy soils but has also been observed in silty and clayey soils, peat and even volcanic ash (Jaramillo et al., 2000; Mataix-Solera and Doerr, 2004; Ritsema et al., 1997; Wallis and Horne, 1992), which suggests that, however slight, SWR is more widespread than initially assumed (de Jonge et al., 2009).

Although the specific substances inducing water repellency in soil remain unknown, its severity has been related to the type of organic matter present in the soil. Also, the phenomenon is known to result from the accumulation of hydrophobic organic acids in root exudates, the formation of fungally and microbially produced compounds or even the direct decomposition of organic matter in soil (Doerr et al., 2000; Goebel et al., 2011). The originating compounds deposit onto mineral surfaces and/or soil aggregates, or form interstitial organic matter (Doerr et al., 2000; Franco et al., 2000). As a result, SWR is restricted to the top few centimetres or decimetres of soil and is usually highly variable in spatial and temporal terms. In fact, SWR peaks in dry periods and diminishes or even disappears altogether in wet periods (e.g. Benito et al., 2016; Rodríguez-Alleres and Benito, 2011; Santos et al., 2013). Therefore, SWR depends on soil moisture, but also on other factors such as temperature, relative humidity and evapotranspiration rate (Benito et al., 2016; Doerr et al., 2000; Goebel et al., 2011). Water repellency is also influenced by soil pH; thus, it is usually more severe in acid soils than in alkaline soils, which has been ascribed to increased fungal activity and decreased humification of organic matter in the more acid soils (Mataix-Solera et al., 2007; Rodríguez-Alleres et al., 2007; Zavala et al., 2009).

High SWR levels are typically associated to perennial plant species producing substantial amounts of resins, wax or aromatic oils such as pine and eucalyptus trees (Badía et al., 2013; Doerr et al., 2005, 2007; Mao et al., 2016; Rodríguez-Alleres and Benito, 2011; Rodríguez-Alleres et al., 2007).

Galicia (NW Spain) is a region of the European temperate–humid zone where 63% of the land is occupied by forests (CMR, 2009). The prevailing climax vegetation is the Atlantic oak grove and the dominant species *Quercus robur*. Repeated deforestation and repopulation have led to this vegetation accounting for only 10% of the plant cover in oceanic Spain, however. Thus, vast expanses of land in NW Spain were planted with two tree species in order to boost the wood-related industry (wood, pulp and paper) in the XX century, namely: *Pinus pinaster* and *Eucalyptus globulus*, which currently occupy 23% and 19%, respectively, of the land surface in the region (CMR, 2009).

Water repellency is a common feature of surface soils with different textures under the relatively dry conditions of NW Spain. The prevailing vegetation plays a crucial role in the development and persistence of repellency in soils. It is especially influential on forest soils under *P. pinaster* and *E. globulus*, and also, to a lesser extent, on soils under grassland and crops. Coarse-textured soils are known to exhibit more persistent repellency and be repellent at greater depths than fine-textured soils (Rodríguez-Alleres et al., 2007, 2012). However, virtually nothing is known about the occurrence and severity of water repellency under *Q. robur* natural woods. This led us to compare SWR and its severity in soils under *Q. robur* natural forests and under *P. pinaster* and *E. globulus* plantations in the northwest of the Iberian Peninsula. The specific objectives of this work were as follows: (*a*) to assess the severity of water repellency in samples from the surface of coarse-textured soil under the three most typical plant species of the region (oak, pine and eucalyptus); (*b*) to examine the variation of water repellency with soil depth and relate it to soil moisture and organic carbon contents; and (*c*) to compare water repellency between field-moist and air-dried samples.

MATERIAL AND METHODS

Study area

The study area was located in the province of Pontevedra (southwest of Galicia, NW Spain), which lies in the temperate–humid Atlantic European zone. The oceanic climate of NW Spain features high annual precipitation (ca. 1400 mm) that peaks in autumn–winter and is much lower in summer. The temperatures are typical of temperate areas and the annual mean is 8–15ºC.

The study was conducted in 30 zones representing the main types of woodland present in the area, namely: 10 zones of *Q. robur* mature forest, 10 of *E. globulus* plantations and another 10 of *P. pinaster* plantations. The soils were either Cambisols or Umbrisols (WRB, 2006) and developed on granite, gneiss or quartz schists. The lithological and climatic features of the area have favoured the development of coarse-textured acid soils with high organic matter contents.

Methods

After litter removal, a representative sample from the top 5 cm of the A horizon was obtained as a composite of subsamples collected at randomly selected sites in each of 30 study zones. Fifteen of the zones were subjected to additional sampling at 5–10 cm, 10–20 cm and 20–40 cm. All samples were collected at the end of the summer period in order to ensure maximum severity in water repellency (Rodriguez-Alleres and Benito, 2012; Rodríguez-Alleres et al., 2007).

The persistence of water repellency in the samples was determined with the water drop penetration test (WDPT, Van't Woudt, 1959). The test involves dropping distilled water over each soil sample and measuring the time it takes to penetrate it. An amount of about 5 g of each soil sample was placed in triplicate in Petri dishes of 70 mm diameter and supplied with five water drops each. A repellency class for each sample was established from the median of 15 measurements, namely: class 0 (non-repellent, WDPT < 5 s), class 1 (slightly repellent, WDPT = 5–60 s), class 2 (strongly repellent, WDPT = 60–600 s), class 3 (severely repellent, WDPT = 600–3600 s), class 4 (extremely repellent, WDPT = 1–3 h), class 5 (extremely repellent, WDPT = 3–6 h) and class 6 (extremely repellent, WDPT > 6 h) (Dekker et al., 2001). Repellency was measured on field-moist samples immediately after recording of their wet weights and also on samples dried at 25ºC in the air.

Soil moisture content was determined gravimetrically. Particle-size distribution was determined after oxidizing the organic matter with H_2O_2, when sieving the sand fractions and using the pipette method to separate silt (50–2 µm) from clay (< 2 µm) fractions (USDA, 2004). Soil acidity (pH) was determined in 1:2.5 soil:water extracts. Total C and N were determined with an elemental analyser. By virtue of the absence of carbonates in the acid soils of the area, total carbon values coincided with organic carbon contents (de Blas et al., 2010). All samples were analysed in triplicate and their mean results taken.

All statistical analyses were performed with the software SPSS v. 17.0. Determinations included correlations (Spearman rank correlation coefficient) and analysis of variance (Kruskal–Wallis ANOVA). Because WDPT was measured in ranked categories rather than as numeric values, the tests were of the non-parametric type.

RESULTS

Table 1 summarizes the properties of the surface soil samples. All soils had sandy loam texture, and sand and clay contents over the ranges 42–75% and 11–26%, respectively, with no substantial differences among plant covers. Carbon and nitrogen contents were high in all soils and not significantly different among them. However, the average C/N ratio differed significantly and was lower (C/N = 16) under oak than under pine or eucalyptus (C/N = 20), which suggests more marked mineralization of organic matter under oak cover. Soil moisture contents were significantly higher under oak (32.4 ± 5.8%) than under pine (20.2 ± 10.1 %) and eucalyptus (21.4 ± 4.1%), the latter two not differing significantly in this respect.

Figure 1 shows the relative frequencies of median WDPT classes for the field-moist soil samples ($WDPT_f$) and those dried at 25ºC ($WDPT_{25}$) taken at a depth of 0–5 cm. All $WDPT_f$ values were very high, with penetration times ranging from 600 s to more than 6 h in the soils under oak, 1 h to more than 6 h under pine and more than 6 h under eucalyptus. The Man–Whitney test revealed no significant differences in $WDPT_f$ among plant species, however. Drying at 25ºC increased water repellency in the soils under oak and made them extremely water repellent (WDPT values from 1 h to more than 6 h). Also, all air-dried samples of soil under pine or eucalyptus were extremely repellent (WDPT > 6 h). The Wilcoxon test revealed no significant differences between $WDPT_f$ and $WDPT_{25}$ for any type of plant species. Twenty two of the 30 soils retained their repellency class after drying; however, drying increased repellency by 1–3 classes in 5 samples, and decreased it by 1–2 classes in 3.

As can be seen from Figure 2, the persistence of water repellency in the deeper soil layers did differ among tree covers, the soils under eucalyptus exhibiting repellency at the greatest depths. In fact, all soils under eucalyptus were repellent down to 40 cm and extremely repellent (WDPT > 6 h) from 0 to 20 cm. The soil layer from 20 to 40 cm was less repellent; thus, 40% of the samples were extremely repellent (WPDT 1–3 h), 40% severely repellent and 20% moderately repellent.

Table 1. Mean and standard deviation of selected properties of samples collected from the topmost layer (0–5 cm) of soils under different tree species. N = 10 in all cases.

	Oak	Pine	Eucalyptus
Sand (%)	56.1 ± 7.8 a	25.0 ± 5.8 a	19.0 ± 3.6 a
Silt (%)	62.6 ± 6.9 a	21.5 ± 5.0 a	15.9 ± 4.3 a
Clay (%)	63.5 ± 8.9 a	20.9 ± 6.1 a	15.6 ± 3.9 a
Soil moisture (%)	32.4 ± 5.8 b	20.2 ±10.1a	21.4 ± 4.1 a
pH	4.1 ± 0.2 a	4.2 ± 0.4 a	4.2 ± 0.3 a
C (g kg^{-1})	124.5 ± 35.9 a	108.8 ± 32.6 a	106.6 ± 22.5 a
N (g kg^{-1})	7.7 ± 1.7 b	5.8 ± 2.6 ab	5.7 ± 1.9 a
C/N	16 ± 2 b	21 ± 6 a	20 ± 5 a

Within-a-row means followed by the same letter are not significantly different ($p \leq 0.05$)

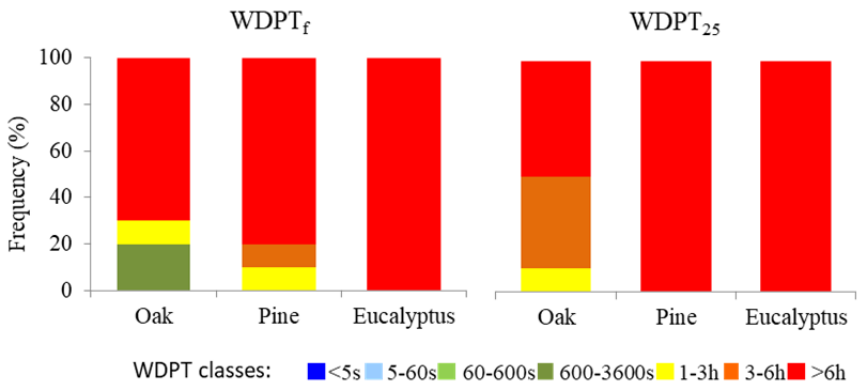

Fig. 1. Relative frequency of median WPDT classes in field-moist ($WDPT_f$) and air-dried ($WDPT_{25}$) surface samples of soils under the three tree species.

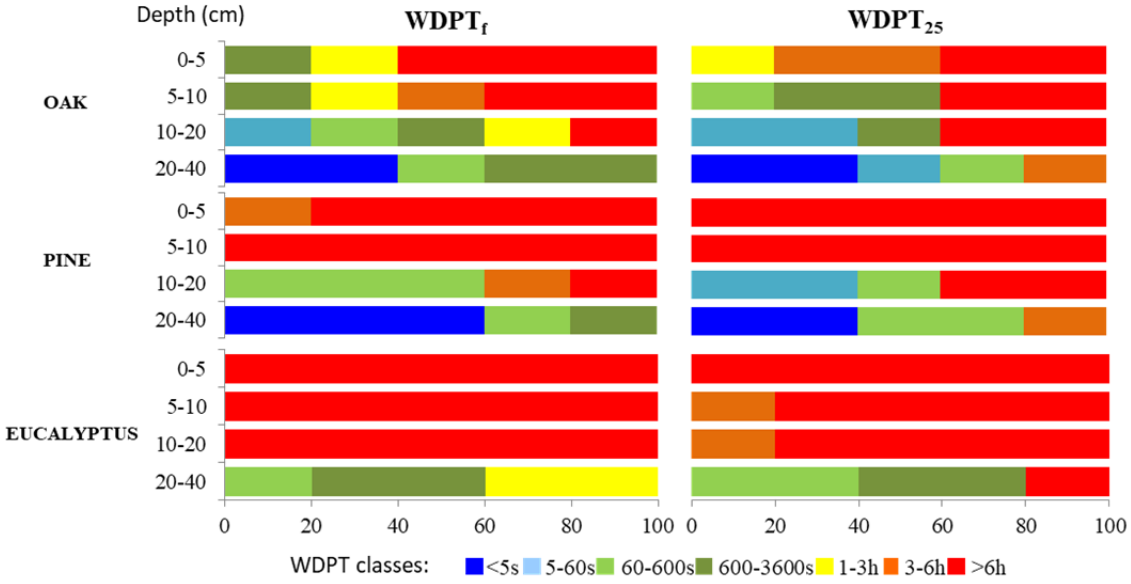

Fig. 2. Relative frequency of median WDPT classes in field-moist ($WDPT_f$) and air-dried samples ($WDPT_{25}$) at different depths of soils under the three tree species.

Table 2. Mean and standard deviation of moisture, C and N contents, and C/N ratio, of samples obtained at different depths in soils under three different tree species. N = 5 in all cases.

	Depth (cm)	Soil moisture (%)	N (g kg^{-1})	C (g kg^{-1})	C/N
Oak	0–5	30.3 ± 7.1 a	7.0 ± 1.3 a	99.6 ± 19.0 a	14 ± 1 ab
	5–10	22.5 ± 6.6 a	6.2 ± 2,0 a	85.1 ± 29.8 a	14 ± 1 ab
	10–20	19.3 ± 8.8 a	4.5 ± 3.1 a	75.8 ± 61.8 a	16 ± 3 ab
	20–40	18.5 ± 10.5 a	3.5 ± 2.9 a	42.2 ± 39.7 a	12 ± 3 c
Pine	0–5	17.8 ± 2.3 a	4.1 ± 0.8 a	87.9 ± 10.1 a	22 ± 5 a
	5–10	16.1 ± 8.3 a	3.5 ± 1.5 a	64.6 ± 25.6 a	19 ± 2 a
	10–20	17.4 ± 8.9 a	3.3 ± 1.4 a	57.1 ± 27.2 a	18 ± 3 a
	20–40	18.1 ± 10.8 a	3.7 ± 1.7 a	64.8 ± 31.7 a	18 ± 3 a
Eucalyptus	0–5	23.0 ± 4.6 a	5.0 ± 1.3 a	111.7 ± 25.3 ab	22 ± 3 a
	5–10	18.1 ± 4.3 a	4.1 ± 1.7 a	78.5 ± 23.8 ab	20 ± 2 a
	10–20	18.6 ± 7.0 a	3.6 ± 1.7 a	61.9 ± 20.8 bc	18 ± 3 a
	20–40	18.1 ± 6.5 a	3.5 ± 1.3 a	59.2 ± 18.3 bc	18 ± 3 a

Within-a-column means followed by the same letter are not significantly different ($p \leq 0.05$)

The soils under pine forest were extremely repellent only in the top 10 cm, below which repellency decreased with increasing depth and 60% of the samples from the 20–40 cm layer were non-repellent. The soils under oak exhibited a similar repellency pattern, the proportion of extremely repellent samples decreasing with increasing depth (from 80% with WPDT > 1 h in the 0–10 cm layer to 40% in the 10–20 cm layer). Below 20 cm, 40% of the samples of soil under oak were non-repellent whereas 40% were severely repellent and 20% moderately repellent. The only significant differences as revealed by the

Man–Whitney test were those between the soils under oak and eucalyptus.

Drying the samples at 25ºC caused no significant changes in water repellency, the Spearman correlation coefficient for $WDPT_f$ and $WDPT_{25}$ being 0.87 ($p < 0.01$).

Table 2 shows the differences in moisture, C, N and C/N among samples obtained at different depths in soils under the three different tree covers.

The moisture content exhibited no significant differences at any depth among forest types despite the fact that the soils under oak were slightly moister in the top 10 cm than were those under pine or eucalyptus.

Overall, C contents decreased with increasing depth in most samples. However, the decrease was only significant between the topmost layer (0–5 cm) and the deeper ones (10–20 cm and 20–40 cm), and only under oak. The C/N ratio changed little with depth in the soils under pine or eucalyptus, the soils under oak having much lower ratios than those under pine or eucalyptus.

Finally, the C content exhibited significant positive correlation with the median $WDPT_f$ (*rho* = 0.40, $p < 0.01$) and $WDPT_{25}$ classes (*rho* = 0.34, $p < 0.01$). The correlation coefficients between the C/N ratio and the median WDPTc and $WDPT_{25}$ classes were 0.49 and 0.54 ($p < 0.01$), respectively. No significant correlation with moisture or N content was observed, however.

DISCUSSION

As in previous studies, the results confirm that water repellency is a widespread phenomenon in coarse-textured forest soils in the NW of the Iberian Peninsula. Also, they confirm that soils under eucalyptus exhibit the highest severity of water repellency in the deeper layers (Rodríguez-Alleres and Benito, 2011, 2012; Rodríguez-Alleres et al., 2007).

Surface soils under eucalyptus and pine forests have also been associated to high levels of water repellency in Portugal (Doerr et al., 1996, 1998; Keizer et al., 2005 a, b; Leighton-Boyce et al., 2005, 2007; Santos et al., 2013; Shakesby et al., 1993), South Africa (Scott, 2000), Australia (Crockford et al., 1991; Doerr et al., 2006), Germany (Buczko et al., 2005, 2007), Italy (Alagna et al., 2017), UK (Doerr et al., 2006), USA (Doerr et al., 2009) and SW Spain (Zavala et al., 2009, 2014). Usually, soil water repellency under oak forest is less persistent than it is under pine or eucalyptus forest (Alanis et al., 2017; Zavala et al., 2009, 2014). However, Jiménez-Morillo et al. (2016) found an increased persistence in soils under oak relative to pine in SW Spain and ascribed this result to the increased content in organic matter of the former (especially in the form of organic films coating the finer soil particles).

The high persistence of water repellency in the surface layers of the soils under the three types of tree cover can be ascribed to a combination of factors including the temperate–humid climate of the area, which facilitates biomass production and as a result of which the soils contain increased amounts of organic matter and hydrophobic substances (Rodríguez-Alleres et al., 2007). Also, the high acidity of the soils boosts fungal proliferation in the biomass it contains and delays mineralization of organic matter by forming humus of the mor or acid mull type (Franco et al., 2003; Rodríguez-Alleres et al., 2012). Also, the coarse texture of the soils increases their water repellency by reducing their specific surface area (Rodríguez-Alleres et al., 2007, 2012). In addition, forest soils under pine and eucalyptus trees contain substantial amounts of resins, wax and aromatic oils that increase the severity of water repellency. De Blas et al. (2010) found evidence that SWR under these tree covers is governed mainly by the concentration of free lipids in hydrophobic coatings. Also, they found the proportions of humic substances and free particulate soil organic matter (SOM) to influence the extent of SWR, the effect depending on the particular type of vegetation. In a subsequent study de Blas et al. (2013) found the free lipid fraction of soils under eucalyptus and pine to consist mainly of sesquiterpenes and diterpenes, respectively; also, they concluded that the major compounds associated to soil water repellency are typically present in higher plants and cannot be synthesized by microorganisms.

The fact that soil water repellency in Spanish forest areas with calcareous soils and a semi-arid climate is typically very low relative to acid forest soils (Arcenegui et al., 2007; Cerdà and Doerr, 2007; Jimenez-Pinilla et al., 2016; Mataix-Solera et al., 2007) has been ascribed to decreased biomass production and the resulting decreased supply of hydrophobic substances to the soil under a dry climate (Jaramillo et al., 2000; Mataix-Solera and Doerr, 2004; Rodríguez-Alleres et al., 2012). Also, the alkalinity of the soils ($pH_{H2O} < 7$) facilitates dissolution of hydrophobic substances and reduces fungal activity (Mataix-Solera and Doerr, 2004; Mataix-Solera et al., 2007).

Few studies have reported so high persistence in water repellency with soil depth as found in this work. Walden et al. (2015) found reforestation with *E. globulus* to induce water repellency across a range of sites in the southwest of Western Australia; contrary to our results, however, they also found SWR to decrease rapidly with increasing depth.

Doerr et al. (2006) examined water repellency in soils differing in texture, organic matter content, moisture and management regime at variable depths and concluded that the last two were reliable predictors for SWR. Also, Vogelmann et al. (2013) concluded that SWR and its persistence in hydrophobic soils decreases with increasing depth and moisture but decreasing organic carbon content. In this work, SWR was positively correlated in a significant manner with the organic C content of the soils, but not with their moisture content. Our results are consistent with those of Mao et al. (2016), Harper et al. (2000), and Zavala et al. (2009), who also found a significant relationship between SOM and SWR, and confirmed earlier findings of our group (Rodríguez-Alleres and Benito, 2011; Varela et al., 2005). On the other hand, Dekker and Ritsema (1994), and Doerr et al. (2005), found no significant correlation between organic C and SWR in sandy soils, possibly because although organic C is a quantitative measure of SOM abundance, SWR persistence is more strongly governed by the composition and quality of organic C in the soil (Cosentino et al., 2010; Zhang et al., 2004). In fact, our results revealed a significant positive correlation between SWR and the C/N ratio that was stronger than that with the content in organic C. The decreased C/N ratio of the soils under oak forest suggests stronger decomposition of organic matter and the presence of more evolved humus relative to the soils under pine and eucalyptus. This may account for the decreased severity of water repellency in the soils under oak relative to eucalyptus and hence for the more marked accumulation of organic matter (organic C and N compounds) under eucalyptus resulting from less marked mineralization of low-quality organic residues.

According to Goebel et al. (2011), persistent water repellency can hinder the decomposition of SOM and temporarily increase the carbon sink strength of the soil. In long term, however, the reduced water availability will also reduce plant productivity and induce changes in plant composition, thereby potentially offsetting the positive effects of an increased SWR on carbon sequestration in the short term.

Our results suggest that the extreme water repellency of the humic horizon of coarse-textured soils under dry conditions in NW Spain (especially under *E. globulus*) can alter their hydrological properties, moisture patterns and water reserves. Properly understanding these consequences is very important to optimize management practices for forest soils with a view to preventing floods, facilitating recharging of underground water and preventing erosion, among others (Benito et al., 2016).

CONCLUSIONS

Water repellency is a widespread property of coarse-textured forest soils in the northwest of the Iberian Peninsula. All samples from the 0–5 cm layer under the three types of plant cover exhibited severe to extreme SWR. Water repellency in the soils under *Quercus robur* natural forest decreased more markedly with increasing depth, especially in relation to the soils under eucalyptus plantation, which were extremely repellent down to 20 cm. Water repellency and its severity increased in the following sequence of forest species: *Q. robur* < *P. pinaster* < *E. globulus.* The differences in water repellency among the soils under different types of vegetation can be ascribed to differences in carbon content and, especially, in C/N ratio.

There were no appreciable differences in water repellency between field-moist and air-dried samples. This result confirms previous recommendations that soils should be sampled at the end of the summer period in order to accurately estimate their potential maximum repellency (Rodríguez-Alleres and Benito, 2012; Rodríguez-Alleres et al., 2007).

Acknowledgements. This study was supported by the Ministerio de Ciencia e Innovación (project AGL2008-01399/FOR).

REFERENCES

Alagna, V., Iovino, M., Bagarello, V., Mataix-Solera, J., Lichner, L., 2017. Application of minidisk infiltrometer to estimate water repellency in Mediterranean pine forest soils. J. Hydrol. Hydromech., 65, 254–263.

Alanís, N., Hernández-Madrigal, V.M., Cerdà, A., Zavala, L.M., Jordán, A., 2017. Spatial gradients of intensity and persistence of soil water repellency under different forest types in Central México. Land Degrad. Develop., 28, 317–327.

Arcenegui, V., Mataix-Solera, J., Guerrero, C., Zornoza, R., Mayoral, A.M., Morales J., 2007. Factors controlling the water repellency induced by fire in calcareous Mediterranean forest soils. European Journal of Soil Science, 58, 1254–1259.

Badía, D., Aguirre, J.A., Martí, C., Márquez, M.A., 2013. Sieving effect on the intensity and persistence of water repellency at different soil depthts and soil types from NE-Spain. Catena, 108, 44–49.

Benito, E., Rodríguez-Alleres, M., Varela, E., 2016. Environmental factors governing soil water repellency dynamics in a *Pinus pinaster* plantation in NW Spain. Land Degrad. Develop., 27, 3, 719–728.

Buczko, U., Bens, O., Hüttl, R.F., 2005. Variability of soil water repellency in sandy forest soils with different stand structure under Scots pine (*Pinus sylvestris*) and beech (*Fagus sylvatica*). Geoderma, 126, 317–336.

Buczko, U., Bens, O., Hüttl, R.F., 2007. Changes in soil water repellency in a pine –beech forest transformation chronosequence: influence of antecedent rainfall and air temperatures. Ecological Engineering, 31, 154–164.

Cerdà, A., Doerr, S.H., 2007. Soil wettability, runoff and erodibility of major dry-Mediterranean land use types on calcareous soils. Hydrol. Process., 21, 2325–2336.

CMR, 2009. Anuario de estatistica agraria 2009. Conselleria de Medio Rural. Xunta de Galicia.

Cosentino, D., Hallett, P.D., Michel, J.C., Chenu, C., 2010. Do different methods for measuring the hydrophobicity of soil aggregates give the same trends in soil amended with residue? Geoderma, 159, 221–227.

Crockford, S., Topalidis, S., Richardson, D.P., 1991. Water repellency in a dry sclerophyll forest – measurements and processes. Hydrol. Process., 5, 405–420.

de Blas, E., Rodríguez-Alleres, M., Almendros, G., 2010. Speciation of lipid and humic fractions in soils under pine and eucaliptus forest in northwest Spain and its effect on water repellency. Geoderma, 155, 242–248.

de Blas, E., Almendros, G., Sanz, J., 2013. Molecular characterization of lipid fractions from extremely water-repellent pine and euclyptus forest soils- Geoderma, 206, 75–84.

De Jonge, L.W., Moldrup, P., Schjonning, P., 2009. Soil infrastructure, interfaces and translocation processes in inner space ('soil-it-is'): towards a road map for the constraints and crossroads of soil architecture and biophysical processes. Hydrology and Earth System Sciences, 13, 1485–1502.

Dekker, L.W., Ritsema, C.J., 1994. How water moves in a water repellent sandy soil. 1. Potential and actual water repellency. Water Resources Research, 30, 2507–2517.

Dekker, L.K., Doerr, S.H., Oostindie, K., Ziogas, A.K., Ritsema, C.J., 2001. Water repellency and critical soil water content in a dune sand. Soil Sci. Soc. Am. J., 65, 1667–1674.

Dekker, L.W., Oostindie, K., Ritsema, C.J., 2005. Exponential increase of publications related to soil water repellency. Aust. J. Soil Res., 43, 403–441.

Doerr, S.H., Shakesby, R.A., Wals, R.P.D., 1996. Soil hydrophobicity variations with depth and particle size fraction in burned and unburned *Eucalyptus globulus* and *Pinus pinaster* forest terrain in the Agueda basin, Portugal. Catena, 27, 25–47.

Doerr, S.H., Shakesby, R.A., Walsh, R.P.D., 1998. Spatial variability of soil water repellency in fire-prone eucalyptus and pine forest, Portugal. Soil Science, 163, 313–324.

Doerr, S.H., Shakesby, R.A., Walsh, R.P.D., 2000. Soil water repellency: its causes, characteristics and hydro-geomorphological consequences. Earth-Science Reviews, 51, 33–65.

Doerr, S.H., Douglas, P., Evans, R.C., Morley, C.P, Mullinger, N.J., Bryant, R., Shakesby, R.A., 2005. Effects of heating and post-heating equilibration times on soil water repellency. Aust. J. Soil Res., 43, 261–267.

Doerr, S.H., Shakesby, R.A., Dekker, L.W., Ritsema, C.J., 2006. Occurrence, prediction and hydrological effects of water repellency amongst major soils and land use types in a humid temperate climate. Eur. J. Soil Sci., 57, 741–754.

Doerr, S.H., Scott, D.F., Dekker, L.W., Ritsema, C.J., Carter, D., 2007. Water repellence of soils: new insights and emerging research needs. Hydrol. Process., 21, 2223–2228.

Doerr, S.H., Woods, S.W., Martin, D.A., Casimiro, M., 2009. Natural background soil water repellency in conifer forests of the north-western USA: Its prediction and relationship to wildfire occurrence. J. Hydrol., 371, 12–21.

Franco, C.M.M., Clarke, P.J., Tate, M.E., Oades, J.M., 2000. Hydrophobic properties and chemical characterisation of natural water-repellent materials in Australian sands. J. Hydrol., 231–232, 47–58.

Franco, C.M.M., Clarke, P.J., Tate, M.E., Oades, J.M., 2003. Chemical characterisation of water repellent materials in

Australian sands. In: Ritsema, C.J, Dekker, L.W. (Eds): Soil Water Repellency: Occurrence, Consequences and Amelioration. Elsevier Science, The Netherlands, pp. 37–50.

Goebel, M.-O., Bachmann, J.B.A., Reichstein, M., Janssens, I.A., Guggenberger, G., 2011. Soil water repellency and its implications for organic matter decomposition-is there a link to extreme climatic events? Global Change Biology, 17, 2640–2656.

Harper, R.J., McKissock, I., Gilkes, R.J., Carter, D.J., Blackwell, P.S., 2000. A multivariate framework for interpreting the effects of soil properties, soil management and land use on water repellency. J. Hydrol., 231–232, 371–383.

Jaramillo, D.F., Dekker, L.W., Ritsema, C.J., Hendrickx, J.M.H., 2000. Occurrence of soil water repellency in arid and humid climates. J. Hydrol., 231–232, 105–111.

Jiménez-Morillo, N.T., González-Pérez, J.A., Jordán, A., Zavala, L.M., de la Rosa, J.M., Jiménez-González, M.A., González-Vila, F.J., 2016. Organic matter fractions controlling soil water repellency in sandy soils from the Doñana National Park (SW Spain). Land Degrad. Develop., 27, 5, 1413–1423.

Jimenez-Pinilla, P., Lozano, E., Mataix-Solera, J., Arcenegui, V., Jordán, A., Zavala, L.M., 2016. Temporal changes in soil water repellency after a forest fire in a Mediterranean calcareous soil: influence of ash and different vegetation type. Sci. Total Environ., 572, 1252–1260.

Johnson, M.S., Lehmann, J., Steenhuis, T.S., de Oliveira, L.V., Fernandes, E.C.M., 2005. Spatial and temporal variability of soil water repellency of Amazonian pastures. Aust. J. Soil Res., 43, 319–326.

Keizer, J.J., Coelho, C.O.A., Matías, M.J.S., Domingues, C.S.P., Ferreira, A.D.J., 2005a. Soil water repellency under dry and wet antecedent weather conditions for selected landcover types in the coastal zone of central Portugal. Aust. J. Soil Res., 43, 3, 297–308.

Keizer, J.J., Ferreira, A.J.D., Coelho, C.O.A., Doerr, S.H., Malvar, M.C., Domingues, C.S.P., Perez, I.M.B., Ruiz, C., Ferrari, K., 2005b. The role of tree stem proximity in the spatial variability of soil water repellency in a eucalypt plantation in coastal Portugal. Aust. J. Soil Res., 43, 3, 251–260.

Leighton-Boyce, G., Doerr, S.H., Shakesby, R.A., Walsh, R.P.D., Ferreira, A.D.J., Boulet, A.K., Coelho, C.O.A., 2005. Temporal dynamics of water repellency and soil moisture in eucalypt plantations, Portugal. Aust. J. Soil Res., 43, 3, 269–280.

Leighton-Boyce, G., Doerr, S.H., Shakesby, R.A., Walsh, R.D.P., 2007. Quantifying the impact of soil water repellency on overland flow generation and erosion: a new approach using rainfall simulation and wetting agents on in situ soils. Hydrol Process., 21, 2337–2345.

Mao, J., Nierop, K.G.J., Rietkerk, M., Sinninghe Damsté J.S., Dekker, S.C., 2016. The influence of vegetation on soil water repellency-markers and soil hydrophobicity. Sci. Total Environment, 566–567, 608–620.

Mataix-Solera, J., Doerr, S.H., 2004. Hydrophobicity and aggregate stability in calcareous topsoils from fire-affected pine forests in southeastern Spain. Geoderma, 118, 1–2, 77–88.

Mataix-Solera, J., Arcenegui, V., Guerrero, C., Mayoral, A.M., Morales, J., Gonzalez, J., García-Orenes, F., Gómez, I., 2007. Water repellency under different plant species in a calcareous forest soil in a semiarid Mediterranean environment. Hydrol. Process., 21, 2300–2309.

Ritsema, C.J., Dekker, L.W., Heijs, A.W.J., 1997. Three-dimensional, fingered flow patterns in a water repellent sandy field soil. Soil Science, 162, 79–90.

Rodríguez-Alleres, M., Benito, E., de Blas, E., 2007. Extent and persistence of water repellency in north-western Spanish soils. Hydrol. Process., 21, 2291–2299.

Rodríguez-Alleres, M., Benito, E., 2011. Spatial and temporal variability of surface water repellency in sandy loam soils of NW Spain under *Pinus pinaster* and *Eucalyptus globulus* plantations. Hydrol. Process., 25, 3649–3658.

Rodríguez-Alleres, M., Benito, E., 2012. Temporal fluctuations of water repellency in forest soils of Galicia, NW Spain. Do soil samples dried at laboratory reflect the potential soil water repellency? Hydrol. Process., 26, 8, 1179–1187.

Rodríguez-Alleres, M., Varela, M.E., Benito, E., 2012. Natural severity of water repellency in pine forest soils from NW Spain and influence of wildfire severity on its persistence. Geoderma, 191, 125–131.

Santos, J.M., Verheijen, F.G.A., Wahren, F.T., Wahren, A., Feger, K.H., Bernard-Jannin, L., Rial-Rivas, M.E., Keizer, J.J., Nunes, J.P., 2013. Soil water repellency dynamics in pine and eucalypt plantations in Portugal-A high resolution time series. Land Degrad. Develop., 27, 5, 1334–1343.

Scott, D.F., 2000. Soil wettability in forested catchments in South Africa as measured by different methods and as affected by vegetation cover and soil characteristics. J. Hydrol., 231–232, 87–104.

Shakesby, R.A., Coelho, C.O.A., Ferreira, A.J.D., Terry, J.R., Walsh, R.P.D., 1993. Wildfire impacts on soil erosion and hydrology in wet Mediterranean forest, Portugal. Int. J. Wildland Fire, 3, 95–110.

USDA, 2004. Soil Survey Laboratory Methods Manual. Soil Survey Investigation report, vol. 42. Version 4.0. USDA-NCRS, Lincoln, NE.

Van't Woudt, B.D., 1959. Particle coatings affect the wettability of soils. Journal of Geophysical Research, 64, 263–267.

Varela, M.E., Benito, E., de Blas, E., 2005. Impact of wildfires on surface water repellency in soils of NW Spain. Hydrol. Process., 19, 3649–3657.

Vogelmann, E.S., Reichert, J.M., Prevedello, J., Consensa, C.O.B., Oliveira, A.É., Awe, G.O., Mataix-Solera, J., 2013. Threshold water content beyond which hydrophobic soils become hydrophilic: The role of soil texture and organic matter content. Geoderma, 209–210, 177–187.

Walden, L.L., Harper, R.J., Mendham, D.S., Henry, D.J., Fontaine, J.B., 2015. Eucalyptus reforestation induces soil water repellency. Soil Research 53, 168–177.

Wallis, M.G., Horne, D.J., 1992. Soil water repellency. Advances in Soil Science, 20, 91–146.

WRB, 2006. World Reference Base for Soil Resources 2006. World Soil Resources Reports, No 103, FAO, Rome.

Zavala, L.M., González, F.A., Jordán, A., 2009. Fire-induced soil water repellency under different vegetation types along the Atlantic dune coast-line in SW Spain. Catena, 79, 153–162.

Zavala, L.M., García-Moreno, J., Gordillo-Rivero, A.J., Jordán, A., Mataix-Solera, J., 2014. Natural soil water repellency in different types of Mediterranean woodlands. Geoderma, 226–227, 170–178.

Zhang, B., Peng, X.H., Zhao, Q.G., Hallett, P.D., 2004. Eluviation of dissolved organic carbon under wetting and drying and its influence on water infiltration in degraded soils restored with vegetation. Eur. J. Soil Sci., 55, 725–737.

Received 23 January 2018
Accepted 23 February 2018

J. Hydrol. Hydromech., 67, 2019, 2, 135–142
DOI: 10.2478/johh-2018-0041

Regionalizing time of concentration using landscape structural patterns of catchments

Bahman Jabbarian Amiri[1, 2*], Junfeng Gao[2], Nicola Fohrer[3], Jan Adamowski[4]

[1] Department of Environmental Science, Faculty of Natural Resources, University of Tehran, Chamran Blvd., Karaj, Iran.
[2] Key Laboratory of Watershed Geographic Sciences, Nanjing Institute of Geography and Limnology, Chinese Academy of Sciences, 73 East Beijing Road, Nanjing 210008, China. E-mail: GaoJunf@niglas.ac.cn
[3] Department of Hydrology and Water Resources, Institute for Nature Conservation and Resource Management, Christian Albrecht Universitaet zu Kiel, Olshausenstr. 75, 24098 Kiel, Germany. E-mail: nfohrer@hydrology.uni-kiel.de
[4] Department of Bioresource Engineering, Faculty of Agricultural and Environmental Sciences, McGill University, Ste-Anne-de-Bellevue, Québec H9X 3V9, Canada. E-mail: jan.adamowski@mcgill.ca
[*] Corresponding author. E-mail: Jabbarian@ut.ac.ir

Abstract: There is an emerging challenge within water resources on how, and to what extent, borrowing concepts from landscape ecology might help re-define traditional concepts in hydrology in a more tangible manner.

A stepwise regression model was adopted in this study to assess whether the time of concentration of catchments could be explained by five landscape structure-representing metrics for land use/land cover, soil and geological patches, using spatial data from 39 catchments.

The models suggested that the times of concentration of the catchments could be predicted using the measures of four landscape structure-representing metrics, which include contiguity index (r^2 = 0.46, $p \leq 0.05$), fractal dimension index (r^2 = 0.51, $p \leq 0.05$), related circumscribing circle (r^2 = 0.52, $p \leq 0.05$), and shape index (r^2 = 0.47, $p \leq 0.05$).

The models indicated that the regularity or irregularity in land use/land cover patch shape played a key role in affecting catchment hydrological response. Our findings revealed that regularity and irregularity in the shape of a given patch (*e.g.*, urban and semi-urban, rangeland and agricultural patches) can affect patch functions in retarding and/or increasing flow accumulation at the catchment scale, which can, in turn, decrease or increase the times of concentration in the catchments.

Keywords: Landscape metrics; Time of concentration; Hydrologic Soil Group; Hydrologic response.

INTRODUCTION

Use of geometrical and mathematical concepts in landscape ecology (*e.g.*, Baker and Cai, 1992; Gustafson, 1998; He et al., 2000; Jaeger, 2000; McGarigal and Marks, 1995; McGarigal et al., 2002; O'Neill et al., 1988; Turner, 1990; Turner and Gardner, 1991) has led to an interesting debate within water resources engineering, planning and management regarding the possibility of explaining hydrological processes in catchments using the metrics of landscape structural patterns. Referring to a well-documented relationship between the pattern and process of surface hydrology (*e.g.*, Van Nieuwenhuyse et al., 2011), it has been hypothesized that hydrological event and response relationships (*e.g.*, Almeida et al., 2014; Fang et al., 2008; Salimi et al., 2016) can be explained explicitly by the landscape attributes of a given catchment. Extending this event-response hypothesis to one of the most significant hydrological response-indicators, time of concentration, using the landscape patterns of a catchment, is a critical area of study.

Response of a catchment to a rainfall event is measured by time of concentration, meaning how quickly or slowly a catchment responds to rainfall input in terms of the time needed for water to flow from the most hydrologically remote point in the catchment to the outlet (USDA, 1986).

There have been extensive applications of time of concentration to hydrological modeling and river engineering works (Fang et al., 2008; Grimaldi et al., 2012; Soulis et al., 2015), but little work has been done in an environmental management context. Knowing a given catchment's behavior in terms of time of concentration can help to prevent and/or minimize the impacts of natural disasters and point source pollution of water resources (Almeida et al., 2014). The suitability of land use allocation at varying scales (from sub-catchment and catchment to basin) can be evaluated for likely hydrological impacts such as the peak discharge, which could be generated due to change in the curve number, an empirical indicator applied in hydrology for estimating direct runoff or infiltration from rainfall excess (USDA, 1986), and consequently that of the time of concentration (Yeo et al., 2007). In this way, catchments of interest could, for example, be developed to increase their resiliency to flooding in a more cost effective manner than allocating significant funds for river engineering projects.

Of the three major landscape features, which are composition, function and structure (Amiri, 2014; Forman and Godron, 1986), the influence of landscape structure on water quantity (Amiri et al., 2016; Lin et al., 2007) and water quality (Amiri and Nakane, 2009; Lee et al., 2009; Paul et al., 2002; Turner and Rabalais, 2003; Uriarte et al., 2011; Uuemma et al., 2007; Wickham et al., 2007) have been studied in catchments.

The study of landscape structure is mainly based on how and to what extent a given function of landscape can be derived from spatial relationships between different shapes of land use and land cover patches within a catchment. Accordingly, there is increasing demand for the development of appropriate indicators, methods and tools to assess how landscape attributes (including composition, structure, and configuration) might affect the functions of a given landscape in hydrological context (Griffith, 2002; Kearns et al., 2005; Rhode et al., 2004).

Landscape-related metrics can also provide reliable information and practical guidelines to develop more environmental-

ly sound approaches to improve the quantity and quality of water resources (Amiri and Nakane, 2009; del Tánago et al., 2016; Lin et al., 2007; Uuemma et al., 2007; Zhou et al., 2014).

The application of percentage-based measures of catchment attributes have dominated regional studies that examined the relationship between time of concentration and catchment geometric attributes (see: McCuen et al., 1984). To the best of our knowledge, there has been no research on hydrological response in general, and time of concentration in particular, from the standpoint of how and to what extent this time-related indicator can explicitly be explained by the structural patterns of catchments.

The objectives of the present study were therefore to: (i) examine whether total variation in time of concentration can be explained by changes in the metrics which represent structural attributes of the landscape; (ii) evaluate to what extent the total variation in time of concentration can be affected by the hydrologic soil groups (HSGs), and geological permeability classes (GPCs) and (iii) develop models which relate changes in the times of concentration to changes in the metrics of the landscape, pedoscape, and lithoscape structures.

MATERIALS AND METHODS

Study area

The study area in the southern basin of the Caspian Sea in Iran was selected due to its diversified land use/land cover, soil types and geological formations (Figure 1; Table 1). The basin area covers 38,467 km^2 (49º48' to 54º41' N lon., 35º36' to 37º19' E. lat.) across a wide range of elevations (–16 m to 4782 m a.s.l.). While 59 rivers drain precipitation from within the basin to the Caspian Sea, limitations in data access and the need to achieve a homogeneous data set led to only 39 catchments being investigated in the present study. These catchments vary in area (32 to 2325 km^2) and in 40-year (1971–2010) mean discharge (0.47 to 21 m^3 s^{-1}), and are dominated by forest cover (57.4%), while rangeland, farmland, urban and semi-urban areas and bodies of water (*e.g.*, wetlands) account for 25.9%, 11.7%, 1.6%, and less than 1% of the total area, respectively.

The underlying bedrock is predominantly made up of granite and andesite. On average, the moderate infilterable soil (S3 group) and the high infilterable soil (S1) (USDA, 1986) cover 53.9% and 4.1% of the catchments, respectively.

Table 1. Distribution statistics of the geometric attributes of the catchments.

Distribution statistic	Catchment metrics				
	Area (km^2)	Slope (%)	Main stream length (km)	Drainage density (km)	Conc. time (min)
Maximum	2325.69	15.47	143.75	63.94	21.59
Minimum	32.82	0.29	5.34	0.20	427.58
Mean	554.74	7.74	43.30	8.78	97.09
Std. dev	584.03	4.48	32.82	14.82	76.18
Median	293.00	7.68	35.16	0.26	82.53
Kurtosis	1.48	–1.05	1.65	5.09	8.44
Skewness	1.47	0.13	1.29	2.27	2.41

Data sets

Digital elevation models (30 m × 30 m) downloaded from the United States Geological Survey (USGS) served to delineate upstream catchment boundaries. A digital land use/land cover (LULC) map (2002; scale 1:250,000) was obtained from the Forest, Range, and Watershed Management Organization of Iran (http://frw.org.ir). Land suitability and geological maps (scale 1:250,000) were obtained from the Iranian Soil and Water Research Institute (http://www.swri.ir) and the Geological Survey of Iran (http://www.gsi.ir), respectively.

Methods

The main steps of the present study are depicted in Figure 2. All the information layers were first transformed into a common digital format, then co-registered with the WGS84 source (zone 39n). The upper catchment boundaries were then delineated by applying the digital elevation model for each of the river gauging stations, applying Digital elevation models (30-m resolution), which were downloaded from the United States Geological Survey (USGS) by Arc Hydro tools in the ArcGIS environment.

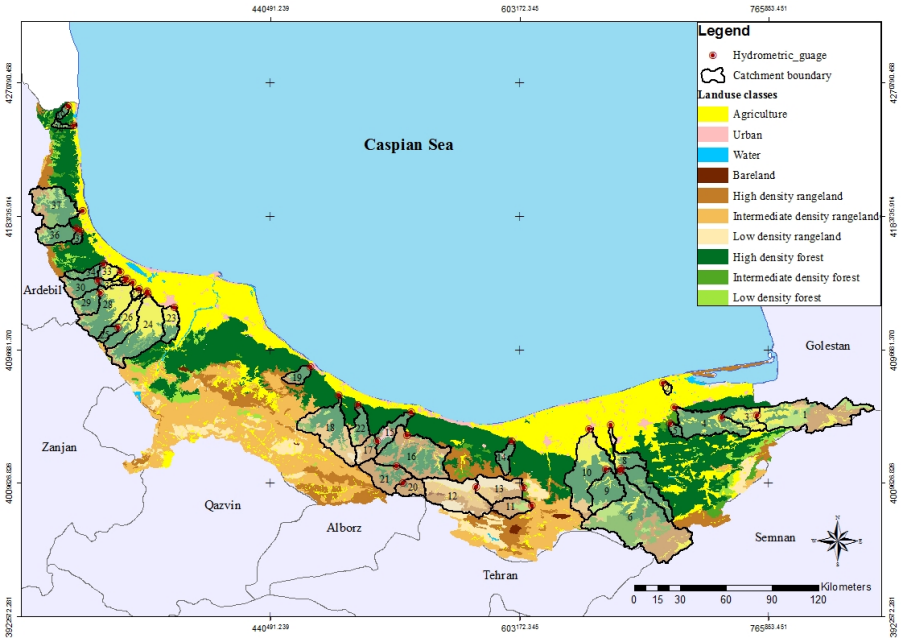

Fig. 1. Geographical location of the catchments in the southern basin of the Caspian Sea.

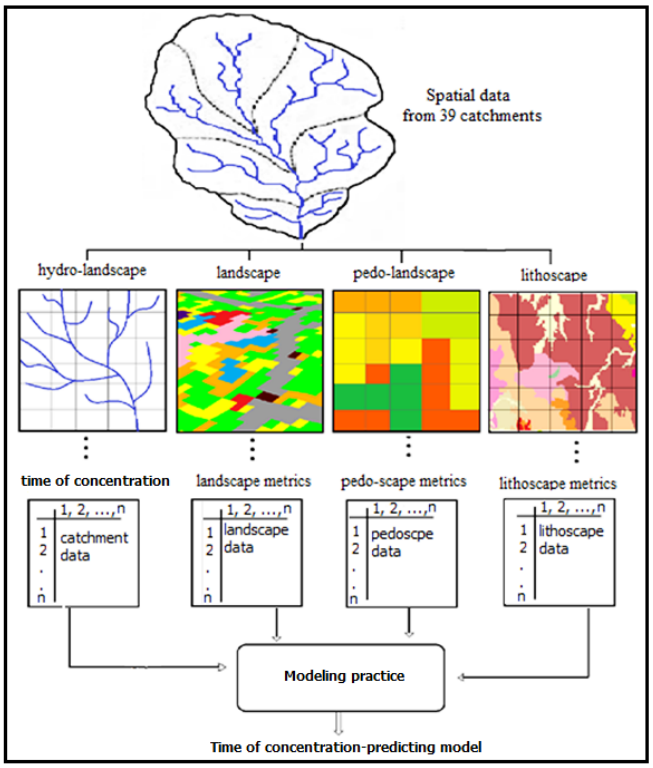

Fig. 2. Main steps of the study.

The study was based on finding a sufficient number of homogeneous catchments in the study area. The main criteria for finding a homogeneous catchment was to select those catchments whose areas vary within three standard deviations of the mean catchment area in our study area.

The LULC map (http://frw.org.ir, 2002) was aggregated into eight classes, including:

- forest (high density, intermediate density, low density; **F1, F2, F3,** respectively),
- rangeland (high density, intermediate density, low density; **R1, R2, R3,** respectively),
- urban and semi-urban (**U**) and,
- agricultural lands (**A**).

Reclassification of the land suitability map (http://www.swri.ir) was conducted to generate a map of hydrologic soil groups (HSGs) with four soil groups, where their infiltration rates decrease, respectively (USDA, 1986). Accordingly, **Group S1** includes sand, loamy sand or sandy loam types of soils, where low runoff potential and high infiltration are their main characteristics (even when thoroughly wetted). **Group S2** is composed of silt loam or loam, where this HSG has a moderate infiltration rate when thoroughly wetted. **Group S3** is formed by sandy clay loam, which has low infiltration rates when thoroughly wetted. **Group S4** soils are clay loam, silty clay loam, sandy clay, silty clay or clay. This HSG has the highest runoff potential and the lowest infiltration (Sangani et al., 2015; USDA, 1986) (Figure 3).

Digital geological maps (http:/www.gsi.ir, scale 1 : 250,000), documenting 19 geological classes (Sangani et al., 2015), were reclassified into three geological permeability classes (GPCs) based on effective porosity, type, size and connectivity of cavities, rock density, pressure gradient and features of the fluid such as viscosity (Fatehi et al., 2015). Spatial variations in geological permeability across the study area was re-classified based on the standpoint of the measure of the rock permeability, which was accordingly termed low permeable rocks **G1**, medium permeable rocks **G2** and high permeable rocks **G3**.

The LULC and HSGs maps were then overlaid on a catchment boundary map, in order to calculate the true extent (%) of each ecological attribute (LULC, HSGs, and GPCs) within the catchments. Thereafter, the landscape structural metrics of the shape index (*shp*), fractal dimension index (*frac*), perimeter-area ratio (*para*), related circumscribing circle (*cir*), and contiguity index (*con*) were calculated at the class level for each of the catchment's ecological attributes (Tables 2 and 3). These landscape metrics were calculated using:

$$shape\,index = \frac{P_{ij}}{minP_{ij}} \tag{1}$$

$$fractal\,dimension\,index = \frac{2\ln\left(0.25P_{ij}\right)}{\ln a_{ij}} \tag{2}$$

$$perimeter-area\,ratio = \frac{P_{ij}}{a_{ij}} \tag{3}$$

$$related\,circumscribing\,circle = 1-\left[\frac{a_{ij}}{a_{ij}^{s}}\right] \tag{4}$$

$$contiguity\,index = \frac{\left[\frac{\sum_{r=1}^{z} C_{ijr}}{a_{ij}}\right]-1}{v-1} \tag{5}$$

where

P_{ij} perimeter (m) of patch *ij*,

a_{ij} area (m^2) of patch *ij*,

a_{ij}^{s} area (m^2) of smallest circumscribing circle around patch *ij*,

C_{ijr} contiguity value for pixel ***r*** in patch *ij*,

v Sum of the values in a 3-by-3 cell template.

This approach in calculating the landscape structure-representing metrics resulted in 15 potentially relevant landscape metrics for a given catchment. For example, in the case of the shape index (*shp*), the following landscape metrics were calculated:

- $F1_{shp}$, $F2_{shp}$, $F3_{shp}$, $R1_{shp}$, $R2_{shp}$, $R3_{shp}$, U_{shp}, A_{shp} (from LULC), namely the shape index for within-catchment patches of high, medium and low density forest; high, medium and low density rangeland; urban and semi-urban and agricultural patches, respectively.
- $S1_{shp}$, $S2_{shp}$, $S3_{shp}$, $S4_{shp}$ (from HSGs), namely the shape index for within-catchment patches of soil, with infiltration rates varying from very high to low, respectively.

$G1_{shp}$, $G2_{shp}$, $G3_{shp}$, (from GPCs), namely the shape index for within-catchment patches of low, medium and high geological permeability, respectively.

FRAGSTATS (McGarigal et al., 2012) was used to calculate landscape metrics of catchment LULCS, HSGs, and GPCs as ecological attributes of the catchments.

Although there are a number of formulae for estimation of time of concentration, each of those formulae can be applied considering their limitations including, but not limited, to catchment area. Accordingly, considering that the catchments' areas vary between 33 to 2325 km^2, the formula of Johnson-Cross (1949) was adopted to calculate the time of concentration as an indicator of hydrological response, using the following formula (Li and Chibber, 2008; Salimi et al., 2017):

$$T_c = 300L^{0.5} \cdot S^{-0.5} \quad (6)$$

where

T_c is the time of concentration (min),

L is catchment length (mi),

S is the catchment slope (ft/mi).

To model the relationship between landscape metrics of a given catchment's ecological attributes and time of concentration, a stepwise regression analysis (entry criterion $p \leq 0.05$, exclusion criterion $p \geq 0.100$) was applied to develop multiple linear regression models through which the times of concentration (dependent variable; min) could be explained by an individual pairing of landscape metric (*cir*, *con, frac*, *para,* and *shp*) and LULCs, HSGs or GPCs (*e.g.*, $T_c = f\,(\mathrm{F1}_{shp})$ independent variables). This yielded the equation:

$$y_i = \beta_0 + \beta_1 x_1 + \beta_2 x_2 + \ldots + \beta_{n-1} x_{n-1} + \varepsilon_i \quad (7)$$

where

y_i is the time of concentration (min) of the catchment,

$x_1 \ldots x_{n-1}$ are the catchment landscape metrics (*cir*, *con, frac, para,* and *shp*),

$\beta_1 \ldots \beta_{n-1}$ are the coefficients of the catchment landscape metrics retained, with $p \leq 0.05$,

β_0 is a constant, with $p \leq 0.05$, and

ε_i is the error for the time of concentration.

Inter-variable collinearity of the developed models was assessed using the variation inflation factor (VIF), where a VIF < 10 for all model parameters indicated a lack of collinearity (Chatterjee et al., 2000; Neter et al., 1996). The models' goodness of fit was evaluated using scatter plots of observed *vs.* predicted values (Figure 4) (Ahearn et. al., 2005). The last critical criteria for choosing the candidate model was to clarify to what extent a given candidate model was useful from the perspective of landscape ecology. All statistical analyses were conducted by IBM SPSS for Windows, Release 19.

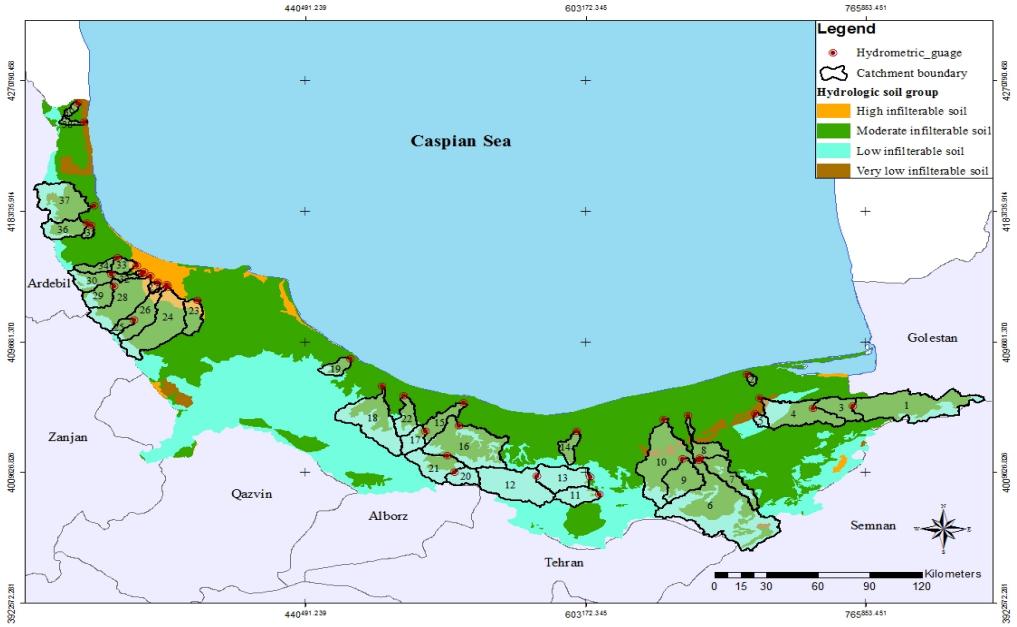

Fig. 3. Spatial distribution of hydrologic soil groups in the southern basin of the Caspian Sea.

Table 2. Catchment metric distribution statistics for land use/land cover classes at the patch level.

Metric	Statistic	Land use/cover classes							
		Rangeland			Farmland (A)	Forest			Urban and semi-urban (U)
		R1	R2	R3		F1	F2	F3	
Cir	Max.	0.85	0.83	0.73	0.93	0.79	0.88	0.91	0.94
	Min.	0.00	0.00	0.00	0.00	0.00	0.00	0.00	0.00
	Median	0.65	0.00	0.00	0.69	0.60	0.64	0.51	0.61
	Mean	0.57±0.29	0.29±0.35	0.12±0.26	0.60±0.27	0.53±0.23	0.51±0.32	0.43±0.33	0.44±0.32
con	Max.	0.99	0.98	0.99	0.99	1.00	0.98	0.99	0.97
	Min.	0.00	0.00	0.00	0.00	0.00	0.00	0.00	0.00
	Median	0.95	0.00	0.00	0.87	0.66	0.73	0.62	0.81
	Mean	0.71±0.38	0.32±0.43	0.15±0.34	0.70±0.32	0.65±0.32	0.62±0.39	0.52±0.40	0.56±0.41
frac	Max.	1.15	1.15	1.09	1.19	1.18	1.27	1.17	1.18
	Min.	0.00	0.00	0.00	0.00	0.00	0.00	0.00	0.00
	Median	1.11	0.00	0.00	1.10	1.09	1.10	1.10	1.07
	Mean	0.91±0.43	0.45±0.55	0.19±0.42	0.97±0.38	0.96±0.37	0.83±0.50	0.74±0.53	0.73±0.52
para	Max.	907.81	908.64	528.61	825.15	772.88	832.33	691.27	700.84
	Min.	0.00	0.00	0.00	0.00	0.00	0.00	0.00	0.00
	Median	41.58	0.00	0.00	122.42	337.77	46.77	41.80	90.85
	Mean	129.10±230.48	110.88±255.43	32.01±117.86	211.87±227.59	272.65±265.01	151.80±201.09	181.42±230.25	124.49±151.50
shp	Max.	4.04	3.67	2.23	4.63	5.97	10.83	3.64	3.61
	Min.	0.00	0.00	0.00	0.00	0.00	0.00	0.00	0.00
	Median	2.49	0.00	0.00	2.11	2.23	2.15	2.11	1.56
	Mean	2.12±1.17	0.88±1.12	0.33±0.72	2.21±1.24	2.26±1.33	2.11±1.97	1.73±1.33	1.28±1.02

Table 3. Catchment metric distribution statistics by hydrologic soil groups and geological permeability group at the patch level across.

Catchment Metric	Statistic	Hydrologic soil group				Geological permeability class		
		S1	S2	S3	S4	G1	G2	G3
cir	Max.	0.84	0.83	0.84	0.76	0.76	0.81	0.82
	Min.	0.00	0.00	0.00	0.00	0.44	0.00	0.00
	Median	0.28	0.55	0.45	0.47	0.66	0.67	0.66
	Mean	0.29±0.31	0.45±0.30	0.38±0.33	0.34±0.31	0.64±0.08	0.60±0.20	0.49±0.34
con	Max.	1.00	1.00	1.00	1.00	1.00	0.99	1.00
	Min.	0.00	0.00	0.00	0.00	0.19	0.00	0.00
	Median	0.87	0.97	0.71	0.94	0.93	0.95	0.93
	Mean	0.50±0.50	0.67±0.44	0.54±0.47	0.55±0.49	0.88±0.14	0.83±0.27	0.65±0.44
frac	Max.	1.13	1.13	1.12	1.12	1.10	1.12	1.12
	Min.	0.00	0.00	0.00	0.00	1.04	0.00	0.00
	Median	1.03	1.06	1.05	1.05	1.07	1.07	1.07
	Mean	0.54±0.54	0.77±0.49	0.63±0.54	0.60±0.54	1.07±0.02	0.99±0.29	0.75±0.50
para	Max.	143.59	665.52	466.91	280.31	1046.17	538.06	183.18
	Min.	0.00	0.00	0.00	0.00	5.73	0.00	0.00
	Median	3.76	5.85	4.16	4.58	80.23	43.56	27.09
	Mean	12.08±26.58	60.15±137.37	62.41±128.38	20.11±49.79	143.76±182.56	115.90±151.00	44.10±51.20
shp	Max.	3.26	2.65	2.93	3.20	2.75	2.68	2.56
	Min.	0.00	0.00	0.00	0.00	1.30	0.00	0.00
	Median	1.36	1.67	1.53	1.46	1.77	1.88	1.66
	Mean	0.87±0.90	1.32±0.90	1.10±0.97	1.05±0.99	1.82±0.29	1.82±0.60	1.28±0.90

RESULTS AND DISCUSSION

Stepwise regression models were developed for the time of concentration using the five landscape structure-related metrics (*con, frac, para*, *cir*, *shp*) for land use land cover, soil and geology (Equations (8) to (12)). Table 4 shows other statistics of these models. The total variation in times of concentration were explained by the landscape structural metrics of catchments in the following multiple linear regression models:

$$\log y = 1.587 + 0.555U_{cir} - 0.530S4_{cir} + 0.469G3_{cir} \quad (8)$$

$$\log y = 1.311 + 0.243U_{con} + 0.444A_{con} - 0.233S3_{con} \quad (9)$$

$$\log y = -3.963 + 0.185U_{frac} + 0.364A_{frac} + \\ + 0.187R1_{frac} + 4.925G3_{frac} \quad (10)$$

$$\log y = 1.806 + 0.001G2_{para} \quad (11)$$

$$\log y = 1.633 + 0.11U_{shp} - 0.165S4_{shp} + 0.221G3_{shp} \quad (12)$$

where

$\log y$ is the logarithmic measure of time of concentration of the catchment in base of 10,

cir is the mean related circumscribing circle index for a given class of the landscape, pedoscape, and lithoscape of the catchment,

con is the mean contiguity index for a given class of the landscape, pedoscape, and lithoscape of the catchment,

frac is the mean fractal dimension circle index for a given class of the landscape, pedoscape, and lithoscape of the catchment,

para is the mean parameter-area ratio index for a given class of the landscape, pedoscape, and lithoscape of the catchment,

shp is the mean shape index for a given class of the landscape, pedoscape, and lithoscape of the catchment,

U is the urban and semi-urban class,

A is the agriculture class,

*R*1 is the high density rangeland class,

*S*3 is the moderate infilterable soil group,

*S*4 is the low infilterable soil group,

*G*2 is the medium permeable geological class, and

*G*3 is the highly permeable geological class.

The regression models suggested that times of concentration of the catchments could be predicted using four landscape structure-representing metrics out of five: contiguity index ($r^2 = 0.46$, $p \leq 0.05$), fractal dimension index ($r^2 = 0.51$, $p \leq 0.05$), related circumscribing circle ($r^2 = 0.52$, $p \leq 0.05$), and shape index ($r^2 = 0.47$, $p \leq 0.05$) (Table 4).

Eqs. (8) to (12) reveal that only seven LULC classes (out of ten), including urban and semi-urban (U), agriculture (A), high density rangeland (R1), moderate infilterable soil group (S3), low infilterable soil group (S4), medium permeable geological class (G2) and highly permeable geological class (G3), were relevant based on the stepwise regression modeling.

Moreover, although there is no model in which the explanatory variable of low permeable geological class (G1) could partially explain total variation in the time of concentration, the presence of the highly permeable geological class (G3) was observed in all the models except for Eqs. (9) and (11).

To be more specific, Eq. (8) suggests that there is a direct association between the measures of time of concentration and the related circumscribing circle indices of urban and semi urban patches (U_{cir}), and highly permeable geological patches ($G3_{cir}$). Accordingly, if the related circumscribing circle indices, hereafter called the ***circularity index***, of the urban and semi-urban patches and that of the highly permeable geological patches increase, the time of concentration for the catchment will increase. The circularity index is a measure for assessing the extent to which the shape of a given patch or class deviates from a convoluted shape and approaches a narrow and elongated one (Turner et al., 2001). It varies from 0 for the convoluted patches to 1 for the elongated ones (Rutledge, 2003).

The model revealed that urban and semi-urban patches, with relatively narrow and elongated shapes, would contribute more to the runoff generation process than urban and semi-urban patches with a relatively convoluted shape in the catchments under study. In contrast, if the circularity index of the low infilterable soil patches ($S4_{cir}$) increases, the time of concentration will decrease for the catchments. It implies that elongating the shape of the low infilterable soil patches due to an increase in the circularity index would contribute to generating an overflow process in a given catchment, rather than a convolution in the shape of the low infilterable soil patches.

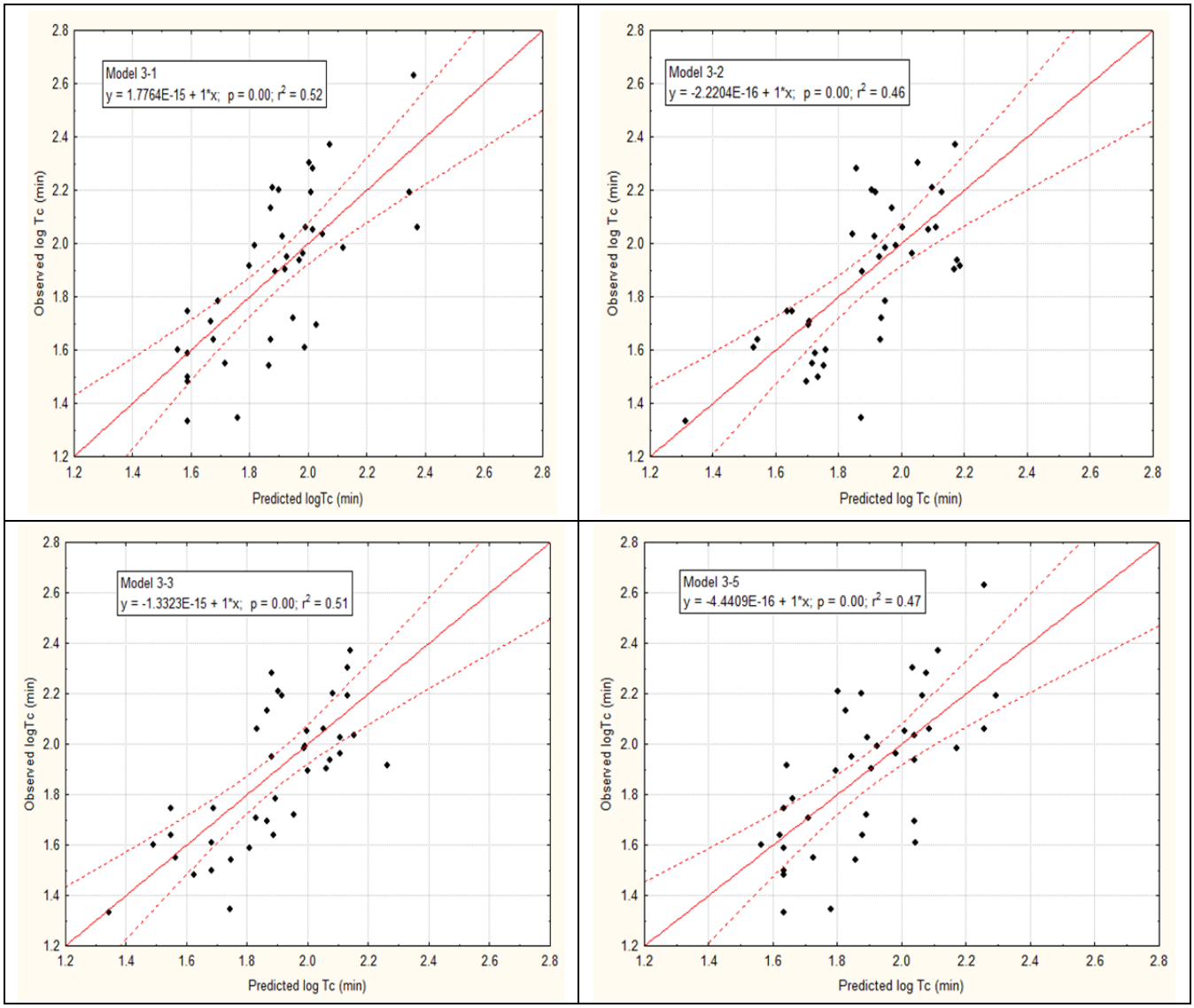

Fig. 4. Predicted vs. observed values for the times of concentration in the study catchments.

Table 4 and Eq. (9) show that 46% of the total variation in times of concentration of the catchments can be explained by the mean measure of the contiguity index of the urban and semi-urban and agricultural patches (A_{con} and U_{con}, respectively), and highly permeable geological patches ($G3_{con}$) called (termed lithoscape metric). Moreover, it suggests that the mean measure of the contiguity indices of the urban and semi-urban and agricultural patches, and that of the highly permeable geological patches, are positively related to the times of concentration of the catchments.

This index indicates to what extent a set of patches are spatially connected and how far homogenous and heterogeneous patches are in relation to each other, respectively. It varies between $0 \leq contiguity\ index \leq 1$ (Rutledge, 2003), and increasing the measure of the index indicates that the patches of interest are larger, more continuous and less dispersed for homogenous patches or less interspersed for heterogeneous patches. A higher contiguity index signifies that more spatially connected and extensive patches can be expected in a given landscape and *vice versa* (Turner et al., 2001).

As a consequence, Eq. (9) suggests if the contiguity indices for the urban and semi-urban class, and agricultural and highly permeable geological patches increase in a given catchment, the time of concentration of the catchment will increase. If the distances for those patches are decreased, instead of contributing to the overflow process, those patches might contribute to the infiltration process within the catchment.

The mean measure of fractal dimension indices of the urban and semi-urban class, and agricultural and high density rangeland patches (U_{frac}, A_{frac} and $R1_{frac}$, respectively), and highly permeable geological patches ($G3_{frac}$) as a lithoscape metric, explains 51% of the total variation in the time of concentration of the catchments (Table 4; Eq. (10)).

The fractal dimension metric varies ($1 \leq fractal\ dimension\ index \leq 2$), and measures the shape complexity of a patch or a set of patches (of a given class) (Rutledge, 2003; Turner et al., 2001). If the metric approaches one, the patch is regular (square) in shape; approaching its upper limit results in a more irregular (convoluted) patch (Rutledge, 2003).

Eq. (10) indicates that the more irregular the shape of the urban and semi-urban patches, and the agricultural and intermediate density rangeland patches, the higher the time of concentration. This function might be due to a retarding role of the convoluted patch shapes in draining water from their surfaces into the drainage networks of the catchments.

Although there is well-documented evidence on the impacts of urban, semi-urban and agricultural areas in contributing to runoff processes at different scales (*e.g.*, Deelstra et al., 2014;

Table 4. Statistics of regression models for the times of concentration in the study catchments based on different landscape structural metrics.

Model		Coefficients			r^2	T_c (min)	Sig.	Collinearity statistics	
No.	Variable	B	Std. error	Beta				Tolerance	VIF
Eq. (8)	Cons.	1.587	0.071		0.52	22.295	0.000		
	$G3_{cir}$	0.469	0.116	0.509		4.038	0.000	0.866	1.155
	U_{cir}	0.555	0.125	0.629		4.427	0.000	0.682	1.467
	$S4_{cir}$	–0.530	0.144	–0.547		–3.693	0.001	0.627	1.594
Eq. (9)	Cons.	1.311	0.116		0.46	11.260	0.000		
	U_{con}	0.243	0.098	0.337		2.470	0.019	0.835	1.198
	A_{con}	0.444	0.121	0.472		3.667	0.001	0.938	1.067
	$S3_{con}$	0.233	0.090	0.364		2.589	0.014	0.789	1.268
Eq. (10)	Cons.	–3.963	2.501		0.51	–1.584	0.122		
	U_{frac}	0.185	0.072	0.323		2.570	0.015	0.915	1.093
	A_{frac}	0.364	0.096	0.460		3.780	0.001	0.975	1.026
	$R1_{frac}$	0.178	0.066	0.326		2.680	0.011	0.974	1.027
	$G3_{frac}$	4.925	2.342	0.264		2.103	0.043	0.917	1.090
Eq. (11)	Cons.	1.806	0.058		0.12	31.310	0.000		
	$G2_{para}$	0.001	0.000	0.342		2.211	0.033	1.000	1.000
Eq. (12)	Cons.	1.633	0.071		0.47	22.868	0.000		
	$G3_{shp}$	0.221	0.053	0.667		4.194	0.000	0.602	1.662
	$S4_{shp}$	–0.165	0.048	–0.547		–3.454	0.001	0.608	1.646
	U_{shp}	0.110	0.039	0.373		2.845	0.007	0.885	1.130

Gallo et al., 2013; Hundecha and Bárdossy, 2004; Niehoff et al., 2002; Olang et al., 2014; Sun et al., 2016; Wijesekara et al., 2012), the findings of the present study suggest that varying the shape of those types of patches from a square shape to a convoluted shape might change their function in the runoff generation process.

Table 4 reveals 47% of the total variation in the time of concentration of the catchments can be explained by the mean measure of the shape index of the urban and semi-urban patches (U_{shp}), and those of the highly permeable geological patches ($G3_{shp}$) and the low infilterable soil patches ($S4_{shp}$) (Eq. (12)).

The shape index can be considered one of the simplest and most understandable measures to assess the overall complexity of a patch (Turner et al., 2001). It varies from 1 to ∞ (Rutledge, 2003). Approaching the low limit implies that the patches of interest are square in shape, while approaching the high limit indicates the patches are of a more irregular shape (Rutledge, 2003). Accordingly, regularity or irregularity in the shape of a given patch, regardless of its prevalent function in a hydrological context, might present a different understanding of patch function in a new arena (termed *landscape hydrology*). These contradictory functions can be inferred from the role of the shape indices of the urban and semi-urban patches (U_{shp}) and highly permeable geological patches ($G3_{shp}$) in Eq. (12).

CONCLUSIONS

This study demonstrated that landscape structural metrics can explain a significant amount of the variation in time of concentration of catchments. To determine the extent that landscape structural metrics could contribute to predicting the time of concentration, a multiple linear regression approach (due to its inherent features that help explore the hidden dimensions of relationships between the components of the system) was applied to develop the models. Possible relationships were examined using geospatial data from 39 catchments, which are geographically distributed in the southern basin of the Caspian Sea. The coefficients of determination for the multiple regression models varied from 0.12 to 0.52.

Applying the models is restricted to the specific range of variables for the areas of the particular catchments under study (32 to 2325 km^2). Below and above this size, local or regional variations might play an important role in explaining the variation in the times of concentration, which varied from 21 to 427 minutes.

The present study showed that landscape structural metrics including the contiguity index (*con*), fractal dimension index (*frac*), related circumscribing circle (*cir*) and the shape index (*shp*) for land use/land cover, soil and geology are significant in explaining hydrological responses in general, and time of concentration, in particular.

Moreover, our findings revealed that regularity and irregularity in the shape of a given patch (*e.g.*, urban and semi-urban, rangeland and agricultural) can affect patch functions (retarding and/or increasing flow accumulation) at the catchment scale, which would, in turn, decrease or increase the times of concentration in the catchments.

It should be noted that the highly permeable geological patches, and the low infilterable soil patches, play a significant and distinct role in advancing or retarding the times of concentration in models for the catchments, depending on the extent of their shape irregularity.

The knowledge obtained regarding landscape metrics in explaining the duration of the time of concentration can help explain the hydrological process explicitly. It would be very useful if future research concentrates on the relationship between the times of concentration of catchments, and landscape composition-representing metrics, and/or landscape configuration-representing metrics.

Acknowledgements. The first author would like to thank the Chinese Academy of Sciences (CAS) and Nanjing Institute of Geography and Limnology (NIGLAS) for supporting this project by providing him with a Visiting Professor fellowship as part of the CAS President's International Fellowship Initiative.

REFERENCES

Ahearn, D.S., Sheibley, R.W., Dahlgren, R.A., Anderson, M., Johnson, J., Tate, K.W., 2005. Land use and land cover influence on water quality in the last free-flowing river draining the western Sierra Nevada, California. J. Hydrol., 313, 3–4, 234–247. DOI: 10.1016/j.jhydrol.2005.02.038.

Almeida, I.K.D, Almeida, A.K., Aache, J.A.A., Steffen, J.L., Alves Sobrinho, T., 2014. Etimation on time of concentrationof overland flowin watersheds: A review. Geociências, 33, 4, 661–671.

Amiri, B.J., Fohrer, N., Cullmann, J., Hörmann, G., Müller, F., Adamowski, J., 2016. Regionalization of tank model using landscape metrics of catchments. Water Resources Management, 30, 14, 5065–5085.

Amiri, B.J., 2014. Environmental Impacts Assessment. Tehran University Press, University of Tehran, 174 p.

Amiri, B.J., Nanake, K., 2009. Modeling the linkage between river water quality and landscape metrics in the Chugoku district of Japan. Journal of Water Resources Management, 23, 931–956.

Baker, W.L., Cai, Y., 1992. The programs for multiscale analysis of landscape structure using the GRASS geographical information system. Landscape Ecology, 7, 291– 302.

Chatterjee, S., Hadi, A.S., Price, B., 2000. The Use of Regression Analysis by Example. John Wiley and Sons, New York, USA.

del Tánago, M.G., Gurnell, A.M., Belletti, B., de Jalón, D.G., 2016. Indicators of river system hydromorphological character and dynamics: understanding current conditions and guiding sustainable river management. Aquatic Sciences, 78, 1, 35–55.

Deelstra, J., Iital, A., Povilaitis, A., Kyllmar, K., Greipsland, I., Blicher-Mathiesen, G., Lagzdins, A., 2014. Reprint of "Hydrological pathways and nitrogen runoff in agricultural dominated catchments in Nordic and Baltic countries". Agriculture, Ecosystems & Environment, 198, 65–73.

Fang, X., Thompson, D.B., Cleveland, T.G., Pradhan, P., Malla, R., 2008. Time of concentration estimated using watershed parameters determined by automated and manual methods. Journal of Irrigation and Drainage Engineering, 134, 2, 202–211.

Fatehi, I., Amiri, B.J., Alizadeh, A., Adamowski, J., 2015. Modeling the relationship between catchment attributes and in-stream water quality. Water Resources Management, 29, 14, 5055–5072.

Forman, R.T.T., Godron, M., 1986. Landscape Ecology. Wiley, New York.

Gallo, E.L., Brooks, P.D., Lohse, K. A., McLain, J.E., 2013. Land cover controls on summer discharge and runoff solution chemistry of semi-arid urban catchments. Journal of Hydrology, 485, 37–53.

Griffith, J., 2002. Geographic techniques and recent applications of remote sensing to landscape-water quality studies. Water, Air, and Soil Pollution, 138, 181–197.

Grimaldi, S., Petroselli, A., Tauro, F., Porfiri, M., 2012. Time of concentration: a paradox in modern hydrology. Hydrological Sciences Journal, 57, 2, 217–228.

Gustafson, E.J., 1998. Quantifying landscape spatial pattern: what is the state of the art? Ecosystems, 1, 2, 143–156.

He, H.S., DeZonia, B.E., Mladenoff, D.J., 2000. An aggregation index (AI) to quantify spatial patterns of landscapes. Landscape Ecology, 15, 591–601.

Hundecha, Y., Bárdossy, A., 2004. Modeling of the effect of land use changes on the runoff generation of a river basin through parameter regionalization of a watershed model. Journal of Hydrology, 292, 1, 281–295.

Jaeger, J.A.G., 2000. Landscape division, splitting index, and effective mesh size: new measures of landscape fragmentation. Landscape Ecol., 15, 115–130.

Kearns, F.R., Maggi, K.N., Carter, J.L., Resh, V.H., 2005. A method for the use of landscape metrics in freshwater research and management. Landscape Ecology, 20, 113–125.

Lee, S.W., Hwang, S.J., Lee, S.B., Hwang, H.S., Sung, H.C., 2009. Landscape ecological approach to the relationships of land use patterns in watersheds to water quality characteristics. Landscape and Urban Planning, 92, 2, 80–89.

Li, M.H., Chibber, P., 2008. Overland flow time of concentration on very flat terrains. Trans. Res. Rec., 2060, 133–140.

Lin, Y.P., Hong, N.M., Wu, P.J., Wu, C.F., Verburg, P.H., 2007. Impacts of land use change scenarios on hydrology and land use patterns in the Wu-Tu watershed in Northern Taiwan. Landscape and Urban Planning, 80, 1, 111–126.

McGarigal, K., Cushman, S.A., Neel, M.C., Ene, E., 2002. FRAGSTATS: Spatial Pattern Analysis Program for Categorical Maps. Computer software program produced by the authors at the University of Massachusetts, Amherst. Available at the following web site: http://www.umass.edu/ landeco/research/fragstats/fragstats.html.

McGarigal, K., Marks, B.J., 1995. FRAGSTATS: Spatial Analysis Program for Quantifying Landscape Structure. USDA Forest Service General Technical Report PNW-GTR-351.

McCuen, R.H., Wong, S.L., Rawls., W.J., 1984. Estimating urban time of concentration. Journal of Hydraulic Engineering, 110, 7, 887–904.

Neter, J., Kutner, H.M., Nachtsheim, C.J., Wasserman, W., 1996. Applied Linear Statistical Models. Irwin, Chicago, IL, USA.

Niehoff, D., Fritsch, U., Bronstert, A., 2002. Land-use impacts on storm-runoff generation: scenarios of land-use change and simulation of hydrological response in a meso-scale catchment in SW-Germany. Journal of Hydrology, 267, 1, 80–93.

Olang, L.O., Kundu, P.M., Ouma, G., Fürst, J., 2014. Impacts of land cover change scenarios on storm runoff generation: a basis for management of the Nyando Basin, Kenya. Land Degradation & Development, 25, 3, 267–277.

O'Neill, R.V., Krummel, J.R., Gardner, R.H., Sugihara, G., Jackson, B., DeAngelis, D.L., Milne, B.T., Turner, M.G., Zygmunt, B., Christensen, S.W., Dale, V.H., Graham, R.L., 1988. Indices of landscape pattern. Landscape Ecology, 1, 153–162.

Paul, J.F., Comeleo, R.L., Copeland, J., 2002. Landscape metrics and estuarine sediment contamination in the mid-Atlantic and southern New England regions. Journal of Environmental Quality, 31, 3, 836–845.

Rhode, S., Kienast, F., Bürgi, M., 2004. Assessing the restoration success of river widenings: a landscape approach. Environmental Management, 34, 4, 574–589.

Rutledge, D.T., 2003. Landscape indices as measures of the effects of fragmentation: can pattern reflect process? Department of Conservation, Wellington.

Salimi, E.T., Nohegar, A., Malekian, A., Hoseini, M., Holisaz, A., 2017. Estimating time of concentration in large watersheds. Paddy and Water Environment, 15, 1, 123–132.

Salimi, E.T., Nohegar, A., Malekian, A., Hoseini, M. and Holisaz, A., 2017. Estimating time of concentration in large watersheds. Paddy and Water Environment, 15, 1, 123–132.

Sangani, M.H., Amiri, B.J., Shabani, A.A., Sakieh, Y., Ashrafi, S., 2015. Modeling relationships between catchment attributes and river water quality in southern catchments of the Caspian Sea. Environmental Science and Pollution Research, 22, 7, 4985–5002.

Sun, N., Yearsley, J., Baptiste, M., Cao, Q., Lettenmaier, D.P., Nijssen, B., 2016. A spatially distributed model for assessment of the effects of changing land use and climate on urban stream quality. Hydrological Processes, 30, 25, 4779–4798.

Turner, R.E., Rabalais, N.N., 2003. Linking landscape and water quality in the Mississippi River basin for 200 years. BioScience, 53, 6, 563–572.

Turner, M.G., Gardner, R.H., O'Neill, R.V., 2001. Landscape Ecology in Theory and Practice. Vol. 401. Springer, New York.

Turner, M.G., Gardner, R.H., 1991. Quantitative Methods in Landscape Ecology. Springer-Verlag, New York.

Turner, M.G., 1990. Spatial and temporal analysis of landscape patterns. Landscape Ecology, 4, 21–30.

Uriarte, M., Yackulic, C.B., Lim, Y., Arce-Nazario, J.A., 2011. Influence of land use on water quality in a tropical landscape: a multi-scale analysis. Landscape Ecology, 26, 8, 1151–1164.

Uuemma, E., Roosaare, J., Mander, U., 2007. Landscape metrics as indicators of river water quality at catchment scale. Nordic Hydrology, 38, 2, 125–138.

USDA, 1986. Urban Hydrology for Small Watersheds. Technical Release 55 (TR-55). 2nd Ed. Natural Resources Conservation Service, Conservation Engineering Division.

Soulis, K.X., Dercas, N., Papadaki, C.H., 2015. Effects of forest roads on the hydrological response of a small-scale mountain watershed in Greece. Hydrological Processes, 29, 7, 1772–1782.

Van Nieuwenhuyse, B.H., Antoine, M., Wyseure, G., Govers, G., 2011. Pattern-process relationships in surface hydrology: hydrological connectivity expressed in landscape metrics. Hydrological Processes, 25, 24, 3760–3773.

Wickham, J.D., Riitters, K.H., Wade, T.G., Coulston, J.W., 2007. Temporal change in forest fragmentation at multiple scales. Landscape Ecology, 22, 4, 481–489.

Wijesekara, G.N., Gupta, A., Valeo, C., Hasbani, J.G., Qiao, Y., Delaney, P., Marceau, D.J., 2012. Assessing the impact of future land-use changes on hydrological processes in the Elbow River watershed in southern Alberta, Canada. Journal of Hydrology, 412, 220–232.

Zhou, T., Ren, W., Peng, S., Liang, L., Ren, S., Wu, J., 2014. A riverscape transect approach to studying and restoring river systems: A case study from southern China. Ecological Engineering, 65, 147–158.

Yeo, I.Y., Guldmann, J.M., Gordon, S.I., 2007. A hierarchical optimization approach to watershed land use planning. Water Resources Research, 43, 11, W11416.

Received 8 August 2017
Accepted 10 February 2018

J. Hydrol. Hydromech., 67, 2019, 2, 143–153
DOI: 10.2478/johh-2018-0043

Assessing methods for the estimation of response times of stream discharge: the role of rainfall duration

Jaime G. Cuevas[1, 2*], José L. Arumí[3], José Dörner[2, 4]

[1] Centro de Estudios Avanzados en Zonas Áridas (CEAZA), Av. Raúl Bitrán 1305, La Serena, Chile.
[2] Centro de Investigación en Suelos Volcánicos (CISVo), Universidad Austral de Chile, Valdivia, Chile.
[3] Facultad de Ingeniería Agrícola, Departamento de Recursos Hídricos, Centro CRHIAM, Universidad de Concepción, Chillán, Chile.
[4] Instituto de Ingeniería Agraria y Suelos, Universidad Austral de Chile, Valdivia, Chile.
[*] Corresponding author. Tel.: +56 51 2204378. E-mail: jxcuevas@ceaza.cl

Abstract: Lagtimes and times of concentration are frequently determined parameters in hydrological design and greatly aid in understanding natural watershed dynamics. In unmonitored catchments, they are usually calculated using empirical or semiempirical equations developed in other studies, without critically considering where those equations were obtained and what basic assumptions they entailed. In this study, we determined the lagtimes (LT) between the middle point of rainfall events and the discharge peaks in a watershed characterized by volcanic soils and swamp forests in southern Chile. Our results were compared with calculations from 24 equations found in the literature. The mean LT for 100 episodes was 20 hours (ranging between 0.6–58.5 hours). Most formulae that only included physiographic predictors severely underestimated the mean LT, while those including the rainfall intensity or stream velocity showed better agreement with the average value. The duration of the rainfall events related significantly and positively with LTs. Thus, we accounted for varying LTs within the same watershed by including the rainfall duration in the equations that showed the best results, consequently improving our predictions. Izzard and velocity methods are recommended, and we suggest that lagtimes and times of concentration must be locally determined with hyetograph-hydrograph analyses, in addition to explicitly considering precipitation patterns.

Keywords: Empirical equations; Lagtimes; Semiempirical equations; Streamflow; Times of concentration.

INTRODUCTION

Streamflow does not respond instantaneously to rainfall; there is a delay between rain and discharge peaks (McCuen, 2009). This gave origin to the concepts of lagtimes (LT) and times of concentration (Tc), which are frequently determined to understand natural watershed dynamics and in hydrological design (de Almeida et al., 2014; Sharifi and Hosseini, 2011). These parameters are essential to accurately calculate the maximum discharge, which is necessary for the proper design of culverts, bridges and many other hydraulic works (Sharifi and Hosseini, 2011).

The most reliable way to determine both LT and Tc is the graphical study of hyetographs and hydrographs for a period of time long enough to determine the natural variability of precipitation and streamflow, and therefore the periods of return of large storms and floods (Bentancor et al., 2014; de Almeida et al., 2017). However, in many cases no background information is available regarding the behavior of a given watershed before the construction of a hydraulic work. Thus, in unmonitored catchments both Tc and LT are usually calculated from empirical, semiempirical, or physically based equations developed in previous studies. Empirical formulae are based on watershed physiographic characteristics, such as terrain slope, channel slope, watershed area, channel length, etc. (e.g., Giandotti, 1940; Kirpich, 1940). These formulae do not consider the temporal and spatial variability of factors that can affect response times. Conversely, semiempirical equations also consider other variables, such as the roughness coefficient or the curve number associated with, for example, the vegetation type and density, which can vary spatially and temporally (Mata-Lima et al., 2007). The usual approach in both empirical and semiempirical models is to establish a mathematical relationship (i.e., a regression) between the times of response and the explanatory variables, with no further consideration of mechanistic processes subjacent to the relation. Finally, the physically based methods rely on hydrological processes, as is the case with the velocity method (NRCS, 1986; see below).

Common equations are obtained in specific settings, which can be appropriate for a given geographical zone. For example, the Kirpich (1940) equation was developed in natural watersheds or those with crops, with a 3–10% slope with a channelized flow (Tucci, 2000). The Izzard (1946) method, derived from laboratory tests, is applicable to roads and pasture areas (Chow et al., 1988). Pasini (1914) and Giandotti (1940) formulae were obtained in rural basins in Italy, while the Temez (1978) formula is from Spain; all of these cases originated in a Mediterranean climate. CDH (1960) is for small mountain basins in the USA. Bransby-Williams (1922) developed his method for tropical India. The watershed lag method (USDA-NRCS, 2010) is for small rural watersheds where superficial flow dominates. Finally, ADOT (1993) was designed for semiarid Arizona (agricultural watersheds). In spite of the previous background information, in many cases no critical consideration of where these equations were obtained is carried out prior to their application. These equations' basic assumptions and the scope of their applicability is often not previously evaluated, they are simply applied to calculate a single LT or Tc, which are assumed to be true values with no further validation. Even worse, the official regulations of several countries are based on imported methods, as is the case in Latin America (de Almeida et al., 2017; DGA, 1995; Vélez and Botero, 2011).

The great diversity of formulae developed in many places around the world usually produce different results for the same location (de Almeida et al., 2014; Sharifi and Hosseini, 2011). This has led to a certain level of chaos that some authors have

attempted to relieve by introducing some order in this regard. For example, Vélez and Botero (2011) recommended calculating the median of the estimations determined with different methods to obtain the correct Tc. Sharifi and Hosseini (2011) proposed a correction of the diverse methods in order to approach the reference Tc calculated by the velocity method (NRCS, 1986). De Almeida et al. (2014) classified 30 methods by means of a hierarchical cluster analysis. Moreover, de Almeida et al. (2017) determined that Ventura's method was the most appropriate for the Brazilian tropical region where they carried out their research.

On the other hand, Bentancor et al. (2014) compared the results of rainfall-discharge Tc determinations with the estimations obtained from three methods, and concluded that none produced the true values. The real merit of this work is that it revitalized the notion that LTs or Tcs are not unique for a given watershed, but depend on precipitation characteristics that are variable from storm to storm, as anticipated by Izzard's (1946) and Morgali and Linsley's (1965) equations. Thus, in this paper, we propose to advance the concept that LTs/Tcs are not fixed for a given watershed (i.e., parameters), but instead allow for variations within the same watershed as a function of rainfall properties (i.e., LT/Tc as variables).

Furthermore, in spite of the fact that some methods can produce accurate results when used in similar physiographical regions to where they were developed, they rarely have a hydrological basis, in contrast with the velocity approach (NRCS, 1986). This method has been considered by several studies as hydraulically sound and used as a reference to compare other estimations (McCuen et al., 1984; Sharifi and Hosseini, 2011; USDA-NRCS, 2010). In this paper, we tested the performance of the velocity approach utilizing more direct data obtained from a hyetograph-hydrograph analysis. We further compared our results with 24 equations, and developed the notion that LT/Tc equations must include precipitation as a predictor.

MATERIALS AND METHODS

Study site

This study was mainly conducted at the Estación Experimental Agropecuaria Austral (EEAA), located in the Los Ríos Region in southern Chile (39° 46' 55" S, 73° 13' 24" W), 4 km north of the city of Valdivia, and 15 km from the Pacific Ocean (Fig. 1). The climate is humid temperate (Amigo and Ramírez, 1998), with an average annual temperature of 12°C. Annual rainfall is 2,500 mm; most of the rain is concentrated in the winter season (June-August). Snowfall is rare. Extreme temperatures during the period 2012–2015 were −1.4°C and 35.4°C.

We studied the Santa Rosa watershed, whose creek is 5–6 m wide at its outlet, with a discharge of 58–1,151 L s^{-1} (in the summer and winter, respectively). The creek forms part of a watershed whose approximate area is 7.6 km^2 (Fig. 1c), flowing through the middle of a 250 m-wide native forest floodplain. A layer of loose sediment is found on the streambed, 34-109 cm thick.

In the flat zones, the geomorphology is mainly composed of alluvial terraces, with the uplands (0.5–3° slope) covered by pastures of *Lolium perenne* L. (perennial ryegrass). A slope covered by *Nothofagus obliqua* deciduous forest (25 m wide, 35° grade) then connects with the floodplain (4° slope), which is covered by evergreen native forest. The pastures are located about 17 m a.s.l., while the Santa Rosa Creek is located 4 m a.s.l. The stream rises up to 160 m a.s.l. between 1.8 and 4.0 km upstream from the main study site (referred to as control point, P0, Fig. 1c), where second-growth, evergreen native forests and exotic tree plantations are found in the mountain headwaters.

The riparian vegetation (swamp forest) found in the floodplain is characterized principally by the trees *Blepharocalyx cruckshanksii*, *Myrceugenia exsucca*, and *Drimys winteri* var. *chilensis*, with few individuals of *Nothofagus obliqua*. However, there are vast zones in the floodplain covered by the herb *Cyperus eragrostis* (sedges), which grow either below gaps in the forest's canopy or in areas with low-stature trees. In terms of land cover, pastures account for 22% of the watershed, swamp forests 16%, exotic tree plantations 0.74%, second-growth evergreen forests 38%, and second-growth deciduous forests on the foothills and the slope adjacent to the swamp forests the remaining 23.26% of the area.

All of the soils are derived from volcanic ash, but they belong to different orders. In the alluvial terraces adjacent to the control point, the soil corresponds to an Andisol, Valdivia series (Duric Hapludand or a Petroduric-Silandic Andosol; CIREN, (2003); WRB, 2006). On the upslope mountains, on the other hand, the soils belong to the order Acrisol (WRB, 2006) (also referred to as Ultisols; Soil Survey Staff, 1999). The corresponding series is Los Ulmos (CIREN, 2001). In general terms, volcanic ash soils are characterized by their very low bulk densities (< 0.9 Mg m^{-3}), high total porosity and water storage capacity, as well as very high values of saturated and unsaturated hydraulic conductivity. A detailed description of soils in the study area can be found in Dörner et al. (2013, 2015).

Hydraulic measurements

A HOBO U20-001-01 pressure logger (Onset Computer Corporation, Bourne, USA) was placed in the middle of the Santa Rosa stream from May 2014 to November 2015 (the P0 point, Fig. 1c). This equipment was hung from a steel chain connected to the top cap of a PVC tube. The barometric pressure compensation logger was also placed in the stream, but within a PVC tube that was closed at the bottom to prevent water from entering. The top end of this PVC tube was left open, but was isolated from rain with a non-hermetic plastic "hat". The same barometer was used for the compensation of all the loggers installed (see below). Measurements were taken every 15 min, and the sensor error was 0.05% full scale (FS), where FS is 9.0 m (see also Cuevas et al., 2018).

To estimate variations in the times of response of four subcatchments nested within the Santa Rosa watershed, a more detailed survey was undertaken between December 2016 and March 2017. Four additional loggers were placed 622 (P1), 1759 (P2), 2608 (P3) and 2639 m (P4) upstream of P0. Two of these loggers were located in the swamp forest, at about the same altitude, while the two farthest points were 40 m a.s.l. in the mountainous forest, where two tributaries converge to form part of the main reach (Fig. 1c). Thus, P3 and P4 belonged to the sequence P0- P1- P2- P3 (or P4), but the latter two did not form part of the same drainage area. The stream channel is present throughout the watershed, but is surrounded by floodplains from P2 downstream, and through most of the extension of the northern reach on the western side of the watershed (Fig. 1c).

Due to the availability of equipment, a Levelogger Junior sensor (model 3001, Solinst, Ontario, Canada) had to be used at P1, while at the other stations we employed HOBO dataloggers. The Solinst sensor has an error of ± 0.1% FS, where FS is 10 m.

Stream velocities were measured with a Seba F1 current meter (Eijkelkamp, The Netherlands) at the studied P0 stream reach, 100 m upstream and 100 m downstream. They were measured at 20 and 80% of the stream depth, in several sections of each of the three studied transects, and 11 times from

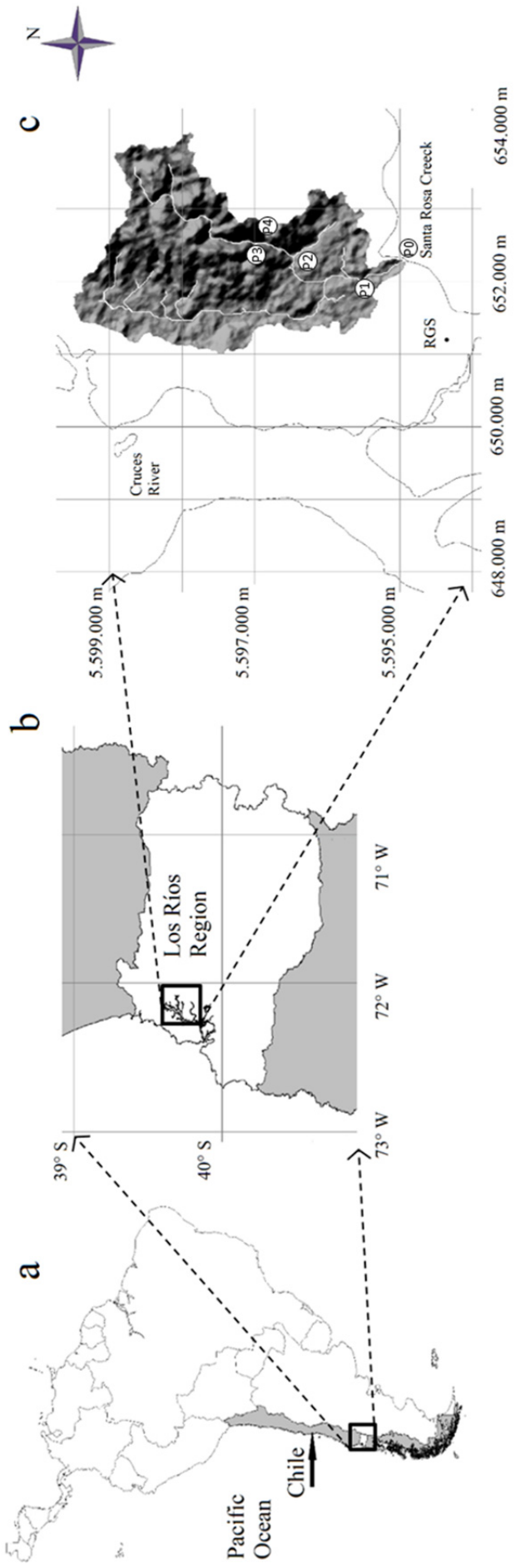

Fig. 1. (a) Location of the study site in southern Chile, in (b) the Los Ríos Region. (c) Delimitation of the Santa Rosa watershed. The labels P0 to P4 indicate gauge points. Streams flow through floodplains indicated by a lighter color, downstream of P2, and through most of the extension of the northern reach on the western side of the watershed. RGS: EEAA rain gauge station. The other station (Miraflores) was located 6 km to the south.

December 2012 to August 2015. The measurements carried out at the three monitoring points were averaged to provide a single value. Additional spot velocity gathering was carried out in March 2017 at P1, P2, P3, and P4. Measurements were not taken before and after a given peak flow (see Discussion: Velocity method estimation).

Two meteorological stations were utilized in this study: one was located at the same experimental station (EEAA, Fig. 1c), 1.2 km from the watershed outlet (Campbell Scientific CR 1000 instruments, Logan, UT, USA, available from http://agromet.inia.cl); and the other, referred to as Miraflores (https://www.centroccbb.cl/clima/), was 6 km from the study site in the city of Valdivia (Davis Vantage Pro 2 weather station, Hayward, CA, USA). However, only the latter had a long data record encompassing almost all of the study period, while the EEAA station only began operating in May 2015. In the main study, we chose to use the Miraflores records to have a larger sample size, but we compared these records with those obtained from EEAA for the common period (May-November 2015). Conversely, for the shorter study of stream stage variation along the stream, rainfall data was obtained from the EEAA station. The Davis station accumulated the rainfall data in 30 min periods (0.2 mm resolution), while the Campbell station reported data hourly (0.1 mm resolution).

Determination of lagtimes

Lagtimes were defined as the time lapse between the middle point of the rainfall event and the discharge peak (USDA-NRCS, 2010; Vélez and Botero, 2011). The middle point was determined as half the time between the start and the end of the rainfall. For these analyses, only well-defined precipitation events and discharge peaks were considered.

We revised the literature to locate a large number of methods (24) proposed to calculate Tc or LT, especially the works of de Almeida et al. (2014), Sharifi and Hosseini (2011), and USDA-NRCS (2010). The formulations of some selected equations appear in Appendix 1. Most equations require knowledge regarding watershed physiographic characteristics, such as area, length of the main channel, channel slope, watershed slope, altitude, etc. (Table 1). This knowledge was obtained from a combination of Google Earth Pro imagery (version 7.1.7.2600; Google Inc., Mountain View, CA, USA) and Geographic Information Systems. This was necessary because no official topographic maps with adequate spatial resolution for this study were available for the area. Consequently, we constructed a digital elevation model (DEM) with a 12.5 m x 12.5 m resolution obtained from the Alaska Satellite Facility web page (https://vertex.daac.asf.alaska.edu/), which, in turn, acquires images from NASA. With this DEM, we generated a three dimensional model (Fig. 1c) with ArcMap 10.3.1 software (ESRI, Redland, CA, USA); this was used to calculate required input variables.

We then calculated the Tc or LT utilizing each one of the methods. As our analysis was focused mainly on LT, while

Table 1. Variables and parameters used for the calculation of lagtimes and times of concentration in the Santa Rosa watershed and subcatchments.

Name	Abbreviation	Value	Unit
2-year, 24-h rainfall	P_2	93	mm
Basin development factor	BDF	0	–
Cross-sectional flow area	a	0.33 (in P3) to 4.0 (in P0)	m^2
Diameter of the circle equivalent to watershed area	Dc	3.11	km
Impervious area in the watershed	IMPERV	2	%
Length of the main channel	L	5.48	km
Length of the shallow concentrated flow	L_s	145	m
Length of the open channel flow (reach 1, upstream)	L_1	560	m
Length of the open channel flow (reach 2, downstream)	L_2	4,920	m
Main channel slope	S	0.0111	m/m
Manning's channel roughness coefficient (Chow, 1959)	*n*	0.11 (dense brush, flood stage reaching branches)	$m^{-1/3}$ s
Manning's roughness coefficient for sheet flow	*n*	0.80 (dense underbrush)	$m^{-1/3}$ s
Maximum watershed altitude for the longest channel	Hmax	70	m a.s.l.
Mean watershed elevation	Hm	61	m a.s.l.
Minimum watershed altitude	Hmin	9	m a.s.l.
Rainfall intensity	i	3.7 (high intensity), 0.03 (low intensity)	mm/h
Retardance coefficient (Izzard, 1946)	cr	0.06	–
Retardance factor, runoff curve number (USDA-NRCS, 2010)	cn', CN	72 (mean for woods, pasture, meadow grass in C soil type)	–
Slope terrain in headwaters	S_h	0.174	m/m
Watershed area	A	7.6	km^2
Watershed mean slope	Y	12.43	%
Wetted perimeter	P_w	1.7 (in P3) to 6.6 (in P0)	m

most equations deal principally with Tc, we applied the following formula (USDA-NRCS, 2010; Vélez and Botero, 2011):

$$LT = 0.6*Tc \quad (1)$$

The velocity method (NRCS, 1986) was analyzed in detail and is explained in Appendix 2 (Equations (A12–A14)). Briefly, it involves the estimation of stream velocities based on hydraulic considerations. The distances where those flows occurred were divided by the velocities, so that the travel times could be determined. The sum of the travel times was then considered as the time of concentration. Although dividing the watershed into three segments along its course is recommended, we chose to use only two segments because there are only two main physiographic units (the upslope mountains above P2, and the lowland, flat area below P2).

Data analyses

Measured LTs were related to common distribution frequencies (Gumbel, Non-normal, Gamma, Weibull, Log-normal, Normal, Rayleigh, and Exponential). The departures between the theoretical distribution and the observed values were evaluated with the Kolmogorov-Smirnov test (Sokal and Rohlf, 1995) (Module Industrial Statistics & Six Sigma/ Process Analysis of Statistica 7.0 software, StatSoft, Inc., Tulsa, OK, USA).

We then compared the observed LTs with the predicted values from 24 methods, and selected the equations with the best agreements. These were improved through the inclusion of rain variables that produced good relationships with LTs, as determined by linear regressions analysing the rain amount per event, rain intensity, event duration, and accumulated rainfall for the seven days prior to the discharge peak. Since most Tc equations are non-linear (Appendix 1) we estimated the new parameters, which are exponents of the input variables, with the Nonlinear Estimation module of Statistica 7.0 software. This procedure operates through the Levenberg-Marquardt algorithm, which carries out a maximum of 50 iterations to minimize the least-squares among observed and predicted LTs from the equations.

RESULTS

Temporal variability of lagtimes at P0

Throughout the period May 2014-November 2015, we detected 100 precipitation events at the Miraflores station that were able to induce rises in streamflow. The highest discharge peak for the year 2014 was due to a rain event of 100 mm in 24 h, which caused a rise in the hydrograph from < 400 to 1,151 L s^{-1}. Even under this extreme scenario, the LT was 22 h. Overall, LTs ranged from 0.6 to 58.5 h, with a mean of 20.1 h. When analyzing data from the EEAA meteorological station, the mean LT was 20.4 h (ranging from 0.6 to 50.5 h, $N = 46$ events). The frequency distribution derived from the Miraflores data was slightly skewed to the right (Fig. 2). All assayed fittings produced non-significant deviations with respect to common theoretical distributions (with the exception of the exponential distribution), while Gumbel produced the lowest Kolmogorov-Smirnov departure ($d_{max} = 0.051$, $P > 0.05$, Fig. 2). When comparing LTs corresponding to autumn, winter, spring, and summer, the median values were 20.2, 17.7, 20.5, and 16.2 h, respectively (Fig. 3).

Spatial variability of lagtimes along the stream

During storm events, the stream stage variation along the stream was evaluated for 11–15 events in the summer of 2017. In Fig. 4, the curves for a representative period are shown. It can be clearly seen that the highest subcatchments anticipated their response to rainfall compared with the lowest subcatchments. In other words, as the size of the nested catchments decreased, the LT also decreased (Table 2). P0 showed a LT very similar to the previous summer (mean 16.0 vs. 17.0 h), even though the sample sizes were not the same ($N = 4$ in 2015; $N = 14$ in 2017). The difference in LTs among the highest stations (P3, P4) and the lowest was about 10 h.

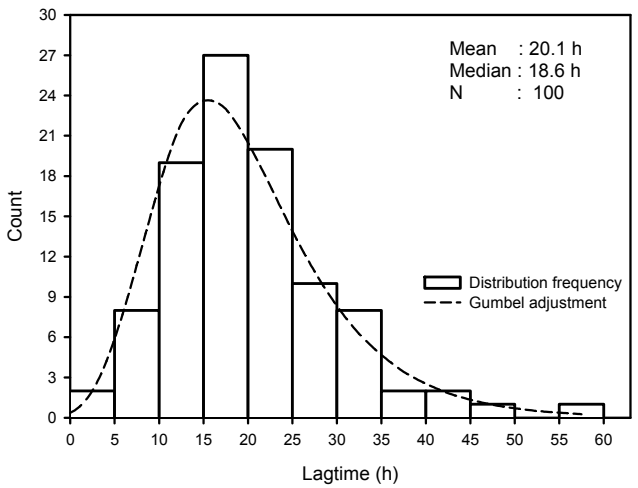

Fig. 2. Frequency distribution of the lagtimes measured from the hyetograph-hydrograph analyses at the P0 point in the Santa Rosa watershed. The Gumbel distribution was adjusted to the observed data.

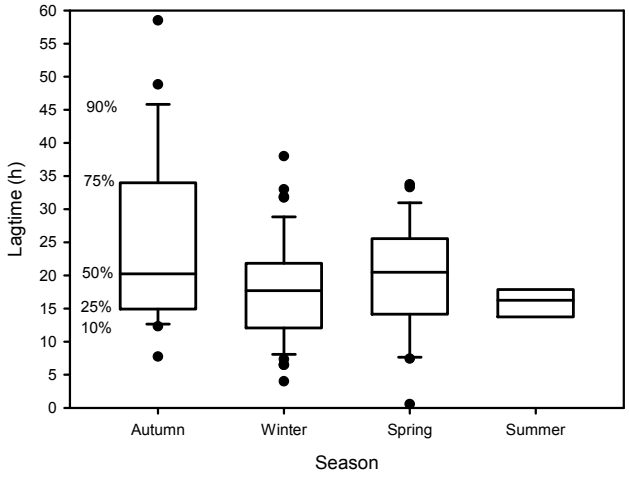

Fig. 3. Box plots for lagtimes at the P0 point of the Santa Rosa stream, as a function of season. The percentages adjacent to the boxes indicate the percentiles, and the dots are the outliers.

Table 2. Lagtimes in subcatchments nested within the Santa Rosa watershed for the period December 14, 2016 – March 9, 2017.

	Subcatchment points of measurement				
Lagtime (h)	P0	P1	P2	P3	P4
Mean	17.0	14.2	8.1	6.1	7.2
Max	27.8	22.2	17.8	16.5	15.3
Min	10.2	8.5	4.5	3.0	3.0
Sample size	14	14	11	15	14

Calculated lagtimes

Most equations that mainly account for the physiographic characteristics of a watershed produced estimations that severely underestimated the observed LTs (Table 3). For example, the Kerby (1959) method predicted a LT = 0.21 h. Even the formula that is currently used in Chile (DGA, 1995; USA California Division of Highways, 1960; Equation (A2) (Appendix 1)) showed a LT < 1 h. The Soil Conservation Service, Texas (USDA-NRCS, 2010), fell in the mid-range among the estimations (LT = 2.8 h) (Equation (A4), Appendix 1). One of the Granato (2012) formulae (RE07, Equation (A7) in Appendix 1) ranked fourth in decreasing order with a LT = 10.4 h. There were three additional equations that produced LTs approaching the observed values and allowed for varying estimations according to rainfall intensities. This was the case for the Izzard (1946) Equation (A11) (Appendix 1), which predicted LTs of 10.4 h for the highest rain intensity measured for the period (3.7 mm h^{-1}), and 258 h with 0.03 mm h^{-1}, the lowest rain intensity. On the other hand, Papadakis and Kazan (1986) Equation (A9), (Appendix 1) and Morgali and Linsley (1965) (Equation (A10) in Appendix 1) only produced good agreements at low rain intensities. The median for the calculated LTs was 2.4 h.

The velocity method

This method approached the observed results and deserves a separate analysis (Equations (A12–A14), Appendix 2). For point P0, the estimated travel time (Tt) for sheet flow was 0.15 h, while the velocity of the shallow concentrated flow would be 0.305 m s^{-1} for a slope of 0.174 m/m. Since the segment length for that flow was 145 m, then the Tt (concentrated flow) was 0.13 h.

For the mountainous area, the open channel flow was applied to the first reach length of 560 m with a calculated velocity of 0.91 m s^{-1}, that is, 0.17 h of travel time. In the lower reach, which is 4,920 m long, a velocity of 0.23 m s^{-1} was estimated, making the equivalent Tt 6.0 h. Thus, the total travel time was 6.4 h (LT = 3.8 h), based on velocity estimations.

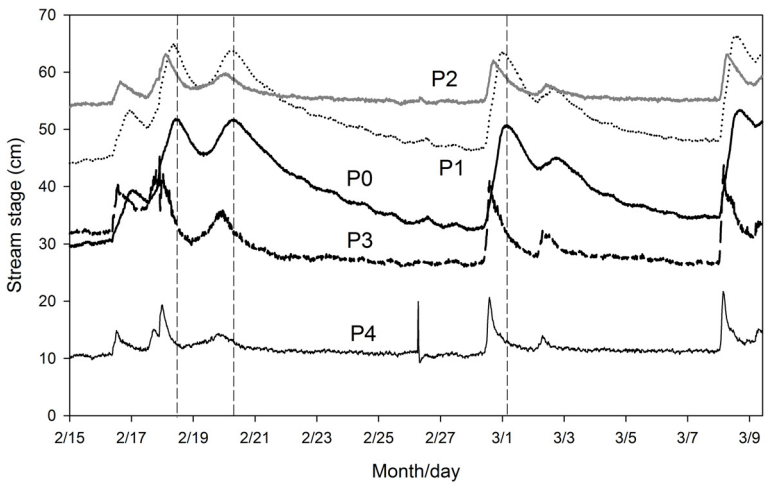

Fig. 4. Variations in stream stage in different subcatchments nested within the Santa Rosa watershed. P0 was the lowest gauge point, and P1, P2, P3 and P4 were located at increasing distances upstream from P0. P3 and P4 were located in different tributaries of the main channel. To facilitate comparisons of timing of different stations, three vertical dashed lines out of the several stage peaks shown have been drawn to coincide with the P0 peaks. A representative period in the year 2017 was selected from a longer three month-evaluation.

Table 3. Estimations of lagtimes (LT) for the Santa Rosa watershed in southern Chile at point P0. Estimations appear in increasing order of LTs.

Method	LT (h)
USDA (Argente-Sanz, 2014)	0.065
Kerby (1959)	0.21
Simas (1996) I	0.3
California Division of Highways (1960)	0.8
Kirpich (1940)	0.9
Soil conservation service: Ohio (USDA-NRCS, 2010)	1.0
Watershed lag method (USDA-NRCS, 2010)	1.2
Dirección General de Carreteras (Témez, 1978)	1.5
Simas (1996) II	1.6
Bransby-Williams (1922)	1.6
Giandotti (1940)	1.8
Ventura (Mata-Lima et al., 2007)	2.0
Soil conservation service: Texas (USDA-NRCS, 2010)	2.8
Folmar and Miller (2008)	3.2
Granato (2012) RE03	3.5
Pasini (1914)	3.9
Sheridan (1994)	6.3
Granato (2012) RE13	7.4
Granato (2012) RE06	7.9
Velocity method (NRCS, 1986)	3.8–9.4
Granato (2012) RE07	10.4
Papadakis and Kazan (1986)	2.4–14.6
Morgali and Linsley (1965)	3.6–24.7
Izzard (1946)	10.4–258.3

Table 4. Stream velocity for different measurement dates in the Santa Rosa Creek (P0 point).

Date	Water velocity (cm s^{-1}) (mean ± SE)
December 4th, 2012	6.2±1.27
May 2nd, 2013	10.5±1.29
July 23rd, 2013	11.8±1.59
June 2nd, 2014	8.6±3.10
June 13th, 2014	10.3±0.86
December 23rd, 2014	8.9±1.26
January 9th, 2015	7.4±1.13
February 9th, 2015	5.9±1.09
June 1st, 2015	12.9±1.80
June 26th, 2015	9.6±1.45
August 6th, 2015	8.6±0.69
Mean	**9.2 ± 0.66**

However, as we directly measured the stream velocity at P3 (0.29 m s^{-1}) and P0 (mean 0.092 m s^{-1}, Table 4), we were able to correct the velocity estimations for the open channel flow, resulting in the following travel times for the first and second reaches: 0.54 and 14.9 h. Thus, the recalculated total *Tt* was 15.7 h (LT = 9.4 h).

Improvement of methods of LT estimation

We took note of the improved predictive power of the three methods that included rainfall intensity as a variable (Izzard, 1946; Morgali and Linsley, 1965; Papadakis and Kazan, 1986). We tested whether there was a significant relationship between observed LTs and the rainfall amount, rainfall intensity, and rainfall duration per event, in addition to the total accumulated rainfall for the seven days prior to the discharge peak. Some relationships were poor, evidenced by their extremely different observed LTs for the same rain amount and intensity (Figs. 5 a, b, d). Conversely, the relationship was much better for rainfall duration vs. LT (r^2 = 0.691, r = 0.831, P < 0.0001) (Fig. 5c). Our conclusions were the same when carrying out these analyses with the EEAA rain data; although the r^2 values were lower due to the lower sample size. The distributions of both rain intensity and duration were skewed to the right, with mean values of 0.94 mm h^{-1} for the first (Fig. 6a) and 27.7 h for the last variable (Fig. 6b).

The lack of fit of rainfall intensity with LT was confirmed by directly introducing the values of the former variable within the selected equations, which produced a poor relationship between predicted and observed LT values (data not shown). We then included rainfall duration as a predictor in the equations. For example, Izzard's equation could be modified to:

$$LT_{\text{mod}} = \frac{0.6 * 526.42 * (0.0000276 * D^a + b) * 17.62}{0.2233 * D^c} \quad (2)$$

where LT_{mod} is the modified Izzard equation, 0.6 is the factor for converting Tc into LT, 17.62 is $L^{1/3}$ (L, main channel length in m), 0.2233 is $S^{1/3}$ (S, main channel slope, m/m), D is the rainfall duration in hours, and a, b, and c are parameters to be adjusted. The other constants come from Izzard's Equation (A11) (Appendix 1).

Following this procedure, the formulae presented by Morgali and Linsley (1965) and Papadakis and Kazan (1986) provided an r^2 = 0 when relating to observed LTs, because the non-linear form of these Equations (A10) and (A9) (Appendix 1) could not account for the linear relation that is subjacent to LT versus D. On the other hand, the non-linear regression produced the following estimations for Izzard: a = 0.992448, b = 0.000357, and c = 0.094489. The coefficient of correlation was r = 0.828 and the coefficient of determination was r^2 = 0.685 (P < 0.001 for model). If b would have been fixed as 0.06–0.09 (the values of the retardance factor for dense pastures and forest plantations, respectively; Bentancor et al., 2014), r^2 would also have been zero.

Parameters a, b, and c were then introduced into Equation (2). The predictions of this equation were tested against the observed LTs, resulting in a linear relationship where points were distributed at both sides of the 1:1 relationship (Fig. 7), being a reasonable adjustment with observed data. The same conclusion was obtained in the analysis with EEAA rainfall data.

DISCUSSION

Comparison among methods of LT estimation

Our measured lagtimes were rather long (mean 20 h), and had a good fit with the Gumbel distribution, a probability density function that is commonly used to describe extreme values, usually high, that rarely occur with respect to most values in the distribution (Gumbel, 1960). Long LTs have also been observed by de Almeida et al. (2017) and have resulted in smooth rises and recessions of hydrographs. The resulting rounded forms contrast with the sharp forms observed in torrential watersheds (Singh and Singh, 2017). It is likely that the large floodplain extension, in both length and width, as well as the type of vegetation, contributed to this pattern. In fact, Granato (2012) points out that lakes, ponds, and wetlands are zones of surface storage, which only some studies explicitly include.

In this study, most equations that only included physiographic watershed characteristics produced estimations that severely underestimated the observed LTs, while those including rainfall properties or stream velocities produced much

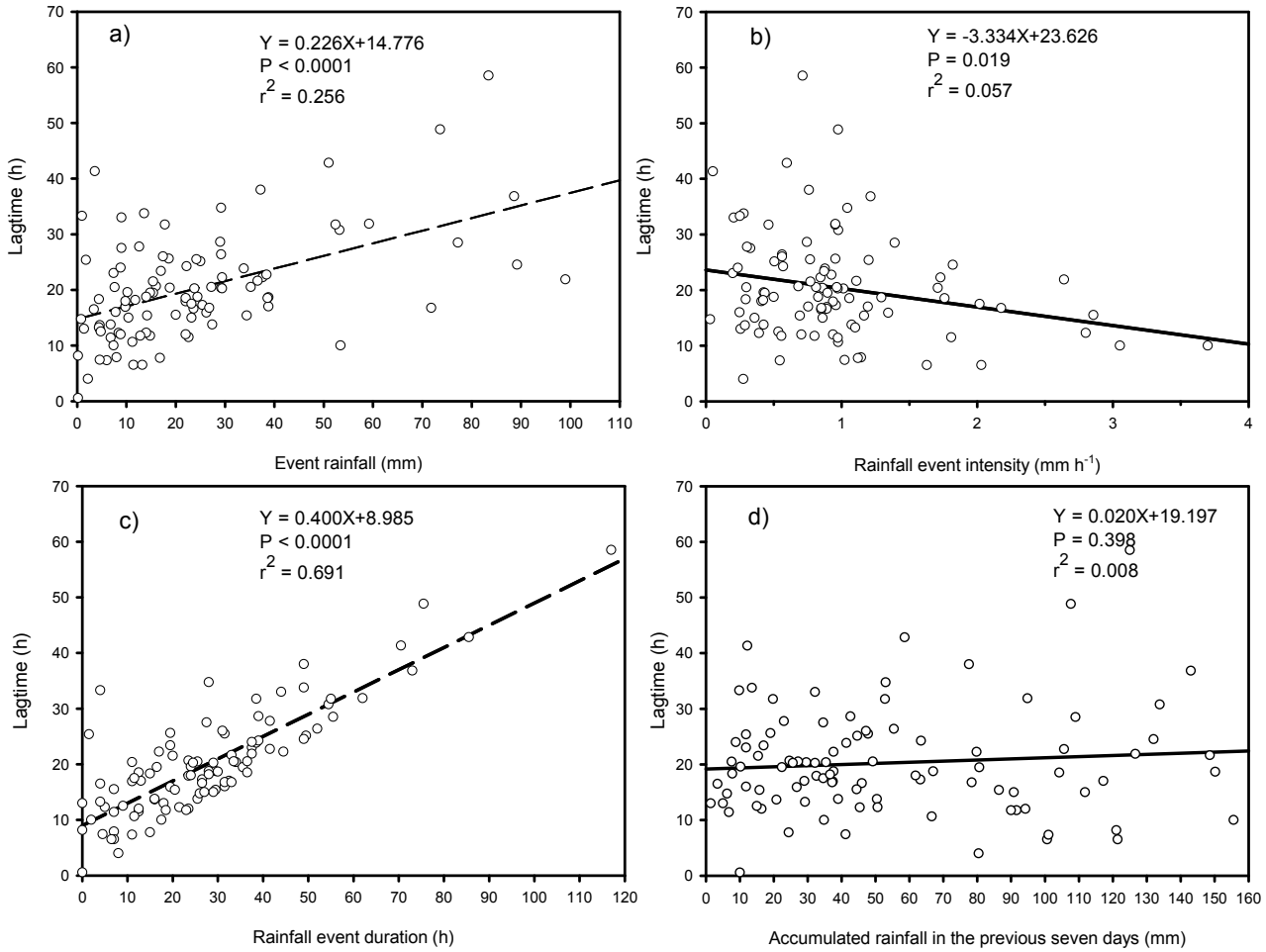

Fig. 5. Linear regressions of different precipitation expressions and lagtimes between the rainfall event and the discharge peak at point P0. Linear equations, model probability (P) and coefficient of determination (r^2) are shown in each panel.

better estimations. An exception to this statement was the Granato (2012) RE07 equation, which produced an estimation of 50% of the observed value, partially including physiography. The relative success of this formula may be related with the fact that the model was specially developed for predicting lagtimes, and accounted for urbanization and the prevalence of engineered drainage features as well (Granato, 2012).

In general, simple watershed attributes such as area, slope, main channel length, and difference in elevation between headwaters and outlets, cannot adequately describe the impediments that water must face throughout its travels along the watershed. In other words, equations that only include physiographic factors assume that only the distance effect could cause a delay in the water's travel time, thus presuming that the substrate is smooth. This assumption would only be valid for urban watersheds, for those with a rocky streambed, or with low vegetation cover. In forested swampy watersheds there is a retardance factor that is not adequately included in the diverse equations examined here. In the studied catchment, the streambed was made up of loose sediments that are home to an extensive hyporheic zone, where water flows are likely to be considerably slower than in open channels (Edwards, 1998). Many tree stems also cross the watercourse, and in the mountain headwaters the presence of dense Chilean bamboo thickets ("quilas") is a factor that can delay the water's movement. Moreover, there is a large cover of *Cyperus* sedges along the floodplain. Sedges inhabit places with a very high groundwater table, even above the ground level for most of the year. When the plains are completely flooded throughout the winter, the impediments for water movement are even greater, and possibly higher than in the forest where stems have a lower density than sedges.

At first sight, the use of some of the evaluated equations was not justified to predict the specific response of the swampy, forested watershed. However, since our aim was to find out which formula was the most appropriate for describing the studied watershed's behaviour, we evaluated all 24 equations most commonly found in the literature. Overall, the calculation of the median to determine the best LT estimation, as recommended by Vélez and Botero (2011), was not successful. The large bias in the number of methods that predicted low LTs produced inaccurate results.

Spatial-temporal variations in lagtime

Our results show that the peak discharge caused by rain appeared earlier in the stations located at the headwaters in forested mountainous areas. The maximum appeared progressively later downstream. Thus, lagtimes were shorter at the headwaters than in the lowlands, coherent with a flood wave that moves from areas high in the mountains (ridges and slopes covered by second-growth evergreen native forests and exotic tree plantations) to the lowland zones covered by swamp forest. There was a delay of 10 hours due to the great distance between highlands and lowlands, compounded by the great areal extension, high roughness, and low slope of floodplains.

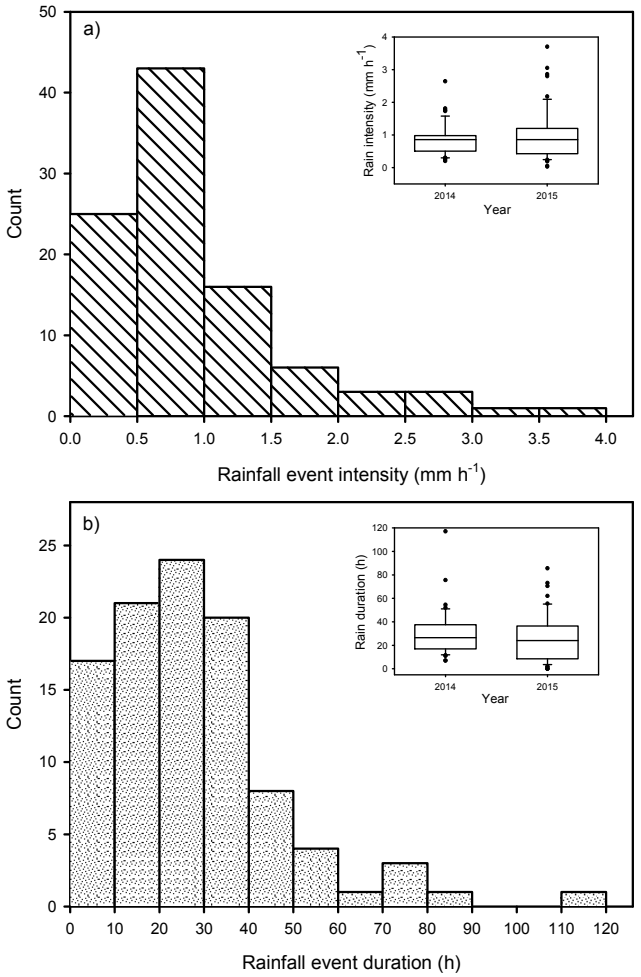

Fig. 6. Distribution frequency of rainfall event intensity (a) and duration (b). Inserted graphs show the values for the years 2014 and 2015, using the same convention as Fig. 3 for boxplots.

A source of uncertainty in this analysis is the assumption that the storms arrived simultaneously to all of the gauging points, since only one meteorological station was used for the hyetograph-hydrograph analysis (EEAA). However, as the watershed is only 4 km long, and we have proven that LTs derived from the farthest station (Miraflores) are very similar to those obtained from EEAA, it is very likely that this pattern also occurs within the watershed. Moreover, the differences in LTs among monitoring points were several hours, making it unlikely that a small difference in storm timing across these points would mask such a significant time difference.

Velocity method estimation

This method relies on the estimation of water velocity for sheet flow and shallow concentrated flow, values that are difficult to measure in the field. However, even allowing for some uncertainty in these estimations, these flows scarcely contributed in terms of total length (160 m) and travel time (0.27 h) in comparison with the longest stream segments in the watershed (5,480 m, *Tt* = 6.2 h). Bentancor et al. (2014) also considered sheet flow negligible based on the small percentage of watershed area where that flow occurs. Therefore, any discrepancy between observed Tcs or LTs and the estimated values must be searched for in the stream velocities of the longest segments. For these reaches, Tt increased up to 15.4 h (LT = 9.2 h) when including measured stream velocities in the field. Thus,

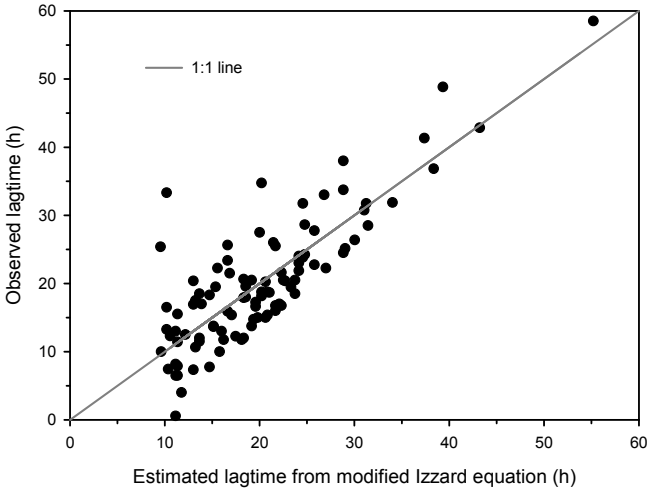

Fig. 7. Comparison of estimated lagtimes calculated with the modified Izzard (1946) equation and those observed in the Santa Rosa watershed (P0 point). The correlation between both variables was $r = 0.828$ ($r^2 = 0.685$).

methodologically, it is preferable to collect these data, rather than estimating them from hydraulic radiuses that are more difficult to measure in many locations along the main stream channel. In addition, the roughness coefficient included in Manning's Equation (A14) (Appendix 2) can be spatially variable, and can perhaps vary in the time domain as well. Even with the corrections of our spot velocity measurements, the calculated LTs still fell short of the observed values (mean 20 h), but it must be considered that the P3 datum was only based on velocity surveys for the summer of 2017. Furthermore, travel times and, consequently, LTs can show large fluctuations if we take into account that stream velocity changes along the channel, in addition to changing daily, monthly and seasonally (Table 4) as a direct function of streamflow (data not shown; see also Wondzell et al., 2007). Even the precipitation factor can influence stream velocity via the discharge magnitude. Thus, the velocity method is promising since it showed one of the highest LT estimations in our data, and because it allows for LT variations throughout time. Further research should measure stream velocities on at least a daily scale to establish relationships with discharge and observed LT/Tc.

Improvement of methods of LT estimation

LT varied as a function of rainfall properties, as noted by Bentancor et al. (2014), with rainfall duration being the variable that best explained the LT variation. Contrasting with our results, when Bentancor et al. (2014) evaluated (in Uruguay) the three methods developed by Kirpich, Morgali and Linsley, and Izzard the observed Tcs were overestimated. Possible explanations may be related to the dominance of pastures in that country, with no trees in the riverbanks nor submerged in the water (L. Bentancor, personal communication).

The relationship between LT and rainfall duration is most likely due to the fact that each storm pulse generates a response hydrograph, which is added to the response of the other pulses (Chow et al., 1988). In other words, a longer storm causes a response with a longer duration. Rainfall duration also had the least departure from the Gumbel distribution as compared to standard distributions (data not shown), coinciding with the LT frequency distribution.

The predictive value of the Izzard equation, which included precipitation as a variable, could be further improved upon. The

parameters that represent exponents of duration (a, c) could be statistically well adjusted. However, b in the original Equation (A11), (Appendix 1) corresponded to the retardance factor (cr). Our result with the modified equation was $b = 0.000357$, which is very low compared to the recommended *cr* for Izzard's equation ($cr = 0.06–0.09$, Bentancor et al., 2014). Fixing this factor to these values was not possible because the resulting equation had a very poor fit. Therefore, b cannot be strictly assimilated to a retardance factor and must only be considered as a parameter for an empirical adjustment of the Equation (2).

Overall, the fit between observed LTs and those derived from the modified Izzard equation was quite good, with points distributed in similar proportions in the over- and underestimation zone (Fig. 7). Bentancor et al. (2014) obtained an $r^2 = 0.56$ between observed and calculated values with the modified Izzard method, including the precipitation intensity.

Precipitation as a predictor

One contribution of this paper is its emphasis on lagtime's dependence upon precipitation characteristics. This changes the notion that each watershed has a fixed LT (i.e., a parameter), to the idea that LT is a factor that can vary in time as a function of rainfall duration (i.e., a variable). LTs can be represented as a frequency distribution that can be associated with a probability density function, which converts LT into a random variable in statistical terms. Of course, LT is a function of rainfall duration, in addition to other factors, but this variable can, in turn, be the consequence of meteorological phenomena whose analysis is beyond the scope of this paper. Regardless, this poses a challenge in hydrological modelling: how can a random variable be incorporated into calculations of maximum discharge associated with a given watershed? This is an issue that does not occur when Tc or LT are considered as single, fixed values.

Scope of applicability

It would be naive to assume that the equations with the best performance in this study would also work well in any possible setting. Clearly, the empirical, semiempirical and physically based methods found in the literature adequately explain the LTs or Tcs in the specific environments where the equations were developed. Moreover, they should work well in regions similar to the original scope of the model's calibration, for example, among semiarid regions (Sharifi and Hosseini, 2011). Consequently, our findings could be applied to areas with similar conditions to those found in the southern regions of Chile, which have a rainy, temperate climate, with most of the precipitation concentrated in the winter. Moreover, dense tree/herb cover, soil type, and geomorphological characteristics, such as extensive floodplains, should also be considered.

We were unable to find another critical evaluation regarding which methods have the best performance in this country; therefore, our results could be applied to improve the official technical handbooks concerning the design of hydraulic works. DGA (1995) includes the use of design hydrographs for different Chilean macrozones, but the zoning is not sufficient and must be further developed. We recommend carrying out a better characterization of LT or Tc considering the specific characteristics of each watershed, along with its unique plant cover and rainfall attributes.

We further recommend a direct determination of LT or Tc by means of hyetograph-hydrograph analyses to define which method functions best in a given region. This method could then be applied with confidence to other similar, unmonitored catchments. In our study, Izzard's modified equation proved to be the best estimator of observed LTs and could therefore be used for predicting this variable in specific rain events with known rainfall durations. This variable is easy to determine and can be measured in a location not necessarily adjacent to the watershed of interest, as in this study. Of course, we could use the relationship LT/rainfall duration shown in Fig. 5c without considering the Izzard formula, but we would lose the opportunity to make some adjustments related to slope and main channel length that are included within Izzard's formulation.

CONCLUSIONS

We found that lagtimes (and times of concentrations) were rather long in the main watershed studied, possibly due to the extensive flat zones within the floodplains, and the retardance imposed by dense herb and tree vegetation. Only methods that included precipitation or stream velocity as predictors agreed reasonably well with observed lagtimes. They were both temporally and spatially variable, according to the rainfall duration and the point of watershed where evaluations were carried out, respectively. Izzard's modified method showed the best fit with observed data, and the velocity method proved promising if more field data were available to account for varying LTs within and across the seasons. In spite of the fact that our suggested equations can be locally applied, our procedure has heuristic value as it stresses the recommendation that lagtimes and times of concentration must be locally determined with rainfall-discharge analyses, in addition to explicitly considering precipitation patterns.

Acknowledgements. Funding was provided by the Fondecyt grant 1110156. INIA hosted the first author during the phase of data collection. We would like to thank the Estación Experimental Agropecuaria Austral staff for their help, especially the Administrator Carlos Villagra. Logistical support was provided by Mr. César Lemus, Mlle. Mélanie Krauth, and Rodrigo Bravo. Additional acknowledgements go to Dr. Carlos Oyarzún (Universidad Austral de Chile) and Dr. Christian Little (INFOR) who supported this research, Drs. Antonio Lara and Mr. David Lobos from CR^2 (Center for Climate and Resilience Research) for lending us part of the equipment used in this study, and to the Water Center CRHIAM Conicyt/Fondap/15130015 for supporting part of the data analysis in addition to the English edition of the document. Finally, two anonymous reviewers contributed with helpful suggestions.

REFERENCES

ADOT (Arizona Department of Transportation), 1993. Highway Drainage Design Manual Hydrology. Phoenix, USA, 336 p.

Amigo, J., Ramírez, C., 1998. A bioclimatic classification of Chile: woodland communities in the temperate zone. Plant Ecol., 136, 1, 9–26.

Argente-Sanz, J.C., 2014. Estudio del comportamiento hídrico de una cuenca hidrológica en Angola. Trabajo Fin de Grado Ingeniería en Geomática y Topografía. Escuela Técnica Superior de Ingeniería Geodésica, Cartográfica y Topográfica, Universidad Politécnica de Valencia, Valencia, España, 61 p.

Bentancor, L., Silveira, L., García-Petillo, M., 2014. Incidencia de la intensidad de lluvia en el tiempo de concentración de microcuencas del Uruguay. Agrociencia-Uruguay, 18, 2, 106−116.

Bransby-Williams, G., 1922. Flood discharge and the dimensions of spillways in India. The Engineer (London), 121, 321−322.

CDH (California Division of Highways), 1960. California culvert practice: reprint of a series of technical abstracts from Cali-

fornia highways and public works. 2nd printing. State of California, Department of Public Works, Division of Highways, Sacramento, USA, 119 p.

Chow, V.T., 1959. Open-Channel Hydraulics. McGraw Hill, New York, USA, 680 p.

Chow, V.T., Maidment, V.R., Mays, L.W., 1988. Applied Hydrology. McGraw-Hill, New York, USA, 572 p.

CIREN (Centro de Información de Recursos Naturales), 2001. Estudio Agrológico X Región. Tomo I. CIREN, Santiago, Chile, 480 p.

CIREN (Centro de Información de Recursos Naturales), 2003. Descripciones de Suelos, Materiales y Símbolos. Estudio Agrológico X Región, Publicación 123. CIREN, Santiago, Chile.

Cuevas, J.G., Arumí, J.L., Zúñiga-Feest, A., Little, C., 2018. An unusual kind of diurnal streamflow variation. J. Hydrol. Hydromech., 66, 1, 32−42.

de Almeida, I.K., Almeida, A.K, Ayach-Anache, J.A., Steffen, J.L., Alves-Sobrinho, T., 2014. Estimation on time of concentration of overland flow in watersheds: a review. Geociências, 33, 4, 661−671.

de Almeida, I.K., Almeida, A.K., Garcia-Gabas, S., Alves-Sobrinho, T., 2017. Performance of methods for estimating the time of concentration in a watershed of a tropical region. Hydrolog. Sci. J., 62, 14, 2406−2414. DOI: 10.1080/02626667.2017.1384549.

DGA (Dirección General de Aguas), 1995. Manual de Cálculo de Crecidas y Caudales Mínimos en Cuencas sin Información Fluviométrica. Dirección General de Aguas, Ministerio de Obras Públicas, Santiago, Chile, 88 p. Available at: http://documentos.dga.cl/FLU398.pdf [Accessed 04 Nov. 2017].

Dörner, J., Dec, D., Zúñiga, F., Horn, R., López, I., Leiva, C., Cuevas, J., 2013. Soil changes in the physical quality of an andosol under different management intensities in Southern Chile. In: Krümmelbein, J., Horn, R., Pagliai, M. (Eds.): Soil Degradation. Adv. Geoecol., 42, 262−281.

Dörner, J., Huertas, J., Cuevas, J.G., Leiva, C., Paulino, L., Arumí, J.L., 2015. Water content dynamics in a volcanic ash soil slope in southern Chile. J. Plant Nutr. Soil Sci., 178, 4, 693−702.

Edwards, R.T., 1998. The hyporheic zone. In: Naiman, R.J., Bilby, R.E. (Eds.): River Ecology and Management, Lessons from the Pacific Coastal Ecoregion. Springer, New York, USA, Chapter 16, pp. 399–429.

Folmar, N.D., Miller, A.C., 2008. Development of an empirical lag time equation. J. Irrig. Drain. E. ASCE, 134, 4, 501−506.

Giandotti, M., 1940. Previsione empirica delle piene in base alle precipitazioni meteoriche, alle caratteristiche fisiche e morfologiche dei bacini; Applicazione del metodo ad alcuni bacini dell'Appennino Ligure. Memorie e Studi Idrografici, 10, 5−13. Available at: http://hydrologie.org/redbooks/a025/Potam_Q2_R1 [Accessed 04 Nov. 2017].

Granato, G.E., 2012. Estimating Basin Lagtime and Hydrograph-Timing Indexes Used to Characterize Stormflows for Runoff-Quality Analysis. Scientific Investigations Report 2012–5110. U.S. Department of the Interior, U.S. Geological Survey, Reston, Virginia, USA, 58 p. Available at: https://pubs.usgs.gov/sir/2012/5110/pdf/sir2012-5110_text.pdf [Accessed 04 Nov. 2017].

Gumbel, E.J., 1960. Multivariate extremal distributions. Bull. Inst. Internat. de Statistique 37, 471−475.

Izzard, C.F., 1946. Hydraulics of runoff from developed surfaces. In: Proc. 26th Annual Meeting of the Highway Research Board. Highway Research Board, Washington, USA, pp. 129−146.

Kerby, W.S., 1959. Time of concentration for overland flow. J. Civil Eng., ASCE, 26, 3, 60−68.

Kirpich, Z.P., 1940. Time of concentration of small agricultural watersheds. Civil Eng., 10, 6, 362–368.

Mata-Lima, H., Vargas, H., Carvalho, J., Gonçalves, M., Caetano, H., Marques, A., Raminhos, C., 2007. Comportamento hidrológico de bacias hidrográficas: integração de métodos e aplicação a um estudo de caso. Rem-Rev. Esc. Minas, 60, 3, 525−536.

McCuen, R.H., 2009. Uncertainty analyses of watershed time parameters. J. Hydrol. Eng., 14, 5, 490–498. DOI: 10.1061/(ASCE)HE.1943-5584.0000011#sthash.qleAhfH8.dpuf

McCuen, R.H., Spiess, J.M., 1995. Assessment of kinematic wave time of concentration. J. Hydraul. Eng. ASCE, 121, 3, 256−266.

McCuen, R.H., Wong, S.L., Rawls, W.J., 1984. Estimating urban time of concentration. J. Hydraul. Eng., 110, 7, 887−904.

Morgali, J.R., Linsley, R.K., 1965. Computer analysis of overland flow. J. Hydraul. Div., 95, 81−100.

NRCS (Natural Resource Conservation Service), 1986. Urban Hydrology for Small Watersheds. Technical Release 55. U.S. Department of Agriculture, Washington, DC, USA, 164 p. Available at: https://www.nrcs.usda.gov/Internet/ FSE_DOCUMENTS/stelprdb1044171.pdf [Accessed 04 Nov. 2017].

Papadakis, C., Kazan, N., 1986. Time of Concentration in Small Rural Watersheds. Technical report 101/08/86/CEE. College of Engineering, University of Cincinnati, Cincinnati, USA, 18 p.

Pasini, F., 1914. Relazione sul progettodella bonifica renana, Bologna, Italy.

Sharifi, S., Hosseini, S.M., 2011. Methodology for identifying the best equations for estimating the time of concentration of watersheds in a particular region. J. Irrig. Drain. E. ASCE, 137, 11, 712–719.

Sheridan, J.M., 1994. Hydrograph time parameters for flatland watersheds. Trans. of Am. Soc. Agr. Eng., 37, 1, 103–113.

Simas, M., 1996. Lag Time Characteristics in Small Watersheds in The United States. A dissertation submitted to School of Renewable Natural Resources, University of Arizona, Tucson, USA, 174 p.

Singh, N., Singh, K.K., 2017. Geomorphological analysis and prioritization of sub-watersheds using Snyder's synthetic unit hydrograph method. Appl. Water Sci., 7, 1, 275–283. https://doi.org/10.1007/s13201-014-0243-1

Soil Survey Staff, 1999. Soil taxonomy: A Basic System of Soil Classification For Making and Interpreting Soil Surveys. 2nd edition. Natural Resources Conservation Service, U.S. Department of Agriculture Handbook 436, Washington, DC, USA, 886 p.

Sokal, R.R., Rohlf, F.J., 1995. Biometry: The Principles and Practice of Statistics in Biological Research. Third edition. W. H. Freeman and Company, New York, USA, 885 p.

Témez, J.R., 1978. Cálculo hidrometeorológico de caudales máximos en pequeñas cuencas naturales. Ministerio de Obras Públicas y Urbanismo (MOPU), Dirección General de Carreteras, Madrid, España, 96 p.

Tucci, C., 2000. Hidrología, Ciência e aplicaçao. Coleção ABRH de Recursos Hídricos 4). Universidade Federal do Rio Grande do Sul, Porto Alegre, Brazil, 944 p.

USDA-NRCS (United States Department of Agriculture-Natural Resources Conservation Service), 2010. Chapter 15: Time of Concentration. In: USDA- NRCS (Ed.): National Engineering Handbook, Part 630 Hydrology. Washington, DC, pp. 15i–15B-3.

Vélez, J.J., Botero, A., 2011. Estimation of the time of concentration and the lag time at San Luis Creek basin, Manizales. Dyna, 78, 165, 58–71. (In Spanish.)

Wondzell, S.M., Gooseff, M.N., McGlynn, B.L., 2007. Flow velocity and the hydrologic behavior of streams during baseflow. Geophys. Res. Lett., 34, L24404. DOI: 10.1029/2007gl031256.

WRB, 2006. World Reference Base for Soil Resources. A Framework for International Classification, Correlation and Communication. 2nd Edition. FAO, World Soil Resources Reports, 103, Rome, Italy, 142 p.

Received 15 November 2017
Accepted 23 May 2018

Appendix 1. Selected formulae to calculate times of concentration or lagtimes. Formulae were chosen to show the diversity of approaches. Other methods can be found in the references included in Table 3.

Equation number	Method	Formula	Units[a]
A1	Kerby (1959)	$Tc = \left[\frac{2.2nL}{Y^{0.5}}\right]^{0.324}$	Tc (min), n ($m^{-1/3}$ s), L (ft), Y (ft/ft)
A2	California Division of Highways (1960)	$Tc = 0.95\left[\frac{L^3}{H}\right]^{0.385}$	Tc (h), L (km), H (m)
A3	Kirpich (1940)	$Tc = \frac{0.02L^{0.77}}{S^{0.385}}$	Tc (min), L (m), S (m/m)
A4	Soil Conservation Service: Texas (USDA-NRCS, 2010)	$Tc = 2.4A^{0.6}$	Tc (h), A (squared miles)
A5	Simas II (1996)	$Tc = \frac{0.0085W^{0.5937}S_{nat}^{\ 0.3131}}{Y^{0.1505}}$	Tc (h), W (ft), S_{nat} (in), Y (ft/ft)
A6	Bransby-Williams (1922)	$Tc = \frac{L}{1.5Dc}\sqrt[5]{\frac{A^2}{S}}$	Tc (h), L (km), A (km^2), Dc (km^2), S (%)
A7	Granato (2012) RE07	$LT = 1.272 * 0.760BLF^{0.571} * (13 - BDF)^{0.681}$	LT (h), BLF ($mile^{1.5}ft^{-0.5}$), BDF (–)
A8	Granato (2012) RE06	$LT = 1.360 * 0.514BLF^{0.565} * (100 - 0.99IMPERV)^{0.394}$	LT (h), BLF ($mile^{1.5}ft^{-0.5}$), IMPERV (%)
A9	Papadakis and Kazan (1986)	$Tc = \frac{0.66L^{0.5}n^{0.52}}{S^{0.31}i^{0.38}}$	Tc (min), L (ft), n ($m^{-1/3}$ s), S (ft/ft), i (in/h)
A10	Morgali and Linsley (1965)	$Tc = \frac{441L^{0.6}n^{0.6}}{i^{0.4}Y^{0.3}}$	Tc (min), L (km), n ($m^{-1/3}$ s), i (mm/h), Y (m/m)
A11	Izzard (1946)	$Tc = \frac{526.42(0.0000276i + c_r)L^{1/3}}{S^{1/3}i^{2/3}}$	Tc (min), i (mm/h), c_r (–), L (m), S (m/m)

[a] Abbreviations: A = watershed area; BDF is the basin development factor, defined as an index of urbanization and the prevalence of engineered drainage features (see Granato, 2012 for further details); BLF is the basin length in miles divided by the square root of the channel slope (ft/mile); c_r = retardance factor; Dc = diameter of the circle with an area equivalent to the watershed area; H = difference in watershed elevation from headwaters to outlet; IMPERV = the percentage of impervious area in the watershed (roofs, highways, etc.); i = intensity of the rainfall excess; L = length of channel from headwater to outlet; LT = lagtime; *n* = Manning's channel roughness coefficient; S = mean channel slope; S_{nat} = storage coefficient used in the curve number method calculated as $S_{nat} = (1000/CN) - 10$, where CN is the runoff curve number; Tc = time of concentration; W= watershed width (area (ft^2)/watershed length (ft)); Y = average watershed slope.

Appendix 2. Detailed description of the velocity method (NRCS, 1986)

The velocity method calculates the stream velocity for three segments selected along the main channel length, based on homogeneity. Travel time is obtained by dividing the segment length by the respective velocity. In the headwaters, three types of flow can be evaluated: sheet flow, shallow concentrated flow, and open channel flow. In the lower segments, only open channel flow is estimated.

The sheet flow is calculated from:

$$Tt = \frac{0.007(n\ell)^{0.8}}{(P_2)^{0.5}S_h^{\ 0.4}} \quad \text{(A12)}$$

where *Tt* is the partial travel time (h), *n* is the Manning's roughness coefficient for sheet flow, ℓ is the sheet flow length (ft), P_2 is the 2-year, 24-hour rainfall (inches), and S_h is the slope of land surface in that segment (ft/ft).

McCuen and Spies (1995) proposed improving the ℓ estimation (considered as default as 100 ft), by means of:

$$\ell = \frac{100\sqrt{S_h}}{n} \quad \text{(A13)}$$

where the symbols were previously defined.

The shallow concentrated flow has the general formula: $V = k*(S)^{0.5}$, where V is the water velocity (ft/s), and can be obtained from Fig. 15-4 in USDA-NRCS (2010).

The open channel flow is calculated using Manning's equation:

$$V = \frac{1.49r^{2/3}S^{1/2}}{n} \quad \text{(A14)}$$

r is the hydraulic radius (ft) calculated as **a**/Pw, where **a** is the cross-sectional flow area (ft^2), Pw is the wetted perimeter (ft), the channel slope (S) is in ft/ft, and *n*, in this case, is the Manning's *n* value for open channel flow (Chow, 1959).

J. Hydrol. Hydromech., 67, 2019, 2, 154–162
DOI: 10.2478/johh-2019-0001

Flow structure within a vegetation patch in a gravel-bed river

Mahsa Jahadi[1], Hossein Afzalimehr[2*], Paweł M. Rowinski[3]

[1] Department of Water Engineering, Isfahan University of Technology, Isfahan Iran.
[2] Department of Civil Engineering, Iran University of Science and Technology, Tehran Iran.
[3] Institute of Geophysics, Polish Academy of Sciences, Warszawa, Poland.
[*] Corresponding author. E-mail: hafzali@iust.ac.ir

Abstract: Investigation of the interactions between submerged vegetation patch and flow structure is of crucial importance for river engineering. Most of hydraulic models have been presented for fully developed flows over uniform vegetation in the laboratory conditions; however, the mentioned interactions are complex in river flows where the flow is not developed along small patch. This reveals a gap between developed and non-developed flow along the vegetation patch. This study was conducted in a gravel-bed river in the central Iran. The results reveal that the flow structure in evolving flow (non-developed flow) along the patch resembles that in shallow mixing layer. Accordingly, a shallow mixing layer model and modified equations are combined to quantify evolving area along the patch. The evolving shallow mixing layer equations for the flow along a non-uniform vegetation patch reach a reasonable agreement with field data. However, the spreading coefficient of this model less than one was reported in literature, 0.06 and 0.12. In addition, the flow immediately downstream the vegetation patch behaves similar to a jet and is parameterized by two conventional models, conventional logarithmic law and mixing layer theory. These models present a reasonable agreement with the measured velocity profiles immediately downstream the patch.

Keywords: Submerged vegetation patch; Mixing layer; Spatially evolving flow; Gravel bed river.

INTRODUCTION

Vegetation in rivers often occurs in patches of different sizes playing significant role in river systems. Schoelynck et al. (2012) found that the frequency distribution of patch sizes is governed by a power-law function, suggesting that the patches are self-organized. In this paper we will focus on hydrodynamics within selected single patch. It is well-known that vegetation patches play significant ecological role and they are suitable for the survival and growth of macrophytes (Schoelynck et al., 2012), they also influence the sediment chemistry (Clarke, 2002). Note that the presence of vegetation patch is different from other obstacles in rivers due to its permeability, however, the presence of an obstacle (e.g., bridge pier) changes the velocity field as well as vegetation patches do (Wang et al., 2015).

Aberle and Järvelä (2015) noticed that patchiness is the subject of many ecological studies but its effect on the flow structure is weakly recognized. Marjoribanks et al. (2016) reported the physical processes driving flow-vegetation interactions at the patch-scale, revealing the necessity of research on the influence of vegetation upon spatial and temporal flow dynamics. Vegetation in hydraulic studies is classified as emergent, submerged or floating but this study refers to submerged vegetation only. Most of literature studies has focused on homogeneously distributed artificial submerged plants in the laboratory flume (Kubrak et al., 2008; 2012; 2013); however, some studies were reported for natural vegetation (e.g. Järvelä, 2002; Nepf and Koch, 1999). There are also a few studies devoted to experimental investigations in the field (e.g. Ackerman and Okubo, 1993; Koch and Gust, 1999; Sukhodolov and Sukhodolova, 2006).

Based on laboratory studies a few researchers argue that the flow within and just above vegetation behaves similarly to a mixing layer rather than the boundary layer (Aberle and Järvelä, 2015; Carollo et al., 2002; Ghisalbert and Nepf, 2002; Marjoribanks et al., 2016; Michalke, 1965). Mixing layer is a free turbulent flow maintained by an internal velocity gradient, developing independently of solid boundaries. On the other hand, the boundary layer is defined as confined turbulent flow maintained by velocity gradient due to no-slip condition and developing over solid boundaries. The canonical mixing layer evolves in the co-flowing liquids of different densities or the flows of different mean velocities such as the flow downstream a splitter plate (Fig. 1) (Sukhodolova and Sukhodolov, 2012; Sukhodolov and Sukhodolova, 2006).

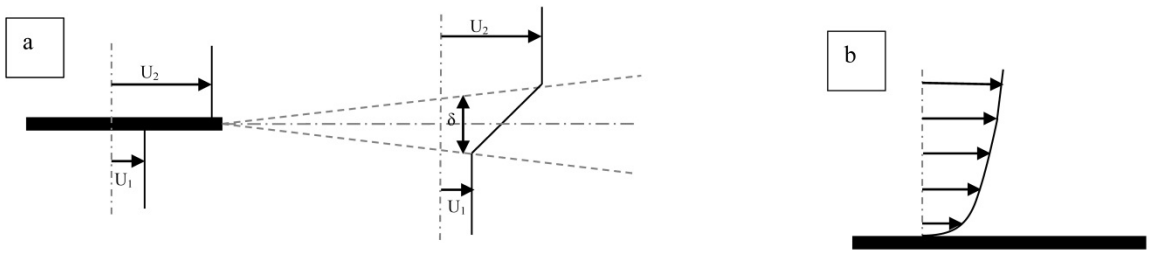

Fig. 1. The schematic representation of a) a canonical free mixing layer downstream a splitter plate and b) a boundary layer in a river (Sukhodolov and Sukhodolova, 2006).

Mean velocity profile in mixing layers is described by hyperbolic tangent function (Michalke, 1965):

$$\frac{u-u_c}{\Delta u}=0.5\tan h\frac{2\left(z-z_c\right)}{\delta} \quad (1)$$

where u_c is convective velocity and is equal to $(u_1+u_2)/2$, Δu, differential velocity, is equal to (u_1-u_2), u_1 and u_2 are the stream wise velocities of the slower and faster layers, respectively, δ is the mixing layer width (Fig. 1) and z_c is the position of the mixing layer center line. The width of the mixing layer equals to the cross-flow distance between locations where velocity inside the mixing layer attains the values of the ambient flow within 10% of accuracy, $\delta(x) = z_{0.9}(x)-z_{0.1}(x)$ (Sukhodolova and Sukhodolov, 2012). In the mixing layer, velocity and the length scales may be related as follows (Pope, 2000):

$$\frac{u_c}{\Delta u}\frac{d\delta}{dx}=\alpha \quad (2)$$

where α is the so-called spreading coefficient varying in the range of 0.06 to 0.12 (Pope, 2000; Sukhodolova and Sukhodolov, 2012).

In addition to the mean velocity, Reynolds stress (RS) plays a significant role in turbulent flow characteristics and is presented by hyperbolic cosine function for mixing layer (Sukhodolov and Sukhodolova, 2012) as:

$$-\frac{u'w'}{\Delta u^2}=\frac{\vartheta_t}{\delta\Delta u}\frac{1}{\cos h^2\eta},\qquad \eta=\frac{2\left(z-z_c\right)}{\delta} \quad (3)$$

where ϑ_t is the eddy viscosity, determined by product of mixing layer width and differential velocity ($\vartheta_t=\gamma\delta\Delta u$), γ is the empirical coefficient equal to 0.01 (Pope, 2000; Rodi, 1980; Sukhodolov and Sukhodolova, 2010; Sukhodolov et al., 2010).

Some researchers have made an attempt to quantify the flow structure above the vegetation patch. For example, Sukhodolov and Sukhodolova (2006, 2012), Sukhodolova and Sukhodolov (2012), investigated the dynamics of the flow over submerged vegetation patch in natural streams and found that the spatially evolving flow within and just above the vegetation patch had not been considered as the conventional mixing layer. Also, Sinsicalchi et al. (2012) reported the effect of energy conservation from mean velocity to turbulence at patch entrance which is not considered in canonical mixing layer. Therefore, Sukhodolova and Sukhodolov (2012), Sukhodolov and Sukhodolova (2012) extended the mixing layer theory by considering the spatial dynamics along a finite-size patch, reporting that the field experiments support the usefulness of the proposed model.

In most cases, the flow depth above the aquatic vegetation is much smaller than the river width, therefore, the flow conditions can be considered shallow. Sediment deposition within the vegetation canopy can amplify that shallowness. The flow shallowness and the bed friction significantly affect the dynamic of the vegetated mixing layer. Indeed, the vertical development of the large scale eddies in a shallow mixing layer is limited by the bed and the free surface (Cheng and Constantinescu, 2015; Kirkil, 2015). Chu and Babarutsi (1988) proposed the following law for the spreading coefficient (α) in a shallow mixing layer:

$$\alpha=\alpha_0\left(1-\frac{S}{S_c}\right) \quad \text{if } S<S_c \quad (4)$$

$$\alpha=0 \quad \text{if } S>S_c$$

where α_0 is considered close to 0.09 (Kirkil, 2015), S reflects the influence of the bed friction on the development of the mixing layer and is defined as (Chu and Babarutsi, 1988):

$$S=\frac{\overline{C_D}\,\delta U_c}{2h\Delta U} \quad (5)$$

$\overline{C_D}$ is equal to $(C_{D1}+C_{D2})/2$, C_{D1} and C_{D2} are equal to $\frac{2\tau_{1,2}}{\rho U_{1,2}^2}$ for the slower and faster streams, respectively, h is the channel depth, δ is the width of mixing layer, S_c is the critical value of S and corresponds to equilibrium between the turbulence production and dissipation. Experiments show that the values of this coefficient vary in the range from 0.06 to 0.12 (Kirkil, 2015).

Understanding the flow structure within and around a patch is important to better estimate the flow resistance and sediment transport in rivers. Sukhodolov and Sukhodolova (2010) assume that the flow downstream of a patch represents an amalgamation of two prototype flows. The flow above the vegetation layer behaves similarly to a jet or mixing layer structures, whereas the flow close to the bed reveals a boundary layer structure.

This paper focuses only on submerged patches to understand the flow structure over submerged aquatic vegetation. The objectives of the present study are to understand whether the shallow mixing layer model can be applied to the flow along a natural non-uniform patch. Also, the application of a combined model using the canonical mixing layer theory and the logarithmic law downstream of the patch is explored to explain the experimental data over the vegetation patch in a coarse-bed river.

MATERIALS AND METHODS

It goes without saying that selecting a suitable study river reach is crucial for the success of experimental investigations. To avoid logistics and safety problems a reach with depths less than 0.5 m was searched. It was also expected that data collection for flow depth lower than 0.1 m could be difficult due to high velocity values. Also, the selected vegetation patch in a river should be far away from other vegetation patches, rocks and structures to remove their influences on the measuring results. Further described straight reach of Pelasjan river fulfills the above expectations. Another not very often mentioned but desired condition is an easy access to the river reach allowing to transport the measuring equipment and the selected reach was perfect from this point of view. Pelasjan River is one of the important tributaries of Zayandehrood River (the largest and permanent river of central Iran, supplying the drinkable, industry and agriculture water for Isfahan province). This reach is located at an elevation of 2085 m, latitude 32º 42′ 49″ N, longitude 50º 28′ 33″ E (Fig. 2). The reach is 65 m long and is located near the Mashhadkaveh village in Isfahan Province, Iran. All field data was collected in May 2016. During dry season, in middle spring and summer, this river flows in a multiple channel pattern. In the selected reach part of the river bed forms an island in the middle section dividing the flow into two branches.

Discharge in this river reach was calculated by using the continuity equation, $Q=\sum A_iV_i$. A_i, is part of the cross- section area within one river branch, V_i, is the mean velocity in each part of the cross- section. A butterfly current meter was used to estimate the mean velocity in each part of the cross-

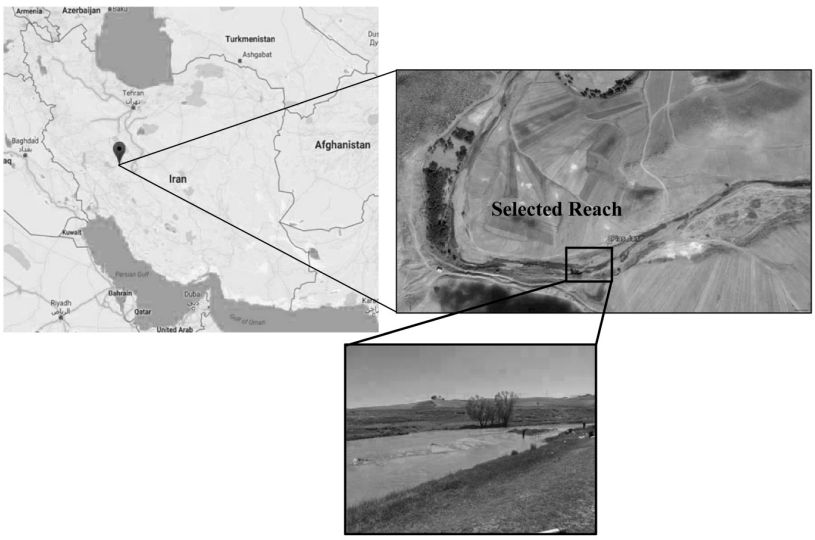

Fig. 2. Location of the Pelasjan River and the selected reach.

section. The measurement of velocity was conducted at 25 different cross sections. At each cross section, the velocity was measured at the vertical direction (z) equal to 0.2 and 0.8 flow depth (h).

By averaging these two velocities, the mean velocity at each subsection was determined. The time of velocity recordings was 50 seconds in each point, repeating each measurement three times. The hydraulic parameters in two river branches on both sides of the island are shown in Table 1.

River topography was surveyed by using a total station device. To achieve this goal, the selected reach was marked by several ropes. The ropes are arrayed forming a mesh of the size 2 m × 1 m (two meter in the longitudinal direction and one meter in the transversal direction). Taking into account the objectives of this study, more measuring points were taken in the vicinity of the selected vegetation patch (20 cm × 20 cm). The measuring points were fed into the Surfer software and calculations were made to build the riverbed map. Figure 3 shows the topography of the selected reach of the Pelasjan River.

Table 1. The hydraulic parameters at both sides of the island for a selected cross section in Pelasjan River.

Parameter	Left side	Right side	River
h (m)	0.33	0.51	0.37
W/h	7.7	38.9	81.3
U (m/s)	0.45	0.91	0.87
Fr	0.25	0.40	0.46
P (m)	3.15	21.03	24.18
A (m^2)	0.8	10.3	11.1
R	0.25	0.49	0.46
Re	113943	442978	400110
Q (m^3/s)	0.36	9.31	9.67

Figure 4 presents the grain size distribution in the neighborhood of the patch in the Pelasjan River obtained by using the traditional Wolman (1954) technique. The median grain size of bed material around the patch (D_{50}) was equal to 10.7 mm.

The maximum dimensions of the selected vegetation patch as shown in Figures 5 and 6 were 2.7 m in length and 1.2 m in width. The height of vegetation varied from 2.5 cm at the leading edge to 17 cm at the end of the patch (trailing edge). Hence, the depth of submergence (the ratio of the water depth to the vegetation height) was between 1.2 and 5.1. The frontal area per bed area, ah, obtained from the following Equation (6) (Nepf, 2012) varies from 0.25 to 7:

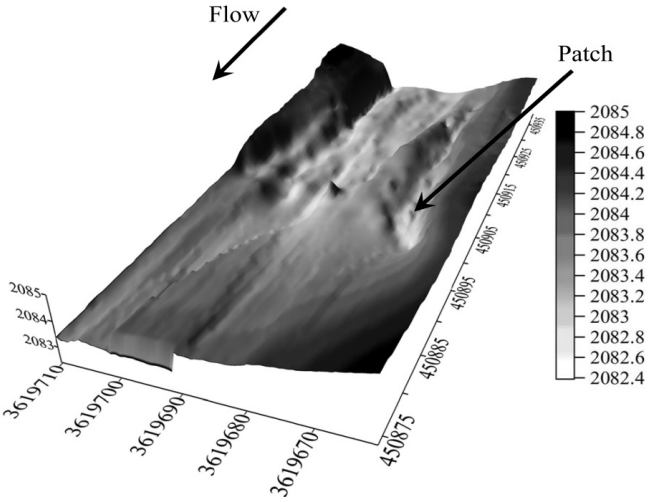

Fig. 3. Topography of the selected reach of the Pelasjan River.

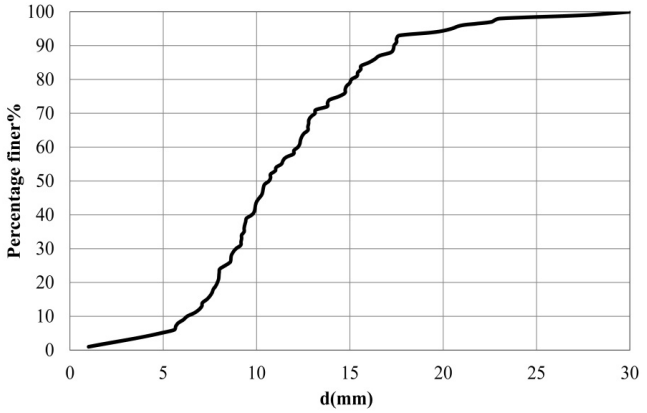

Fig. 4. Grain size distribution around the selected patch.

$$ah = \frac{d \cdot h_p}{\Delta S^2} \tag{6}$$

where h_p is the vegetation height, d is the diameter of the individual vegetation stem, ΔS is the average spacing between the stems. This patch is considered dense according to Nepf's classification (Nepf, 2012).

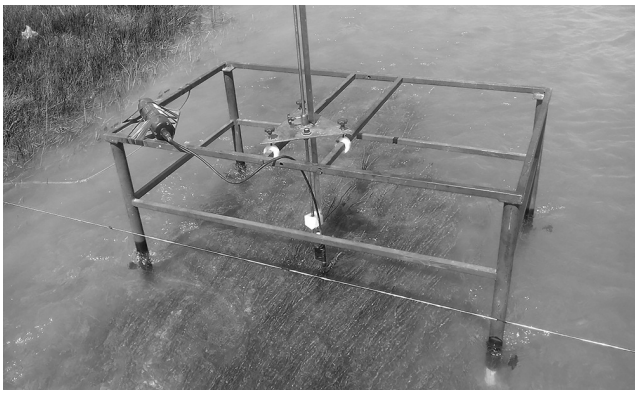

Fig. 5. Vegetation patch in selected reach of Pelasjan River.

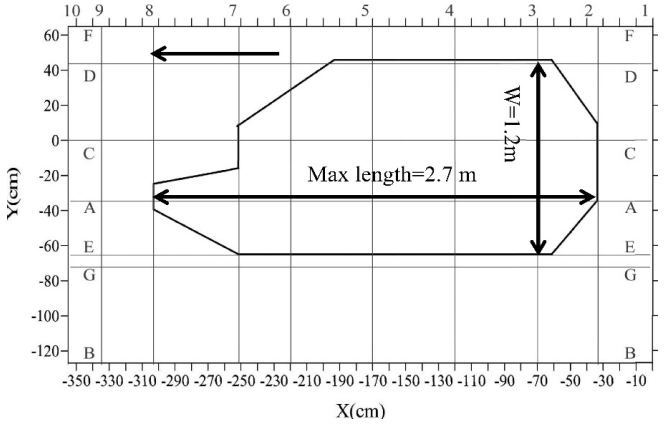

Fig. 6. The dimensions of the vegetated patch and the location of different cross-sections.

Turbulent velocity measurements were carried out with use of Acoustic Doppler Velocimetry (ADV). The ADV was mounted on a steel table frame with the length-width equal to 140 × 80 cm^2. To remove the wake effect of the legs, the ADV was installed at the upstream side in the middle of the frame. To start the work, at first, the macro balance of this frame was adjusted by the mobile legs and using a three-screw leveling located on the frame table. Velocity measurements were conducted along the patch at different cross-sections (Fig. 6). The measured profiles labels and the vegetation characteristics are presented in Table 2. For each velocity profile, in average 20 point velocities were measured. Measuring points were located more densely near the bed and at the top of the vegetation. The velocity profile in a vegetation-free zone was also measured for comparison purposes.

The frequency of data sampling was 200 Hz. The sampling time at each point was 120 s, however, in some points it took 300 s to collect data, revealing no difference in results. In other words, this time of 120 s was enough to obtain fully steady statistical characteristics of the flow. For this purpose, the variation of variance values of time-averaged mean velocity, Reynolds stress and higher order statistical moments of turbulence with respect to sampling number were examined. It is important to note that sporadic abrupt spikes appearing in velocity time series were removed to avoid their significant influence on the turbulence characteristics and Goring and Nikora's (2002) method was used for that purpose.

RESULTS AND DISCUSSION

Shallow mixing layer model along the vegetation patch

Figure 7 presents the mean horizontal velocity distribution within and in the vicinity of the vegetation patch. This figure shows that resistance to flow by patch deflects the flow away causing the decrease of the mean horizontal velocity along the patch. Rate of mean velocity reduction increased significantly at the leading edge of patch (C_2) due to the deceleration; however, the reduction in velocity at some points (such as C_4, 85 cm downstream of the leading edge) is high due to the heterogeneous pattern of natural vegetation and growth of the vegetation height. For further understanding, Figure 8 (a and b) displays the rate of mean velocity reduction and the rate of mean Reynolds stress enhancing along the C line upstream of the patch.

The reduction in velocity affects Reynolds stress (RS) by increasing the gradient of RS at the patch entrance (C_2). The rate of increasing in mean RS is also considerable in some other points along the patch (e.g., C_4) due to increasing flow resistance generated by the growth of vegetation height along the patch. Siniscalchi et al. (2012) reported that the greatest reduction in velocity occurs only at the patch entrance, increasing the turbulence production in this region. The mean velocity reduction along the vegetation patch leads to the minimum value of mean velocity downstream of the patch.

Velocity and Reynolds stress gradient in vertical direction (z) in Figure 8 (c and d) show similar trend at the top of patch where the increased velocity gradient generates a shear layer.

This region observed by Ghisalberti and Nepf (2002), Nepf and Vivoni (2000), Nepf (2012) and Siniscalchi et al. (2012) resembles to mixing layer, although the influence of the entrance region is not considered in mixing layer theory (Siniscalchi et al., 2012).

Figure 8 shows the energy conversion from the mean flow to turbulence at the leading edge (C_2). It is also manifested by the

Table 2. The characteristics of the measuring profiles.

Section	*h* (m)	*hp* (m)	*h*/*hp*	*ah*	Section	*h* (m)	*hp* (m)	*h*/*hp*	*ah*
C_1	0.22	----	----	----	A_4	0.11	0.03	4.4	0.25
C_2	0.18	0.035	5.1	0.40	A_5	0.165	0.07	2.5	0.65
C_3	0.16	0.053	3.0	0.71	A_6	0.17	0.07	2.6	0.53
C_4	0.13	0.06	2.2	1.20	A_7	0.19	0.11	1.8	1.48
C_5	0.15	0.12	1.3	2.40	A_8	0.225	0.10	2.3	1.41
C_6	0.2	0.17	1.2	6.93	A_9	0.295	----	----	----
C_7	0.23	0.17	1.4	5.66	A_{10}	0.335	----	----	----
C_8	0.325	----	----	----	E_3	0.2	0.05	4.0	0.40
C_{10}	0.34	----	----	----	E_5	0.17	0.09	1.9	0.90
D_3	0.16	0.035	4.6	0.53	G_3	0.27	----	----	----
D_5	0.2	0.14	1.4	5.04	G_5	0.25	----	----	----
D_7	0.33	----	----	----	G_7	0.24	----	----	----
F_3	0.23	----	----	----	B_1	0.165	----	----	----
F_5	0.305	----	----	----	B_3	0.22	----	----	----
A_1	0.25	----	----	----	B_5	0.29	----	----	----
A_2	0.2	0.025	8	0.25	B_7	0.305	----	----	----
A_3	0.16	0.035	4.6	0.25	B_8	0.3	----	----	----

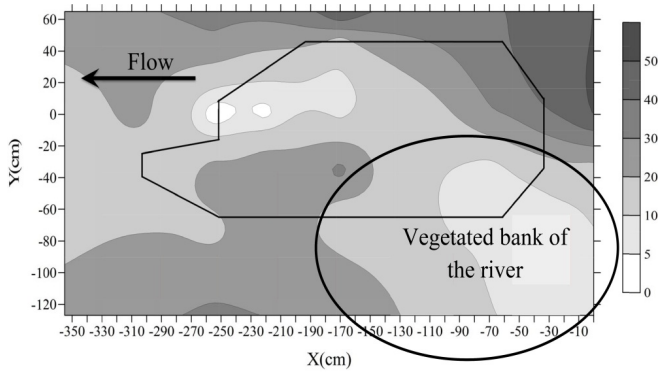

Fig. 7. The mean horizontal velocity (cm/s) around the patch.

existence of the peak point in energy spectrum (Figure 9) within the frequency range around 6–8Hz. Figure 9 displays also energy spectra close to the crest of vegetation patch at different distances from the leading edge. Inside the patch the spectra for the vertical component of velocity reach the peak point due to shedding vortices, confirming the previous works by Ghisalberti and Nepf (2002), Sinsicalchi et al. (2012), White and Nepf (2007). Spectral energy along the patch is higher (3.5–10 cm^2/s) at lower frequency (≈2–5 Hz), in comparison with that at the leading edge (around 2 cm^2/s). Sinsicalchi et al. (2012) reported similar trend in vegetation patch in a laboratory study.

These frequency ranges are lower at some points downstream of the patch (C_3), but are higher (C_4) than the estimated ones from $f_{KH} = 0.032(u_c/\theta)$, where θ is the momentum thickness (as suggested by Ghisalberti and Nepf (2002)). These higher and lower values are related to the heterogeneous layout of natural vegetation. However, the estimated value based on Ghisalberti and Nepf (2002) function, for the mean characteristic of the vegetation patch (around 2.6 Hz) conform with the frequency range (≈2–5 Hz) obtained in this study.

Equations (7) and (9) are derived from RANS equation within the vegetation, just above the bed and near the water surface, respectively (Sukhodolova and Sukhodolov, 2012):

$$\overline{u}_{1e}^2 = \overline{u}_{1d}^2 + \left(\overline{u}_{01}^2 - \overline{u}_{1d}^2\right)\exp\left[-\left(C_D a\right)_1 x\right] \tag{7}$$

where $\overline{u}_{1e}$ is the mean velocity inside the vegetation and close to the bed in developing area, a is the projected area of vegetation, C_D is the drag coefficient, $(C_D\, a)_1$ is averaged in the layer just above the bed inside the vegetation. $\overline{u}_{1d}$ is the averaged velocity within the patch and close to the bed for the developed flow, which is presented as (Sukhodolova and Sukhodolov,

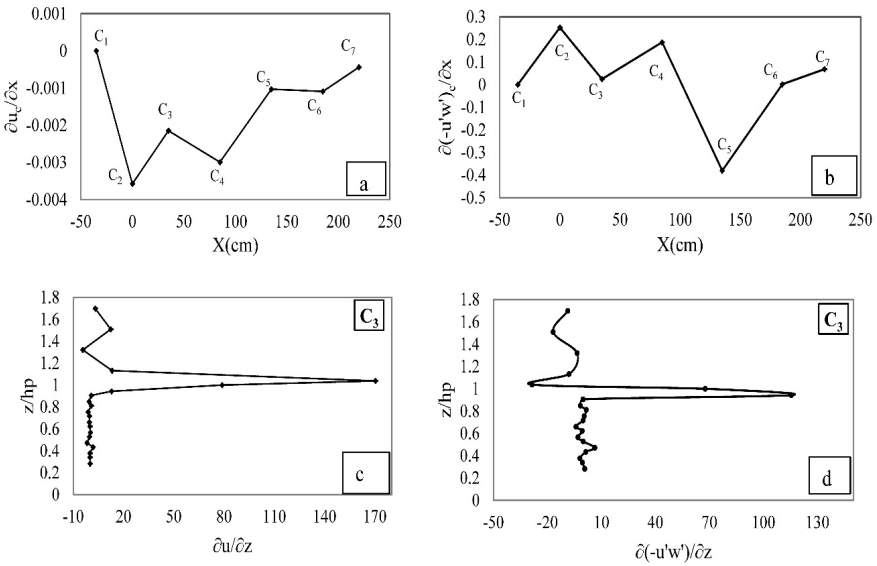

Fig. 8. a) Mean velocity gradient along the flow at C line, b) mean Reynolds stress gradient along the flow at C line, c) velocity gradient in vertical direction (z) at C3 and d) Reynolds stress gradient in vertical direction (z) at C3.

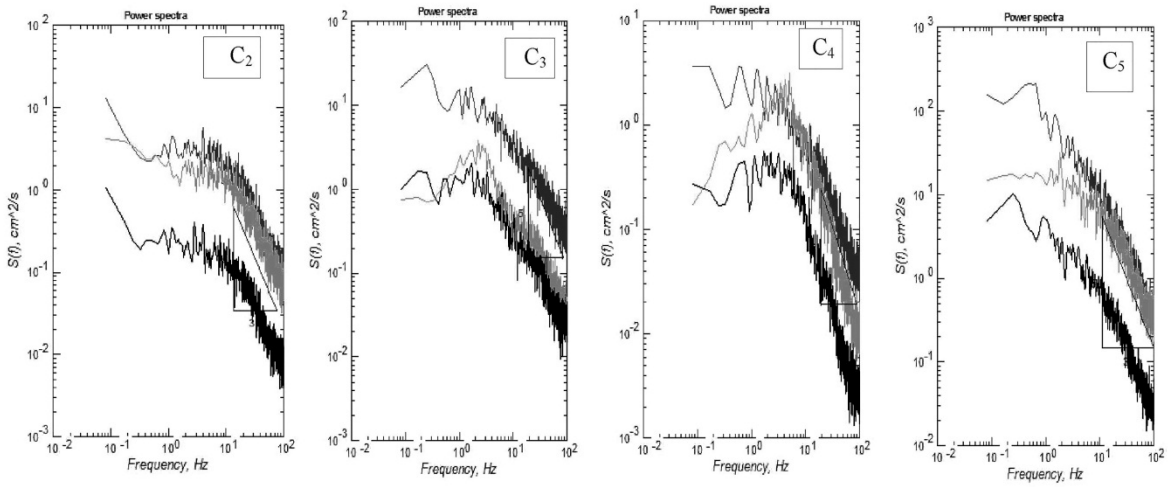

Fig. 9. Spectral function close to the crest of vegetation at C_2 (the leading edge), C_3(at 35 cm downstream of the leading edge), C_4 (85 cm downstream of the leading edge) and C5 (135 cm downstream the leading edge).

2012):

$$\overline{u}_{1d} = \sqrt{\frac{2gS_0}{(C_D a)_1}} \tag{8}$$

$$u_{2e}^2 = u_{02}^2 + 2gS_0 x \tag{9}$$

To consider the effect of developing flow along the patch within the mixing layer width, Equations (7) to (9) are inserted into Equation (2). The mean value of the spreading coefficient (in Equations 1 and 2) suggested for vegetated mixing layer (solid line in Fig. 10) is equal to 0.09 (Pope, 2000; Sukhodolova and Sukhodolov, 2012), whereas the calculated one by means of formula (4) is 0.032 (dashed line in Figure 9).

Obviously the results depend on the estimation of drag coefficient (C_D) in the above formulae. Assuming $C_D = \frac{2\tau_b}{\rho U_d^2}$, $f = \frac{8\tau_b}{\rho U_d^2}$ and the simplified model for predicting the hydraulic resistance proposed by Kouwen et al. (1969), the drag coefficient can be represented as (Hsieh and Shiu, 2006):

$$\sqrt{\frac{2}{C_D}} = c_1 \ln\left(\frac{A}{A_P}\right) + c_2 \qquad (R^2 = 0.92) \tag{10}$$

where A is the total cross sectional area of the flow, A_P is part of the total cross-sectional area occupied by the vegetation, c_1 and c_2 are the coefficients, depending on vegetation properties. By applying a standard least square method for 25% of experimental data, the empirical coefficients in Equation (10) were estimated as $c_1 = 1.4$ and $c_2 = -1.03$. Equation (10) was validated by using the remaining 75% data and next the drag coefficient was obtained.

Figure 10 presents the measured (symbols) and the computed (lines) values of the mixing layer width (δ) defined along the central line (C), revealing much better agreement when the spreading coefficient is calculated based on Equation 4 rather than the suggested value in literature (0.09). This better agreement is probably obtained due to the included sediment deposition within the patch, and the growth of the patch in the flow direction, leading to lower flow depth over the vegetation crest downstream of the patch.

Figures 11 and 12 show how the shallow mixing layer develops along the vegetation patch. The vertical profiles of mean velocity along the patch in Figure 11 indicate relatively good agreement with the evolving shallow mixing layer model. The velocity profile in the vegetated mixing layer consists of two different mean velocities and the inflection point, showing Kelvin- Helmholtz instability. In Figure 11 the mean point velocity and the flow depth are normalized by the mean-depth velocity (u_{02}) and vegetation height (h_p), respectively.

Figure 12 illustrates relatively good agreement of Reynolds stress (RS) profiles with the results based on the evolving shallow mixing layer model. The distribution of RS in the vegetated mixing layer reaches the maximum value close to the crest of vegetation due to Kelvin-Helmholtz instabilities.

The empirical coefficient of eddy viscosity model γ (Equation 3) agrees with the nominal value (0.01) for free and shallow mixing layers. However, we should report that Ghisalberti and Nepf (2002, 2004) and Sukhodolov and Sukhodolova (2010, 2012) observed much larger value of γ. The larger values of this coefficient might be related to stronger organization of coherent structures in a vegetated shear layer (Ghisalberti and Nepf, 2006), at the same time the heterogeneous conditions of natural vegetation may disturb the coherent structures making the value of γ smaller in this study.

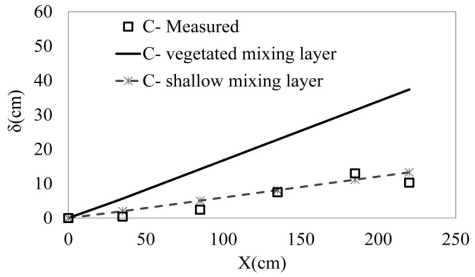

Fig. 10. The thickness of the measured (symbol) and estimated (line) mixing layer along C line with $\alpha = 0.09$ (solid line) and $\alpha = 0.032$ obtained by Equation (3) (dashed line).

Although the evolving mixing layer model achieved the reasonable agreement with measured velocity and Reynolds stress profiles, there is small deviation between the model and the measured data. This discrepancy might be related to the three dimensional coherent vortices that were ignored in evolving mixing layer theory. Moreover, the concept of evolving shallow mixing layer was developed for parallel streams. However, the growth of vegetation distorts the parallel flow. Hence non parallel streams and heterogeneous shallow lateral flows which are not considered in the shallow mixing layer theory may explain the small deviations of the model results from the measured data.

Validity of a combined model based on canonical theory and the boundary layer concept

One may learn about the differences and similarities between the canonical mixing layer and the mixing layer downstream of the vegetation patch from Figure 13 in which the results of measurements (symbol) and calculations (lines) of the width of the mixing layer are presented. Note that by getting away from the end of the patch the measured width of the mixing layer (δ) (symbol) increases rapidly to reach the maximum value. The flow close to the bed has the structure of boundary layer and when this layer extends along the patch, the width of mixing layer (δ) decreases. In canonical mixing layer theory (solid line), this contraction of mixing layer width is not observed in Figure 13. Subsequently the canonical mixing layer is only valid immediately downstream the patch where the width of mixing layer (δ) increases. Just downstream of the vegetation patch, the mean value of the suggested range of spreading coefficient (0.09) shows relatively good agreement with the estimated one by formula (4) and the measured data. By applying negative value of spreading coefficient in expression (2), –0.09, the mixing layer theory is modified (dashed line), and it is valid for other profiles downstream of the patch. This negative value demonstrates the contraction of mixing layer caused by boundary layer development.

Figure 14 shows the measured and the predicted velocity profiles downstream of the vegetation patch based on conventional mixing layer and assuming a negative value (–0.09) for spreading coefficient where the mixing layer contracts by expanding the boundary layer. It is worth mentioning that the velocity distribution close to the bed (relative flow depth, z/h, is less than 0.2) is predicted based on logarithmic law. Above this layer, the velocity distribution is estimated based on the mixing layer formulae (1) and (2), showing relatively good agreement with the experimental observations. The velocity profile downstream of the vegetated mixing layer (Figure 14) contains the

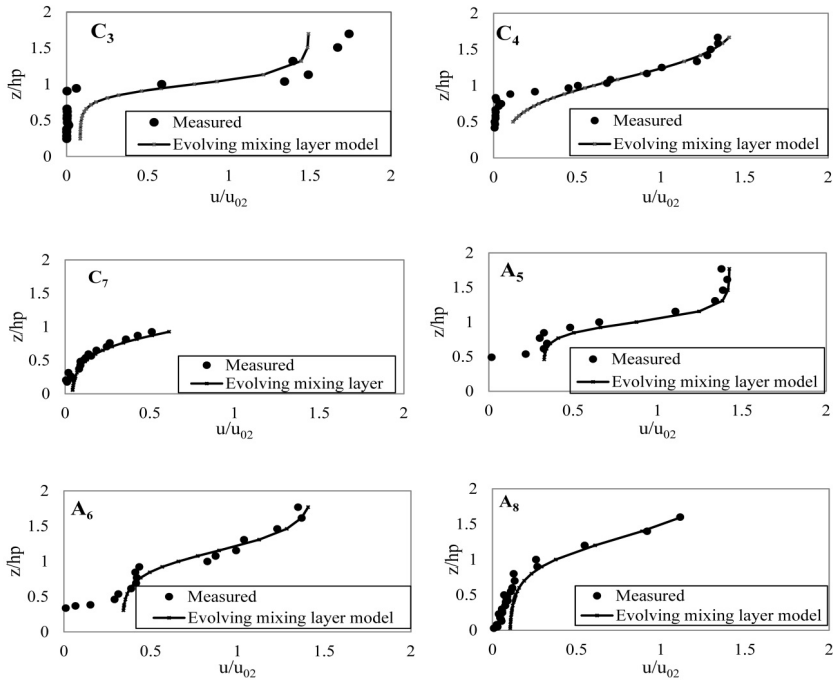

Fig. 11. Comparison of the measured and the computed velocity profile along the patch using the evolving mixing layer model.

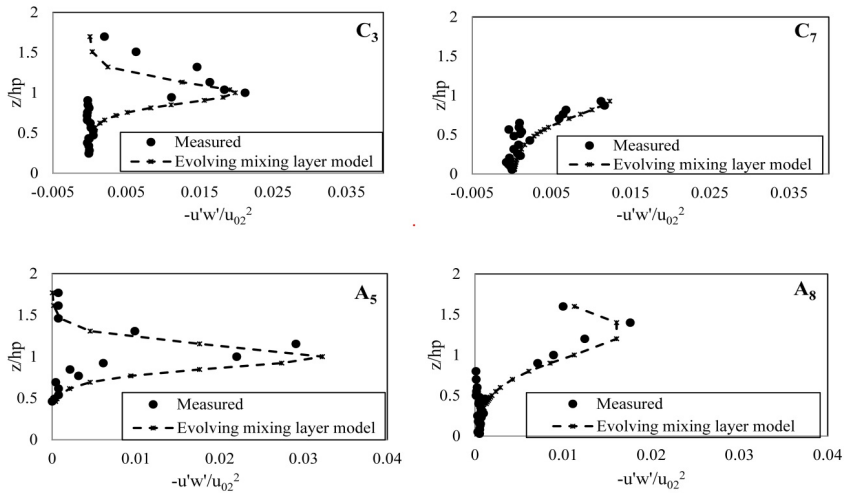

Fig. 12. Comparison of the measured and the computed Reynolds Stress distributions along the vegetation patch using the evolving mixing layer model.

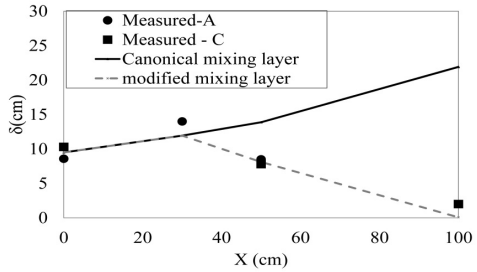

Fig. 13. The width of mixing layer downstream of the patch: measured (symbol), calculated based on a canonical mixing layer (solid line).

flow with different mean velocities and the inflection points. However, there is a slight discrepancy between the measured and the estimated values downstream of the patch due to spatially evolving flow (Figure 14). No extension of the flow structure is considered in conventional mixing layer formula.

Distributions of turbulent Reynolds stress components downstream of the patch are illustrated in Figure 15. The flow downstream of the vegetation patch consists of two parts, showing jet-like structure and the shear layer. These two parts are evident in RS profile in Figure 15. By getting away from the end of the vegetation patch, these profiles reach a better agreement with RS profile close to the riverbed, where no canopy occurs, due to the contraction of mixing layer.

Figure 15 illustrates also the predicted Reynolds stress profiles downstream of the vegetation patch based on conventional mixing layer and a negative value (–0.09) for spreading coefficient. The RS distributions close to the bed (relative flow depth, z/h, is less than 0.2) may be predicted as:

$$-u'w' = g\,h\,S\left(1-\frac{z}{h}\right); \qquad S = S_0 - \frac{\partial h}{\partial x} \tag{11}$$

where, S_0 is the mean slope. Above this layer, the RS distribution is estimated based on the mixing layer functions (3). A reasonably good agreement between the measured and the predicted values of RS at downstream of the patch was observed in Figure 15. It is worth mentioning that this model is not valid for flows in vegetation-free zones (Figure 15). There-

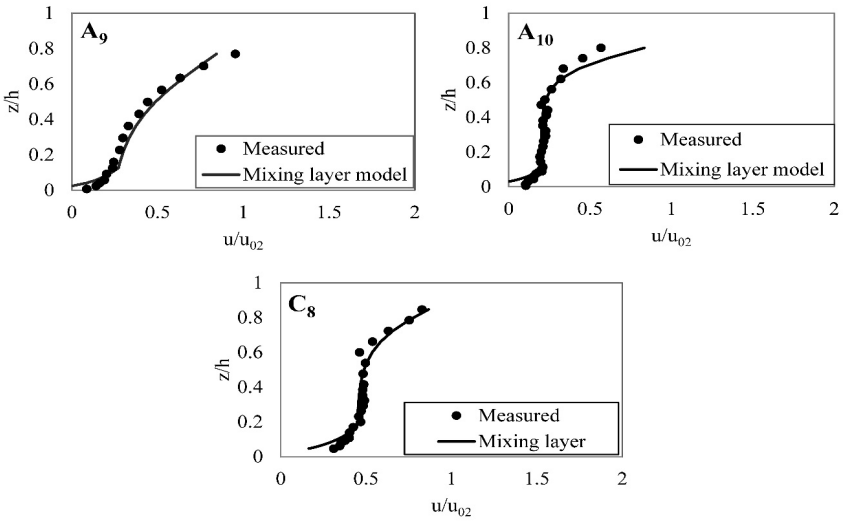

Fig. 14. Comparison of measured (symbol) and computed (solid line) velocity profile downstream of the patch.

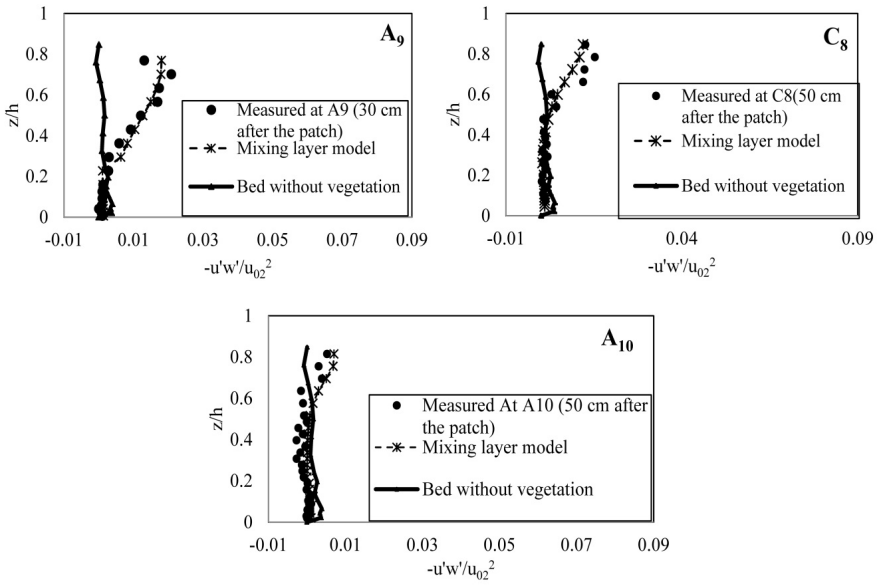

Fig. 15. Comparison of measured (symbol) and computed (solid line) RS distributions downstream of the vegetation patch.

fore, it is reasonable that the distributions in such two cases differ from each other. The RS profile, over bed without vegetation, is presented only to compare the jet-like structure downstream of the vegetation patch with the boundary layer structure over the bed without the effect of vegetation.

The coefficient of eddy viscosity, γ, immediately downstream of the patch is about 1.3 times larger than the nominal value which is related to the stronger organization of coherent structures in vegetated shear layer (Ghisalberti and Nepf, 2006).

By getting away from the patch, the coefficient (γ) decreases to the value of 0.5 times smaller than the nominal value (A_{10}) due to disappearing of the mixing layer.

CONCLUSIONS

An attempt was made in field to study the flow structure along a non-uniform vegetation patch. The results show that the pattern of mean velocity distribution along the submerged vegetation patch is similar to a mixing layer. However, the effect of spatially evolving flow over the patch is not considered in the canonical mixing layer approach. In addition, taller and denser vegetation towards the end of the patch, and deposition within the patch cause the flow becomes shallow and lead to additional decrease of the mixing layer width. Thus the results of computation of the mixing layer thickness by using the spreading coefficient equation for shallow mixing layer are in a better agreement with experimental results than the suggested values in literature.

To consider the effect of the entrance region of a patch, the extension of the shallow mixing layer model was examined for the non-uniform vegetation patch. The results show a reasonably good agreement for non-developed flows. The slight deviation of the model from the measured values occurs due to non-parallel streams, heterogeneous shallow lateral river flow and three-dimensional vortices which are not considered in the shallow mixing layer theory.

Field study demonstrates that downstream of the vegetation patch the flow above the vegetation layer behaves like a mixing layer or jet-like structure. At the same time the boundary layer of the river bed grows and finally becomes superimposed onto the mixing layer structure. The boundary layer has a tendency to expand. So by growing the thickness of boundary layer, the mixing layer structure contracted. This is the reason why the width of the mixing layer is reduced after its peak. Examination of the conventional mixing layer theory with the boundary layer law downstream of the vegetation patch leads to the following conclusions:

1- Two types of flow models, namely the canonical mixing layer model and the logarithmic law, are valid for the developed flow, while the flow along the patch cannot be treated as developed. However, an agreement between those two types of flow models and the field measurements is reasonable downstream of the vegetation patch.

2- Immediately downstream of the vegetation patch, where the width of the mixing layer is growing thanks to the jet-like structure, the canonical mixing layer analogy with the proposed value range for spreading coefficient (0.06 to 0.12) led to reasonable results.

3- In the region where the boundary layer is expanding and the width of the mixing layer is contracting the canonical mixing layer needs to be modified. In this region by accounting a negative value for spreading coefficient this theory seems rational. This negative value reflects the contraction trend of the mixing layer structure.

Acknowledgement. This work was partially supported within statutory activities No 3841/E-41/S/2017 of the Ministry of Science and Higher Education of Poland.

REFERENCES

Aberle, J., Järvelä, J., 2015. Hydrodynamics of vegetated channels, In Rivers – physical, fluvial and environmental processes. In: Rowiński, P., Radecki-Pawlik, A. (Eds.): GeoPlanet: Earth and Planetary Sciences, Springer International Publishing, pp. 519–541. DOI: 10.1007/978-3-319-17719-9.

Ackerman, J., Okubo, A., 1993. Reduced mixing in marine macrophyte canopy. Funct. Ecol., 7, 305–309.

Carollo, F.G., Ferro, V., Termini, D., 2002. Flow velocity measurment in vegetated Channels. J. Hydraul. Eng., 128, 7, 664–673. DOI: 10.1061/(ASCE)0733-9429(2002)128:7(664).

Cheng, Z., Constantinescu, S.G., 2015. For field structure of turbulent shallow mixing layers between parallel streams. In: E-Proceedings of the 36th IAHR World Congress. IAHR, The Hague, The Netherlands.

Chu, V.H., Babarutsi, S., 1988. Confinement and bed friction effects in shallow turbulent mixing layers. J. Hydraul. Eng., 114, 1257–1274.

Clarke, S.J., 2002. Vegetation growth in rivers: influences upon sediment and nutrient dynamics. Prog. Phys. Geog., 26, 2, 95–106.

Ghisalberti, M., Nepf, H., 2002. Mixing layers and coherent structures in vegetated aquatic flows. J. Geophys. Res., 107(C2). DOI: 10.1029/2001JC000871.

Ghisalberti, M., Nepf, H.M., 2004. The limited growth of vegetated shear layers. Water Resour. Res., 40, W07502. DOI: 10.1029/2003WR002776.

Ghisalberti, M., Nepf, H.M., 2006. The structure of the shear layer inflows over rigid and flexible canopies. Environ. Fluid Mech., 6, 277–301.

Goring, D.G., Nikora, V.I., 2002. Despiking acoustic Doppler velocimeter data. J. Hydraul. Eng., 128, 1, 117–126.

Hsieh, P.C., Shiu, Y.S., 2006. Analytical solutions for water flow passing over a vegetal area. Adv. Water. Resour., 29, 9, 1257–1266.

Järvelä, J., 2002. Flow resistance of flexible and stiff vegetation: a flume study with natural plants. J. Hydrol., 269, 44–54.

Kirkil, G., 2015. Detached eddy simulation of shallow mixing layerdevelopment between parallel streams. J. Hydro-Environ. Res., 9, 2, 304–313.

Koch, E., W., Gust, G., 1999. Water flow in tide- and wave-dominated beds of the seagrass *Thalassia testundinum*. Marine Ecol. Prog., 184, 63–72.

Kouwen, N., Unny, T.E., Hill. H.M, 1969. Flow retardance in vegetated channels. J. Irrig. Drain. Div., 95, 2, 329–342.

Kubrak, E., Kubrak, J., Rowiński, P.M., 2008. Vertical velocity distributions through and above submerged, flexible vegetation. Hydrolog. Sci. J., 53, 4, 905–920. DOI: 10.1623/hysj.53.4.905.

Kubrak, E., Kubrak, J., Rowiński, P.M., 2012. Influence of a method of evaluation of the curvature of flexible vegetation elements on the vertical distributions of flow velocities. Acta Geophys., 60, 4, 1098–1119. DOI: https://doi.org/10.2478/s11600-011-0077-2.

Kubrak, E., Kubrak, J., Rowiński, P.M., 2013. Application of one-dimensional model to calculate water velocity distributions over elastic elements simulating Canadian waterweed plants (*Elodea Canadensis*). Acta Geophys., 61, 1, 194–210. DOI: https://doi.org/10.2478/s11600-012-0051-7.

Marjoribanks, T., Parson, D.R., Lane, S., 2016. Does the canopy mixing layer model apply to hightly flexible aquatic vegetation? Insights from numerical modeling. Environ. Fluid Mech., 17, 2, 277–301. DOI: 10.1007/s10652-016-9482-z.

Marjoribanks, T.I., Hardy, R.J., Lane, S.N., Tancock, M.J., 2016. Patch-scale representation of vegetation within hydraulic models. Earth Surf. Process. Landforms., 42, 699–710. DOI: 10.1002/esp.4015.

Michalke, A., 1965. spatially growing disturbances in an inviscid shear layer. J. Fluid. Mech., 23, 521–544.

Nepf, H., Vivoni, E., 2000. Flow structure in depth-limited, vegetated flow. J. Geophys. Res., 105(C12), 28547–28557. DOI: 10.1029/2000JC900145.

Nepf, H., 2012. Hydodynamic of vegetated channels. J. Hydraul. Res., 50, 3, 262–279.

Nepf, H.M., Koch, E.W., 1999. Vertical secondary flows in submersed plant-like arrays. Limnol. Oceanogr., 44, 1072–1080.

Pope, S.B., 2000. Turbulent Flows. Cambridge University Press.

Rodi, W., 1980. Turbulence Models and Their Application in Hydraulics. IAHR Monograph Series. Balkema, Rotterdam.

Schoelynck, J., DeGroote, T., Bal, K., Vandenbruwaene, W., Meire, P., Temmerman, S., 2012. Self-organised patchiness and scale-dependent bio-geomorphic feedbacks in aquatic river vegetation. Ecography, 35, 760–768. DOI: 10.1111/j.1600-0587.2011.07177.x.

Sinsicalchi, F., Niora, V., Albera, J., 2012. Plant patch hydrodynamics in streams: Mean flow, turbulence and drag forces. Water. Resour. Res., 48, W01513.

Sukhodolov, A., Sukhodolova, T., 2006. Evolution of mixing layers in turbulent flow over submerged vegetation: Field experiments and measurement study. River flow. In: Ferreira, R.M.L. et al. (Eds.): Proc. 3rd Int. Conf. on Fluvial Hydraulics. Lisbon, Portugal, pp. 525–534.

Sukhodolov, A.N., Sukhodolova, T.A., 2010. Case study: Effect of submerged aquatic aquatic plants on turbulence structure in Lowland River. J. Hydraul. Eng. ASCE, 136, 7, 434–446.

Sukhodolov, A.N., Schnauder, I., Uijttewaal, W.S.J., 2010. Dynamics of shallow lateral shear layers: Experimental study in a river with a sandy bed. Water Resour. Res., 46, W11519. DOI: 10.1029/2010WR009245.

Sukhodolova, T. A., Sukhodolov. A. N. , 2012. Vegetated mixing layer around a finite-size patch of submerged plants: 1. Theory and field experiments. Water. Resour. Res., 40, W10533.

Sukhodolov, A., Sukhodolova,T., 2012. Vegetated mixing layer arounda finite-size patch of submerged plants: 2. Turbulence and coherent structures. Water Resour. Res., 48, W12506, DOI: 10.1029/2011WR011805.

Wang, G., Shi, F., Chen, P.P., Sui, J., 2015. Impact of bridge pier on the stability of ice jam. J. Hydrodyn., 27, 6, 865–871.

White, B., Nepf, H., 2007. Shear instability and coherent structures in shallow flow adjacent to porous layers. J. Fluid. Mech., 593, 1–32.

Wolman, M.G., 1954. A method of sampling coarse river bed material. Trans. AGU, 35, 6, 951–956.

Received 10 May 2017
Accepted 8 December 2017

J. Hydrol. Hydromech., 67, 2019, 2, 163–170
DOI: 10.2478/johh-2018-0042

Water surface topology of supercritical junction flow

Gašper Rak[1*], Marko Hočevar[2], Franci Steinman[1]

[1] Chair of Fluid Mechanics, Faculty for Civil and Geodetic Engineering, University of Ljubljana, Jamova 2, 1000 Ljubljana, Slovenia.
[2] Laboratory for Water Turbine Machinery, Faculty of Mechanical Engineering, University of Ljubljana, Ljubljana, Slovenia.
[*] Corresponding author. Tel.: +386 1 4254052. E-mail: gasper.rak@fgg.uni-lj.si

Abstract: The complexity of flow conditions at junctions amplifies significantly with supercritical flow. It is a pronounced three-dimensional two-phased flow phenomenon, where standing waves with non-stationary water surface are formed. To analyse the hydrodynamic conditions at an asymmetric right-angled junction with incoming supercritical flows at Froude numbers between 2 and 12, an experimental approach was used. For a phenomenological determination of the relations between the integral parameters of incoming flows and the characteristics of standing waves at the junction area, water surface topographies for 168 scenarios at the junction were measured using non-intrusive measurement techniques. The new, phenomenologically derived equations allow for determination of location, height and extent of the main standing waves at the junction. Research results give important information on the processes and their magnitude for engineering applications.

Keywords: Junction; Hydraulic experimentation; Standing wave; Supercritical flow; Flow patterns.

INTRODUCTION

At junctions of two or more open channels, especially under supercritical incoming flows (Froude number Fr is greater than 1; Fr gives the ratio of the flow inertia to the external gravity field – $Fr = \frac{v}{\sqrt{gl}}$), a turbulent three-dimensional flow is generated. Due to high flow velocities and turbulent shear stress the two-phase flow with strong water surface dynamics along the shear layer between both incoming flows also occurs. Junctions are commonly found elements in natural hydrographic networks and hydraulic structures, and a knowledge of flow conditions at a junction is important for both the planning of developments at the junction itself, of riparian and potential bridging structures, as well as for the understanding of accompanying processes, such as sediment transport dynamics and variations in bathymetry. Despite the high quality of modern 3D numerical models, their use in precise simulations of flow conditions at junctions is only possible with adequately set initial and boundary conditions, acquired by field or laboratory measurements. To analyse the characteristics of the flow with high Froude numbers at the junction the experimental approach was selected. Experiments were conducted with an experimental apparatus of a T-shaped junction. At the junction of two supercritical incoming flows typical water flow patterns or standing waves form due to high, predominantly vertical dynamics of the water surface. The topography of these standing waves was recorded using a non-intrusive LIDAR measurement method with high spatial and temporal resolution allowing for the analysis of its main characteristics. Based on the analysis of flow patterns at the junction for a large set of scenarios, the phenomenologically derived equations between the integral parameters of incoming flows and characteristics of standing waves were developed. These equations describe the characteristics of standing waves at right-angled junctions, which, by calculating the magnitude and height of wave peaks, allows for the proper planning of developments at such junctions (designing junction structures on sewer systems, freeboard and hydraulic structures (e.g. culverts) at torrent junctions, junctions of road drainage channels etc.).

PREVIOUS RESEARCH

Research of hydraulic conditions at the junction began with an experiment by E. H. Taylor in 1944, yielding a one-dimensional model for determining the ratio of depths up- and downstream of the junction based on the law of conservation of momentum for subcritical flow (Froude number Fr is smaller than 1). Both sub- and supercritical flows were observed by Bowers, (1950); Behlke and Pritchett, (1966); Greated, (1968); Best and Reid, (1984); Hager, (1989a); Hager, (1989b); Mignot et al., (2008); Pinto Coelho, (2015). Research of hydraulic conditions at the junction also included different Froude numbers in the up- and downstream sections, different junction angles, including symmetric and asymmetric junctions. Velocity fields, water mixing zones and flow conditions in junctions with and without bed discordance of the tributary channel were observed. Christodoulou (1993) analysed conditions for formation of hydraulic jump at junctions with angles of 17° and 90° for weak supercritical flow in the main channel ($Fr \leq 2$) and subcritical flow in the tributary channel. For supercritical approach flow Pfister and Gisonni (2014) and Saldarriaga et al. (2017) investigated flow conditions at junction manholes on circular conduits.

Limited research has been done so far in the field of hydrodynamic conditions and water surface topography at an asymmetric junction with incoming supercritical flows at higher Froude numbers ($Fr \geq 2$). The analyses of hydrodynamic conditions were mostly focused on the subcritical flow regime and supercritical flow regime at lower Froude numbers ($Fr \leq 2$) for different types of junction, but water surface topology of supercritical junction flow was previously studied only by Schwalt and Hager (1995). Their experimental research included several different scenarios, all with supercritical flow of high Froude number ($Fr \leq 12$) and with horizontal bottom throughout. They provided equations for the description of unobstructed junction flow (main dimensions of standing waves). However, their research focused on junctions with angles of 30° and 60°, so that their equations do not apply for junctions with junction angles greater than 60°.

EXPERIMENTAL SET-UP AND MEASURING TECHNIQUE

Model set-up

The junction of two supercritical incoming flows was investigated at the hydraulic laboratory of the Faculty of Civil and Geodetic Engineering, the University of Ljubljana. The asymmetric junction with a 90° angle between main channel and tributary channel (T-junction) was considered. The model is shown in Figure 1, where the main parts are marked with numbers: 1 – pipeline system equipped with valves and flowmeter; 2 – pressure vessels with adjustable height of the openings; 3 – main channel; 4 – tributary channel; 5 – rails with carrier for mounting and precise positioning of measurement devices; 6 – laser scanner; 7 – free overflow at the end of the model. The lengths of main and tributary channels upstream of the junction were 1 m to ensure equal upstream conditions while the length of main channel downstream of the junction was 5 m. The length of channels upstream of the junction and roughness of the glass wall were sufficient for the development of supercritical steady uniform flow at the inflow. The width of all channels was constant at 0.5 m. A horizontal bottom of all sections was maintained throughout the entire model. Glass plates were used for construction of the experimental apparatus: sharp edges, minimising the effect of the boundary layer and improving visibility though the model walls. Using large-size glass plates and rationally optimised construction also enabled the minimisation of the number and effect of joints in the entire model and thus disturbance of the flow by streamline separation.

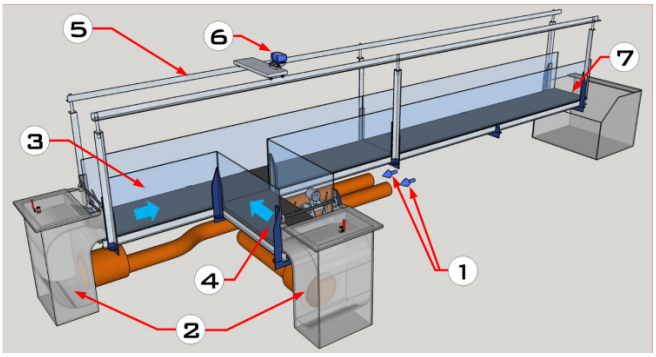

Fig. 1. Experimental set-up.

The inflows into the main and tributary channels from the reservoir were separated from each other with two pipelines. For independent settings of discharge to each inflow, both pipelines were equipped with a valve and ABB FlowMaster electromagnetic flowmeters with a nominal diameter of 150 mm. The inflows with desired characteristics (flow depth, Froude number) were provided with pressure vessels, where flaps at both pressure vessels allowed for the adjustment of the opening to 0.1 mm. Outflow from the model was provided with free overflow at the end of the main channel. Froude numbers at low depths (1 cm) exceeded 20 while higher depths (5 cm) resulted in larger discharge and due to the limited capacity of the pump achievable Froude numbers were below 4. Characteristics of the incoming flows provided in the model are presented in Table 1.

The experimental apparatus was equipped with a frame structure for mounting and precise positioning of measuring devices and accessories (Fig. 1). The frame structure with rails and a rail carrier was separately mounted on a rigid metal supporting construction to suppress vibrations. Separate mounting of the frame structure to the model base also prevented the transmission of vibrations from the glass channel to the measuring equipment and the occurrence of additional measurement uncertainty.

Table 1. Maximum values of discharge and Froude numbers at different depths of the incoming flows.

Water depth of inflows (mm)	Max. discharge of inflows (m^3/s)	Max. velocities of the inflows (m/s)	Max. Froude number (–)
10	0.035	7.0	22.3
20	0.05	5.0	11.3
30	0.055	3.7	6.8
40	0.06	3.1	4.9
50	0.065	2.6	3.7
60	0.07	2.3	3.0

Measuring equipment and measurements

The main characteristics of standing waves along the junction for which phenomenological equations were developed, were obtained from a 3D mesh model of water surface topographies. Models of water surface topography were constructed from measurements with a laser scanner (Rak et al., 2017) (Fig. 2).

We used LIDAR instrument LMS400 manufactured by SICK AG. The device operates in the visible red light wavelength λ = 650 nm. Its systematic measurement uncertainty is ±4 mm, while the statistical measurement uncertainty is ±3 mm. The beam diameter is 1 mm. For measurements we used configuration with a line scanning frequency 270 Hz and angular resolution 0.2° (totalling 94500 distance measurements per second). For each scenario the water surface topography was measured over 2 m length with 22 cross sections and two centerlines per section (Fig. 3).

For each cross section the water surface profile was determined based on averaging measurements from 6,000 scan lines. Every scan line was composed of 350 measurement points, i.e. a total of 2,100,000 points in the entire point cloud of each cross section were recorded. A detailed description of measurement method, achieved measurement uncertainty and construction of water surface topography is given by Rak et al. (2017 and 2018). For referencing of measurements a local three-dimensional coordinate system was selected as shown in Fig. 3. The origin ($X = 0$, $Y = 0$, $Z = 0$) is located in point A.

Description of experimental scenarios at the T-junction

The independent adjustment of discharge and water depth of the incoming flow allowed for the settings of desired characteristics (flow depth, velocities and Froude number). Scenarios are classified into three groups. In the first group, Froude numbers of the incoming flows were between 2 and 12, while the water depths of incoming flows were set in 5 mm increments from 10 mm to 30 mm. In each individual scenario the water depth of both incoming flows was identical. A total of 101 different scenarios were analysed in this group. In group 2, range of Froude number values was the same ($2 \leq Fr \leq 12$). We varied the incoming flow depth in the tributary channel (10 mm, 20 mm and 30 mm) while the depth in the main channel remained constant at 30 mm. A total of 53 different scenarios were analysed. In group 3, we varied the incoming flow depth in the main channel (10 mm, 20 mm and 30 mm) while depth in the tributary channel remained constant at 30 mm. Froude number of incoming flows of the junction were between 2 and 12. In group 3, a total of 57 different scenarios were analysed.

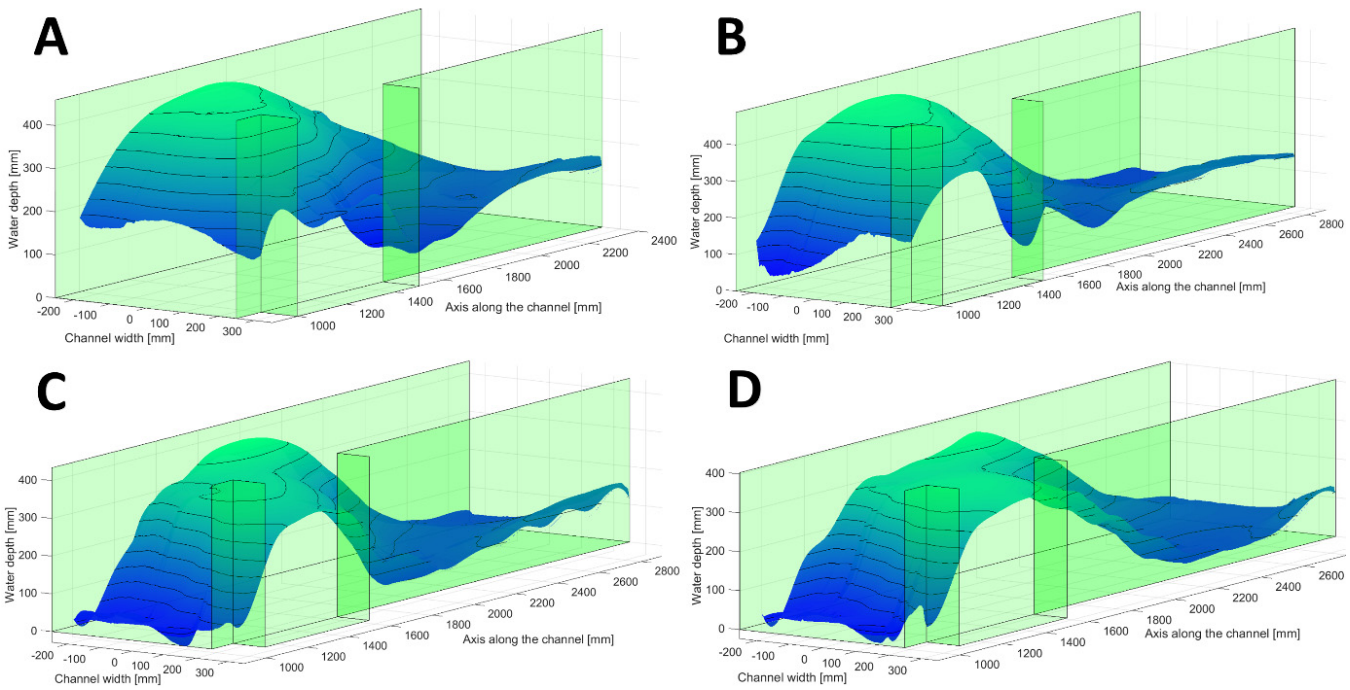

Fig. 2. Constructed water surface topographies along the junction using LIDAR data for 4 scenarios with different flow geometry and hydraulic conditions: A: $h_m = h_t = 25$ mm, $Fr_m = 7.92$ and $Fr_t = 5.79$; B: $h_m = 30$ mm, $h_t = 20$ mm, $Fr_m = 6.76$ and $Fr_t = 7.04$; C: $h_m = 30$ mm, $h_t = 10$ mm, $Fr_m = 5.99$ and $Fr_t = 11.99$; D: $h_m = 30$ mm, $h_t = 10$ mm, $Fr_m = 6.9$ and $Fr_t = 11.05$).

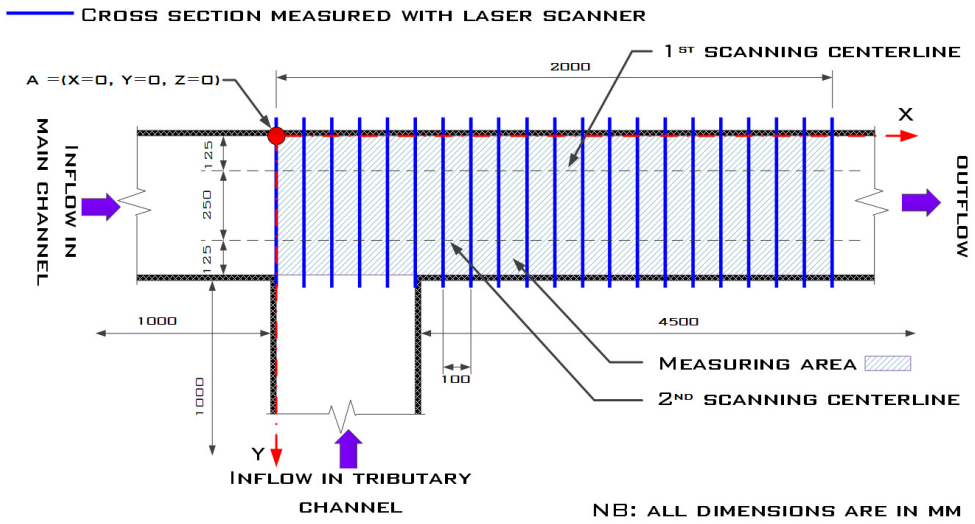

Fig. 3. Junction with lines of the measured cross sections.

For each scenario, we also control the flow conditions with values of Reynolds and Weber number. Reynolds number *Re* gives the ratio of inertial forces to the viscous forces within a fluid and is defined as $Re = \frac{\rho v l}{\mu}$. Values of Reynolds numbers were between 0.4 x 10^4 and 1.1 x 10^5. The Weber number *We* gives the ratio of inertial forces and forces due to surface tension. The Weber numbers were calculated using the following equation: $We = \frac{v^2 \rho l}{\kappa}$. To avoid the effect of forces due to surface tension on the flow the value of Weber number has be greater than 100 (Peakall and Warburton, 1996). In our scenarios values of the Weber number were between 120 and 6.2 x 10^3. The integrated table with input parameters and results for all scenarios can be found in the first author´s doctoral dissertation (publicly available) (Rak, 2017).

Development of equations with regression analysis

To explore the forms of relationship between input data and characteristics of standing waves at the junction on the basis of experimental data, different regression models were considered, with the power-law approach proving to be the most appropriate. Due to the large set of measured scenarios, the system of nonlinear equations was overdetermined. To obtain a system of linear equations, we used a logarithm operation. To solve the system of equations and to determine the coefficients and exponents of power-law formulation, we used the least-squares method. Input parameters (geometric and hydraulic parameters,

i.e. water depth, discharge of inflows, angle of junction) were used as predictors as well as some derived parameters (Fr numbers, reference lengths etc.). In the design of equations we verified the influence of each input and derived parameters on the characteristics of the standing waves. We defined 14 significant characteristics of standing waves (angle of mixing cone, peak heights, location of peaks etc.), for which simple design equations were developed with reasonable values of coefficients and exponents. Only the most influential parameters were included in the formulation, while the final equation was determined according to agreement between the measured values and the values calculated with the newly defined equation. The most appropriate formulation of the phenomenological equations was also verified by correlation analysis.

RESULTS

Although all the scenarios address hydraulic characteristics of the supercritical junction flow, diverse topographies of water surface occur. Four main types of flow patterns were observed at the junction. Among them cases with humped wave at the junction were considered as the most interesting and were selected for further analysis. Finally, a comparison of the present predictions with other researchers' results is provided.

Water flow patterns

The analysis of measurements of water surface topography in all scenarios showed that junction flow patterns do not only depend on Froude number but also on water velocities and water depths in the both approach branches. Therefore, a new quantity of ratio between momentums in main and tributary channels was introduced:

$$M_R = \frac{M_m}{M_m + M_t} \tag{1}$$

where M_m and M_t describe the rate of flow momentums in the main and tributary branches:

$$M_m = v_m^2 \cdot h_m \cdot b_m \cdot \rho_w \tag{2}$$

$$M_t = v_t^2 \cdot h_t \cdot b_t \cdot \rho_w \cdot \tag{3}$$

The channels width is constant ($b_m = b_t$) and there is no multi-phase flow upstream of the junction, so $\rho_w = const$.

On the basis of measurements and on the ratio between momentums of incoming flows the water flow patterns were classified into four main groups:

1) $Fr_m \leq 2$ → For Froude number below 2 the hydraulic jump or dammed flow occurs in both channels already upstream of the junction. Similar results were reported by Schwalt and Hager (1995); Hager (2010). Energy dissipation in the mixing zone of both incoming flows is greater at the T-shaped junction than at junctions of narrower angles.

2) $M_m \leq M_t$; $Fr_{m,t} > 2$ → For momentum in the tributary channel equal to or greater than momentum in the main channel, in both channels (between the outlet from the pressure vessels and the junction) hydraulic jump or submerged outflow from the pressure vessel is present. If submerged outflow is present the flow is dammed to a greater extent and hydraulic jump would occur at a greater distance upstream of the junction than the distance between the inlet and junction was in our experiment. In situations with much greater momentum of the incoming flow in the tributary channel than that in the main channel the hydraulic jump in the tributary channel occurs just before the junction. In junctions with a narrower angle it is possible that the supercritical flow of the tributary channel is preserved throughout the junction, while the flow in the main channel is dammed (Schwalt and Hager, 1995). This is not the case in the T-shaped junction (Fig. 4, left).

3) $M_t \leq M_m \leq 2.5 \cdot M_t$; $Fr_{m,t} > 2$ → The momentums of the incoming flows in both channels are large enough to retain supercritical characteristics within the junction. Along a junction a standing humped wave occurs, while flows from main and tributary channel remain supercritical throughout the junction and also in the downstream channel. The height of the standing humped wave in the area of the junction is much greater than the potential water depth in the junction if hydraulic jump occurs in either of the channels upstream of the junction (Fig. 4, middle).

4) $M_m \geq 2.5 \cdot M_t$; $Fr_m > 2$ → The momentum of the incoming flow in the main channel is much greater than in the tributary channel, therefore choking of the flow occurs in the area of the junction within the main channel but supercritical conditions are preserved throughout the junction as well as further downstream of it. Disturbance of the flow caused by inflow from the tributary channel results in the mixing zone while the tributary flow is dammed (Fig. 4, right).

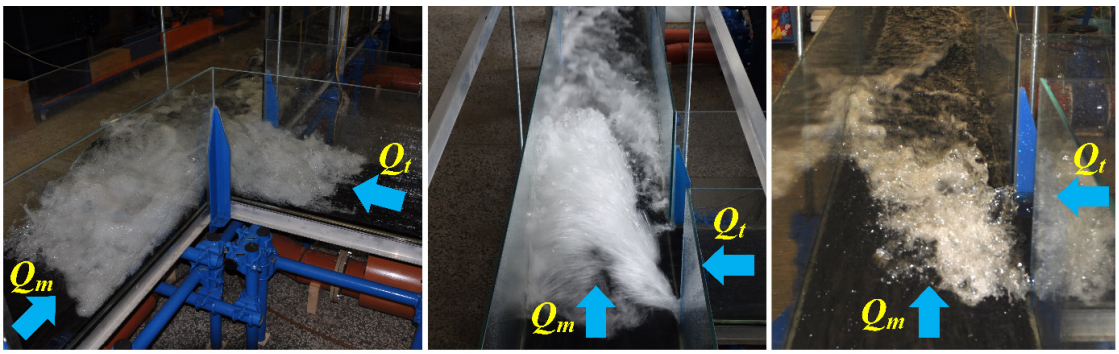

Fig. 4. Flow patterns in a junction: hydraulic jumps in both incoming channels ($h_m = h_t = 25$ mm, $Fr_m = 8$, $Fr_t = 8$) (left); humped wave ($h_m = h_t = 20$ mm, $Fr_m = 8$, $Fr_t = 6$) (middle); choking of the main channel flow, while the side incoming flow is dammed ($h_m = h_t = 20$ mm, $Fr_m = 8$, $Fr_t = 2$) (right).

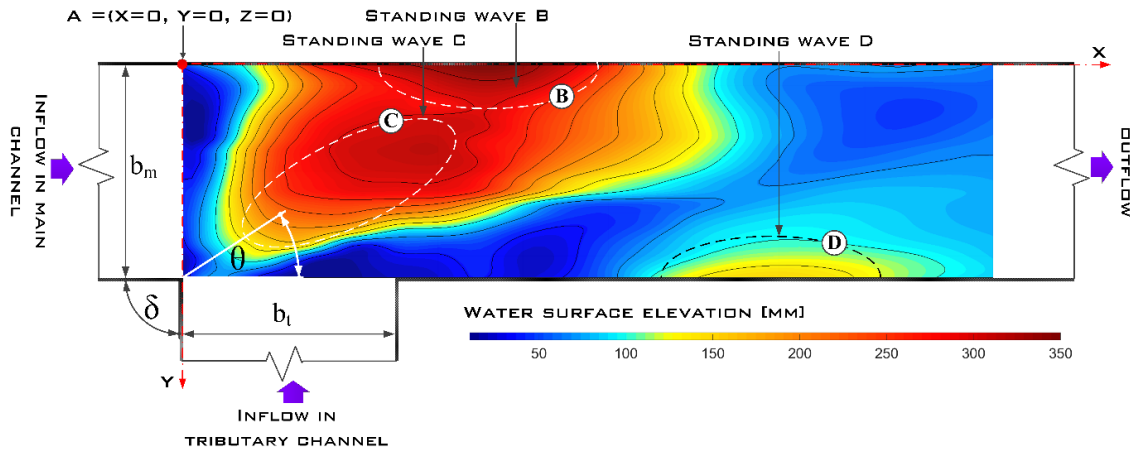

Fig. 5. The main flow patterns of water flow for which parametric relations with input parameters are given.

Topology of water surface of standing waves

Although depths of the incoming flows in both channels upstream of the junction are low, a humped wave is formed over the junction due to high velocities of the incoming flows. The humped wave is characterised by high velocity and complex, non-stationary topography of the water surface. Due to the disturbance and turbulence of the water flow in the mixing zone the air entrainment and the two-phased flow occurs. In the case of humped wave, the water surface was found to be more than ten times higher than the depth of incoming flows to the junction while flow over the junction remains supercritical. The measurements show that intensive vertical dynamics translates to about 80% of energy dissipation of the incoming flows but nonetheless the flow retains in the supercritical regime throughout (downstream of the junction as well). Characteristics of standing waves, which were considered in phenomenological analysis are presented in Fig. 5 with letters C, B and D, following the definition of Schwalt and Hager (1995). Standing wave C is formed along the mixing zone of both incoming flows. Due to the incoming flow from the tributary channel streamlines in the main channel are deflected toward the lateral wall, where wave B occurs. Reflection of wave B leads to wave D along the wall on the opposite side.

The main characteristics of standing waves are defined with longitudinal coordinate (X), transverse coordinate (Y) and height of the wave peaks (Z). The origin of the coordinate system is at the beginning of the junction (longitudinal axis), at the lateral wall of the main channel (transverse axis), and at the bottom of the channel (vertical axis) (Fig. 3 and 5).

The range of validity of equations is set based on our selection of scenarios. Equations are in the valid range when the following conditions are met: $0.6 \tilde{<} \left[M_R = \frac{M_m}{M_m + M_t} \right] \tilde{<} 0.8$; $Fr_m > 6$; $Fr_t > 3$; $b = b_m = b_t$ and $\delta = 90°$

Equations give dimensions and location of standing waves. To set the peak height of the wave crest both equation of mean water surface level and equation of fluctuation of water surface are considered. Notations are specified at the end of this article.

Results of parametric modelling

In the following results of parametric modelling of standing wave properties at the junction are provided.

The angle of mixing zone θ or crest of wave C is set as:

$$\theta = \tan^{-1}\left(\frac{b - y_{MC}}{x_{MC}}\right) \tag{4}$$

where $\tan\theta$ was calculated using parametric analysis:

$$\tan\theta = \left(\frac{b - y_{MC}}{x_{MC}}\right) = 0.9 \cdot \left(\frac{h_t}{h_m}\right)^{1.2} \cdot f^{0.8} \tag{5}$$

Main characteristics of the wave C

- Longitudinal coordinate of the peak of wave C

$$X_{MC} = \frac{x_{MC}}{b} = 1.1 \cdot (\cos\theta)^{(-4.5)} \cdot \left(\frac{h_t}{h_m}\right)^{(-0.6)} \cdot Fr_m^{0.8} \cdot Fr_t^{0.1} \cdot \left(\frac{b}{\overline{h}}\right)^{(-0.85)} \tag{6}$$

- Transverse coordinate of the peak of wave C

$$Y_{MC} = \frac{y_{MC}}{\overline{h}} = b - 2 \cdot (\sin\theta)^{(-1.5)} \cdot \left(\frac{h_t}{h_m}\right)^{3.7} \cdot Fr_m^{(-2.5)} \cdot Fr_t^{3.7} \tag{7}$$

- The peak height of wave C (mean value)

$$Z_{MC} = \frac{h_{MC}}{\overline{h}} = Fr_m \cdot Fr_t^{1.4} \cdot \left(\frac{b}{\overline{h}}\right)^{(-0.6)} \tag{8}$$

- Free-water surface fluctuations at the peak of wave C

$$H'_{MC} = \frac{h'_{MC}}{h} = 0.11 \cdot Fr_m^{1.1} \cdot Fr_t^{0.2} \tag{9}$$

- Actual height of the peak of wave C

$$Z_{MC,act} = Z_{MC} \pm H'_{MC} \tag{10}$$

Main characteristics of wave B (at the wall opposite the inflow of the tributary channel)

- Longitudinal coordinate of the peak of wave B

$$X_{MB} = \frac{x_{MB}}{b} = (\cos\theta)^4 \cdot Fr_m^{0.25} \cdot Fr_t^{0.15} \tag{11}$$

- The peak height of wave B (mean value)

$$Z_{MB} = \frac{h_{MB}}{\overline{h}} = 1.1 \cdot Fr_m^{0.9} \cdot Fr_t^{1.5} \cdot \left(\frac{b}{\overline{h}}\right)^{(-0.6)} - 1 \quad (12)$$

- Free-water surface fluctuations at the peak of wave B

$$H'_{MB} = \frac{h'_{MB}}{\overline{h}} = 0.16 \cdot Fr_m^{0.6} \cdot Fr_t^{0.75} \quad (13)$$

- Actual height at the peak of wave B

$$Z_{MC,act} = Z_{MB} \pm H'_{MB} \quad (14)$$

- Longitudinal coordinate of downstream end of the crest of wave B

$$X_{EB} = \frac{x_{EB}}{\overline{h}} = 0.75 \cdot \left(\frac{h_t}{h_m}\right)^{(-1.3)} \cdot Fr_m^{1.5} \cdot Fr_t^{(-0.9)} \cdot \left(\frac{b}{\overline{h}}\right)^{0.75} + \frac{b}{2\overline{h}} \quad (15)$$

Main characteristics of the wave D (reflection of wave B - along the wall on side of the tributary channel)

- Longitudinal coordinate of the peak of wave D

$$X_{MD} = \frac{x_{MD}}{b} = 1 + 0.45 \cdot \left(\frac{h_t}{h_m}\right)^{(-2.1)} Fr_m^{2.3} \cdot Fr_t^{(-1.2)} \cdot \left(\frac{b}{\overline{h}}\right)^{(-0.5)} \quad (16)$$

- The peak height of wave D (mean value)

$$Z_{MD} = \frac{h_{MD}}{\overline{h}} = 2.3 \cdot Fr_m^{0.7} \cdot Fr_t^{0.8} \cdot \left(\frac{b}{\overline{h}}\right)^{(-0.55)} . \quad (17)$$

- Free-water surface fluctuations at the peak of wave D

$$H'_{MD} = \frac{h'_{MD}}{\overline{h}} = 0.1 \cdot Fr_m^{\frac{2}{3}} \cdot Fr_t^{\frac{2}{3}} \quad (18)$$

- Actual height at the peak of wave D

$$Z_{MD,act} = Z_{MD} \pm H'_{MD} \quad (19)$$

Correlation between measured values in the model and calculated values with the newly proposed phenomenological equations is high despite nonstationariness and complexity of the phenomenon. Correlation factor is mainly $R^2 \geq 0.9$. Values of the correlation factors R^2 for each equation are given in Table 2. There is deviation in certain points but they still fall within ±10% confidence interval. A lower correlation coefficient ($R^2 \sim 0.6$–0.7) is achieved for fluctuating.

According to previous research, a modelling of high-speed two-phase flow without the scale effect would be possible, when Froude number, Weber number and Reynolds number are identical in the laboratory model and the larger model or prototype. Physically, it is only possible when a full-scale model is used (Murzyn and Chanson, 2008; Pfister and Chanson, 2014). Therefore, our results could not be simply extrapolated to a larger scale, based upon a Froude similarity. To do this, it would be appropriate to extend our research with the set of additional experimental set-ups to enable scale-up investigations. To minimise the scale effect some condition has to considered (e.g. Reynold number, Weber number or Morton number).

Table 2. Values of the correlation factors for all equations.

Characteristics of standing waves	R^2
Angle of mixing zone	0.97
Longitudinal coordinate of the peak of wave C	0.93
Transverse coordinate of the peak of of wave C	0.95
The peak height of wave C	0.96
Free-water surface fluctuations at the peak of wave C	0.66
Longitudinal coordinate of the peak of wave B	0.94
The peak height of wave B	0.89
Free-water surface fluctuations at the peak of wave B	0.80
Longitudinal coordinate of downstream end of the crest of wave B	0.84
Longitudinal coordinate of the peak of wave D	0.93
The peak height of wave D	0.93
Free-water surface fluctuations at the peak of wave D	0.62

Comparison with Schwalt-Hager results

The results of the present experiments were compared with the findings of Schwalt and Hager (1995), who experimentally set equations for the characteristics of standing waves in junctions in a similar way as in our work. Their research included experiments with junction angles up to 60°, so they limited the range of validity of their equations with angles of junction up to 70°. Since it is the only experiment comparable to ours, we did a side by side comparison of characteristics of standing waves that were included in both experiments despite the disagreement in valid junction angles. On the other hand, Hager (2010) stated that at the right-angled junction the backwater effect always occurs in both inflow channels. Our experiments prove otherwise—humped wave (a water surface pattern that was formed in the Schwalt-Hager experiment) also forms with a right-angled junction at certain conditions.

Some equations of Schwalt-Hager (1995) contain cos δ as a denominator, so their results were not directly comparable since in our case cos $\delta = 0$ for $\delta = 90°$. These are, for example, longitudinal coordinate of the peak height of wave C and distance of wave end from the junction for wave B. According to our experiments, the characteristics of standing waves depend on the angle of the mixing zone or wave C (the latter being dependent on the momentum of both main and tributary channel flows). Fig. 6 shows that the Schwalt-Hager (1995) equations underestimate the angle of the mixing zone in comparison with our results. Similarly, the equations of Schwalt and Hager (1995) also underestimate other topographic characteristics of standing waves at the junction with the exception of equations for longitudinal coordinates of standing wave peaks, which overestimate the values. This disagreement is to be expected – in junctions with narrower angle momentum is directed along the channel downstream of the junction. Therefore, standing waves were also formed further in the downstream direction. Contrary, vertical dynamics and the height of standing waves, as well as the dissipation of energy (due to transverse dynamic of water mass) are much bigger in the junction with a 90° angle. These properties also lead to concentration of the phenomena in the area of the junction.

Due to the use of classical measuring instruments the Schwalt-Hager research did not analyse water surface fluctuations of standing waves. Although other authors (Chachereau and Chanson, 2010; Murzyn and Chanson, 2009) did set fluctuations of water surface at the hydraulic jump in the channel, direct comparison with fluctuations in our experiment is not possible due to the significantly different dynamics of the water surface at the junction. However, both research studies show that fluctuations of the water surface of turbulent flow depend on the hydraulic characteristics of the incoming flow(s).

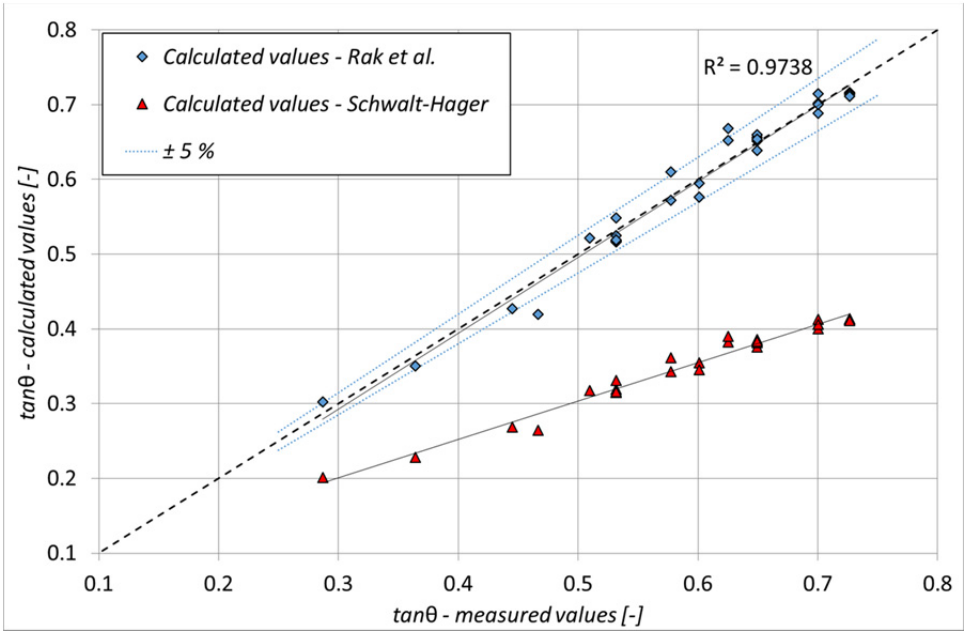

Fig. 6. Comparison between the values calculated with new equations determined in our study and Schwalt-Hager equations, and measurements in the experiment of the T-junction.

CONCLUSION

The topology of the water surface at a right-angled junction subjected to supercritical incoming flows is described. In an extensive experimental research study with non-intrusive measurement method, the topographies of the water surface at the junction were systematically measured. On the basis of analysis of the flow characteristics in the area of the junction the water flow patterns were classified by the parameters of the incoming flows, followed by a detailed analysis of characteristics of humped-shaped standing waves forming at the junction. Based on the measured water surface topography of the individual scenario where the humped wave occurred, the main characteristics of standing waves were determined. Dimensions of standing waves and their locations were used in a topological analysis and for development of dimensionless phenomenological equations providing the relations between input geometrical and hydraulic parameters, and the characteristics of the distinct standing wave patterns in the junction area. Despite the strongly developed turbulent two-phase flow with high water surface dynamics in the junction area, the correlation analysis revealed a very good fit across the entire range of the measured values in many scenarios. Knowing the characteristics of the phenomenon where supercritical flow is preserved across the junction, while high wave peaks occur along the junction that highly exceed incoming flow depths as well as knowing the relations between input parameters and wave characteristics brings important new knowledge in water engineering.

REFERENCES

Behlke, C.E., Pritchett, H.D., 1966. The design of supercritical channel junction. Highway Research Record, 133, 17–35.

Best, J., Reid, I., 1984. Separation zone at open channel junction. J. Hydraul. Eng., 110, 11, 1588–1594.

Bowers, C.E., 1950. Studies of open channel junctions. Project Report 24. Part V. Hydraulic model studies for Whiting Field Naval Air Station. University of Minnesota, St. Anthony Falls Hydraulic Laboratory, Minneapolis.

Chachereau, Y., Chanson, H., 2010. Free-surface fluctuations and turbulence in hydraulic jumps. Exp. Therm. Fluid Sci., 35, 6, 896–909.

Christodoulou, G.C., 1993. Incipient hydraulic jump at channel junction. J. Hydraul. Eng., 119, 3, 409–423.

Greated, C.A., 1968. Supercritical flow through junctions. La Houille Blanche, 23, 3, 693–695.

Hager, W.H., 1989a. Supercritical Flow in Channel Junctions. J. Hydraul. Eng., 115, 5, 595–616.

Hager, W.H., 1989b. Transitional Flow in Channel Junctions. J. Hydraul. Eng., 115, 2, 243–259.

Hager, W.H., 2010. Wastewater Hydraulics: Theory and Practice. 2nd Edition. Springer Verlag, Heidelberg, Berlin.

Mignot, E., Riviere, N., Perkins, R., Paquier, A., 2008. Flow patterns in a four-branch junction with supercritical flow. J. Hydraul. Eng., 134, 6, 701–713.

Murzyn, F., Chanson, H., 2008. Experimental assessment of scale effects affecting two-phase flow properties in hydraulic jumps. Exp. Fluids., 45, 3, 513–521.

Murzyn, F., Chanson, H., 2009. Free-surface fluctuations in hydraulic jumps: Experimental observations. Exp. Therm. Fluid Sci., 33, 7, 1055–1064.

Peakall, J., Warburton, J., 1996. Surface tension in small hydraulic river models – the significance of the Weber number. J. Hydrol., 35, 2, 199–212.

Pfister, M., Chanson, H., 2014. Two-phase air-water flows: Scale effects in physical modelling. J. Hydrodyn. Ser. B, 26, 2, 291–298.

Pfister, M., Gisonni, C., 2014. Head losses in junction manholes for free surface flows in circular conduits. J. Hydraul. Eng., 140, 9, 1–6.

Pinto Coelho, M.M., 2015. Experimental determination of free surface levels at open-channel junction. J. Hydraul. Res., 53, 3, 394–399.

Rak, G., 2017. Topološka struktura vodne gladine na sotočju pri deročem toku (Water surface topology of supercritical confluence flow). Doctoral dissertation, University of Ljubljana, Faculty of Civil and Geodetic Engineering, 112 p. (in Slovene, with English captions and extended summary).

https://repozitorij.uni-lj.si/ IzpisGradiva.php?id= 99202 &lang=eng
Rak, G., Steinman, F., Hočevar, M., 2017. Measuring water surface topography using laser scanning. Flow Meas. Instrum., 56, 35–44.
Rak, G., Hočevar, M., Steinman, F., 2018. Construction of water surface topography using LIDAR data. Stroj. Vestn.-J. Mech. E., 64, 1–11.
Saldarriaga, J., Rincon, G., Moscote, G., Trujillo, M., 2017. Symmetric junction manholes under supercritical flow conditions. J. Hydraul. Res., 53, 3, 135–142.
Schwalt, M., Hager, W.H., 1995. Experiments to supercritical junction flow. Exp. Fluids, 18, 429–437.

Received 1 February 2018
Accepted 7 March 2018

NOMENCLATURE
Subscripts:

C = standing wave in the mixing zone (humped wave)
B = standing wave at the wall opposite tributary inflow
D = standing wave at the side of tributary inflow (reflection of wave B)
m = main channel
t = tributary (side) channel
M = maximum value (wave height)
E = downstream end of standing wave

Symbols:

X = axis along the main channel
Y = axis perpendicular to the main channel (aligned with tributary channel)
Z = vertical axis
A ($X = 0$, $Y = 0$, $Z = 0$) = origin of coordinate system (start of junction, left edge of the main channel (opposite the tributary channel), bottom of the channel)
M_R = quantity of ratio between momentums in main and tributary channels (–)
M_m = momentum of the inflow in the main channel
M_t = momentum of the inflow in the tributary channel
δ = angle of junction (in our experiment $\delta = 90°$)
θ = angle of mixing zone (such as line of crest at the contact of two supercritical flows)
h_m = water depth of inflow in the main channel (m)
h_t = water depth of inflow in the tributary channel (m)
v = velocity of water flow (m/s)
v_m = velocity of inflow in the main channel (m/s)
v_t = velocity of inflow in the tributary channel (m/s)
H' = dimensionless form of free surface fluctuation height (–)
h' = fluctuation height (m)
$b = b_m = b_t$ = width of all channels (constant in our experiment) (m)
$\bar{b} = (b_m \cdot b_t)^{0.5}$ = ratio of width of both channels (m)
l = characteristic length (m)
ρ = water density ($kg \cdot m^{-3}$)
μ = dynamic viscosity ($kg \cdot m^{-1} \cdot s^{-1}$)
g = gravitational acceleration (m/s^2)
κ = surface tension ($N \cdot m^{-2}$)

Derivatives:

$\bar{h} = (h_m \cdot h_t)^{0.5}$ = characteristic water depth at the junction, calculated by characteristics of both inflows (m)

$Fr_m = \frac{v_m}{\sqrt{(g \cdot h_m)}}$ = Froude number of inflow in the main channel (–)

$Fr_t = \frac{v_t}{\sqrt{(g \cdot h_t)}}$ = Froude number of inflow in the tributary channel (–)

$f = \frac{Fr_m \cdot Fr_t}{(Fr_m + Fr_t)}$ = ratio of Froude numbers of both inflows (–)

J. Hydrol. Hydromech., 67, 2019, 2, 171–178
DOI: 10.2478/johh-2019-0002

Formation and movement of ice accumulation waves under ice cover – an experimental study

Jun Wang[1], Yifan Wu[1], Jueyi Sui[2*], Bryan Karney[3]

[1] College of Civil Engineering, Hefei University of Technology, Hefei, China.
[2] Environmental Engineering Program, University of Northern British Columbia, Prince George, Canada.
[3] Department of Civil Engineering, University of Toronto, Toronto, Canada.
[*] Corresponding author. E-mail: jueyi.sui@unbc.ca

Abstract: Ice jams in rivers often arise from the movement of frazil ice as cover-load under ice cover, a process which is conceptually similar to the movement of sediment as bed-load along a river bed. The formation and movement of an ice-accumulation wave is one facet of a larger class of cover-load movements. The movement of an ice-accumulation wave obviously plays a crucial role in the overall process of ice accumulation. In the present study, experiments under different flow and ice conditions help reveal the mechanics of formation and evolution of ice-accumulation waves. In particular, suitable criteria for formation of an ice-accumulation wave are investigated along with the resulting speed of wave propagation. The transport capacity of frazil ice under waved accumulation is modeled by comparing those of experiments collected in laboratories, and the resulting equation is shown to be in good agreement with measured experimental results.

Keywords: Cover-load; Experimental results; Frazil ice; Ice-accumulation wave; Ice jam; Ice transport capacity; Moving speed.

INTRODUCTION

Both ice covers and ice jams occur frequently in northern rivers in the winter. The formation of an ice cover can cause serious water level fluctuations due to channel blockage and the increase in resistance associated with flow under the ice cover. If there is sufficient supply of ice, its accumulation under an ice cover can initiate formation of an ice jam with an associated increase in water level. As a consequence, ice-induced flooding may occur and hydraulic structures, such as pump stations and bridge piers/abutments, may be damaged or destroyed (Beltaos, 2012; Sui et al., 2002).

During the formation of a frazil ice jam, the rate of arrival of the incoming frazil ice clearly plays a fundamental role in determining both the thickness of the ice jam and the associated likelihood of flooding (Sui et al., 2005). Thus, for ice jams in natural rivers, estimation of the ice transport capacity is a crucial step in the assessment of risk (Gao et al., 2003). Overall, ice transport capacity plays a key role in determining the variation in water level under ice jammed condition (Sui et al., 2005; Wang et al., 2007a).

Many researchers have explored the mechanics of ice jam evolution using field measurements, laboratory experiments or both (Beltaos and Burrell, 2010; Sui et al., 2008). For example, using long-term field measurements, Beltaos studied ice jam thicknesses and water level variations during river breakup on the Matapedia River in Canada (Beltaos and Burrell, 2010). To measure flow and floating ice velocities, as well as ice cover thicknesses, Morse et al. used ADCP and IPS to assess field conditions in the St Lawrence River (Morse et al., 2011). Additionally, they recorded wind speed and air temperature, variables which also affect the ice process. Based on field measurements in the Hequ Reach of the Yellow River, Sui et al. investigated the evolution of frazil ice jams and the associated variation in water level (Sui et al., 1994, 2005). They not only described the variation of ice jam thickness, but developed a formula for estimating both ice jam thickness and water level. To better understand ice accumulation, Wang et al. experimented with S-shaped and U-shaped flumes (Wang et al., 2007b, 2011) and were able to determine the critical Froude number for the initiation of jammed conditions in curved channels.

Numerical simulations of ice accumulation and the associated variation in water level have been undertaken by some researchers. Beltaos used RIVJAM model to simulate changes in water level caused by ice jams in a wide channel (Beltaos, 1993). Zufelt and Ettema simulated the variation in water level during both the formation of an ice jam and it subsequent breakup (Zufelt and Ettema, 2000). Zufelt and Ettema used an one-dimensional ice-water coupling equation to describe the dynamics of an ice jam. By means of either a one-dimensional or a two-dimensional model, Shen (2010) and Wang et al. (2011, 2013) simulated the formation of an ice jam and both ice accumulation and transport under jammed conditions. All of the previous simulation work forms the foundation of the present study.

Various methodologies exist for estimating the ice discharge during ice flowing periods. Frazil jam and surface ice jam are totally difference phenomena with different transport mechanisms. Since there are rarely research work regarding under-cover transport and accumulation of frazil ice, we still included some important research results regarding surface ice jam in this paper. For example, Beltaos (1995) proposed following formula for the surface ice discharge during ice flowing period in early winter:

$$Q_i = N_i B_i V_S D_i (1 - p) \tag{1}$$

where Q_i is the surface ice discharge; N_i is the surface concentration of the ice in flowing water; B_i is the width of the water surface; V_S is the surface water velocity; D_i is the thickness of flowing ice blocks; and p is the porosity of the ice jam. In addition, Nuttal (1973), Calkins and Ashton (1976) and Ackerman and Shen (1983) have also studied the surface ice discharge. On the basis of research work of Ackerman and

Shen (1983), Urroz-Aguirre (1988) also develop the following formula for estimating the surface ice discharge during the ice flowing period:

$$\frac{Q_i}{Q} = 2.4\left(\frac{1}{\theta}\right)^{0.682}\left(\frac{Di}{L}\right)^{1.181}\left(\frac{L}{B}\right)^{0.845}\left(\frac{gB^5S_0}{Q^2}\right)^{0.317Q^{0.135}} \quad (2)$$

where, Q_i and Q is the ice discharge and flow discharge, respectively; θ is the side slope of the channel bank; L is the equivalent diameter of ice block; B is the bottom width of the channel; g is the gravitational acceleration; and S_0 is the longitudinal slope of the channel bed. Based on laboratory experiments, Wang (2002) proposed a formula to determine ice discharge. Shen and Wang (1995) obtained the transport capacity formula of frazil granules. By comparing ice transport under ice cover (cover bed load) to sediment transport on river bed (bed load), Wang et al. (1993) claimed that both formulas proposed by Bagnold (1956) and Luque and Beek (1976) could be used to calculate ice transport capacity during the period when the ice jam is quasi-equilibrium. By using a small-scale, curved flume of rectangular cross section, Urroz and Ettema (1994) carried out experiments to study the initiation mechanisms of ice jam and the factor affecting to the maximum conveyance of ice under the curved channel. Urroz and Ettema (1994) identified two principal ice-jam initiation mechanisms, namely, lodgement and gorging. They claimed that channel roughness was found to have a significant effect in helping the arching mechanism that produces lodging.

Yet due partly to the high risk of conducting field measurements, and partly due to the complexity of the physical processes, ice accumulation in rivers is perhaps one of least understood subjects in river hydraulics. The majority of past work has focused on the ice accumulation that first produces an ice jam and the resulting variations in water level. Relatively little work has considered the formation and evolution of the ice-accumulation wave, with the few existing studies being quite basic. Based on experiments carried out in laboratory, Ettema and Huang (1988) determined the equilibrium thicknesses and forms of ice rubble accumulations beneath barges moving through ice-covered channels. They pointed out that significant amounts of ice may accumulate beneath a barge moving at creeping speed through a navigation channel covered by a sheet of ice, and that accumulation thickness decreases with increasing barge speed. However, in present study, the forces acting on ice particles are studied in order to obtain relations for the development of the ice-accumulation wave and the influence of the transport capacity, then, using experimental results, attempts to better understand the mechanics of an ice-accumulation wave.

ICE-ACCUMULATION WAVE

Experimental setup

The experimental study has been conducted in the flume at Hefei University of Technology. As shown in Figure 1, the flume has a dimension of 34.38 m long, 0.6 m deep and 0.4 m wide. There are 22 observation cross sections along the flume with an equal distance of 1.2 m. The ice-hoper for adding model ice into the flume was placed at cross section 4. The model frazil ice used in this experimental study is made by polypropylene with the mass density of 0.918 g/cm^3, which is nearly the same as the mass density of natural ice of 0.917 g/cm^3. The model frazil ice particles used in this experimental study are uniform. They have a shape of oblate spheroid with a diameter of 0.35 cm, and maximum thickness of 0.20 cm. Flow depths are 10 cm, 15 cm, 20 cm, and 25 cm, respectively. The average approaching flow velocity are: 0.16 m/s, 0.17 m/s, 0.18 m/s, 0.19 m/s, 0.20 m/s, and 0.21 m/s, respectively. The incoming ice discharge varies from 0.01 Liter/s to 0.04 Liter/s.

Formation of ice-accumulation wave

The incoming ice floes from upstream are entrained and submerged under an ice cover if the water velocity is sufficiently high. Frail jam starts to form when the velocity is low enough so that frazil will float to the underside of the cover. This process marks the initiation of a river ice jam. The transport of frazil ice under the ice cover will clearly be significantly affected by flow velocity and grain size of the frazil ice particles. Field measurements and experiments show that the mechanics of movement of frazil ice particles under an ice cover is conceptually similar to the movement of sediment along a riverbed. Similar to bed load and suspended load of sediment in water, there are also suspended ice particles and "bed load" (defined as "cover load") ice particles in the water. Under specific flow and incoming ice conditions, similar to a sand-wave on a river bed, the cover load may develop waves. Such an "ice-accumulation wave" is an important type of ice movement under an ice cover. Yet the movement of "ice-accumulation wave" under an ice cover tends to be even more complicated than a sand wave due to its larger grain size and the continuing inflow of ice from the upstream.

As shown in Figure 2, along the flow direction, "A", "B" and "C" represents the "wave starting point", "wave crest", and "wave trough" of an ice-accumulation wave, respectively. Observations show that movement can be separated into three stages.

a) First, after initial formation of an ice cover, due to the drag force and shear force resulted from flowing current, the incoming frazil ice particles start to accumulate under the ice cover if the flow velocity is sufficiently high. The flow structure around the ice-accumulation wave gradually evolves. As shown in Figure 2, the A-B section of ice-accumulation wave is the stoss side of the ice-accumulation wave, and B-C section is the lee side of the ice-accumulation wave. Streamlines along the stoss side have the similar shape to ice accumulation surface of A-B section. However, streamlines along the lee side have a vortex shape due to associated turbulent effects.

b) Due to the continuous incoming frazil ice from upstream, the thickness at the wave crest of ice-accumulation wave increases. The flow structure results in high pressure on

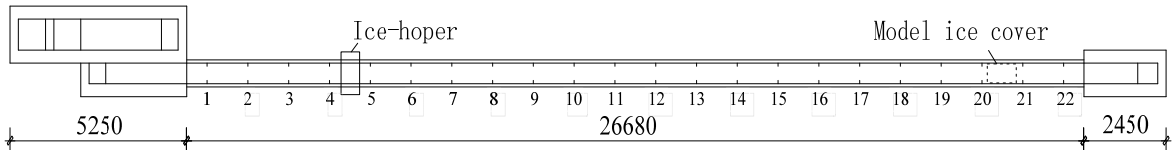

Fig. 1. The setup of experimental flume in the laboratory.

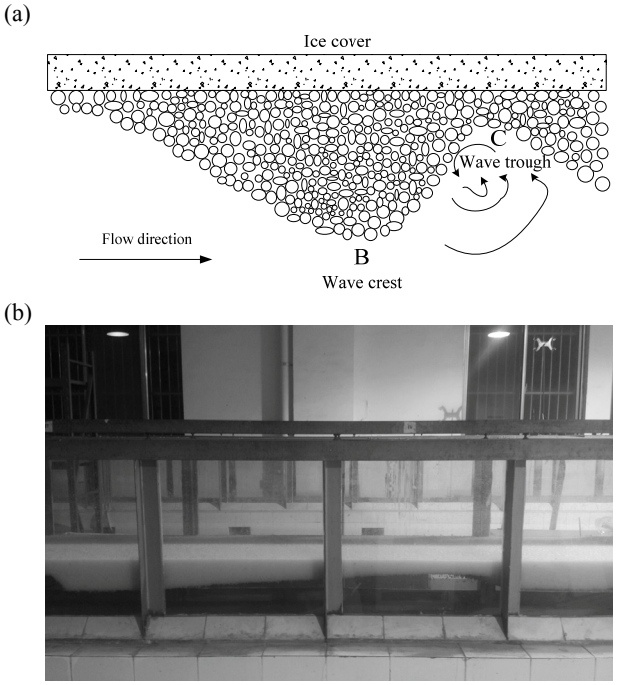

Fig. 2. The movement of "ice-accumulation wave". (a) Conceptual waved accumulation of frazil ice jam. (b) Waved accumulation of frazil ice jam in laboratory.

the stoss side of the ice-accumulation wave and low pressure on the steep lee side. This pressure difference produces the form drag force on the ice-accumulation wave. The drag force caused by the ice-accumulation wave and the continuous incoming frazil ice cause the ice-accumulation wave to propagate downstream. The wave height of ice-accumulation wave (vertical distance from wave trough to wave crest) gradually increases. Progressively more frazil ice particles on the stoss side A-B of ice-accumulation wave begin to move. The transport speed of frazil ice particles gradually increases. More and more frazil ice particles accumulate in the vicinity of wave crest. As a consequence, the stoss side A-B of ice-accumulation lengthens relative to the lee side.

c) With the gradual accumulation of ice, the flow intensity under ice jam increases with the turbulence intensity greatest at the wave crest. As a consequence, the transport speed of frazil ice particles there is the greatest. After passing the wave crest point (B), ice particles enter the lee side B-C. The lee side experiences vortex flow, and thus the flow intensity on the lee side decreases significantly. Thus, there is insufficient energy on the lee side to further transport the ice particles and ice accumulates there. Thus, both the wave crest and lee side move downstream and the ice-accumulation wave naturally propagate from upstream to downstream.

As does the movement of a sand wave on a riverbed, the formation and development of ice-accumulation wave is closely related to the flow intensity. Under open channel conditions, the interaction between flowing water and riverbed results in the formation of sand waves on the riverbed. The sand wave is but one type of riverbed surface forms. The instability of the viscous sublayer on the riverbed forms and develops the sand wave. Some researchers point out that the formation of sand waves also has a close relationship to the surface water waves (Shen and Wang, 1995). They developed a set of dimensionless variables to account for these effects.

There are also some important differences between the movement of "cover-load" and bed load. For bed load, the gravity force acting on sediment particle is larger than the buoyancy force since sand has a larger mass density than that of water. However, for the cover-load, though the buoyancy force generates a net upward force, its relative intensity is much less than that experienced by the sediment (that is, the sediment density different from water much more than the ice does). Additionally, the shear stress acting on these two different kinds of solid particles in water is also different. Thus, the incipient velocity for frazil ice particle to start to move should be less than that for sediment particle with the same grain size. Clearly, less energy is needed to transport ice particle downstream. Therefore, as observed in experiments, the wavelength of ice-accumulation wave is much greater than that typical of sand dunes in water. In our experiments, the measured wavelength of ice-accumulation waves ranges from 0.9 m to 1.2 m. Additionally, the wave height of ice-accumulation wave changes with the flow intensity.

It should be noticed that the wave length is affected by many variables, such as ice particle size, flow intensity, energy slope, etc. However, in this experimental study, only one size of frazil ice particles is used. Further research work regarding wave length affected by other factors should be continued.

As observed in experiments, after moving some distance, the suspended frazil ice particles in water gradually accumulate under ice cover, and then are transported downstream as cover-load. During the development of frazil ice jam, ice jam thickness also increases. The cross-sectional area for the flow under an ice jam decreases, and the flow velocity (and intensity) increases. Once the flow intensity reaches to a threshold level, the accumulated frazil ice particles start to form an ice-accumulation wave. With further increase in flow intensity, both the wavelength and wave height of ice-accumulation wave increase and the movement of the ice-accumulation wave becomes obvious.

However, similar again to the case of sand waves, the ice-accumulation wave cannot be maintained if the flow intensity is too great. Under a high enough flow intensity, the frazil ice particles will not accumulate but will be transported downstream as wash-load. The flow intensity is thus crucial for the development of an ice-accumulation wave as is the rate of incoming frazil. Experiments show that, if the incoming ice discharge is too low, an ice-accumulation wave is unlikely to form. However, if the incoming ice discharge suddenly increases, a single ice-accumulation wave will likely develop. During the development and disappearance of an ice-accumulation wave, flow intensity also changes. In the present study, the flow Froude number was used to describe the threshold flow intensity relevant for an ice-accumulation wave. Depending on the particle size, there exists the minimum flow intensity (or Froude number) for developing the ice-accumulation wave. The minimum flow Froude number is defined as the lower critical Froude number for the development of ice-accumulation wave. There is also the upper critical Froude number that allows for development of ice-accumulation wave.

Based on laboratory experiments, the relationship between water depth (H/B, where H is water depth and B is the channel width) and critical Froude number (Fr) for development of ice-accumulation wave has been plotted in Figure 3. Figure 3 makes quite evident the upper Froude number for developing ice-accumulation wave. However, the lower critical Froude number for developing ice-accumulation wave is not as clearly evident. This may be caused by the continuous variation in flow intensity during the development of ice-accumulation wave. Even if the initial flow intensity (or Froude number) is too low for an ice-accumulation wave to develop, with the continuous

accumulation of frazil ice under ice cover, the flow intensity (Froude number) gradually increases. When flow intensity reaches the threshold value, the ice-accumulation wave will form. If the flow intensity is more than the upper critical Froude number, namely, the flowing water has so much energy that frazil ice particles are unable to accumulate under ice cover, they will be delivered downstream. One can also see from Figure 3, under the condition of the same discharge, when water depth (H/B) is small, it is more difficult to develop ice-accumulation wave since the flow intensity is strong.

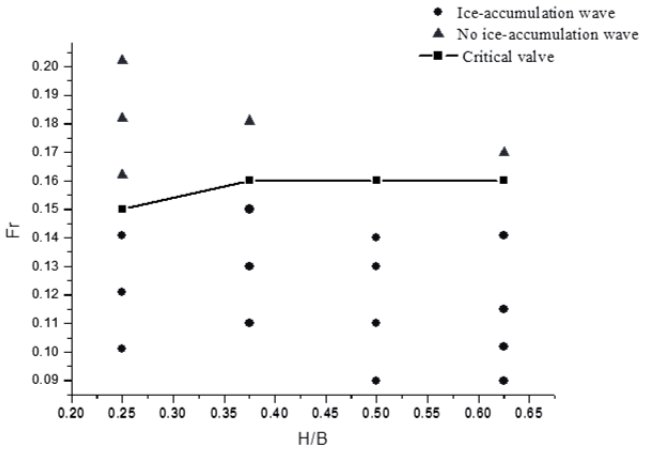

Fig. 3. Relationship between water depth (H/B) and critical Froude number (Fr) for development of ice-accumulation wave.

Figure 4 shows the relationship between the wave height (H_S/B, where H_S is the wave height) and flow Froude number for the same water depth (H = 0.15 m). One can see from Figure 4, the more the flow Froude number, and the larger the wave height.

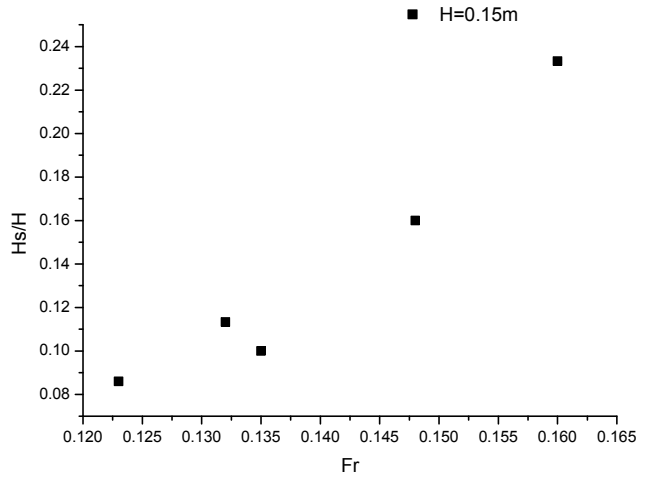

Fig. 4. Dependence of wave height (H_S/B) on flow Froude number (Fr) for the same flow depth of H = 0.15 m.

As for a sand wave, the development of an ice-accumulation wave likely results from an instability of viscous sublayer close to the ice cover boundary. At the beginning of the development of ice jam, the non-uniform distribution of ice jam thickness leads to the difference in flow velocity profiles at different locations, and therefore the formation of ice-accumulation wave. The development of ice-accumulation wave is not only controlled by flow intensity, but also affected by the imbalanced shear forces acting on frazil ice particles, as well as the turbulence energy of flow. Due to rapid changes in the elevation of bottom surface of ice accumulation, the flow intensity also quickly changes. This relation tends to facilitate development of an ice-accumulation wave.

Characteristics of ice-accumulation wave

During the development of ice-accumulation wave, flow current acts on the bottom of ice-accumulation wave. Depending on the kinetic energy of flowing water, the moving speed of ice particle is different, and thus the changes in ice accumulation. On the other side, different moving speed and amount of the cover-load will also affect the structure of flowing current. As a consequence, the kinetic energy of flow current will change. This interaction between moving ice particles and flowing current exists during the entire movement of ice-accumulation wave.

In present study, we chose the first ice-accumulation wave from the upstream as the main focus, and pressure forces acting on flowing water body under ice-accumulation wave are given in Figure 5.

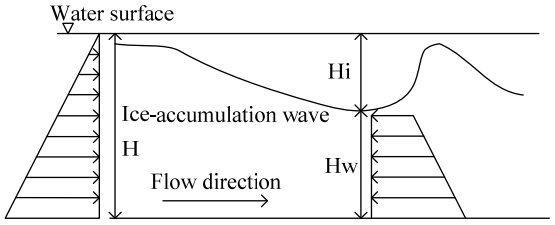

Fig. 5. Pressure forces acting on flowing water under ice-accumulation wave.

The continuity equation can be written as

$$HV = H_w V_W \tag{3}$$

where H is water depth at the frontal edge of ice-accumulation wave (or total water depth); V is the average flow velocity at the frontal edge of ice-accumulation wave; H_W is water depth under the wave crest of ice-accumulation wave; V_W is the average flow velocity under the wave crest of ice-accumulation wave. The momentum equation along the flow direction for control volume of water under ice-accumulation wave can be written as

$$\sum F = \rho Q\left(V_W - V\right) \tag{4}$$

where ΣF is total force in flow direction; ρ is mass density of water; Q is the discharge.

The key forces acting on ice-accumulation wave include the difference of pressure force (F_P) between the pressure force at upstream cross section (at the frontal edge of ice cover) and the pressure force at downstream cross section (at wave crest of ice-accumulation wave) and the form drag force (F_1) acting on the ice-accumulation wave. The mass force along the flow direction can be ignored since the channel bed is horizontal and the water surface slope is tiny. These forces can be further described as following,

$$F_P = \frac{1}{2}\rho g B H_i^2 \tag{5}$$

$$F_1 = \frac{1}{2} C_0 H_i \rho B V^2 \tag{6}$$

Combining Equations (3), (4), (5), and (6), results in

$$\rho H B V \left(\frac{HV}{H - H_i} - V \right) = \frac{1}{2} \rho g B H_i^2 - \frac{1}{2} C_0 H_i \rho B V^2 \tag{7}$$

where C_0 is the drag coefficient; H_i is the wave height of ice-accumulation wave. Thus, we finally obtain the following relations:

$$H_i = \frac{H}{2} + \frac{C_0 V^2}{2g} - \frac{\left[\left(gH + C_0 V^2 \right)^2 - 4gH \left(2 + C_0 \right) V^2 \right]^{\frac{1}{2}}}{2g} \tag{8}$$

$$\frac{H_i}{H} = \frac{1}{2} \left\{ 1 + C_0 \left(\frac{V}{\sqrt{gH}} \right)^2 - \left[\left(1 + C_0 \left(\frac{V}{\sqrt{gH}} \right)^2 \right)^2 - \left(8 + 4C_0 \right) \left(\frac{V}{\sqrt{gH}} \right)^2 \right]^{\frac{1}{2}} \right\} \tag{9}$$

From Equation (9), one can see that the wave height of ice-accumulation wave (H_i) depends on the flow Froude number (Fr) which is used to describe the flow intensity. The larger the flow Froude number (Fr) is, the larger the wave height (H_i). However, as the flow Froude number (Fr) increases to certain level, the wave height (H_i) decreases. The form drag force coefficient of ice-accumulation wave (C_0) depends on the incoming ice discharge (Q_i), grain size of ice particle (d_i) and roughness coefficient of bottom surface of ice-accumulation wave (n). The form drag force coefficient of ice-accumulation wave (C_0) can be expressed following,

$$C_0 = F\left(Q_i, d_i, n \right) \tag{10}$$

Experiments indicate that the incoming ice discharge (Q_i) is the most important factor affecting the form drag force coefficient of ice-accumulation wave (C_0). This coefficient (C_0) ranges from 5.5 to 12.5, it increases with the increase in the discharge of the incoming ice (Q_i).

The mechanics of ice-accumulation wave helps to better understand ice accumulation process under ice cover. The moving speed of ice-accumulation wave (V_i) is obviously a key variable for describing the development process of ice-accumulation wave. The moving speed of ice-accumulation wave is the key factor controlling ice transport. Additionally, the moving speed of ice-accumulation wave will affect the turbulence intensity of the flow under the ice jam. As deduced from experiments, the transport speed of the ice-accumulation wave mainly depends on the flow Froude number, as shown in Figure 6.

As shown in Figure 6, with a flow depth of H = 0.15 m, the moving speed of ice-accumulation wave has a strong relationship with flow Froude number. Thus, if the flow depth is the same, the propagation speed of ice-accumulation wave clearly increases with flow Froude number. One can also say that, after formation of ice-accumulation wave, the celerity of the ice-accumulation wave will increase with the flow intensity.

Figure 7 shows the relationship between moving speed of ice-accumulation wave and the water depth of (H/B) for the initial average flow velocity of V = 0.16 m/s under open flow condition. Figure 7 indicates that the moving speed of ice-accumulation wave decreases with the increase in the water depth. The increase in water depth results in the decrease in the transport capacity of ice particles under ice cover.

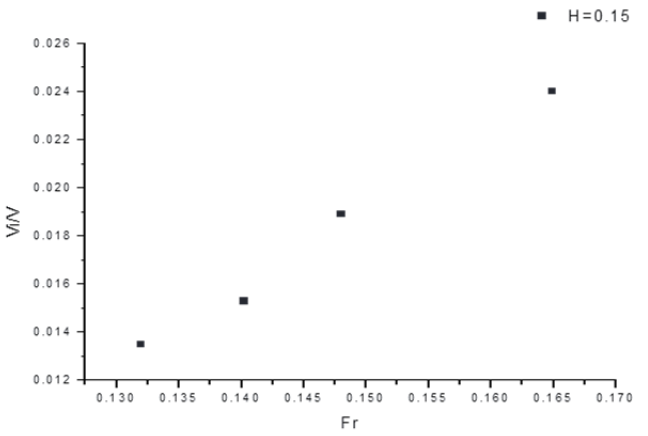

Fig. 6. Relationship between the moving speed of ice-accumulation wave (V_i/V) and flow Froude number (Fr) for flow depth of H = 0.15 m.

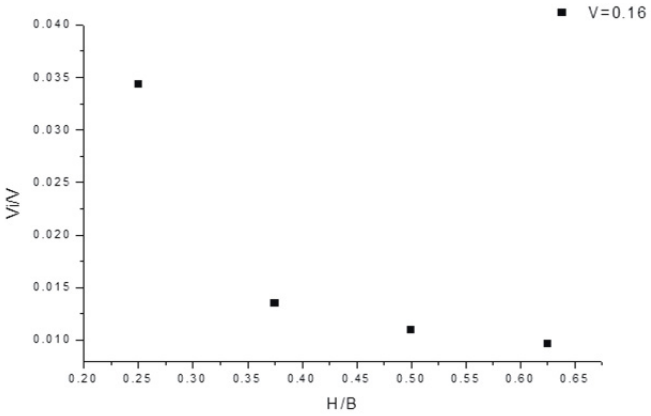

Fig. 7. Relationship between moving speed of ice-accumulation wave and water depth for the initial average flow velocity of V = 0.16 m/s.

Considering all factors affecting the moving speed of ice-accumulation wave, the moving speed of ice-accumulation wave (V_i) can be written as follows:

$$V_i = F\left(V, H, g, n_i, n_b, \rho_i, \rho, B, d_i, h_i, Q, Q_i, L, T, J \right) \tag{11}$$

where V is the average flow velocity of flow under ice jam; n_b and n_i is the roughness of channel bed and ice jam, respectively; ρ_i and ρ is the mass density of ice and water, respectively; h_i is the water depth under ice jam; L is the length of the ice jam; T is the air temperature during river freeze-up; and J is the hydraulic slope. Neglecting dependent variables and less significant factors, Equation (11) can be further reduced to the following form:

$$\frac{V_i}{V} = k_1 \left(\frac{V}{\sqrt{gH}} \right)^a \left(\frac{H}{B} \right)^b \left(\frac{Q_i}{Q} \right)^c \left(\frac{d_i}{h_i} \right)^m \tag{12}$$

where k, a, b, c, d, m are coefficients.

Based on data collected from experiments in laboratory, the moving speed of ice-accumulation wave has strong relationships with the flow intensity (*Fr*), ice discharge (Q_i/Q) and water depth (H/B). Based on experiment data, the following regression formula has been derived for determining the propagation speed of ice-accumulation wave with regression coefficient of 0.94 as shown in Figure 8.

$$\frac{V_i}{V} = 0.5107\left(\frac{V}{\sqrt{gH}}\right)^{1.745}\left(\frac{H}{B}\right)^{-0.301}\left(\frac{Q_i}{Q}\right)^{0.026} \tag{13}$$

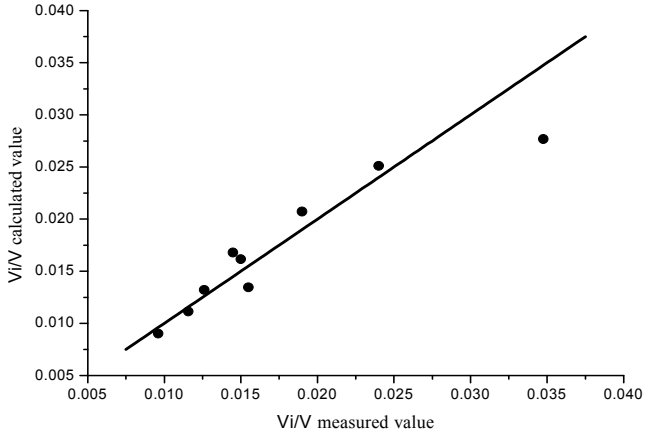

Fig. 8. Comparison of calculated moving speed of ice-accumulation wave to the measured moving speed of ice-accumulation wave.

One can see from Eq. (13), with the increase in flow intensity (*Fr*), the propagation speed of ice-accumulation wave increases; the propagation speed of ice-accumulation wave decreases with the increase in water depth, however, an increase in ice discharge (Q_i/Q) results in an increase in the propagation speed of ice-accumulation wave. Unfortunately, we only have one uniform model ice particle (d_i = 0.35 cm), and the impact of grain size of ice particles on the moving speed of ice-accumulation wave cannot be considered. In our future studies, we will consider the effects of different grain size of ice particles on ice accumulation process.

Transport capacity of cover-load

The movement of the cover-load is the most important form of ice particle transport under an ice cover. Experiments show that the existence of the ice-accumulation wave affects the transport capacity of cover-load. Thus, ice-accumulation waves significantly alter the ice transport capacity of the cover-load. Before reaching the equilibrium condition, the ice transport capacity under ice jam is continually changing. As shown in Figure 9, the ice transport capacity at one cross section at any instant is defined as ice transport discharge (Q_T) under the ice-accumulation wave under the condition of specific incoming ice discharge, flow condition and specific grain size of ice particle. Obviously, the ice transport capacity under ice-accumulation wave is an unsteady variable before ice jam reaches equilibrium condition. After ice jam achieves equilibrium condition, the ice

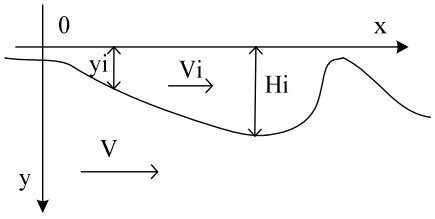

Fig. 9. Ice-accumulation wave and variable used.

transport capacity associated with the ice-accumulation wave must clearly equal the rate of incoming ice discharge from the upstream.

During the accumulation process of ice jam, the mass conservation equation can be written as follows:

$$\frac{\partial Q_T}{\partial x} + (1-p)B\frac{\partial y_i}{\partial t} = 0 \tag{14}$$

where Q_T is the ice transport capacity; t is time, p is the porosity of accumulated ice jam and p = 0.4 in this study, y_i is the ice jam thickness at any cross section. When the movement speed of ice-accumulation wave is V_i, the equation for the movement of ice-accumulation wave can be written

$$\frac{\partial y_i}{\partial t} + V_i\frac{\partial y_i}{\partial x} = 0 \tag{15}$$

Combining Equations (14) and (15), we obtain

$$\frac{\partial Q_T}{\partial x} - (1-p)BV_i\frac{\partial y_i}{\partial x} = 0 \tag{16}$$

At any location x_0 at instant t_0,

$$Q_T(y,t_0) - Q_T(h_0,t_0) = \int_{h_0}^{y}(1-p)BV_i dy = (1-p)BV_i(y-h_0) \tag{17}$$

where h_0 is the thickness of ice jam at the cross section of wave trough of ice-accumulation wave.

At the cross section of wave trough of ice-accumulation wave, the ice transport capacity could be ignored. Then, the transport capacity of cover-load under ice cover can be determined by following equation:

$$Q_T = \alpha(1-p)BH_iV_i \tag{18}$$

where α is the correction coefficient for bottom form of ice-accumulation wave. It ranges from 0.6 to 0.8; H_i is the wave height at wave crest of ice-accumulation wave. Although almost all ice particles transported under ice jam are cover-load under ice jam, the effect of suspended ice particles in water should be also considered by adjusting the correction coefficient for bottom form of ice-accumulation wave (α). Therefore, for the waved accumulation of ice particles under ice cover, the transport capacity of cover-load can be determined as following,

$$Q_T = 0.255\alpha(1-p)BVH\left\{1+C_0\left(\frac{V}{\sqrt{gH}}\right)^2 - \left[\left(1+C_0\left(\frac{V}{\sqrt{gH}}\right)^2\right)^2 - (8+4C_0)\left(\frac{V}{\sqrt{gH}}\right)^2\right]^{0.5}\right\}\left(\frac{V}{\sqrt{gH}}\right)^{1.745}\left(\frac{H}{B}\right)^{-0.301}\left(\frac{Q_i}{Q}\right)^{0.026} \tag{19}$$

$$\frac{Q_T}{Q}=0.255\alpha(1-p)\left\{1+C_0\left(\frac{V}{\sqrt{gH}}\right)^2-\left[\left(1+C_0\left(\frac{V}{\sqrt{gH}}\right)^2\right)^2-(8+4C_0)\left(\frac{V}{\sqrt{gH}}\right)^2\right]^{0.5}\right\}\left(\frac{V}{\sqrt{gH}}\right)^{1.745}\left(\frac{H}{B}\right)^{-0.301}\left(\frac{Q_i}{Q}\right)^{0.026} \quad (20)$$

Both Equation (20) and the formula for determining the surface ice discharge proposed by Beltaos (1995) have been derived based on mass conservation theorem, but can be used to determine the ice transport capacity under different conditions. The relation proposed by Beltaos (1995) can be used for calculating the surface ice discharge during river ice flowing period before river freeze-up. Equation (20) can be used to determine the ice transport capacity under waved ice accumulation. Urroz-Aquirre (1988) used models of ice floes to experimentally study ice transport capacity in a trapezoidal flume. Since it is difficult to determine both the shear force and roughness coefficient of the bottom of ice accumulation, calculation results using formulas for determining light bedload proposed by both Bagnold (1956) and Luque and Beek (1976) deviated far away from measured results, and cannot be used for determining ice transport capacity under waved accumulation. The formula for determining ice transport capacity in present study has been derived based on the mass conservation equation and the equations for the movement of ice-accumulation wave. Using measured data from experiments, the proposed formula has been validated.

As shown in Figure 8, based on measured ice transport capacities, the calculated ice transport capacities (Q_T/Q) using the proposed Equation (20) agree closely with those of measured ice transport capacities (Q_T/Q), especially if the ice transport capacities are relatively low.

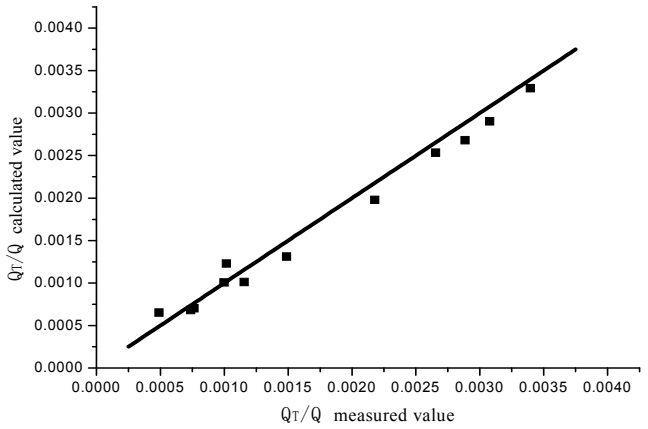

Fig. 8. Comparison of the calculated Q_T/Q to those of measured results.

However, it must be pointed out that only one uniform model ice having the grain size diameter of 0.35 cm was available and used in this relation. The impact of grain size of ice particles on ice transport capacity under waved accumulation of ice is yet to be explored.

CONCLUSIONS

Laboratory experiments under different flow and incoming ice conditions have been carried out to study the mechanics, movement and characteristics of development of ice-accumulation wave and ice transport capacity. A criterion for the formation of ice-accumulation wave has been proposed and the dependence of wave height ice on flow Froude number (*Fr*) has been assessed. Results indicate that higher flow Froude numbers result in larger ice waves. The propagation speed of the ice-accumulation wave is investigated based on mass conservation. A relation for estimating the celerity of an ice-accumulation wave has been derived. The transport capacity of frazil ice under waved accumulation of ice has also been studied based on mass conservation equation and the transport based on waved ice accumulation. It is found that, under the condition of the same flow depth, the moving speed of ice-accumulation wave clearly increases with flow Froude number. Also, the propagation speed of ice-accumulation wave decreases with the increase in the water depth, whereas an increase in water depth results in the decrease in the transport capacity. Finally, an estimate of ice transport capacity has been established. Calculated ice transport capacities using derived equation agree well with measured results for the case of known and uniform ice particle sizes.

Acknowledgement. This study is supported by the National Natural Science Foundation of China (Funding Number: 51379054). The authors are grateful for the financial support.

REFERENCES

Ackerman, N.L., Shen, H.T., 1983. Mechanics of ice jam formation in rivers. CRREL Report 83–31. U. S. Army Cold Regions Research and Engineering Laboratory, Hanover, New Hampshire, U.S.A.

Bagnold, R.A., 1956. The flow of cohesionless grains in fluids. Phil Trans of Royal Society of London, 249, A, 235–297.

Beltaos, S., 1993. Numerical computation of river ice jams. Canadian Journal of Civil Engineering, 20, 1, 88–89.

Beltaos, S., 1995. River Ice Jam. Water-Resources Publications, LLC, Water Resources Publications LLC, Highlands Ranch, Colorado, U.S.A., pp. 155–172.

Beltaos, S., 2012. Distributed function analysis of ice jam flood frequency. Cold Regions Science and Technology, 71, 2, 1–10.

Beltaos, S., Burrell, B.C., 2010. Ice-jam model testing: Matapedia River case studies, 1994 and 1995. Cold Regions Science and Technology, 60, 1, 29–39.

Calkins, D.J., Ashton, G.D., 1976. Arching of model ice floes: effect of mixture variation on two block sizes. CRREL Report 76–42, U S Army Cold Regions Research and Engineering Laboratory, Hanover, New Hampshire, U.S.A.

Ettema, R., Huang, H.P., 1988. Ice-rubble accumulation beneath barges in ice-covered waters. IAHR Journal of Hydraulic Research, 26, 4, 379–412.

Gao, P., Jin, G., Lu, B., 2003. Preliminary study on ice regime in the Middle Route of South to North Water Transfer Project". China Journal of Hydraulic Engineering, 11, 96–101.

Luque, R.F., Beek, R.V., 1976. Erosion and transport of bedload sediment. Journal of Hydraulic Research, 14, 2, 127–144.

Morse, B., Hessami, M., Bourel, C., 2011. Characteristics of ice in the St. Lawrence River. Canadian Journal of Civil Engineering, 30, 4, 766–774.

Nuttall, J.B., 1973. River modification and channel improve-

ments. In: Proceedings of the Seminar on Ice Jams in Canada. National Research Council of Canada, Ottawa.
Shen, H.T., 2010. Mathematical modeling of river ice processes. Cold Regions Science and Technology, 62, 1, 3–13.
Sui, J., Fang, D., Zhou, Y., 1994. The variations of water level of ice jams. China Journal of Hydrology, 2, 18–24.
Sui, J., Karney, B., Fang, D., 2005. Variation in water level under ice-jammed condition – Field investigation and experimental study. Nordic Hydrology, 36, 1, 65–84.
Sui, J., Karney, B., Sun, Z., Wang, D., 2002. Field investigation of frazil jam evolution - a case study. Journal of Hydraulic Engineering, 128, 781–787.
Sui, J., Wang, J., Balachandar, R., Sun, Z., Wang, D., 2008. Accumulation of frazil ice along a river bend. Canadian Journal of Civil Engineering, 35, 158–169.
Urroz, G., 1988. Studies of ice jams in river bends. PhD Thesis. The University of Iowa, Iowa, U.S.A.
Urroz, G., Ettema, R., 1994. Small-scale experiments on ice jam initiation in a curved channel. Canadian Journal of Civil Engineering, 21, 5, 719–727.
Wang, J., 2002. A study on ice jam in balance transporting discharge. Journal of Hydroelectric Engineering, 1, 61–67.
Wang, J., Chen, P., Sui, J., 2011. Numerical simulations of ice jams in natural channels. China Journal of Hydraulic Engineering, 42, 9, 1117–1121.
Wang, J., Fu, H., Yin, M., Gao, Y., 2007a. Analysis of stages under ice-covered in winter. Advances in Water Science, 18, 1, 102–107.
Wang, J., Gao, Y., Yin, Y., Guo, L., Zhao, H., 2007b. An experimental study of ice jam formation and its thickness distribution in a curved channel. Journal of Glaciology and Geocryology, 29, 5, 764–769.
Wang, J., He, L., Chen, P., Sui, J., 2013. Numerical simulation of mechanical breakup of river ice-cover. Journal of Hydrodynamics, 25, 3, 415–421.
Wang, D., Shen, H.T., Sun, Z., 1993. Transport of frazil granules in Hequ reach of the Yellow River. Journal of Sediment Research, 4, 1–10.
Zufelt, J.E., Ettema, R., 2000. Fully coupled model of ice-jam dynamics. Journal of Cold Regions Engineering, 14, 1, 24–41.

Received 26 May 2017
Accepted 30 January 2018

J. Hydrol. Hydromech., 67, 2019, 2, 179–190
DOI: 10.2478/johh-2018-0009

Comparison of alternative soil particle-size distribution models and their correlation with soil physical attributes

Fatemeh Afrasiabi[1], Habib Khodaverdiloo[1*], Farrokh Asadzadeh[1], Martinus Th. van Genuchten[2, 3]

[1] Department of Soil Science, Urmia University, Urmia 57135-165, Iran.
[2] Department of Earth Sciences, Utrecht University, Utrecht, Netherlands.
[3] Center for Environmental Studies, CEA, São Paulo State University, UNESP, Rio Claro, SP, Brazil.
[*] Corresponding author. E-mail: h.khodaverdiloo@urmia.ac.ir

Abstract: Complete descriptions of the particle-size distribution (PSD) curve should provide more information about various soil properties as opposed to only the textural composition (sand, silt and clay (SSC) fractions). We evaluated the performance of 19 models describing PSD data of soils using a range of efficiency criteria. While different criteria produced different rankings of the models, six of the 19 models consistently performed the best. Mean errors of the six models were found to depend on the particle diameter, with larger error percentages occurring in the smaller size range. Neither SSC nor the geometric mean diameter and its standard deviation correlated significantly with the saturated hydraulic conductivity (K_{fs}); however, the parameters of several PSD models showed significant correlation with K_{fs}. Porosity, mean weight diameter of the aggregates, and bulk density also showed significant correlations with PSD model parameters. Results of this study are promising for developing more accurate pedotransfer functions.

Keywords: Lake Urmia (Iran); Particle-size distribution models; Pedotransfer functions; Soil physical properties.

INTRODUCTION

The particle-size distribution (PSD) is a fundamental physical property of soils. Knowing the soil PSD is critical for a range of hydrological, geological, agricultural, and geotechnical applications, including soil classification, as summarized well by Bayat et al. (2015). For example, the soil PSD is widely used to estimate such key soil attributes as infiltration (e.g., Ghorbani-Dashtaki et al., 2016; Parchami-Araghi et al., 2013), the saturated hydraulic conductivity (Jabro, 1992; Saxton et al., 1986), soil water retention (Arya and Paris, 1981; Ghorbani Dashtaki et al., 2010; Khodaverdiloo et al., 2011) and movement (Nemes et al., 2003), soil erosion (Beke et al., 1989; Xu et al., 2013), the cation exchange capacity of soils (Ersahin et al., 2006; Liao et al., 2015; Manrique et al., 1991) and various chemical sorption parameters of soils (Khodaverdiloo and Samadi, 2011).

Predictions of many soil properties and functions often need more detailed soil textural data than only the sand, silt and clay (SSC) fractions. Therefore, many studies were undertaken to provide more detail regarding the soil PSD. For example, Shirazi and Boersma (1984) and Shirazi et al. (1988) transformed the standard textural triangle into a new diagram based on mean particle size and standard deviations of particle size to provide greater resolution in detecting classified soils within a textural class. Accordingly, parameters other than SSC are often used to reflect the soil PSD in various predictive functions (e.g. Ghorbani Dashtaki et al., 2010). Examples are the geometric mean diameter (d_g) and its standard deviation (σ_g), the coefficient of uniformity (C_u), the coefficient of curvature (C_c), and the diameter of soil particles having a specific percentage of smaller particles (e.g., D_{10}, D_{30}, D_{50}, D_{60}, etc.), which then may serve as measures of soil gradation or other properties. Mathematically representing PSD data hence provides several benefits in soil mechanics, physics, hydrodynamic and geotechnical applications (Fredlund et al., 2000), as well as helps to convert PSD data of various particle-size classification systems to the desired formulation (Nemes et al., 1999; Skaggs et al., 2001). These applications require the definition of complete PSD curves using some mathematical model that best fits experimental data.

Consequently, various equations have been introduced over the years to describe the soil PSD, each of which often has its own specific advantages and limitations (Bayat et al., 2015; Fredlund et al., 2000). A careful selection of the most appropriate PSD model may have a significant impact on the estimated soil particle distribution density at a given particle size (Nemes et al., 1999) and hence is important to more precisely estimate soil properties (e.g., Bittelli et al., 1999; Hwang and Powers, 2003). Several studies have attempted to compare different PSD mathematical expressions for soils (e.g., Bayat et al., 2015; Buchan et al., 1993; Hwang et al., 2002; Hwang, 2004; Bah et al., 2009). However, these studies generally compared only a limited number of PSD models (Bagarello et al., 2009; Buchan et al., 1993; Hwang, 2004; Vipulanandan and Ozgurel, 2009), invoked only few statistical criteria for the comparisons (Bagarello et al., 2009; Bayat et al., 2015; Buchan et al., 1993; Hwang, 2004; Vipulanandan and Ozgurel, 2009) and/or applied the analyses to a relatively narrow range of soil textural classes (Buchan et al., 1993; Vipulanandan and Ozgurel, 2009; Zhao et al., 2011). Since the performance of a PSD model depends on the type and range of soil textures involved (e.g., Bagarello et al., 2009; Buchan, 1989; Fredlund et al., 2000; Hwang, 2004; Hwang et al., 2002; Zhao et al., 2011), conclusions obtained with such studies may not necessarily be extended or generalized to soil textures other than those used in the comparisons. Additionally, PSD models have often been evaluated in terms of their general performance for describing the entire PSD curve, but frequently not for predicting specific (and practically-important) PSD points or parameters. A given model may well be accurate globally in terms of generating the entire PSD curve, while failing locally to predict specific points or selected parameters of the curve.

Soil PSD data are commonly used to derive pedotransfer functions (PTFs) for estimating soil hydraulic and other properties that are more difficult to measure directly. Traditionally,

soil SSC percentages have been used as input data for the PTFs (e.g., Carsel and Parrish, 1988; Chapuis, 2012; Jabro, 1992; Patil and Singh, 2016; Saxton et al., 1986). While attempts have been made to test parameters other than SSC to represent soil particle size information in PTFs, it is not obvious which PSD models are most suitable for this purpose. Also, there is often no clear physical basis of the parameters in some of PSD models. Many PSD model parameters frequently are purely empirical without any physical significance. For these reasons, studies are still needed to obtain optimal correlations of PSD parameters with soil properties in terms of underlying physical concepts.

The objectives of this study were to (1) evaluate the performance of 19 models for describing PSD data of selected soils in northwestern Iran using a broad database in terms of soil textures, (2) provide a functional evaluation of the models to predict selected practically-important PSD points or parameters using different efficiency criteria, (3) compare results obtained with the general and functional evaluations, and (4) correlate physically based PSD model parameters with selected soil physical properties to examine their suitability to serve as input for pedotransfer functions.

MATERIALS AND METHODS

Soil datasets

Twenty four locations neighboring the western edge of threatened hypersaline Lake Urmia in northwestern Iran were sampled for this study. The locations were selected such that soils with a wide range of soil textures were included in the database. Figure 1 shows the textural distributions of the samples. The study area was located between geographical coordinates of 45° 05′ and 45° 08′ E, and 37° 32′ and 37° 38′ N, at 1290 to 1350 m above mean sea level, and with mean annual precipitation and temperature of approximately 300 mm and 11.8°C, respectively, with xeric soil moisture and mesic soil temperature regimes (Banaei, 1998).

Three replicate surface (0–30 cm depth) soil samples were collected at each site. After clay deflocculation using sodium-hexametaphosphate and mechanical agitation, soil PSD curves were determined using a combination of hydrometer (Gee and Or, 2002) and mechanical sieving methods. Fine particle fractions (<0.15 mm) were determined by sedimentation, whereas the coarser fractions (≥ 0.15 mm) were obtained by sieving. The sieve analysis involved nested columns of sieves (2, 1, 0.5, 0.25 and 0.15 mm), which were shaken with a mechanical shaker. Twelve data points were obtained from the hydrometer analysis by recording the soil suspension density at times of 30, 40 and 60 s, and at 3, 10, 15, 30, 60, 90, 120, 240 and 1440 min. A total of 16 hydrometer particle size limits hence were obtained for each soil sample.

Once the cumulative PSD curves (i.e., $F(d)$ as a function of the particle diameter, d) were obtained, the geometric mean d_g and geometric standard deviation σ_g of the soil particle diameters were determined using methods proposed by Shirazi and Boersma (1984). We also determined the mean weight diameter (MWD) of soil aggregates after dry sieving.

Soil particle data larger than 53 μm as measured with the sieve method were used to obtain direct estimates of the "measured" sand content. These measured values were then used to test the accuracy of the PSD models to predict the sand content from the complete grain size distribution using complete F ($d \geq$ 53 μm). We further compared the SSC contents obtained with the hydrometer data at sedimentation times of 40 s and 7 hr, further referred to as the "nominal" SSC contents, with PSD model-predicted $F(d)$ values corresponding to diameters (d) of 2–0.05, 0.05–0.002, and < 0.002 mm for sand, silt, and clay, respectively.

We also estimated "measured" particle-size diameters corresponding to 10, 30, and 60% of the cumulative PSD curve (i.e. D_{10}, D_{30}, and D_{60}, respectively) by linear interpolation from the nearest lower and higher measured data points (a common procedure to determine D_{10}, D_{30}, and D_{60} values). These measured values were compared with D_{10}, D_{30}, and D_{60} values "predicted" with the complete $F(d)$ models.

Several other soil physical parameters were obtained at the study site. The field-saturated soil hydraulic conductivity (K_{fs}) was measured using constant head single-ring methods (Razzaghi et al., 2016; Reynolds, 2008), while the soil bulk density (ρ_b) was determined using core sampling (Blake and Hartge, 1986). To determine total porosity (Φ), the soil cores were slowly saturated by soaking them from below to a water level just below the top of the core. This procedure was carried out over a period of 2 days to obtain as complete saturation as possible by minimizing entrapped and dissolved air in the cores. Soil water contents as determined subsequently by oven-drying the saturated samples at 105°C for 24 hr were regarded to be equivalent to porosity, Φ (Khodaverdiloo et al., 2011).

Particle-size distribution models

In this study we compared the performance of 19 different mathematical models for $F(d)$ in describing observed cumulative PSD data of the sampled Urmia soils. The models are listed in Table 1. The references cited in the second column of Table 1 provide details of the corresponding model shown in the third column.

Fitting procedure

An iterative nonlinear optimization procedure was used to fit the parametric functions $F(d)$ in Table 1 to the observed cumulative PSD data. The optimization procedure produced values of the unknown parameters that provided the best fit with the data (Bagarello et al., 2009; Bah et al., 2009; Hwang et al., 2002). Optimized values of the model parameters were determined by minimizing the following objective function:

$$SSE = \sum_{i=1}^{n} (O_i - P_i)^2 \quad (1)$$

where SSE represents the sum of squared errors between the measured (O_i) and predicted (P_i) cumulative PSD fractions, and n the number of particle size data points.

The optimization procedure was implemented using the least-square curve fitting toolbox in the MATLAB R2011a environment (The MathWorks Inc., Natick, MA). The final fitted parameter values in each case were tested by using at least three different initial parameter estimates as done by Hwang et al. (2002) and Bah et al. (2009), among others. The optimization process in most or all cases converged to the same final values, thus avoiding the problem of selecting local minima.

Criteria for model comparison

After optimization of the model parameters, values of the cumulative PSD fractions as calculated with the $F(d)$ models were compared with their corresponding observed values to test how well the calibrated models fitted the observed PSD data.

Table 1. Particle-size distribution models, $F(d)$, tested in this study.

Model	Reference	Equation[#]	Parameters
AD	Andersson (1990)	$F(d) = f_o + b \arctan(c\ log\ \frac{d}{d_o})$	f_o, b, c, d_o
G (Gompertz)	Nemes et al. (1999)	$\mathrm{F(d)} = \alpha + \gamma \exp\{-\exp[-\beta(d-\mu)]\}$	α, β, μ , γ
Fred-3p (Fredlund with 3 parameters)	Fredlund et al. (2000)	$F(d) = \frac{1}{\{\ln[\exp(1)+(\frac{\alpha}{d})^n]\}^m}\{1-[\frac{\ln\left(1+\frac{0.001}{d}\right)}{\ln\left(1+\frac{0.001}{d_m}\right)}]^7\}$	a, n, m d_m = 0.0001
Fred-4p (Fredlund with 4 parameters)	Fredlund et al. (2000)	$F(d) = \frac{1}{\{\ln[\exp(1)+(\frac{\alpha}{d})^n]\}^m}\{1-[\frac{\ln\left(1+\frac{d_f}{d}\right)}{\ln\left(1+\frac{d_f}{d_m}\right)}]^7\}$	n, m, d_f, α d_m = 0.0001
ORL (Offset-Renormalized Lognormal)	Buchan et al. (1993)	$G(X) = (1-\varepsilon)F(X) + \varepsilon$ F(X) defined by SLN model	μ, σ, ε
ORN (Offset-Nonrenormalized Lognormal)	Buchan et al. (1993)	$\mathrm{G(X)} = \mathrm{F(X)} + c$ F(X) defined by SLN model	μ, σ, c
SH-C	Shiozawa and Campbell (1991)	$G(X) = \varepsilon F_1(X) + (1-\varepsilon)F_2(X)$ F(X) defined by SLN model	μ, σ, ε
MLG (Modified Logistic Growth function)	Liu et al. (2004)	$F(d) = \frac{1}{[1+a\exp(-bd^c)]}$	a, b, c
Wei (Weibull)	Assouline et al. (1998)	$F(d) = c + (1-c)\{1-\exp(-a\,D^b)\}$ $D = \frac{(d-\ d_{min})}{(d_{max}-d_{\min})}$	c, a, b
SLN (Simple Lognormal)	Buchan (1989)	$F(X) = \frac{1}{2}(1-\mathrm{erf}\left(\frac{X-\mu}{\sigma\sqrt{2}}\right)\ \ X \le \mu$ $X = \ln(d)$	μ, σ
Norm (Normal)	Buchan et al. (1993)	$F(X) = \frac{1}{2}(1+\mathrm{erf}\left(\frac{X-\mu}{\sigma\sqrt{2}}\right)\ \ X > \mu$ $X = \ln(d)$	μ, σ
VG	Haverkamp and Parlange (1986)	$F(d) = \left[1+\left((\frac{d_g}{d})^n\right)\right]^{-m}$	d_g, n (m = 1–1/n)
BEST (Beerkan Estimation of Soil Transfer)	Lassabatère et al. (2006)	$F(d) = [1+\ (\frac{d_g}{d})^N]^{-M}$	d_g, N, M M = 1–2/N
Fr(B) (Fractal)	Bird et al. (2000)	$F(d) = cd^{(3-Dm)}$	c, Dm
Fr (T-W) (Fractal)	Tyler and Wheatcraft (1992)	$F(d) = (\frac{d}{1.5})^{(3-Dm)}$	Dm
L-P (Log-power)	Kolev et al. (1996)	$F(d) = A\exp(B\ \log d)$	A, B
Exp (Exponential)	Gimenez et al. (2001)	$F(d) = cd^{-\beta}$	c, β
Log (Logarithmic)	Zhuang et al. (2001)	$F(d) = a\ \ln d + b$	a, b
J	Jaky (1944)	$F(d) = \exp\{\frac{1}{\mathrm{p}^2}\left[\ln\left(\frac{\mathrm{d}}{\mathrm{d}_0}\right)\right]^2\}$	p >1 (d_0 = 2 mm)

[#] d: particle diameter in mm; $F(d)$: cumulative fraction with a diameter smaller than d; erf: error function

The accuracy of the models was evaluated using the Nash-Sutcliffe Efficiency (*NSE*), the root mean square error (*RMSE*), the coefficient of determination (R^2), the index of agreement (δ), the relative error (*Er*), Akaike's information criterion (*AIC*), the standard deviation of error (*STDEV*), the maximum error (MAX_e), the mean absolute error percentage (*MAEP*), the maximum absolute error percentage (MAX_{aep}), and the geometric mean of error ratio (*GMER*). Mathematical representations of these criteria are given in Table 2.

We used the various statistical measures in Table 2 to evaluate different aspects of the optimizations. This was done since some of the criteria emphasize the optimizations more from a perspective of variances, while other statistics capture the bias better. For example, *RMSE* is an index of the absolute error.

Table 2. Efficiency criteria used to evaluate the accuracy of the PSD models.

Criteria	Model Equation[#]
R^2	$R^2 = \{\frac{\sum_{i=1}^{n}(O_i-\bar{O})(P_i-\bar{P})}{\sqrt{[\sum_{i=1}^{n}(O_i-\bar{O})]^2}\sqrt{[\sum_{i=1}^{n}(P_i-\bar{P})]^2}}\}^2$
RMSE	$RMSE = \sqrt{\frac{1}{n}\sum_{i=1}^{n}(P_i-O_i)^2}$
AIC	$AIC = N\ln(\frac{SSE}{n}) + 2(P+1) + \frac{2(P+1)(P+2)}{n-P-2}$
Er	$Er = \sqrt{\frac{\sum_{i=1}^{n}(P_i-O_i)^2}{\sum_{i=1}^{n}(O_i)^2}}$
NSE	$NSE = 1 - \frac{\sum_{i=1}^{n}(P_i-O_i)^2}{(O_i-\bar{O})^2}$
δ	$\delta = 1 - \{\frac{\sum_{i=1}^{n}(O_i-P_i)^2}{\sum_{i=1}^{n}(\lvert P_i-\bar{O}\rvert + \lvert O_i-\bar{O}\rvert)^2}\}$
GMER	$GMER = \exp(\frac{1}{n}\sum\ln(\frac{P_i}{O_i}))$
STDEV	$STDEV = STDEV(P_i-O_i)$
MAX_e	$MAX_e = \mathrm{MAX}\lvert P_i-O_i\rvert$
MAEP	$MAEP = (\sum_{i=1}^{n}\lvert\frac{P_i-O_i}{P_i}\rvert)/n\times 100$
MAX_{aep}	$MAX_{aep} = \mathrm{Max}_{i=1}^{n}\left(\lvert\frac{P_i-O_i}{P_i}\rvert/n\times 100\right)$

[#] n refers to the number of calculated (P_i) and measured (O_i) values of the cumulative PSD curve; over-lined symbols represent mean values; *SSE* is the sum of squared errors; P is the number of model parameters.

However, models with more fitting parameters will almost always result in a better overall fit. The *AIC* is for this reason often used to compare models with different numbers of fitting parameters. In this study we used the corrected *AIC* as suggested by Bolster and Hornberger (2007).

NSE values were selected to indicate whether or not the observed mean is as good a predictor as the model. On the other hand, R^2 is an indicator of the extent to which the model explains the total variance of the observed data. To overcome some of the limitations of R^2, Willmott (1981) proposed the index of agreement, δ, to better reflect the degree at which observations are estimated accurately by the predictions. However, relatively high values (more than 0.65) of δ may be obtained even for poor model fits, and δ hence is not overly sensitive to systematic over- or under-predictions. We used *GMER* to test the possible under- or over-estimations in the model predictions, while MAX_e is used to show the outliers. Since errors within the lower range of the model output may be masked by relatively high errors in the higher range of the output, *MAEP* and MAX_{aep} have been used to compare the errors and outliers, respectively, of the models as percentages of the observed values. For a perfect prediction *RMSE, SD,* MAX_e, *MAEP,* MAX_{aep} and *Er* equal zero and *NSE*, δ, R^2, and GMER equal 1. Models with lower *AIC* values are considered to be the more likely to be accurate.

Since most or all statistical criteria evaluate only some aspect of the correspondence between measured and calculated values, we suggest that a complete assessment of model performance should include a combination of criteria. We evaluated for this reason initially all of the criteria in Table 2 for the $F(d)$ models. The criteria subsequently were classified into groups using a hierarchical cluster analysis (HCA) based on the levels of similarity among their standardized values. Finally, a subset of the criteria was selected among the distinct groups to evaluate and compare the performance of the models. The selected criteria were then used to classify the models into groups using HCA. The cluster analysis was conducted using the Minitab 16 software.

Once the different $F(d)$ models and their optimized parameters were determined, measured K_{fs}, log K_{fs}, MWD, and $\boldsymbol{\Phi}$ values were correlated with either the conventional PSD parameters (i.e., sand/silt/clay percentages), geometric representations of the PSDs (d_g and σ_g), selected PSD mechanical parameters (notably D_{50} and D_{60}), and the optimized parameters of the most accurate $F(d)$ models. This is to find the best representation(s) of the soil PSDs to predict relevant soil physical quality indices, and to interpret correlations of soil PSD data with field properties. For the functional evaluation of the models against the field data we used selected practically-important PSD parameters such as sand, silt and clay percentages, d_g and σ_g, and D_{30}, D_{50} and D_{60} as calculated with the $F(d)$ models.

The accuracy of the models in terms of predicting K_{fs}, log K_{fs}, MWD, and $\boldsymbol{\Phi}$ values was assessed using a weighted version of R^2 (i.e., wR^2) following Krause et al. (2005):

$$wR^2 = \begin{cases} |b|.R^2 & \text{for } b \le 1 \\ |b|^{-1}.R^2 & \text{for } b > 1 \end{cases} \quad (2)$$

where the weighting factor, b, and R^2 are, respectively, the gradient and the coefficient of determination of the regression of predicted versus observed values of a given parameter. The advantage of Eq. (2), as opposed to R^2, is that only a single but more effective criterion is used for the comparisons. Models which systematically over- or under-predict observed data all the time will still result in R^2 values close to 1.0, even if all predictions are incorrect. This problem can be avoided by using additional information about the regression. Such information is provided by the gradient b and the intercept a of the regression on which R^2 is based. For good agreement the intercept a should be close to zero (which means that an observed value at or near zero would also result in a prediction at or near zero), while the gradient b should be close to 1.0. By using wR^2, systematic under- or over-predictions are quantified, together with the regression as such, thus leading to a more comprehensive reflection of model results (Krause et al., 2005).

RESULTS AND DISCUSSION

Statistical descriptions of selected physical and chemical properties of the soils used in this study are presented in Table 3. The data show that the soils differed widely in their PSD. For example, *CV* values of clay and silt contents were 48 and 55%, respectively, while the soil textural classes ranged from sandy loam to clay as shown in Fig. 1. On the other hand, pH values were within a relatively narrow range among the soils studied. The calcium carbonate equivalent (CCE) of all soils was above 7.3% and the pH was equal to 7.5 or more, which indicates that the soils were calcareous and alkaline. The organic matter (OM) content varied widely among the soils (*CV* = 53%). Most

Table 3. Maximum (Max), Minimum (Min), Mean and Standard Deviation (STDEV) of selected physico-chemical properties of the soil samples.

Soil property	Maximum	Minimum	Mean	STDEV	Range	CV
Clay (%)	52	8	27	13	45	48
Silt (%)	60	30	44	8	30	18
Sand (%)	59	8	29	16	51	55
pH	8.5	7.5	8.2	0.5	1	5.5
CCE (%)	33.5	17.3	23.3	7.2	16	31
OM (%)	5.98	0.89	2.94	1.55	5	53
ρ_b (g cm^{-3})	1.46	0.94	1.22	0.11	0.52	9.31
EC (dS m^{-1})	85.4	0.8	14.4	22.9	85	159
ESP (cmol$_{(+)}$ kg^{-1})	71.0	4.0	25.5	18.0	67	71
K_{fs} (cm day^{-1})	970.6	0.34	201.2	260.4	970	129.4

EC, Electrical conductivity; ESP, Exchangeable sodium percentage; CCE, Calcium carbonate equivalent; OM, Organic matter content; ρ_b, Bulk density, K_{fs}, Saturated hydraulic conductivity.

of the soils were either saline/sodic (n = 14) or non-saline/non-sodic (n = 8).

Comparison of the fitting ability of the PSD models

Box plots of the statistical criteria of the applied PSD models for the 24 soils are given in Fig. 2. Results indicate that the values of R^2, δ, *NSE*, and *GMER* differed in a narrow range among the models (CV < 6.2%). This shows that these criteria are not very effective in representing differences in the accuracy of the models. By comparison, *AIC* varied moderately (CV = 18.7%), whereas *RMSE*, MAX_e, *MAEP*, *STDEV*, and MAX_{aep} varied more widely (CV > 50%) among the models.

Mean values of R^2 ranged from 0.820 to 0.994 (Fig. 2). The Wie and Fred-4p models for $F(d)$ showed the highest R^2 values, ONL, Fred-3p and MLG models showed similar intermediate performance, while the Fr(T-W), Fr(B), Exp, and L-E models had the lowest R^2 values. The favorable fitting capability of Wie and Fred-4p reflects their flexibility in terms of describing a wide range of PSD shapes (Bayat et al., 2015). The Wei model also has a physical basis and no overlap in the effects of its parameters on the shape and position of the PSD curve. The Fred-4p model performed slightly better than the Fred-3p model. This indicates that Fred-3p is probably accurate enough for most soils, with the advantage of having one parameter less (Fredlund et al., 2000). These results are consistent with those by Bayat et al. (2015) who found no difference between the Fred-4p and Fred-3p models in terms of R^2 and *RMSE* when applied to the UNSODA database with a broad range of soil textural classes. However, they suggested using the Fred-3p model according to the *AIC* criterion. The favorable performance of Fred-4p in describing PSD data was reported also by Hwang et al. (2002) for soils covering a wide range of textures.

Of the three models assuming lognormal curves containing three parameters (i.e., ORL, ONL and SH-C), the R^2 values were higher for ONL as compared to the ORL and SH-C models. These results agree with those by Hwang et al., (2002), but differ from findings by Buchan et al. (1993) who, for a limited number of soils, found higher average R^2 values for the SH-C model than the two other models. However, we note that the CV of the R^2 values in our study was only about 6.2% among the studied models. This shows that the models are difficult to rank conclusively in terms of their R^2 values. Similarly, the low values of the coefficient of variation of δ, *NSE*, and *GMER* (<4.3%) makes it difficult to properly rank those models.

RMSE values of the models ranged from a low of 0.019 for AD to a high of 0.106 for Fr(T-W). Fr (T-W) is a single power-low exponent model which could not properly characterize the PSD across the whole range of measured data points. For this reason Bitteli et al. (1999) proposed the use of three separate power laws for the clay, silt and sand particle sizes.

The G, Norm, J, Exp, Log, L-E, Fr(B), and Fr(T-W) models performed the poorest as reflected by their high mean *AIC* values, whereas the other models performed well with very similar low mean *AIC* values (*AIC* < –109), as can be seen in Figure 2. In terms of their *AIC*, the Fred-3p, MLG, Wei and Fred-4p models ranked first to fourth. This result differs from that of Shangguan et al. (2014), who found that AD and Wei had the lowest mean *AIC* values and hence were considered the best PSD models among eleven models that they compared. Considering the average *AIC* values of all of the soils they studied, Botula et al. (2013) suggested that the number of fitting parameters does not always explain the differences in the quality of the fittings. They found lower *AIC* values for Fred-4p relative to the models having three, two and one parameters. Bayat et al. (2015) similarly suggested that an increase in the number of fitting parameters in the PSD models does not necessarily lead to better performance. The Gompertz model with four parameters showed the poorest performance in their study. Even though the *AIC* has a penalty on the number of parameters, the Wei, Fred-3p, MLG models with three parameters were still among the best PSD models in our study.

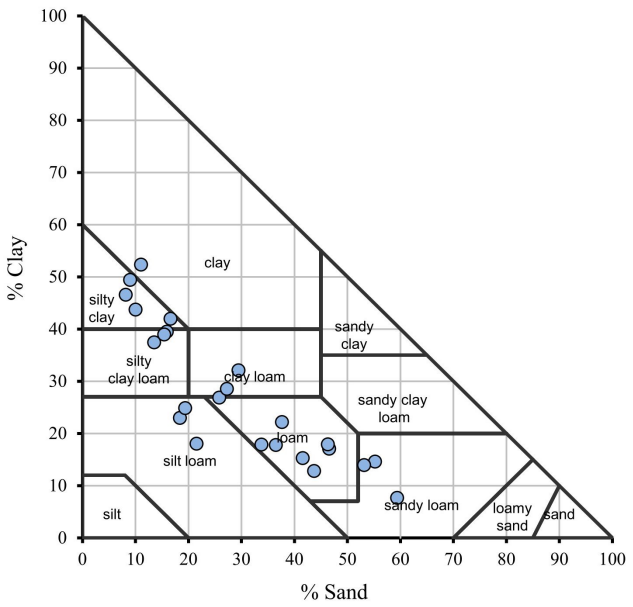

Fig. 1. Textural distribution of the 24 soil samples.

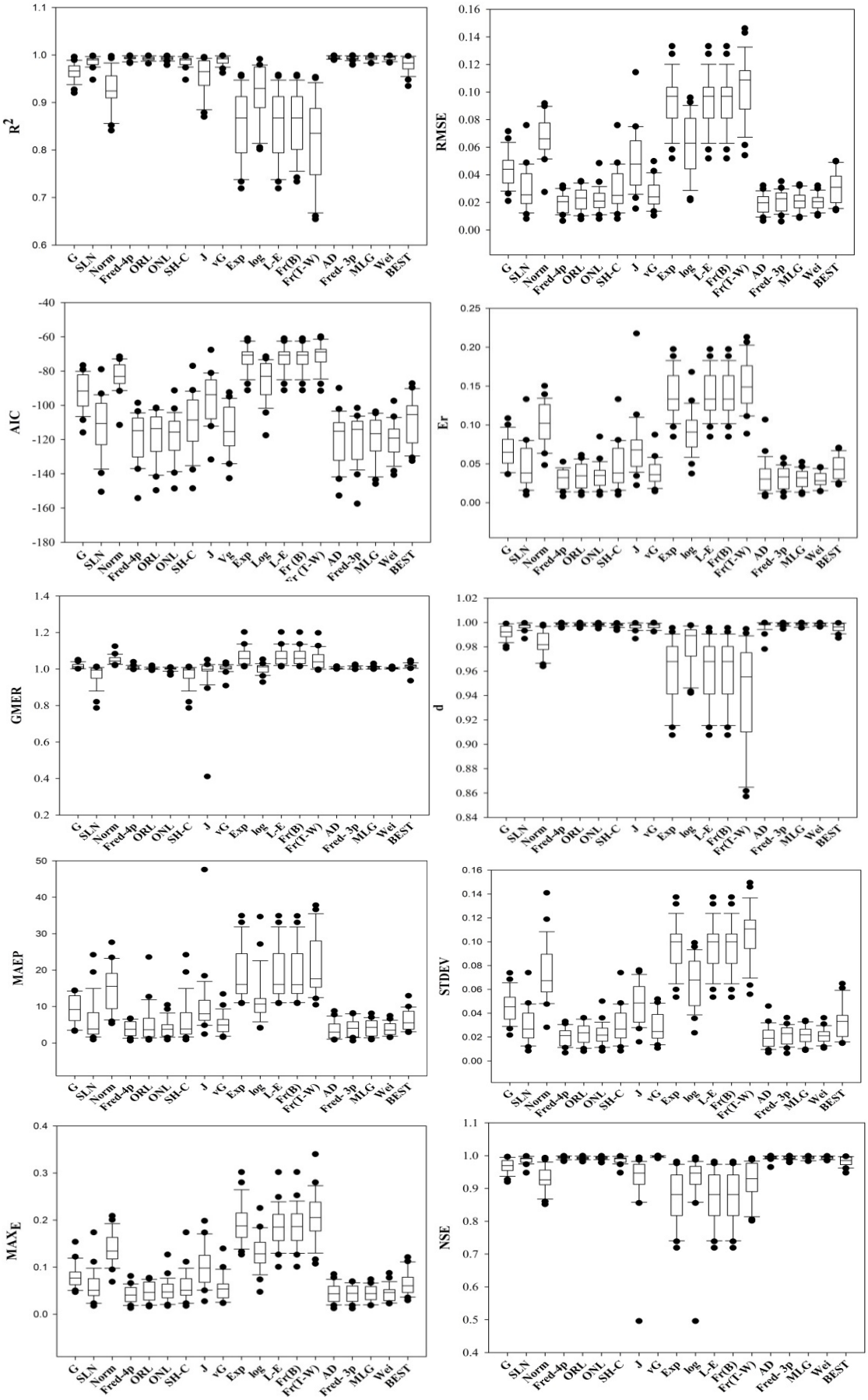

Fig. 2. Box plots of the statistical criteria used to describe the accuracy of 19 models in fitting the cumulative particle-size distribution data of 24 soil samples. The box plots show medians, interquartile ranges, and outliers. The full names and other information about the models (horizontal axes) are given in Table 1. The statistical criteria (vertical axes) are listed in Table 2.

Table 4. Rankings of the six most accurate PSD models in terms of various statistical criteria.

Ranking	R^2		AIC	RMSE	Er	d	MAX_{aep}	NSE	STDEV	GMER	MAX_e	MAEP
1	AD		Wei	AD	Fred-4p	Fred-4p	Fred-4p	VG	Fred-4p	ONL	Fred-4p	AD
2	Wei		Fred-3p	Fred-4p	MLG	Wei	Wei	Fred-4p	AD	ORL	Fred-3p	Wei
3	Fred-4p		AD	Wei	Fred-3p	Fred-3p	MLG	Wei	Wei	AD	MLG	Fred-4p
4	Fred-3p		MLG	Fred-3p	AD	MLG	Fred-3p	AD	Fred-3p	Wei	AD	ONL
5	MLG		Fred-4p	MLG	ONL	ONL	AD	Fred-3p	MLG	VG	Wei	Fred-3P
6	ONL		ORL	ONL	ORL	ORL	ONL	MLG	ONL	Log	ORL	MLG

Regarding the relative error (*Er*), Bagarello et al. (2009) considered that *Er* values of less than 5% indicate a satisfactory fitting performance of the PSD function. In our study Fred-4p, MLG, Fred-3p, ONL, AD, ORL, vG, BEST, Wei, SH-C, and SLN all had *Er* values less than 5%, which would suggest that these models all performed well. Other models had *Er* values larger than 5%. The *Er* values of Exp, L-E, Fr(B) and Fr(T-W) in particular were very high (≥ 13%).

The mean value of MAX_e among the models differed widely from 0.042 to 0.207, indicating outlier error values of 4.2 to 20.7 percent in the cumulative fractions. The Fred-4p, Fred-3p, MLG, and Wei models showed the lowest (and very similar) outlier errors (MAX_e = 0.042 to 0.046). On the other hand, the Fr(T-W), Fr(B), L-E, and Exp models had the highest outliers ($MAX_e \geq$ 0.136).

The highest *MAEP* values were obtained with the Exp, Log, L-E, Fr(B), Fr(T-W), and Norm models (*MAEP* values between 12.5 and 21.5%). *MAEP* values of the G and J models were moderate (about 10%) and those of the other models about 6% or less. The lowest *MAEP* values were obtained for Fred-4p, Fred-3p, Wei, MLG, and AD; *MAEP* values of these models were very similar, varying between 3.91 and 4.41%.

The tendency of the models to predict cumulative fractions with outlying errors is most effectively described using MAX_{aep}. This efficiency criterion varied widely among the models from 6.7 to 47.6% (Fig. 2). The lowest values were obtained for the Fred-4p, Fred-3p, and MLG models, which produced fairly similar values between 6.7 and 8.2%. A relatively large group of models (i.e. G, Wei, BEST, AD, and ONL) had moderate MAX_{aep} values ranging from 12.9 to 16.5%. MAX_{aep} values of the other models were higher than 23.6%.

The *STDEV* of the errors of the models ranged from 0.02 to 0.11 (Fig. 2). The models having the highest standard deviations were VG, L-E, Fr(B), and Fr(T-W), whereas Fred-4p, Fred-3p, MLG, and AD models had the lowest variations in the error (i.e. the lowest *STDEV* values). These and several other efficiency criteria are partly in agreement with published results. For example, in a study evaluating the accuracy of 11 PSD models for the conversion of Chinese data to the FAO/USDA System, Shangguan et al. (2014) reported much better performance of the AD, Fred-4p, MLG, and Wei models compared to the other models. Botula et al. (2013), Zhao et al., (2011) and Hwang (2004) found the fractal models as well as the Exp and L-E models to be less accurate in their study. Evaluating the performance of 14 PSD models for characterizing the size distribution of sediments of dams in China, Zhao et al. (2011) identified Fred-4p as the best performing model, while of the 3-parameter formulations the Wei model performed the best. The J model was found to perform the best among the one-parameter models. Zhao et al. (2011) furthermore found the fractal models, Exp, Log and L-E to be the least accurate. Buchan et al. (1993) reported similar results. However, our study indicated ORL, ONL and SLN to be superior to the J model. Hwang et al. (2002) and Liu et al. (2003) identified Fred-4p as the best PSD model for a wide range of soil types.

Table 4 shows the ranking of the six most accurate models of our study in terms of the various efficiency criteria we used. The data show that using different criteria will lead to different rankings of the models. For example, if one uses NSE to rank the models, VG would be the most accurate model followed by Fred-4p, Wei, AD, Fred-3p, and MLG. On the other hand, according to the MAX_{aep} criterion, the Fred-4p model was the most accurate followed by Wei, MLG, Fred-3p, and AD, while RMSE values ranked the models as Wei, Fred-4p, Fred-3p, MLG, and ONL (Table 4). However, we note that the differences in the values of most of the criteria among the most accurate models are generally not very substantial.

Mean absolute error percentages over all soils as obtained with the six most accurate models are plotted against the particle diameter in Fig. 3. The plots indicate that the prediction error of the models depends upon the diameter at which the cumulative PSD fraction is calculated. Much higher error percentages occurred when predicting the cumulative fraction for smaller particles. When evaluating the accuracy of a certain PSD model, an important issue here is that one should consider the range of soil particle sizes for which the model will be used. A model may be accurate enough for predicting the particle diameter at a certain point or within a certain range, or maybe even on average over the entire PSD curve, but not within another range of particular sizes. Applying the model to inappropriate ranges of particle sizes may lead to large errors.

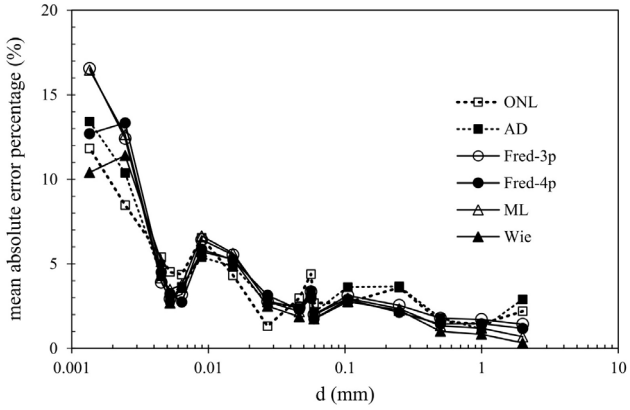

Fig. 3. Mean absolute error percentages of the six most accurate models as a function of soil particle diameter.

Classifying the evaluation criteria and PSD models

Figure 4 shows results when classifying the evaluation criteria in groups based on the level of similarity among their values. If, in this figure, the similarity of two criteria is high, their correlation will also be high. In general, the efficiency criteria were classified in two major groups, each having six subgroups.

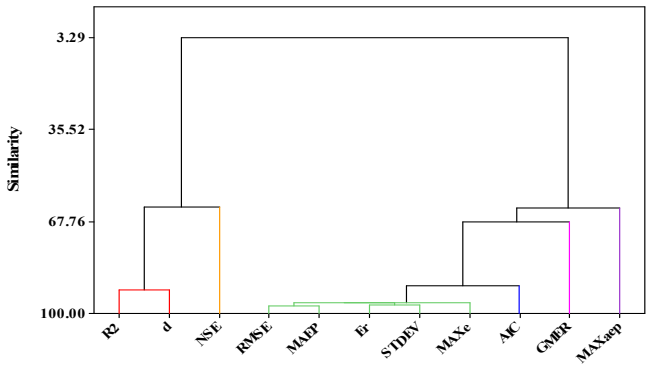

Fig. 4. Hierarchical cluster analysis of the criteria used to evaluate the accuracy of the particle-size distribution models. Information regarding the statistical criteria is given in Table 2.

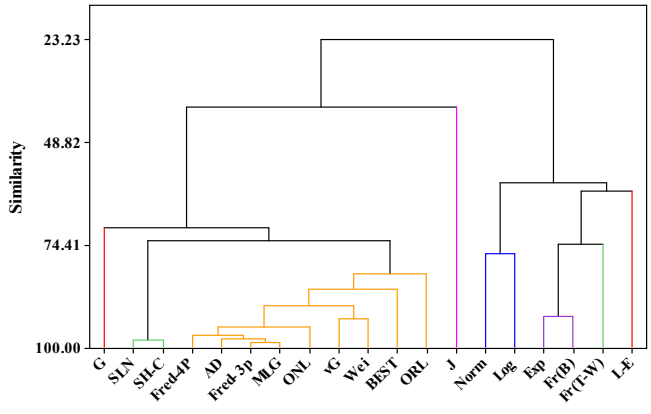

Fig. 5. Hierarchical cluster analysis of the 16 particle-size distribution models in groups based on the level of similarity among their R^2, NSE, STDEV, AIC, and GMER values. The full names and other information about the models are given in Table 1; information regarding the statistical criteria is given in Table 2.

According to these results, six criteria (i.e., R^2, *NSE*, *STDEV*, *AIC*, *GMER* and MAX_{aep}) were selected. The selected criteria were then used to classify the models into groups using a hierarchical cluster analysis based on the level of similarity in their performance (Fig. 5). According to Fig. 5, the PSD models could be classified into eight distinct group/subgroups. The similarity among the Fred-4p, Fred-3p, AD, MLG, ONL, vG, and Wei models was more than 80%. This reflects the similar performance of these seven models in terms of characterizing the PSD of our soils.

Evaluating the soil texture-dependency of the PSD models

In order to evaluate model performance per textural class, soil samples were divided into two groups based on their textural class (i.e., fine-textured and coarse-textured soils). The fine-textured (FT) soils group (n = 9) included 3 silty clay loams, 2 clay loams, one silty clay and one clay, whereas the coarse-textured (CT) soils group (n = 14) included 3 silty loams, 8 loams and 3 sandy loams. The minimum, maximum and mean contents of sand were, respectively, 8, 29, and 16% for the fine-textured and 30, 59, and 38% for the coarse-textured soils. The values for clay content of the FT and CT soil groups were 28, 52, and 41% and 8, 27, and 18%, respectively.

Several comparative studies have shown that performance of the PSD models may depend upon soil texture (e.g. Bagarello et al., 2009; Buchan, 1989; Fredlund et al., 2000; Hwang, 2004; Hwang et al., 2002; Zhao et al., 2011). These studies revealed that many or most PSD models performed better for fine-textured soils, which would imply that their performance should improve with an increase in the clay content in the soils (e.g. Fredlund et al., 2000; Hwang, 2004; Hwang et al., 2002; Zhao et al., 2011). We compared the efficacy of the best models (Fred-4p, Fred-3p, AD, MLG, ONL, and Wei) in the two soil textural groups using the t-test ($P \leq 0.05$) in terms of their mean *RMSE*, *MAEP* and *STDEV* values over all of the soils involved (Fig. 6). No matter which criterion was used for the comparison, all of the models performed significantly ($P \leq 0.05$) better in the fine textured (FT) soils group as compared to the coarse textured (CT) soils (Fig. 6).

The above results partially confirm literature findings. For example, Buchan (1989) pointed out that a log-normal (L-N) model could properly explain all regions of silty clay, silty clay loam, and silt loam soils, whereas sandy clay loams, sandy clays, and much of the clay soils should not be modeled with the L-N model. Liu et al., (2003) similarly found that the Fred-3p and MLG model produced comparable results for silty clay loam and silt loam soils, but yielded worse results for sandy loam soils. In another study, Botula et al., (2013) found that the AD model performed better for relatively fine-textured soils. The generally better performance of the PSD models for fine-textured soils may be attributed to the fact that the values of the cumulative fractions for finer particles are lower than those of coarser particles, which may lead to higher prediction errors for coarser particles. This then would produce higher values of the prediction errors for soils containing coarser particles.

We note that the rankings of the models in terms of their *RMSE* values were not the same for the fine-textured (FT) and coarse-textured (CT) groups. The ranking was Wei> Fred-4p > AD > MLG> Fred-3p > ONL for the CT group, and AD > ONL > Fred-4p > Fred-3p > MLG > Wei for the FT group. However, the ranking for all the soils combined (regardless of their texture) was AD > Fred-4p > Wei >Fred-3p > MLG > ONL.

Functional evaluation of the PSD models

The data in Table 5 indicate the different performance of the PSD models when estimating different soil PSD indicators or parameters. For example, while the AD and SH-C models predicted the nominal sand fraction (as calculated using hydrometer records at 40 s) more accurately, the ONL, Wei and VG models showed better predictions of the silt and clay fractions. The measured sand fraction (particles larger than 53 μm as estimated using sieving) was predicted more accurately with the Fred-3p and VG models. Generally, the models were more accurate in predicting the sand and clay fractions than the silt content (Table 5).

While several models were relatively accurate in estimating d_g, σ_g, D_{50}, and D_{60} values of the soils, no model was able to predict D_{30} values with acceptable accuracy (Table 5). We note that a common procedure to measure SSC fractions is to use hydrometer readings at specific times of particle settlement in soil suspensions. Resulting size fractions may not necessarily be the same as their actual values (i.e. particles of specific size groups). Also, a common procedure to measure D_{30}, D_{50}, and D_{60} is to linearly interpolate between measured cumulative PSD data that are immediately higher and lower than the required point on the PSD curve. Since the PSD curve is generally non-linear rather than linear, linear interpolation is not always appropriate and hence values derived from the fitted PSD models may be preferred.

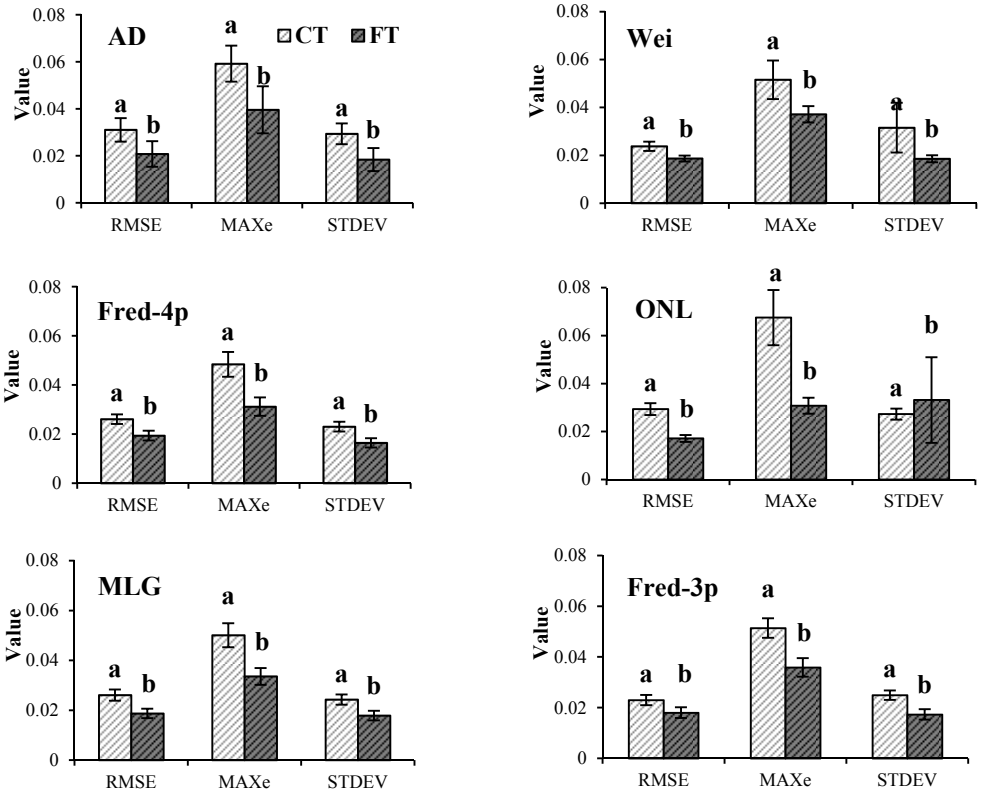

Fig. 6. Comparison of the efficacy of the six most promising particle-size distribution models for the fine-textured (FT) and coarse-textured (CT) soils. The full names and other information about the models are given in Table 1. Information regarding the statistical criteria is given in Table 2. For each criterion the non-similar letters show statistically significant differences ($P \leq 0.05$).

Table 5. Weighted R^2 (equation 2, wR^2) values of the studied particle-size distribution models to predict selected parameters of soil PSD.

	Sand	Silt	Clay	Sand measured	d_g	σ_g	D_{60}	D_{50}	D_{30}
AD	0.991	0.786	0.881	0.928	0.981	0.669	0.946	0.853	0.005
BEST	0.209	0.003	0.151	0.231	0.984	0.823	0.953	0.90	0.010
Exp	0.807	0.004	0.652	0.694	0.852	0.303	0.701	0.579	0.016
Fred-4p	0.883	0.767	0.952	0.938	0.982	0.900	0.962	0.880	0.008
Fred-3p	0.893	0.731	0.936	0.946	0.974	0.873	0.974	0.850	0.010
Fr(B)	0.807	0.004	0.652	0.695	0.852	0.302	0.016	0.013	0.016
Fr(T-W)	0.761	0.00	0.615	0.647	0.819	0.113	0.641	0.496	0.018
G	0.786	0.554	0.818	0.831	0.901	0.929	0.930	0.835	0.001
J	0.826	0.005	0.822	0.665	0.497	0	0.529	0.532	0.010
SLN	0.962	0.590	0.876	0.833	0.827	0.877	0.770	0.768	0.006
Log	0.694	0.000	0.790	0.603	0.806	0.432	0.727	0.850	0.004
L-E	0.807	0.004	0.652	0.694	0.852	0.303	0.696	0.560	0.017
MLG	0.903	0.825	0.961	0.938	0.988	0.891	0.966	0.860	0.009
Norm	0.692	0.406	0.591	0.731	0.746	0.727	0.778	0.811	0.006
ONL	0.937	0.892	0.933	0.901	0.948	0.808	0.908	0.867	0.007
ORL	0.928	0.779	0.882	0.917	0.995	0.567	0.918	0.824	0.008
SH-C	0.963	0.592	0.867	0.834	0.827	0.877	0.770	0.769	0.006
VG	0.889	0.741	0.962	0.940	0.927	0.855	0.911	0.857	0.009
Wei	0.913	0.883	0.967	0.933	0.999	0.950	0.961	0.873	0.008

Correlation of PSD parameters with soil physical properties

We next correlated various representations of the soil PSD (e.g. SSC, d_g and σ_g, D_{50} and D_{60}, as well as the model parameters of the most accurate PSD models) with selected soil physical properties. While neither SSC nor d_g, σ_g, D_{50} and D_{60} showed significant statistical correlations with either K_{fs} or $\log K_{fs}$, the fitted parameters of several PSD models correlated significantly with K_{fs} and/or $\log K_{fs}$, as shown in Table 6. Most of the correlations were stronger with $\log K_{fs}$ as compared to K_{fs}. Since K_{fs} is known to be one of the most variable soil properties, finding effective inputs to derive PTFs for K_{fs} remains a challenge (e.g. Mbonimpa et al., 2002). Our results suggest that the use of fitting parameters of the PSD models provides an attractive alternative to account for the effects of soil texture on K_{fs}.

Correlations between the mean weight diameter (MWD) of soil aggregates with selected PSD model parameters were generally higher for either SSC, d_g or D_{50} and D_{60} (Table 6). While, Φ and ρ_b correlated significantly with selected fitting parameters of the PSD models, ρ_b showed also significant correlation with many or most geometric (d_g), mechanical (D_{50} and D_{60}), and agronomic (clay and sand) representations of the PSDs (Table 6), with the exception of the parameters m (Fred-3p) and c (Wei) which showed essentially no correlations. The parameters d_f (Fred-4p), δ (ONL), b_0 (AD), c_0 (AD) correlated only with σ_g, while m (Fred-4p) had a significant positive correlation

Table 6. Correlations between various PSD model parameters and selected soil physical properties.

	K_{fs}	logK_{fs}	MWD	Φ	ρb	d_g	σ_g	D_{50}	D_{60}	*Clay*	*Silt*	*Sand*
α (Fred-4p)	–0.36	–0.26	–0.67**	–0.27	0.52*	0.87**	0.61**	0.78***	0.87***	–0.67***	–0.66***	0.87***
d_f (Fred-4p)	0.18	0.23	–0.14	–0.03	–0.06	0.21	0.50*	0.08	0.17	–0.02	–0.24	0.13
m (Fred-4p)	0.39	0.30	0.17	–0.19	-0.11	–0.17	–0.08	–0.08	–0.13	–0.19	0.55**	–0.07
n (Fred-4p)	–0.38	–0.66*	–0.27	–0.14	0.48*	0.54**	0.05	0.64**	0.64**	–0.48*	–0.36	0.58**
c(ONL)	–0.48*	–0.44*	–0.63**	–0.28	0.61**	0.88***	0.50*	0.78***	0.85***	–0.66***	–0.68***	0.87***
μ (ONL)	–0.32	–0.38	–0.62**	–0.43*	0.68**	0.95***	0.46*	0.87***	0.91***	–0.92***	–0.45*	0.97***
δ (ONL)	–0.01	–0.28	–0.16	–0.07	–0.19	–0.11	0.67**	–0.37	–0.22	0.19	–0.09	–0.11
b_0 (AD)	0.11	0.24	–0.22	-0.20	0.01	0.20	0.57**	–0.04	0.05	–0.25	–0.03	0.22
c_0(AD)	–0.25	–0.29	0.22	0.32	–0.15	–0.23	–0.60**	0.08	0.01	0.21	–0.03	–0.16
d_0(AD)	–0.37	–0.30	–0.62**	–0.27	0.57**	0.96***	0.41	0.94***	0.96***	–0.73***	–0.68**	0.91***
f_0 (AD)	–0.23	–0.25	–0.36	0.19	0.09	0.41	0.02	0.40	0.44*	–0.05	–0.58**	0.31
α (Fred-3p)	–0.40	–0.38	–0.65**	–0.28	0.60**	0.95***	0.48*	0.91***	0.96***	–0.73***	–0.68***	0.93***
m (Fred-3p)	0.38	0.39	0.43	0.05	–0.40	–0.36	–0.02	–0.35	–0.41	0.24	0.31	–0.34
n (Fred-3p)	–0.42*	–0.65**	–0.38	–0.17	0.49*	0.60**	0.04	0.72***	0.70***	–0.61**	–0.27	0.65**
a (MLG)	0.59**	0.53*	0.47*	0.40	–0.72***	–0.59**	–0.25	–0.53**	–0.60**	0.57**	0.31	–0.62**
b (MLG)	0.46*	0.39	0.59**	0.37	–0.62**	–0.68***	–0.64**	–0.58**	–0.71***	0.63**	0.46*	–0.75***
c (MLG)	–0.43*	–0.60**	–0.52*	–0.20	0.55**	0.75***	0.33	0.77***	0.79***	–0.71***	–0.39	0.80***
a (Wei)	–0.02	–0.20	0.32	0.29	–0.31	–0.50*	–0.79***	–0.36	–0.43*	0.32	0.57**	–0.54**
b (Wei)	–0.33	–0.53**	–0.43	–0.19	0.48*	0.60**	–0.00	0.72***	0.69***	–0.75***	–0.07	0.67***
c (Wei)	–0.37	–0.25	–0.19	0.27	–0.08	–0.05	–0.15	–0.01	–0.00	0.37	–0.34	–0.12
d_g	–0.27	–0.35	–0.53*	–0.42*	0.65**	1.00						
σ_g	–0.11	0.04	–0.40	–0.27	0.26	–0.40	1.00					
D_{50}	–0.33	–0.37	–0.53*	–0.29	0.63**	0.97***	0.25	1.00				
D_{60}	–0.35	–0.34	–0.61**	–0.28	0.63**	0.97***	0.40	0.95***	1.00			
Clay	0.18	0.33	0.51**	0.44*	–0.61**	–0.82***	–0.32	–0.76***	–0.77***	1.00		
Silt	0.39	0.22	0.35	0.11	–0.37	–0.54**	–0.36	–0.63**	–0.63**	0.11	1.00	
Sand	–0.34	–0.38	–0.59**	–0.41*	0.68***	0.97***	0.43*	0.93***	0.94***	–0.88***	–0.58**	1.00

*, **, and ***: indicate significant correlation at $P \leq 0.05$, $P \leq 0.01$, and $P \leq 0.001$, respectively. Soil bulk density (ρ_b), soil total porosity (Φ), Field saturated soil hydraulic conductivity (K_{fs}), Mean Weight Diameter of soil aggregates (MWD).

only with silt content (Table 6). The values of α (Fred-4p), d_f (Fred-4p), n (Fred-4p), c (ONL), μ (ONL), d_0 (AD), α (Fred-3p), n (Fred-3p), c (MLG), and b (Wei) correlated positively with soil particle size. These parameters increased with the size of soil particles, while the parameters a (MLG), b (MLG), and a (Wei) decreased with increasing soil particle size. Furthermore, as shown in Table 6, values of α (Fred-4p), d_f (Fred-4p),c (ONL), μ (ONL), δ (ONL), b_0 (AD), α (Fred-3p) increased with a widening of the PSD range (as reflected by the standard deviation of the soil particle diameter, σ_g). However, c_0 (AD), b (MLG), and a (Wei) decreased with increasing σ_g values.

CONCLUSIONS

In this preliminary study we investigated the feasibility of 19 models to describe measured soil particle-size distributions (PSDs) of 24 different soils in terms of different efficiency criteria. Results indicate that rankings of the model performance differed depending upon the particular efficiency criteria considered. For example, *RMSE*, MAX_e, and *STDEV* values varied widely among the PSD models, which implies that these criteria all represented different aspects of the accuracy of the models. Six models were found to provide the most accurate results: a modified logistic growth function (MLG), Fredlund type models with 3 and 4 parameters (Fred-3p and Fred-4p), an Anderson type model (AD), an offset nonrenormalized lognormal function (ONL), and a Weibull type function (Wei). Prediction errors of these models depended on the particle diameter at which the cumulative PSD fraction was estimated. Accuracies were found to decrease with increasing soil particle diameter. This implies that one should consider the range of sizes of the soil particles for which the model will be used. A model may be acceptable for some range of the particle diameter, or the entire PSD, but not necessarily for other particle sizes. Based on the mean values of the *RMSE*, MAX_e, and *STDEV*, all of the selected models performed significantly better for fine-textured soils as compared to coarse-textured soils.

The fitting parameters of selected PSD models showed statistically significant correlations with several soil quality indices such as K_{fs}, MWD, soil porosity, and soil bulk density. These results may be used to advantage in future studies to derive more accurate pedotransfer functions (PTFs) for estimating the unsaturated soil hydraulic properties and/or related soil physical parameters from PSD data. Still, we acknowledge that the number of soil samples (n = 24) used in this study is not sufficient to draw strong conclusions. A similar analysis as followed herein, but with a much larger soils database, may be needed to obtain more definite conclusions.

Acknowledgements. This work was supported by the Iran National Science Foundation [grant No. 91002216] and Urmia University [grant No. 93/K/023].

REFERENCES

Andersson, S., 1990. Markfysikaliska undersokningar I odlad jord, XXVI. Om mineraljordens och mullens rumsutfyllande egenskaper. En Teoretisk Studie. Swedish University of

Agricultural Sciences, Uppsala, Sweden. (In Swedish.)
Arya, L.M., Paris, J.F., 1981. A physicoempirical model to predict the soil moisture characteristic from particle-size distribution and bulk density data. Soil Sci. Soc. Am., J., 45, 6, 1023–1030.
Assouline, S., Tessier, D., Bruand, A., 1998. A conceptual model of the soil water retention curve. Water Resour. Res., 34, 223–231.
Bagarello, V., Provenzano, G., Sgroi, A., 2009. Fitting particle size distribution models to data from Burundian soils for the BEST procedure and other purposes. Biosyst Eng., 104, 435–441.
Bah, AR., Kravchuk, O., Kirchhof, G., 2009. Fitting performance of particle-size distribution models on data derived by conventional and laser diffraction techniques. Soil Sci. Soc. Am. J., 73, 1101–1107.
Banaei, M.H., 1998. Soil moisture and temperature regime map of Iran. Soil and Water Research Institute, Ministry of Agriculture, Iran.
Bayat, H., Rastho, M., Zadeh, M.M., Vereecken, H., 2015. Particle size distribution models, their characteristics and fitting capability. J. Hydrol., 529, 872–889.
Beke, G., Lindwall, C., Entz, T., Channappa, T., 1989. Sediment and runoff watercharacteristics as influenced by cropping and tillage practices. Can. J. Soil Sci., 69, 3, 639–647.
Bird, N.R.A., Perrier, E., Rieu, M., 2000. The water retention function for a model of soil structure with pore and solid fractal distributions. Eur. J. Soil Sci., 51, 55–63.
Bittelli, M., Campbell, G.S., Flury, M., 1999. Characterization of particle-size distribution in soils with a fragmentation model. Soil Sci. Soc. Am. J., 63, 782–788.
Blake, G.R., Hartge, K.H., 1986. Bulk density. In: Klute, A. (Ed.): Methods of Soil Analysis. Part 1. 2nd Ed. Agron. Monogr. 9. ASA. Madison. WI. 375 p.
Bolster, C.H., Hornberger, G.M., 2007. On the use of linearized Langmuir equations. Soil Sci. Soc. Am. J., 71, 1796–1806.
Botula, Y.D., Cornelis, W.M., Baert, G., Mafuka, P., Van Ranst, E., 2013. Particle size distribution models for soils of the humid tropics. J. Soils Sed., 13, 686–698.
Buchan, G.D., 1989. Applicability of the simple lognormal model to particle-size distribution in soils. Soil Sci., 147, 155–161.
Buchan, G.D., Grewal, K.S., Robson, A.B., 1993. Improved models of particle- size distribution: An illustration of model comparison techniques. Soil Sci. Soc. Am. J., 57, 901–908.
Carsel, R.F., Parrish, R.S., 1988. Developing joint probability distributions of soil water retention characteristics. Water Resour. Res., 24, 755–769.
Chapuis, R.P., 2012. Predicting the saturated hydraulic conductivity of soils: a review. Bull Eng Geol Environ., 71, 401–434.
Ersahin, S., Gunal, H., Kutlu, T., Yetgin, B., Coban, S., 2006. Estimating specific surface area and cation exchange capacity in soils using fractal dimension of particle size distribution. Geoderma, 136, 3, 588–597.
Fredlund, M.D., Fredlund, D.G., Wilson, G.W., 2000. An equation to represent grain-size distribution. Can. Geotech. J., 37, 817–827.
Gee, G.W., Or, D., 2002. Particle-size analysis. In: Dane, J.H., Topp, G.C. (Eds.): Methods of Soil Analysis. Part 4. SSSA Book Series No. 5. SSSA, Madison, WI. pp. 255–293.
Ghorbani Dashtaki, S., Homaee, M., Khodaverdiloo, H., 2010. Derivation and validation of pedotransfer functions for estimating soil water retention curve using a variety of soil data. Soil Use Manage., 26, 68–74.
Ghorbani-Dashtaki, S., Homaee, M., Loiskandl, W., 2016. Towards using pedotransfer functions for estimating infiltration parameters. Hydrol. Sci. J., 61, 1477–1488. DOI: 10.1080/02626667.2015.1031763.
Gimenez, D., Rawls, W.J., Pachepsky, Y., Watt, J.P.C., 2001. Prediction of a pore distribution factor from soil textural and mechanical parameters. Soil Sci., 166, 79–88.
Haverkamp, R., Parlange, J.Y., 1986. Predicting the water retention curve from a particle size distribution: 1. Sandy soils without organic matter. Soil Sci., 142, 325–339.
Hwang, S.I., 2004. Effect of texture on the performance of soil particle size distribution models. Geoderma, 123, 363–371.
Hwang, S.I., Powers, S.E., 2003. Using particle-size distribution models to estimate soil hydraulic properties. Soil Sci. Soc. Am. J., 67, 1103–1112.
Hwang, S.I., Lee, K.P., Lee, D.S., Powers, S.E., 2002. Models for estimating soil particle-size distributions. Soil Sci. Soc. Am. J., 66, 1143–1150.
Jabro, J.D., 1992. Estimation of saturated hydraulic conductivity of soils from particle size distribution and bulk density data. Am. Soc. Agric. Eng., 35, 557–560.
Jaky, J., 1944. Soil Mechanics. Egyetemi Nyomada, Budapest, Hungary.
Khodaverdiloo, H., Samadi, A., 2011. Batch equilibrium study on sorption, desorption, and immobilization of cadmium in some semiarid-zone soils as affected by soil properties. Soil Res., 49, 5, 444–454.
Khodaverdiloo, H., Homaee, M., Van Genuchten, M.T., Ghorbani Dashtaki, S., 2011. Deriving and validating pedotransfer functions for some calcareous soils. J. Hydrol., 399, 93–99.
Kolev, B., Rousseva, S., Dimitrov, D., 1996. Derivation of soil water capacity parameters from standard soil texture information for Bulgarian soils. Ecol. Model., 84, 315–319.
Krause, P., Boyle, D.P., Bäse, F., 2005. Comparison of different efficiency criteria for hydrological model assessment. Adv Geosci., 5, 89–97.
Lassabatère, L., Angulo-Jaramillo, R., Soria Ugalde, J.M, Cuenca, R., Braud, I., Haverkamp, R., 2006. Beerkan estimation of soil transfer parameters through infiltration experiments – BEST. Soil Sci. Soc. Am. J., 70, 521–532.
Liao, K., Xu, S., Zhu, Q., 2015. Development of ensemble pedotransfer functions for cation exchange capacity of soils of Qingdao in China. Soil Use Manag., 31, 483–490.
Liu, J., Xu, S., Liu, H., 2003. Investigation of different models to describe soil particle- size distribution data. Adv. Water Sci., 14, 588–592.
Liu, J., Xu, S., Liu, H., Guo, F., 2004. Application of parametric models to description of particle-size distribution in loamy soils. Acta Pedologica Sinica, 41, 375–379.
Manrique, L.A., Jones, C.A., Dyke, P.T., 1991. Predicting cation exchange capacity from soil physical and chemical properties. Soil Sci. Soc. Am. J., 55, 787–794.
Mbonimpa, M., Aubertin, M., Chapuis, R.P., Bussiere, B., 2002. Practical pedotransfer functions for estimating the saturated hydraulic conductivity. Geotech. Geol. Eng., 20, 235–259.
Nemes, A., Wosten, J.H.M., Lilly, A., Voshaar, J.H.O., 1999. Evaluation of different procedures to interpolate particle-size distributions to achieve compatibility within soil databases. Geoderma, 90, 187–202.
Nemes, A., Schaap, M.G., Wösten, J.H.M., 2003. Functional evaluation of pedotransfer functions derived from different scales of data collection. Soil Sci. Soc. Am. J., 67, 1093–1102.

Parchami-Araghi, F., Mirlatifi, S.M., GhorbaniDashtaki, S., Mahdian, M.H., 2013. Point estimation of soil water infiltration process using Artificial Neural Networks for some calcareous soils. J. Hydrol., 481, 35–47.

Patil, N.G., Singh, S.K., 2016. Pedotransfer functions for estimating soil hydraulic properties: A review. Pedosphere, 26, 4, 417–430.

Razzaghi, S., Khodaverdiloo, H., Dashtaki, S.G., 2016. Effects of long-term wastewater irrigation on soil physical properties and performance of selected infiltration models in a semi-arid region. Hydrol. Sci. J., 61, 10, 1778–1790.

Saxton, K.E., Rawls, W.J., Romberger, J.S., Pependick, R.I., 1986. Estimating generalized soil water characteristics from soil texture. Soil Sci. Soc. Am. J., 55, 1231–1238.

Shangguan, W., Yongjiu, D., Gutierrez, C.G., Yuan, H., 2014. Particle-size distribution models for the conversion of Chinese data to FAO/USDA system. Sci. World J. DOI: 10.1155/2014/109310.

Shiozawa, S., Campbell, G.S., 1991. On the calculation of mean particle diameter and standard deviation from sand, silt, and clay fractions. Soil Sci., 152, 427–431.

Shirazi, M.A., Boersma, L., 1984. A unifying quantitative analysis of soil texture. Soil Sci. Soc. Am. J., 48, 142–147.

Shirazi, M.A., Hart, J.W., Boersma, L., 1988. A unifying quantitative analysis of soil texture: improvement of precision and extension of scale. Soil Sci. Soc. Am. J., 52, 1, 181–190.

Skaggs, T.H., Arya, L.M., Shouse, P.J., Mohanty, B.P., 2001. Estimating particle size distribution from limited soil texture data. Soil Sci. Soc. Am. J., 65, 1038–1044.

Tyler, S.W., Wheatcraft, S.W, 1992. Fractal scaling of soil particle-size distributions: analysis and limitations. Soil Sci. Soc. Am. J., 56, 362–369.

Vipulanandan, C., Ozgurel, H.G., 2009. Simplified relationships for particle-size distribution and permeation groutability limits for soils. J. Geotech. Geoenviron. Eng., 135, 1190–1197.

Willmott, C.J., 1981. On the validation of models. Phys. Geogr. 2, 184–194.

Xu, G., Li, Z., Li, P., 2013. Fractal features of soil particle-size distribution and total soil nitrogen distribution in a typical watershed in the source area of the middle Dan River, China. Catena, 101, 17–23.

Zhao, P., Shao, M., Horton, R., 2011. Performance of soil particle-size distribution models for describing deposited soils adjacent to constructed dams in the China loess plateau. Acta Geophysica, 59, 124–138.

Zhuang, J., Jin, Y., Miyazaki, T., 2001. Estimating water retention characteristic from soil particle-size distribution using a non-similar media concept. Soil Sci., 166, 308–321.

Received 28 June 2017
Accepted 19 October 2017

J. Hydrol. Hydromech., 67, 2019, 2, 191–200
DOI: 10.2478/johh-2018-0023

Using Beerkan experiments to estimate hydraulic conductivity of a crusted loamy soil in a Mediterranean vineyard

Vincenzo Alagna[1], Vincenzo Bagarello[1], Simone Di Prima[2*], Fabio Guaitoli[3], Massimo Iovino[1], Saskia Keesstra[4, 5], Artemi Cerdà[4, 6]

[1] Department of Agricultural, Food and Forest Sciences, University of Palermo, Viale delle Scienze, 90128 Palermo, Italy.
[2] Agricultural Department, University of Sassari, Viale Italia, 39, 07100 Sassari, Italy.
[3] Assessorato regionale dell'Agricoltura, dello Sviluppo Rurale e della Pesca Mediterranea, UO S5.05, Viale Regione Siciliana 2771, 90145 Palermo Italy.
[4] Team Soil Water and Land Use, Wageningen Environmental Research, Wageningen UR, Droevendaalsesteeg 3, 6700 AA Wageningen, The Netherlands.
[5] Civil, Surveying and Environmental Engineering, The University of Newcastle, Callaghan 2308, Australia.
[6] Department of Geography, University of Valencia, Blasco Ibáñez, 28, 46010 València, Spain.
[*] Corresponding author. E-mail: sdiprima@uniss.it

Abstract: In bare soils of semi-arid areas, surface crusting is a rather common phenomenon due to the impact of raindrops. Water infiltration measurements under ponding conditions are becoming largely applied techniques for an approximate characterization of crusted soils. In this study, the impact of crusting on soil hydraulic conductivity was assessed in a Mediterranean vineyard (western Sicily, Italy) under conventional tillage. The BEST (Beerkan Estimation of Soil Transfer parameters) algorithm was applied to the infiltration data to obtain the hydraulic conductivity of crusted and uncrusted soils. Soil hydraulic conductivity was found to vary during the year and also spatially (i.e., rows vs. inter-rows) due to crusting, tillage and vegetation cover. A 55 mm rainfall event resulted in a decrease of the saturated soil hydraulic conductivity, K_s, by a factor of 1.6 in the inter-row areas, due to the formation of a crusted layer at the surface. The same rainfall event did not determine a K_s reduction in the row areas (i.e., K_s decreased by a non-significant factor of 1.05) because the vegetation cover intercepted the raindrops and therefore prevented alteration of the soil surface. The developed ring insertion methodology on crusted soil, implying pre-moistening through the periphery of the sampled surface, together with the very small insertion depth of the ring (0.01 m), prevented visible fractures. Consequently, Beerkan tests carried out along and between the vine-rows and data analysis by the BEST algorithm allowed to assess crusting-dependent reductions in hydraulic conductivity with extemporaneous measurements alone. The reliability of the tested technique was also confirmed by the results of the numerical simulation of the infiltration process in a crusted soil. Testing the Beerkan infiltration run in other crusted soils and establishing comparisons with other experimental methodologies appear advisable to increase confidence on the reliability of the method that seems suitable for simple characterization of crusted soils.

Keywords: Hydraulic conductivity; Water infiltration measurements; Soil surface crust; Vineyard; BEST procedure.

INTRODUCTION

The impact of raindrops on a bare soil surface can result in physical and chemical changes of the exposed soils. The mechanical alteration of the upper soil aggregates can determine development of a surface crust (Assouline, 2004). This type of crust, named structural crust, differs from a depositional crust (West et al., 1992), which is formed by deposition of detached, fine particles transported in suspension by runoff (Fox et al., 1998). The hydraulic properties of crusts vary significantly as compared with the non-altered soil (Fox et al., 1998). Different physical rainfall properties may be related with structural crust development, such as intensity (Freebairn et al., 1991), kinetic energy (Eigel and Moore, 1983) and momentum (Brodie and Rosewell, 2007; Rose, 1960). The initial or wetting phase in crust formation is defined as surface sealing (Römkens, 1979). During the drying cycle, this layer consolidates and may differ from the wetting phase in its mechanical and hydraulic properties (Mualem et al., 1990). This drying phase is known as crusting (Römkens, 1979).

The hydrodynamic properties of such a layered system (crust layer, underlying soil) may severely affect the partition between infiltration and runoff at the soil surface, especially in arid and semi-arid areas where crusting is a common phenomenon (Angulo-Jaramillo et al., 2016; Assouline, 2004). Water infiltration measurements are becoming common for an indirect characterization of sealed/crusted soils (Bedaiwy, 2008). For instance, Vandervaere et al. (1997) developed a field method using a tension infiltrometer and a minitensiometer inserted laterally at the crust-underlying soil interface. The minitensiometer is used to detect the arrival of the wetting front and thus to separate the water infiltration in the crust solely from that in the entire crust-soil medium. However, minitensiometer installation may be problematic, especially for crust layer thinner than 1 cm. Moreover, in crusts with high surface roughness, some issue may be encountered to ensure the hydraulic contact between the disk and the surface crust.

The Beerkan Estimation of Soil Transfer (BEST) parameters procedure developed by Lassabatere et al. (2006) is a very attractive method for practical use since it allows an estimation of both the soil water retention and hydraulic conductivity functions. The BEST method focuses specifically on the van Genuchten (1980) relationship for the water retention curve with the Burdine (1953) condition and the Brooks and Corey (1964) relationship for hydraulic conductivity. BEST estimates shape parameters of the assumed relationships, which are tex-

ture dependent, from particle-size analysis by physical-empirical pedotransfer functions, and scale parameters from Beerkan experiments (Haverkamp et al., 1996), i.e. three-dimensional (3D) field infiltration experiments at ideally zero pressure head. Following Reynolds and Elrick (2005), ring infiltration data are essentially representative of vertical soil water transmission parameters since rings establish downward flow. BEST substantially facilitates the hydraulic characterization of unsaturated soils, and it is gaining popularity in soil science (e.g., Di Prima et al., 2018b; Gonzalez-Sosa et al., 2010). Alternative algorithms, i.e., BEST-slope (Lassabatere et al., 2006), BEST-intercept (Yilmaz et al., 2010) and BEST-steady (Bagarello et al., 2014b), and field procedures based on BEST method were developed (Alagna et al., 2016). The ability of the BEST method to assess the effect of surface crust on the soil hydraulic properties was demonstrated by Souza et al. (2014) in a cropped soil located in the north-eastern region of Brazil. Moreover, Di Prima et al. (2017, 2018a) successfully applied a Beerkan experiment involving different heights of water pouring on the infiltration surface to explain surface runoff and sealing generation phenomena occurring during intense rainfall events. These authors concluded that if any seal forms at the surface, the Beerkan infiltration test should detect its impact on flow and BEST estimates should essentially indicate the hydraulic properties of the surface layer. In fact, the BEST method was developed for non-layered soils that are assumed to be uniform and have a uniform soil water content at the beginning of the infiltration run (Lassabatere et al., 2006, 2009) and should not contain a macropore network (Lassabatere et al., 2014). However, completely homogeneous soils are very rare in natural environments (Reynolds and Elrick, 2002). Therefore, the hydraulic conductivity obtained by an infiltrometer method, such as BEST, should probably be considered as an equivalent conductivity, i.e. the conductivity of a rigid, homogeneous and isotropic porous medium characterized by infiltration rates that are the same as those actually measured on the real soil (Bagarello et al., 2010). For the case of stratified media, the layer with the lowest hydraulic conductivity generally controls the flow and, consequently, cumulative infiltration at the surface (Alagna et al., 2013). Therefore, water infiltration data can be regarded as representative of the hydraulic behavior of the least permeable layer, and therefore the derived BEST parameters can be assigned to this layer. This approach was proposed by Lassabatere et al. (2010) for a stratified medium with a low permeability sedimentary layer at the surface, Yilmaz et al. (2013, 2010) for the characterization of crusted reactive materials and, recently, Coutinho et al. (2016) for a permeable pavement for stormwater management in an urban area. Although Souza et al. (2014) firstly demonstrated the ability of BEST to properly characterize a crusted soil, testing this assumption is necessary to assess the real potential of BEST for the case of a soil with a fine layering organization. In other words, while discrepancies between crusted and no-crusted soils are expected to be detected by the BEST procedure, in the scientific literature there is no exhaustive testing of the BEST capacity to yield reliable hydraulic properties of the crust layer solely.

In this paper we tested the BEST method in an agricultural setting with the general objective to carry out a hydraulic characterization of a loamy soil in a vineyard under conventional tillage located at Marsala (western Sicily, Italy). In particular, both row and inter-row areas were sampled since a crust layer only developed in the latter area. Therefore, the specific objective was to check the ability of the BEST method to yield plausible estimates of saturated hydraulic conductivity of crusted and non-crusted soils. The ability of the proposed technique to give a hydraulic characterization of the surface crust was then assessed by numerical simulation of the infiltration process in the two-layer system formed by the crust and the underlying soil.

MATERIAL AND METHODS

Study site

The experimental site is located close to Marsala (western Sicily, Italy), in the homeland of Sicilian viticulture (37°48'5.10" N and 12°30'44.79" E). Elevation is 111 m a.s.l. and soil surface is flat. The soil is a typic Rhodoxeralf with a depth of 1 m and a small amount of gravel. According to USDA classification, the soil texture, determined on two replicated soil samples, is loam (Table 1). A weather station is located 5 km away from the sampling site (37°79'35.64"N and 12°56'81.59"E). It is positioned at the same elevation as the sampling site and it is part of a network of stations managed by Servizio Informativo Agrometeorologico Siciliano – SIAS.

Table 1. Clay (%), silt (%) and sand (%) content (Soil Survey Staff, 2014), soil textural classification, hydraulic shape parameters m, n and η (–), dry soil bulk density, ρ_b (g cm^{-3}), and saturated soil water content, θ_s (cm^{3}cm^{-3}), of the sampled vineyard soil. Coefficient of variation (%) in brackets.

Variable	Site characteristic
clay	19.7
silt	49.6
sand	30.7
textural classification	loam
m	0.079
n	2.172
η	14.6
ρ_b	1.128 (5.1)
θ_s	0.575 (3.8)

At the experimental site, the common soil management for the vineyards of Marsala was applied during the two years of sampling (2015 and 2016) (Figure 1). The soil is tilled to a depth of 0.10–0.15 m in October, after the first autumn rainfalls. Faba bean (*Vicia faba* L. var. *minor*) is sown in November between the rows. In March, the legume biomass is cut and immediately incorporated into the soil with a rotary tiller to a depth of 0.20 m. Finally, a new rotary tillage is performed in May and, only for the second year, this was also done in June. This soil management practice is applied between the rows. Along the rows, a mechanical topper is used at each soil tillage date to a depth of 0.10 m.

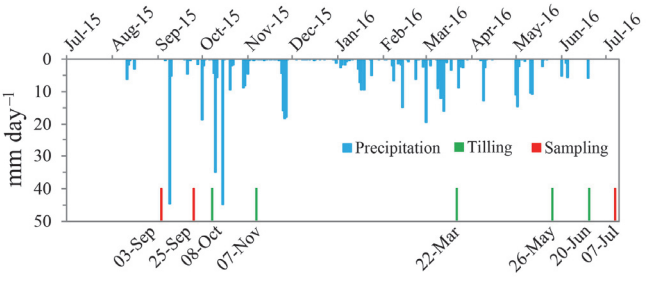

Fig. 1. Precipitation and soil management program during the study period. The sampling dates are reported.

Soil sampling

An area of approximately 100 m^2 was sampled on three different sampling campaigns covering two growing seasons. The first two campaigns were carried out at the beginning and the end of September 2015, respectively, and the third campaign was performed at the beginning of July 2016. Between the first two sampling campaigns, the soil was left bare and not tilled, and a total rainfall of 55 mm fell (Figure 1), which is approximately 10% of the average annual precipitation for the area. In particular, a 29-mm event occurred during the morning of 9 September, with a maximum recorded intensity of 25 mm h^{-1}. During the same day, a total of 44.6 mm of precipitation was recorded. This rainfall led to the development of a weak but clearly detectable surface crust (thickness of ~4 mm) (Figure 2). This phenomenon was only observed between the rows and not along the rows. The second sampling was done one week after the last rainfall event. Finally, a third sampling campaign was carried out during the following dry season in order to sample the soil after the ordinary tillage practices and with moisture conditions comparable to the first sampling date.

On each sampling date, a total of 10 undisturbed soil cores (5 cm in height by 5 cm in diameter) were collected at the soil surface close to the points where the infiltration tests were performed, 5 along the rows and 5 between the rows. These cores were used to determine the dry soil bulk density, ρ_b (g cm^{-3}), and the soil water content at the time of the experiment, θ_i (cm^3 cm^{-3}). The soil porosity was calculated from the ρ_b data, assuming a soil particle density of 2.65 g cm^{-3}. A disturbed soil sample (0–10 cm depth), collected both along and between the rows, was used to determine the particle size distribution (PSD), using conventional methods (Gee and Bauder, 1986). Fine size fractions were determined by the hydrometer method, whereas the coarse fractions were obtained by mechanical dry sieving. The clay, silt and sand percentages were determined from the measured PSD according to USDA standards.

Fig. 2. Surface crust layer developed after the intense storms fallen the 9th of September 2015, and encountered on the soil surface between the vineyard rows during the second field campaign (see Figure 1). Photo by V. Alagna.

Beerkan experiments

For each sampling date, an area of approximately 100 m^2 was chosen and 14 Beerkan infiltration runs (Lassabatere et al., 2006) were carried out using a 15 cm inner-diameter ring. Seven runs were carried out along the rows and seven on the bare inter-rows area. The steel ring was positioned between two vine stocks along the row and in the same orthogonal direction between the rows. The ring was inserted to a depth of about 0.01 m into the soil surface to avoid lateral loss of the ponded water. On crusted soil, to prevent fracture of the upper layer during ring insertion, the soil outside the hedge of the ring was moistened with 5 cm^3 of water by means of a syringe before insertion. Due to the very limited thickness of the crust, insertion of the minitensiometer requested by the Vandervaere et al. (1997) method would have been problematic resulting in disruption of the crust. After ten minutes, the ring was carefully inserted to the pre-established short depth applying a slight pressure and a gentle rotation. This site preparation was essential to prevent visible crust surface perturbation.

According to the guidelines by Lassabatere et al. (2006), for each run a known volume of water (150 mL) was poured in the cylinder at the start of the experiment and the elapsed time during its infiltration was measured. When the amount of water had completely infiltrated, another identical volume of water was poured on the confined infiltration surface and the time needed for the complete infiltration was logged. The procedure was repeated 15 times for each run by applying water at a small distance (3 cm of height) from the infiltration surface. As is commonly suggested in practical application of a ponding infiltration method, the energy of the water due to the application was dissipated on the fingers of a hand in order to minimize soil disturbance (Reynolds, 2008).

As mentioned before, BEST focuses specifically on the following relationships to describe the water retention curve (Burdine, 1953; van Genuchten, 1980) and the hydraulic conductivity function (Brooks and Corey, 1964):

$$\frac{\theta-\theta_r}{\theta_s-\theta_r}=\left[1+\left(\frac{h}{h_g}\right)^n\right]^{-m} \tag{1a}$$

$$m=1-\frac{2}{n} \tag{1b}$$

$$\frac{K(\theta)}{K_s}=\left(\frac{\theta-\theta_r}{\theta_s-\theta_r}\right)^{\eta} \tag{2a}$$

$$\eta=\frac{2}{n\times m}+3 \tag{2b}$$

where θ (cm^3 cm^{-3}) is the volumetric soil water content, θ_r (cm^3 cm^{-3}) is the residual volumetric soil water content, θ_s (cm^3 cm^{-3}) is the saturated volumetric soil water content, h_g (mm) is the van Genuchten pressure scale parameter, K (L T^{-1}) is the soil hydraulic conductivity, and n, m and η are shape parameters linked to the soil textural properties. In BEST, these last parameters are estimated from the analysis of the PSD with the pedotransfer function included in the procedure. Taking into account that a low spatial and temporal variability is expected for soil texture at the field scale (Warrick, 1998), representative values of the shape parameters for the field site were obtained by averaging the individual determinations (Table 1). BEST considers θ_r to be zero, and θ_s was assumed to coincide with soil porosity in this investigation, as suggested by many authors (e.g., Castellini et al., 2018; Coutinho et al., 2016; Di Prima, 2015; Mubarak et al., 2010, 2009; Xu et al., 2009; Yilmaz et al., 2010). Moreover, Di Prima et al. (2017) demonstrated that the assumed coincidence between saturated soil water content and porosity affects only marginally K_s estimation.

BEST-slope estimates sorptivity, S (mm $h^{-0.5}$), by fitting the experimental cumulative infiltration data on the explicit transient two-term equation by Haverkamp et al. (1994):

$$I(t) = S\sqrt{t} + \left[A(1-B)S^2 + Bi_s\right] t \quad (3)$$

where I (mm) is 3D cumulative infiltration and t (h) is the time. Then, K_s (mm h^{-1}) is estimated as a function of S as follow:

$$K_s = i_s - AS^2 \quad (4)$$

where i_s (mm h^{-1}) is the experimental steady-state infiltration rate, which is estimated by linear regression analysis of the last data points describing steady-state conditions on the I vs. t plot and corresponds to the slope of the regression line. The constants A (mm^{-1}) and B can be defined for the specific case of a Brooks and Corey relation (Eq. 2) and taking into account initial soil water content, θ_i (cm^3 cm^{-3}), as (Haverkamp et al., 1994):

$$A = \frac{\gamma}{r(\theta_s - \theta_i)} \quad (5a)$$

$$B = \frac{2-\beta}{3}\left[1-\left(\frac{\theta_i}{\theta_s}\right)^{\eta}\right] + \left(\frac{\theta_i}{\theta_s}\right)^{\eta} \quad (5b)$$

where γ (parameter for geometrical correction of the infiltration front shape) and β are coefficients that are commonly set at 0.75 and 0.6, respectively, for $\theta_i < 0.25\ \theta_s$, and r (mm) is the radius of the source. Finally, h_g is estimated by the following relationship (Lassabatere et al., 2006):

$$h_g = -\frac{S^2}{c_p(\theta_s - \theta_i)\left[1-\left(\frac{\theta_i}{\theta_s}\right)^{\eta}\right] K_s} \quad (6)$$

where:

$$c_p = \Gamma\left(1+\frac{1}{n}\right)\left\{\frac{\Gamma\left(m\eta - \frac{1}{n}\right)}{\Gamma(m\eta)} + \frac{\Gamma\left(m\eta + m - \frac{1}{n}\right)}{\Gamma(m\eta + m)}\right\} \quad (7)$$

in which Γ stands for the Gamma function.

Numerical simulations

Numerical simulations of the infiltration process were carried out to assess the ability of the Beerkan method to distinguish between crusted and non-crusted soils. In particular, the assumption was tested that the crust layer can be characterized by the parameters derived by BEST. The numerical simulations were carried out using the graphical software package VS2DI (Healy and Ronan, 1996), developed by the U.S. Geological Survey for simulating the movement of water and transport of solute or heat in variably saturated porous media. In particular, the finite-difference method was used to solve the Richards equation for water flow. According to Nasta et al. (2012), a zero pressure head boundary condition was imposed on the soil surface delimited by the ring, while free drainage was set at the bottom of the modeled domain. The BEST derived parameters were used in VS2DI to obtain the simulated cumulative infiltration curves. In particular, the parameters estimated along the row and on the bare inter-row area during the second field campaign (i.e., after development of a crusted layer in the latter area) were used to define the hydraulic properties of the underlying soil and the crust layer (thickness of 4 mm), respectively. Moreover, with the aim to assess the impact of the hydraulic conductivity of the crust layer on the simulated curves, different K_s values of the crust layer (from 94 to 166 mm h^{-1}) were considered. This range was established by considering the experimental K_s value for the crust layer plus or minus approximately 30% of this value. Then, the simulated cumulative infiltration curves ($I_{SIMULATION}$) were compared with the mean experimental infiltration curve obtained on the crusted soil during the second field campaign (I_{BEST}) using the root mean square error ($RMSE$):

$$RMSE = \sqrt{\frac{\sum_{i=1}^{N}\left[I_{SIMULATION}(t_i) - I_{BEST}(t_i)\right]^2}{N}} \quad (8)$$

where N is the total number of data pairs (15 in this investigation), and t_i is the time required for the infiltration of a given water depth.

Data analysis

Data sets were summarized by calculating the mean, M, and the associated coefficient of variation, CV. In particular, the cl, si, sa, ρ_b, and θ_s values were assumed to be site specific and therefore they were determined only in duplicate (cl, si, sa, $N = 2$) or, considering their low variability (ρ_b, θ_s), the arithmetic mean and the associated CV were calculated (Table 1). Temporal variability of θ_i was determined on the basis of ten replicate samples on each sampling date (Table 2).

Table 2. Minimum (Min), maximum (Max), mean, and coefficient of variation (CV, in %) of the soil water content at the time of sampling, θ_i (cm^3cm^{-3}), values for different sampling dates (sample size $N = 10$ for each sampling date).

Statistic	Sept 3, 2015	Sept 25, 2015	Jul 7, 2016
Min	0.051	0.093	0.047
Max	0.073	0.133	0.087
Mean	0.064 A	0.114 B	0.067 A
CV	12.0	10.9	18.1

The values in a row followed by the same upper case letter were not significantly different according to the Tukey Honestly Significant Difference test ($P < 0.05$). The values followed by a different upper case letter were significantly different.

Sorptivity values were assumed normally distributed. The K_s and h_g data were assumed to be log-normally distributed since the statistical distribution of these data is generally log-normal (Lee et al., 1985; Warrick, 1998). The geometric mean and the associated CV were therefore calculated to summarize K_s and h_g values using the appropriate ‘‘log-normal equations” (Lee et al., 1985). Statistical comparison between two sets of data was conducted using two-tailed t-tests, whereas the Tukey Honestly Significant Difference test was applied to compare three sets of data. The ln-transformed K_s and h_g data were used in the statistical comparison. A probability level, $P < 0.05$, was used for all statistical analyses. Since a fitting of the infiltration model to the transient data is required with BEST, the quality of the fit was evaluated by controlling both the general shape and the

relative error defined as (Lassabatere et al., 2006):

$$Er = \sqrt{\frac{\sum_{i=1}^{k}\left[I^{\exp}(t_i) - I_{est}(t_i)\right]^2}{\sum_{i=1}^{k} I^{\exp}(t_i)^2}} \quad (9)$$

where k is the number of data points considered for the transient state, I^{exp} is the experimental cumulative infiltration and I_{est} is the estimated cumulative infiltration using Eq. (3).

RESULTS AND DISCUSSION

Impact of surface crusting on soil hydraulic properties

The 42 infiltrations runs analyzed with the BEST-slope algorithm yielded plausible, i.e. positive, K_s values in all cases. In addition, the fitting of the infiltration model to the transient phase of the infiltration run always yielded low relative errors, denoting an acceptable approximation for transient cumulative infiltration according to the criterion proposed by Lassabatere et al. (2006) (Figure 3).

During the second field campaign, crusting phenomena, affecting water infiltration, were only detected between the rows. The protective role of vegetation along the rows was therefore effective, intercepting raindrops and preventing surface sealing (Dunne et al., 1991). The protective role along the vine-rows is well known, while in vine inter-rows the mulching practice is commonly applied to protect soil from raindrop impact (Celette et al., 2008). For the second campaign, the mean K_s value obtained between the rows was 1.64 times lower than the one obtained along the rows (Table 3). This latter value, equal to 212.4 mm h^{-1}, did not significantly differ from those of the first and third sampling dates. In addition, during the first and third campaigns, Beerkan runs carried out along and between the rows yielded similar K_s values, due to the absence of a crust between the rows. This experimental information suggested that cover influenced crusting development and consequently both the temporal and the spatial variation of the soil hydrological characteristics at the field site.

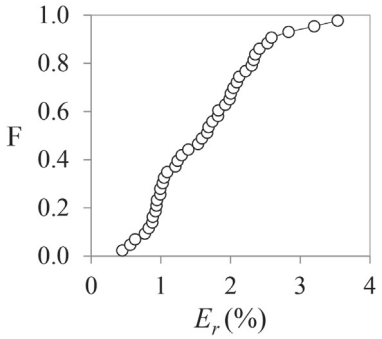

Fig. 3. Cumulative frequency distribution of the relative errors, E_r (%), of the fitting of the infiltration model to the transient phase of the infiltration runs.

Bradford et al. (1987) reported for 20 soils varying in texture from sand to clay a reduction in infiltration rate after 60 min of simulated rainfall (intensity of 63 mm h^{-1}), due to the effect of surface sealing on infiltration. Bagarello et al. (2014a), Alagna et al. (2016) and Di Prima et al. (2017) applied on five soils having different texture a BEST derived procedure to explain surface runoff and disturbance phenomena at the soil surface

Table 3. Minimum (Min), maximum (Max), mean, and coefficient of variation (CV, in %) of the saturated soil hydraulic conductivity, K_s (mm h^{-1}), soil sorptivity, S (mm h$^{-0.5}$), and the water pressure scale parameter, h_g (mm), values obtained from BEST experiments carried out along and within the rows on different sampling dates (sample size N = 7 for each variable and each date).

Variable	Rows/Inter-rows	Statistic	Sept 3, 2015	Sept 25, 2015	Jul 7, 2016
K_s	Rows	Min	188.1	159.1	158.4
		Max	289.1	369.1	234.2
		Mean	223.6 a A	212.4 a A	199.2 a A
		CV	15.4	27.6	14.1
	Inter-rows	Min	193.0	97.0	160.6
		Max	261.8	251.3	272.3
		Mean	229.5 a A	129.3 b B	192.5 a A
		CV	10.3	31.7	20.2
S	Rows	Min	105.5	84.0	87.7
		Max	130.6	99.8	112.9
		Mean	114.3 a A	94.4 a B	99.3 a B
		CV	6.8	5.6	9.1
	Inter-rows	Min	107.2	74.3	86.7
		Max	120.8	97.8	96.8
		Mean	113.5 a A	84.3 b B	91.2 b B
		CV	3.5	8.6	4.4
h_g	Rows	Min	–56.4	–50.3	–53.9
		Max	–40.1	–24.0	–32.3
		Mean	–47.7 a A	–37.9 a A	–40.7 a A
		CV	11.2	27.8	20.1
	Inter-rows	Min	–51.4	–66.8	–43.6
		Max	–40.8	–27.7	–23.7
		Mean	–45.8 a AB	–49.6 a A	–35.5 a B
		CV	9.3	31.5	19.7

For a given variable, the values in the column followed by a different lower case letter were significantly different according to a two tailed t test ($P < 0.05$). The values in a row followed by a different upper case letter were significantly different according to the Tukey Honestly Significant Difference test ($P < 0.05$).

occurring during intense rainfall events. These authors reported K_s values of the disturbed soil from nine to 33 times lower than the undisturbed soils. In particular, Di Prima et al. (2017) applied this methodology in a vineyard with a sandy-loam texture. These authors compared this simple methodology with rainfall simulation experiments establishing a physical link between the two methodologies through the kinetic energy of the rainfall and the gravitational potential energy of the water used for the Beerkan runs. They also indirectly demonstrated the occurrence of a certain degree of compaction and mechanical breakdown using a mini disk infiltrometer (Decagon, 2014). With this device, they reported a reduction of the unsaturated hydraulic conductivity by 2.3 times due to the seal formation. In another investigation carried out in Brazil with the BEST procedure, non-crusted soils were three times more conductive than the crusted soil (Souza et al., 2014).

Although this investigation was essentially focused on soil hydraulic conductivity, an analysis of the S and h_g parameters was carried out since they also depend on the measured infiltration curve. The means of soil sorptivity varied from 84.3 to 114.3 mm $h^{-0.5}$ (difference by a factor of 1.36) and the associated *CV*s ranged from 3.5% to 9.1% (Table 3). In all cases (sampling dates, position), relative variability was smaller for S than for K_s. This result was considered physically plausible. In fact, S is more expressive of the capillary forces exerted by the soil matrix, which are known not to vary much in space. Therefore, the estimates of S appeared plausible on the basis of the physical meaning of this variable (Alagna et al., 2016). Slightly but significantly lower S values were obtained during the last two sampling dates. During the first field campaign similar S values were obtained at the two positions, whereas during the second field campaign the effect of the crust layer on S was statistically significant although not very noticeable because the mean of S obtained between the rows was only 1.12 times lower than that obtained along the rows. Therefore, the crust layer determined a reduced ability of the porous medium to adsorb water due to capillarity (Alagna et al., 2016). This last effect was not persistent since the differences between the row and the inter-row area were smaller on the third sampling date. However, the sign of a decrease with time of the differences between means of S was weak since the factor of difference decreased only from 1.12 to 1.09.

The means of the pressure scale parameter varied from –49.6 to –35.5 mm (difference by a factor of 1.4) and the associated *CV*s ranged from 9.3% to 31.5% (Table 3). The h_g parameter is expected to be smaller (more negative) for a crust than for the underlying soil due to compaction and dispersion of fine material from aggregates (Smith, 1990). However, in this investigation the presence of a crust did not clearly affected the h_g parameter. As a matter of fact, a smaller h_g value in the inter-row area than the row area was only detected on the second sampling date, i.e. when a crust layer developed in the former zone. However, the h_g differences were not statistically significant.

Seasonal dynamics in hydraulic conductivity

For the first and the third campaign, the Beerkan runs carried out between the rows (inter-row areas) yielded comparable and statistically similar K_s values (Table 3). In both cases, the average K_s values were approximately 20 times higher than the expected saturated conductivity on the basis of the soil textural characteristics alone (e.g., K_s = 10.4 mm h^{-1} for a loam soil according to Carsel and Parrish, 1988). This circumstance suggested that soil macroporosity generated by soil tillage in the ploughed horizon likely influenced measurement of K_s (Alagna et al., 2016; Di Prima et al., 2017; Josa et al., 2010). In these conditions, the soil structure is expected to be particularly fragile, especially with reference to macroporosity, and hence unstable (Jarvis et al., 2008), which implies that clogging of the largest pores at the soil surface, as a consequence of the aggregates breakdown occurring during a rainstorm, can easily mitigate tillage effects on soil hydraulic properties (Ciollaro and Lamaddalena, 1998).

As discussed in the former section, the presence of the crust layer during the second field campaign clearly affected water infiltration between the rows. In particular, the presence of this layer implied that K_s was 1.5–1.8 times lower than that measured in the absence of the crusted layer. Crusting at the soil surface determined an increased hydraulic resistance to water penetration into soil (Alagna et al., 2013) since differences between the K_s datasets (second against both first and third sampling campaigns) were statistically significant. Crusting also resulted in a decrease of the lowest measurable K_s values, while the highest values remained unchanged (Table 3).

The tillage practices carried out in the spring 2016 removed any existing soil crust and thereby increased soil infiltration properties (Chahinian et al., 2006), suggesting a cycling occurrence of crusting phenomena within the year.

Many studies in the literature have reported similar dynamics, even in vineyards. In fact, infiltration experiments constitute an indirect measurement closely associated with sealing or crusting (Römkens et al., 1990), and the saturated hydraulic conductivity may vary considerably during the year if these phenomena occur. In particular, rainfall and wetting–drying cycles favor soil reconsolidation and soil-surface sealing or crusting, whereas tillage removes existing layering (Pare et al., 2011). For instance, Biddoccu et al. (2017) studied temporal variability of soil hydraulic properties in a vineyard on a silt loam soil. These authors reported hydraulic conductivity values measured during the summer four times lower than those measured during the wet season, due to the presence of a structural crust resulting from rainfall events following a long time after the last spring tillage.

Numerical validation

Figure 4 summarizes the numerical validation exercise that was carried out in this investigation. The smallest *RMSE* value was obtained for a crust layer having K_s = 133.2 mm h^{-1}. This value differed by a negligible factor of 1.03 from the in situ K_s value obtained on the layered system (crust layer, underlying soil; Table 3). Figure 4 also shows the comparison between the experimental cumulative infiltration curve and those simulated by assuming a non-layered system, i.e. all crust or all non-altered soil. The vertical homogeneity hypothesis yielded 3.6 to 6.3 times higher *RMSE* values as compared with the more realistic soil layering hypothesis. Both simulations (Figures 4b and 4c) supported the hypothesis that the experimental K_s value of 129 mm h^{-1} was representative of the hydraulic behavior of the least permeable layer (i.e., the crust layer). Therefore, the derived BEST parameters could properly be assigned to this layer, which controlled the flow and consequently cumulative infiltration of the stratified medium.

The results reported in this investigation were in agreement with those by Souza et al. (2014) and their suggestion that the Beerkan-based methodology should be usable to distinguish between crusted and non-crusted soils. Indeed, the hydrodynamic properties of both the crust and the underlying soil play a key role during a rainstorm, affecting the partition between infiltration and runoff (Assouline and Mualem, 2006, 2002).

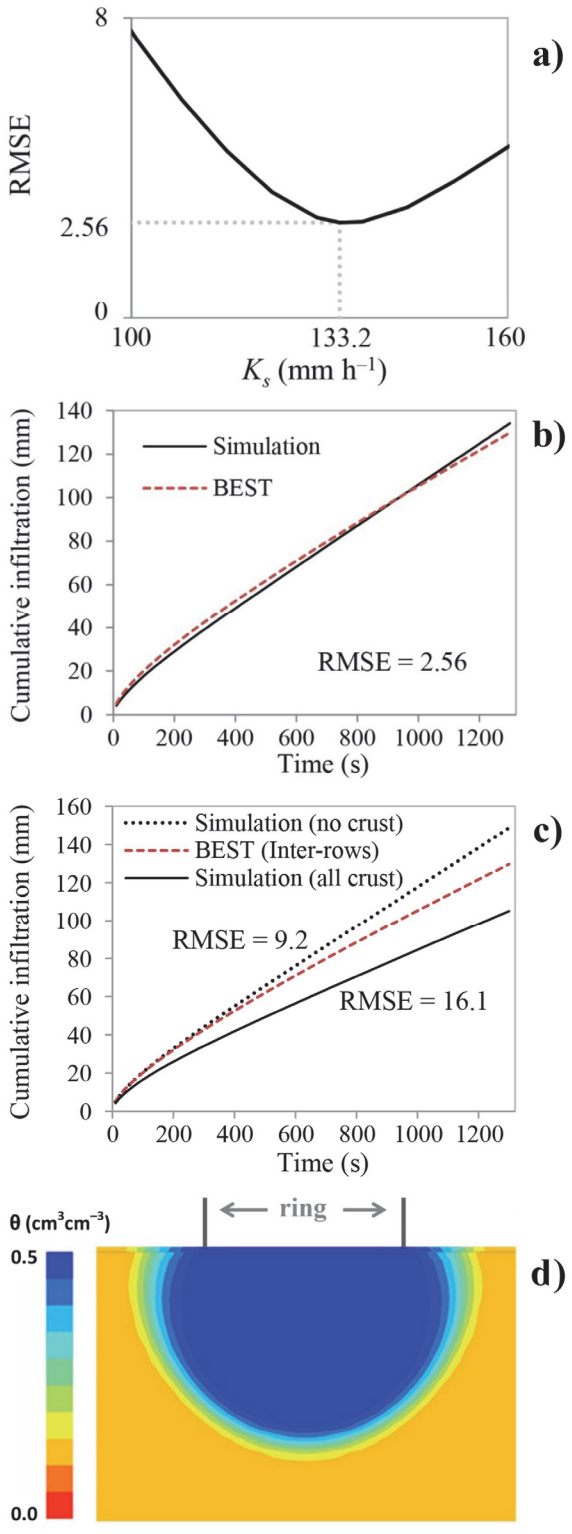

Fig. 4. (a) Root mean square error (*RMSE*) between the simulated and the experimental BEST curves vs. saturated soil hydraulic conductivity, K_s, values of the surface crust. (b) Infiltration curve simulated with a K_s value of the surface crust equal to 133.2 mm h^{-1} (line) compared with the measured curve on the second field campaign in the inter-row area (dashed line). (c) Infiltration curves simulated considering a vertically homogeneous soil profile (dotted and solid lines) compared with the measured curve on the second field campaign in the inter-row area (dashed line). (d) Soil water content profile simulated with K_s = 133.2 mm h^{-1} at the soil surface.

However, transient methods, as the Beerkan one, appears appropriate to characterize crusted soils, since the properties of the surface layer play a major role at early stages of the infiltration process (Vandervaere et al., 1997). Recently, Di Prima et al. (2016) showed that BEST-slope is less sensitive to the attainment of steady-state and allows to obtain accurate estimates of saturated soil hydraulic conductivity with less water and hence shorter experimental times than the other two BEST algorithms. For these reasons, BEST-slope appears more suitable, among the alternative algorithms, to characterize a crust layer.

Hydraulic conductivity functions

Two different approaches were applied in this investigation to check the ability of the BEST procedure to yield a different information between crusted and non-crusted soil. The first approach considered temporal changes of K_s values obtained between the rows before and after the intense storms fallen in September 2015 that led to the development of a weak but clearly detectable surface crust. As discussed above, with this approach, the third field campaign allowed us to detect the restoring of higher K_s values because tillage removed the crust. Figure 5a depicts the soil hydraulic conductivity functions obtained from averaged parameters for the different sampling dates at the vine inter-row area. While the curves of the first and the third sampling dates are close to one another, the curve of the second campaign departs from them rather clearly. Indeed, this result could be viewed as a suggestion that this latter curve might represent a crust layer characteristic curve. The second approach, developed with reference to the second sampling date, considered the spatial variation (i.e., rows vs. inter-rows) of conductivity, i.e. taking into account the protective role of the vegetation. A shift between the hydraulic conductivity functions for the row and inter-row areas was also detected, with the soil of the latter area denoting a reduced ability to conduct water for a given soil water content value (Figure 5b). Therefore, both approaches suggested that the BEST procedure was appropriate to show the impact of crusting on soil hydraulic conductivity.

Applicability of the Beerkan runs for the assessment of the crusted soil

A perplexity on the possibility to collect reliable data on crusted soils by a ponding infiltration experiment is related to the need to insert the ring into the soil. The doubt is that ring insertion could determine fractures in the crusted layer and these fractures could directly connect the ponded depth of water during the run with the underlying, non-crusted, soil layer (Vandervaere et al., 1997). In other terms, ring insertion could impede, in practice, measurement of fluxes though the crusted layer. In this investigation, fractures were not visually detected at the soil surface, perhaps because the soil was not very dry when the experiment on the crusted layer was performed (Table 2), the ring insertion depth was small (0.01 m), and insertion was carried out a few minutes after moistening the insertion circumference. Other ponding infiltration techniques, such as the single-ring pressure infiltrometer (Reynolds and Elrick, 1990) or, particularly, the simplified falling head technique (Bagarello et al., 2004), presuppose appreciably deeper insertions of the ring and, consequently, more risk to disrupt or alter the fragile crust layer at the soil surface during ring insertion. Therefore, the Beerkan run seems a more appropriate ponding infiltration run to prevent, or minimize, substantial alteration of

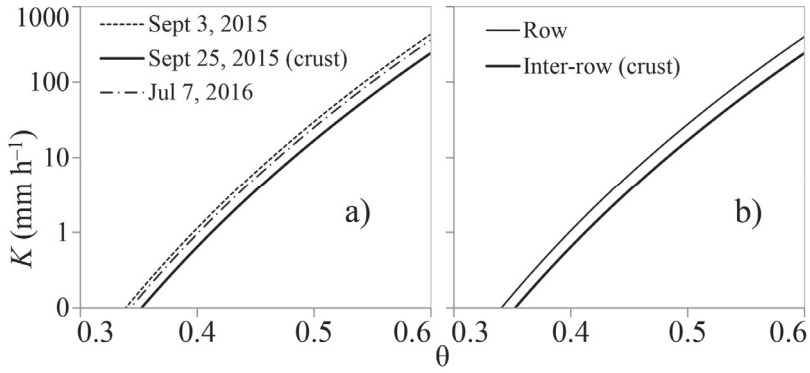

Fig. 5. Soil hydraulic conductivity functions obtained from averaged parameters for (a) different sampling dates and (b) along and between the vine-rows.

the surface to be sampled. Obviously, this conclusion needs additional testing but the premises are encouraging, also considering that Beerkan runs were successfully conducted in other crusted soils (Souza et al., 2014). In future application of the method, especially on well-developed crusts, it could be advisable to separately determine the particle size distribution for the crust layer and the subsoil, since alteration of the surface soil layer exposed to rain is known to also induce displacement of fine particles in the vertical direction (Levy et al., 1986).

CONCLUSIONS

A loam soil was sampled in a Mediterranean vineyard located at Marsala (western Sicily, Italy), with Beerkan infiltration experiments carried out along the rows direction and in the inter-rows during two consecutive growing seasons. Beerkan tests along with BEST-slope algorithm led to plausible estimates of soil hydraulic properties in both crusted and uncrusted conditions, allowing to assess the effect of the cycling occurrence of crusting due to rainfalls and wetting–drying cycles on the vineyard inter-rows.

A sampling strategy implying Beerkan tests carried out along and between the vine-rows was successfully applied. This strategy allowed to assess the reduction in hydraulic conductivity with extemporaneous measurements alone. Its main advantage is that it allows a rapid assessment of crusting severity affecting water infiltration. At the sampled site, the impact of crusting on saturated soil hydraulic conductivity was moderate.

In conclusion, the hypothesis that the Beerkan runs are suitable enough to detect the effect of the crust on flow and BEST estimates appeared reasonable. In the future, the Beerkan-based methodology should be checked in other crusted soils. Comparisons should also be established with other experimental methodologies. The applied methodology in this investigation could be used to explore in the future the functional dynamics of the crust layer under natural rainfall conditions.

Acknowledgements. This study was supported by grants from the Research Project CISV (grant n° 2014COMM-0363 CUP 872114000570002). S.D.P. also thanks I.A., E.B. and R.D.O.

REFERENCES

Alagna, V., Bagarello, V., Di Prima, S., Giordano, G., Iovino, M., 2013. A simple field method to measure the hydrodynamic properties of soil surface crust. Journal of Agricultural Engineering, 44, 74–79. https://doi.org/10.4081/jae.2013.(s1):e14

Alagna, V., Bagarello, V., Di Prima, S., Giordano, G., Iovino, M., 2016. Testing infiltration run effects on the estimated water transmission properties of a sandy-loam soil. Geoderma, 267, 24–33. https://doi.org/10.1016/j.geoderma.2015.12.029

Angulo-Jaramillo, R., Bagarello, V., Iovino, M., Lassabatere, L., 2016. Soils with specific features. In: Infiltration Measurements for Soil Hydraulic Characterization. Springer International Publishing, pp. 289–354. https://doi.org/10.1007/978-3-319-31788-5_4

Assouline, S., 2004. Rainfall-induced soil surface sealing. Vadose Zone Journal, 3, 570–591.

Assouline, S., Mualem, Y., 2002. Infiltration during soil sealing: The effect of areal heterogeneity of soil hydraulic properties. Water Resources Research, 38, 1286. https://doi.org/10.1029/2001WR001168

Assouline, S., Mualem, Y., 2006. Runoff from heterogeneous small bare catchments during soil surface sealing. Water Resources Research, 42, W12405. https://doi.org/10.1029/2005WR004592

Bagarello, V., Iovino, M., Elrick, D., 2004. A Simplified Falling-Head Technique for Rapid Determination of Field-Saturated Hydraulic Conductivity. Soil Science Society of America Journal, 68, 66. https://doi.org/10.2136/sssaj2004.6600

Bagarello, V., Stefano, C.D., Ferro, V., Iovino, M., Sgroi, A., 2010. Physical and hydraulic characterization of a clay soil at the plot scale. Journal of Hydrology, 387, 54–64. https://doi.org/10.1016/j.jhydrol.2010.03.029

Bagarello, V., Castellini, M., Di Prima, S., Iovino, M., 2014a. Soil hydraulic properties determined by infiltration experiments and different heights of water pouring. Geoderma, 213, 492–501. https://doi.org/10.1016/j.geoderma.2013.08.032

Bagarello, V., Di Prima, S., Iovino, M., 2014b. Comparing Alternative Algorithms to Analyze the Beerkan Infiltration Experiment. Soil Science Society of America Journal, 78, 724. https://doi.org/10.2136/sssaj2013.06.0231

Bedaiwy, M.N.A., 2008. Mechanical and hydraulic resistance relations in crust-topped soils. Catena, 72, 270–281. https://doi.org/10.1016/j.catena.2007.05.012

Biddoccu, M., Ferraris, S., Pitacco, A., Cavallo, E., 2017. Temporal variability of soil management effects on soil hydrological properties, runoff and erosion at the field scale in a hillslope vineyard, North-West Italy. Soil and Tillage Research, 165, 46–58. https://doi.org/10.1016/j.still.2016.07.017

Bradford, J.M., Ferris, J.E., Remley, P.A., 1987. Interrill soil erosion processes: I. Effect of surface sealing on infiltration,

runoff, and soil splash detachment. Soil Science Society of America Journal, 51, 1566–1571.

Brodie, I., Rosewell, C., 2007. Theoretical relationships between rainfall intensity and kinetic energy variants associated with stormwater particle washoff. Journal of Hydrology, 340, 40–47. https://doi.org/10.1016/j.jhydrol.2007.03.019

Brooks, R.H., Corey, T., 1964. hydraulic properties of porous media. Hydrol. Paper 3. Colorado State University, Fort Collins.

Burdine, N.T., 1953. Relative permeability calculation from pore size distribution data. Petr. Trans. Am. Inst. Min. Metall. Eng. 198, 71–77.

Carsel, R.F., Parrish, R.S., 1988. Developing joint probability distributions of soil water retention characteristics. Water Resour. Res., 24, 755–769. https://doi.org/10.1029/WR024i005p00755.

Castellini, M., Di Prima, S., Iovino, M., 2018. An assessment of the BEST procedure to estimate the soil water retention curve: A comparison with the evaporation method. Geoderma, 320, 82–94. https://doi.org/10.1016/j.geoderma.2018.01.014

Celette, F., Gaudin, R., Gary, C., 2008. Spatial and temporal changes to the water regime of a Mediterranean vineyard due to the adoption of cover cropping. European Journal of Agronomy, 29, 153–162. https://doi.org/10.1016/j.eja.2008.04.007

Chahinian, N., Moussa, R., Andrieux, P., Voltz, M., 2006. Accounting for temporal variation in soil hydrological properties when simulating surface runoff on tilled plots. Journal of Hydrology, 326, 135–152. https://doi.org/10.1016/j.jhydrol.2005.10.038

Ciollaro, G., Lamaddalena, N., 1998. Effect of tillage on the hydraulic properties of a vertic soil. Journal of Agricultural Engineering Research, 71, 147–155. https://doi.org/10.1006/jaer.1998.0312

Coutinho, A.P., Lassabatere, L., Montenegro, S., Antonino, A.C.D., Angulo-Jaramillo, R., Cabral, J.J.S.P., 2016. Hydraulic characterization and hydrological behaviour of a pilot permeable pavement in an urban centre, Brazil. Hydrol. Process., 30, 4242–4254. https://doi.org/10.1002/hyp.10985

Decagon, 2014. Minidisk Infiltrometer User's Manual. Decagon Devices, Inc., Pullman, USA, 24 p.

Di Prima, S., 2015. Automated single ring infiltrometer with a low-cost microcontroller circuit. Computers and Electronics in Agriculture, 118, 390–395. https://doi.org/10.1016/j.compag.2015.09.022

Di Prima, S., Lassabatere, L., Bagarello, V., Iovino, M., Angulo-Jaramillo, R., 2016. Testing a new automated single ring infiltrometer for Beerkan infiltration experiments. Geoderma, 262, 20–34. https://doi.org/10.1016/j.geoderma.2015.08.006

Di Prima, S., Bagarello, V., Lassabatere, L., Angulo-Jaramillo, R., Bautista, I., Burguet, M., Cerdà, A., Iovino, M., Prosdocimi, M., 2017. Comparing Beerkan infiltration tests with rainfall simulation experiments for hydraulic characterization of a sandy-loam soil. Hydrological Processes, 31, 3520–3532. https://doi.org/10.1002/hyp.11273

Di Prima, S., Concialdi, P., Lassabatere, L., Angulo-Jaramillo, R., Pirastru, M., Cerda, A., Keesstra, S., 2018a. Laboratory testing of Beerkan infiltration experiments for assessing the role of soil sealing on water infiltration. Catena, 167, 373–384. https://doi.org/10.1016/j.catena.2018.05.013

Di Prima, S., Rodrigo-Comino, J., Novara, A., Iovino, M., Pirastru, M., Keesstra, S., Cerda, A., 2018b. Assessing soil physical quality of citrus orchards under tillage, herbicide and organic managements. Pedosphere, 28, 3, (in press).

Dunne, T., Zhang, W., Aubry, B.F., 1991. Effects of rainfall, vegetation, and microtopography on infiltration and runoff. Water Resour. Res., 27, 2271–2285. https://doi.org/10.1029/91WR01585

Eigel, J.D., Moore, I., 1983. Effect of rainfall energy on infiltration into a bare soil. FAO.

Fox, D.M., Le Bissonnais, Y., 1998. Process-based analysis of aggregate stability effects on sealing, infiltration, and interrill erosion. Soil Science Society of America Journal, 62, 717–724.

Fox, D.M., Le Bissonnais, Y., Bruand, A., 1998. The effect of ponding depth on infiltration in a crusted surface depression. Catena, 32, 87–100. https://doi.org/10.1016/S0341-8162(98)00042-3

Freebairn, D.M., Gupta, S.C., Rawls, W.J., 1991. Influence of Aggregate Size and Microrelief on Development of Surface Soil Crusts. Soil Science Society of America Journal, 55, 188. https://doi.org/10.2136/sssaj1991.03615995005500010033x

Gee, G.W., Bauder, J.W., 1986. Particle-size analysis. In: Klute, A. (Ed.): Methods of Soil Analysis, Part 1: Physical and Mineralogical Methods. SSSA Book Series. Soil Science Society of America, American Society of Agronomy, pp. 383–411.

Gonzalez-Sosa, E., Braud, I., Dehotin, J., Lassabatère, L., Angulo-Jaramillo, R., Lagouy, M., Branger, F., Jacqueminet, C., Kermadi, S., Michel, K., 2010. Impact of land use on the hydraulic properties of the topsoil in a small French catchment. Hydrol. Process., 24, 2382–2399. https://doi.org/10.1002/hyp.7640

Haverkamp, R., Ross, P.J., Smettem, K.R.J., Parlange, J.Y., 1994. Three-dimensional analysis of infiltration from the disc infiltrometer: 2. Physically based infiltration equation. Water Resour. Res., 30, 2931–2935. https://doi.org/10.1029/94WR01788

Haverkamp, R., Arrúe, J., Vandervaere, J., Braud, I., Boulet, G., Laurent, J., Taha, A., Ross, P., Angulo-Jaramillo, R., 1996. Hydrological and thermal behaviour of the vadose zone in the area of Barrax and Tomelloso (Spain): Experimental study, analysis and modeling. Project UE n. EV5C-CT 92, 00-90.

Healy, R.W., Ronan, A.D., 1996. Documentation of computer program VS2Dh for simulation of energy transport in variably saturated porous media; modification of the US Geological Survey's computer program VS2DT (USGS Numbered Series No. 96–4230), Water-Resources Investigations Report. U.S. Geological Survey : Branch of Information Services [distributor].

Jarvis, N., Etana, A., Stagnitti, F., 2008. Water repellency, near-saturated infiltration and preferential solute transport in a macroporous clay soil. Geoderma, 143, 223–230. https://doi.org/10.1016/j.geoderma.2007.11.015

Josa, R., Ginovart, M., Solé, A., others, 2010. Effects of two tillage techniques on soil macroporosity in sub-humid environment. Int. Agrophys., 24, 139–147.

Lassabatere, L., Angulo-Jaramillo, R., Soria Ugalde, J.M., Cuenca, R., Braud, I., Haverkamp, R., 2006. Beerkan estimation of soil transfer parameters through infiltration experiments–BEST. Soil Science Society of America Journal, 70, 521. https://doi.org/10.2136/sssaj2005.0026

Lassabatere, L., Angulo-Jaramillo, R., Soria-Ugalde, J.M., Šimůnek, J., Haverkamp, R., 2009. Numerical evaluation of a set of analytical infiltration equations. Water Resources Research, 45, W12415. https://doi.org/10.1029/2009WR007941

Lassabatere, L., Angulo-Jaramillo, R., Goutaland, D., Letellier, L., Gaudet, J.P., Winiarski, T., Delolme, C., 2010. Effect of the settlement of sediments on water infiltration in two urban

infiltration basins. Geoderma, 156, 316–325. https://doi.org/10.1016/j.geoderma.2010.02.031

Lassabatere, L., Yilmaz, D., Peyrard, X., Peyneau, P.E., Lenoir, T., Šimůnek, J., Angulo-Jaramillo, R., 2014. New analytical model for cumulative infiltration into dual-permeability soils. Vadose Zone Journal, 13, 12. https://doi.org/10.2136/vzj2013.10.0181

Lee, D.M., Elrick, D.E., Reynolds, W.D., Clothier, B.E., 1985. A comparison of three field methods for measuring saturated hydraulic conductivity. Canadian Journal of Soil Science, 65, 563–573.

Levy, G., Shainberg, I., Morin, J., 1986. Factors affecting the stability of soil crusts in subsequent storms. Soil Science Society of America Journal, 50, 196–201. https://doi.org/10.2136/sssaj1986.03615995005000010037x

Mualem, Y., Assouline, S., Rohdenburg, H., 1990. Rainfall induced soil seal (A) A critical review of observations and models. Catena, 17, 185–203.

Mubarak, I., Mailhol, J.C., Angulo-Jaramillo, R., Ruelle, P., Boivin, P., Khaledian, M., 2009. Temporal variability in soil hydraulic properties under drip irrigation. Geoderma, 150, 158–165. https://doi.org/10.1016/j.geoderma.2009.01.022

Mubarak, I., Angulo-Jaramillo, R., Mailhol, J.C., Ruelle, P., Khaledian, M., Vauclin, M., 2010. Spatial analysis of soil surface hydraulic properties: Is infiltration method dependent? Agricultural Water Management, 97, 1517–1526. https://doi.org/10.1016/j.agwat.2010.05.005

Nasta, P., Lassabatere, L., Kandelous, M.M., Šimůnek, J., Angulo-Jaramillo, R., 2012. Analysis of the role of tortuosity and infiltration constants in the Beerkan method. Soil Science Society of America Journal, 76, 1999–2005.

Pare, N., Andrieux, P., Louchart, X., Biarnes, A., Voltz, M., 2011. Predicting the spatio-temporal dynamic of soil surface characteristics after tillage. Soil and Tillage Research, 114, 135–145. https://doi.org/10.1016/j.still.2011.04.003

Reynolds, W., 2008. Saturated hydraulic properties: ring infiltrometer. In: Carter, M.R., Gregorich, E.G. (Eds.): Soil Sampling and Methods of Analysis. 2nd ed. CRC Press, Boca Raton, pp. 1043–1056.

Reynolds, W.D., Elrick, D.E., 1990. Ponded infiltration from a single ring: I. Analysis of steady flow. Soil Science Society of America Journal, 54, 1233. https://doi.org/10.2136/sssaj1990.03615995005400050006x

Reynolds, W., Elrick, D., 2002. Pressure infiltrometer. In: Dane, J.H., Topp, C. (Eds.): Methods of Soil Analysis, Part 4. SSSA Book Series. Soil Science Society of America, American Society of Agronomy, pp. 826–836.

Reynolds, W.D., Elrick, D.E., 2005. Chapter 6 Measurement and characterization of soil hydraulic properties. In: Álvarez-Benedí, J., Muñoz-Carpena, R. (Eds.): Soil-Water-Solute Process Characterization – An Integrated Approach. CRC Press, Boca Raton Römkens, M., 1979. Soil crusting: when crusts form and quantifying their effects [Soil hydraulic properties]. Agricultural Reviews and Manuals ARM NC.

Römkens, M., Prasad, S., Parlange, J., 1990. Surface seal development in relation to rainstorm intensity. Catena, Supplement, 17, 1–11.

Rose, C., 1960. Soil detachment caused by rainfall. Soil Science, 89, 28–35.

Smith, R.E., 1990. Analysis of infiltration through a two-layer soil profile. Soil Science Society of America Journal, 54, 1219–1227. https://doi.org/10.2136/sssaj1990.03615995005400050004x

Souza, E.S., Antonino, A.C.D., Heck, R.J., Montenegro, S.M.G.L., Lima, J.R.S., Sampaio, E.V.S.B., Angulo-Jaramillo, R., Vauclin, M., 2014. Effect of crusting on the physical and hydraulic properties of a soil cropped with Castor beans (*Ricinus communis* L.) in the northeastern region of Brazil. Soil and Tillage Research, 141, 55–61. https://doi.org/10.1016/j.still.2014.04.004

van Genuchten, M.T., 1980. A closed-form equation for predicting the hydraulic conductivity of unsaturated soils. Soil Science Society of America Journal, 44, 892–898.

Vandervaere, J.-P., Peugeot, C., Vauclin, M., Angulo Jaramillo, R., Lebel, T., 1997. Estimating hydraulic conductivity of crusted soils using disc infiltrometers and minitensiometers. Journal of Hydrology, HAPEX-Sahel 188–189, 203–223. https://doi.org/10.1016/S0022-1694(96)03160-5

Warrick, A.W., 1998. Spatial variability. In: Hillel, D. (Ed.): Environmental Soil Physics. Academic Press, San Diego, CA, pp. 655–675.

West, L., Chiang, S., Norton, L., 1992. The morphology of surface crusts. Soil Crusting: Chemical and Physical Processes, 301–308.

Xu, X., Kiely, G., Lewis, C., 2009. Estimation and analysis of soil hydraulic properties through infiltration experiments: comparison of BEST and DL fitting methods. Soil Use and Management 25, 354–361. https://doi.org/10.1111/j.1475-2743.2009.00218.x

Yilmaz, D., Lassabatere, L., Angulo-Jaramillo, R., Deneele, D., Legret, M., 2010. Hydrodynamic characterization of basic oxygen furnace slag through an adapted BEST method. Vadose Zone Journal, 9, 107. https://doi.org/10.2136/vzj2009.0039

Yilmaz, D., Lassabatere, L., Deneele, D., Angulo-Jaramillo, R., Legret, M., 2013. Influence of carbonation on the microstructure and hydraulic properties of a basic oxygen furnace slag. Vadose Zone Journal, 12. https://doi.org/10.2136/vzj2012.0121

Received 23 June 2017
Accepted 15 February 2018